THE AERODYNAMICS OF WINGS IN LOW-DENSITY HYPERSONIC FLOW

RICHARD WALTER JEFFERY M.Sc.,D.I.C.

MAY 1975

A Thesis submitted for the degree of
Doctor of Philosophy of the University of London

Department of Aeronautics,
Imperial College,
Prince Consort Road,
LONDON SW7

ABSTRACT

A description of some features of low-density hypersonic flow past simple flat plate models and more complicated waverider shapes. Flat plate measurements, including the effects of a forward facing step, are compared with the results from a Monte Carlo calculation for exactly similar free stream conditions. Heat transfer and surface pressure measurements on waverider models are measured in both a low-density and a high-density facility and compared with simple prediction methods. Modifications to the wind tunnel, the design techniques for the models and the theoretical method for calculating tunnel stagnation conditions are described in an Appendix.

CONTENTS

7. NITROGEN TUNNEL TESTS: DELTA AND CARET WING STUDIES

APPENDIX A

LIST OF SYMBOLS USED

C_L	Lift coefficient
$\bar{V}$	Rarefaction parameter
M	Mach number
c	Chapman-Rubesin constant
Re	Reynolds number
L	Lift
D	Drag
W	Weight
A	Wing area
Kn	Knudsen number
λ	Mean free path
d	Typical body dimension
δ^*	Boundary layer displacement thickness
θ	Body surface angle
p	Pressure
γ	Ratio of specific heats
K	Hypersonic similarity parameter
μ	Viscosity
ρ	Density
U	Velocity
T	Temperature
$\bar{\chi}$	Viscous interaction parameter
a, b	Constants in viscous interaction theory
$\bar{c}$	Mean molecular speed
n	Molecular number density
N	Number flux

σ Ω	Molecular collision cross section
R	Gas constant
S	Molecular speed ratio
m	Molecular weight
b	Wing semi-span per unit chord
h	Wing thickness per unit chord
Ω c	Parameters of Squire's theory
y	Spanwise wing position
$\dot{q}$	Heat transfer rate
h	Enthalpy
ℓ	Wall thickness
c	Specific heat of model
ζ	Wing position parameter
C_H	Heat transfer coefficient
K	Heat transfer parameter
χ_ϵ	Cheng's viscous interaction parameter

SUBSCRIPTS

L	Based on length
∞	Free stream conditions
x	Distance in 'x' direction
w	Wall conditions
o	Stagnation conditions
fb	Free stream/body collisions
bf	Body/free stream collisions
μ	Based on viscosity
i	Incident stream
r	Reflected stream

fm	Free molecular
MAX	Maximum value
c	Cavity conditions
f	Originating in free stream
b	Originating in body

1. INTRODUCTION

Advanced hypersonic aerospace vehicles fall into three main groups; the bluff re-entry body, the lifting re-entry vehicle and the hypersonic transport aircraft. For all of these vehicles the period of hypersonic flight will take place at very high altitude in conditions of low air density where viscous effects will be important. These can significantly influence the aerodynamic characteristics of both slender and bluff hypersonic vehicles. Boylan and Griffith [1] report a reduction in C_L of 25% and a 40% reduction in lift to drag ratio at altitudes between 60 and 100 km and a comparison between wind tunnel tests and flight results for the Apollo Command Module show a strong viscous influence on trim angle of attack. A theoretical study by Boylan and Potter [2] predicts that the reduction in lift coefficient for the Gemini capsule at altitudes above 80 km could cause an error of 50 km in lateral range.

There is also an interest in the overall performance benefits to be gained from lifting re-entry vehicles. The increased lift to drag ratio is desirable not only because of improvements to aerodynamic heating loads but also for improved range. It would seem that a hypersonic lift to drag ratio of at least 2 is required, since for values less than 2 there are increasingly severe limitations on speed of recall, choice of landing site and permissible inclination of orbit of any re-entering space vehicle. For an Appollo-type capsule with aerodynamic braking to transfer into a Martian orbit the entry corridor is 3 n.m wide for a ballistic trajectory and 30 n.m when aerodynamic lift is used; for this type of vehicle an incidence of 20° produces an L/D of 0.4, but this alone widens the entry corridor ten times.

Viscous effects are important at the altitudes for which a lifting body would manoeuvre to select a landing site. Tests on a cone [3] indicate that the maximum lift to drag ratio is dependent on the value of the rarefaction parameter. Based on vehicle length, this parameter is defined as:

$$\bar{V}_L = M_\infty \left(\frac{c}{Re_{\infty,L}}\right)^{\frac{1}{2}} \quad .$$

For $\bar{V}_L > 0.01$ viscous effects modify the aerodynamic forces on the vehicle and for a 9° half angle cone with a base diameter of 8 ft and loading parameter defined by:

$$W/C_L.A = 100 \quad lbm/ft^2$$

aerodynamic viscous effects are important at altitudes above 175,000 ft. At 190,000 ft the lift to drag ratio is down 8% on the inviscid value and at 220,000 ft is down by 22%. For high lift drag ratio vehicles this decreased performance is due mainly to increased drag rather than decreased lift.

Future re-usable re-entry vehicles will need to provide both volume and the means to generate lift with the least amount of drag. If the vehicle be manoeuvrable, then the aerodynamic lift may be used to slow down the vehicle and a knowledge of the aerodynamics at high angles of attack is needed. Second-generation space-shuttle vehicles may well be of the lifting-body configuration in which some shape provides both the volume and the lift from an integrated wing-body shape. To some extent this has already been achieved on the existing re-entry capsules, albeit with poor aerodynamic performance during a ballistic trajectory. Küchemann [4] has suggested that the propulsion system should also be integrated into the one overall shape and proposes that the pressure fields over the vehicle could be used to support external combustion. Since the area of a propulsive nozzle for complete jet expansion grows rapidly with flight Mach number, the nozzle could be a part of the vehicle and the exhaust used to fill out or streamline the base of the body to reduce drag.

The proposed first generation space shuttle is a non-integrated vehicle, being made up from discrete components; separate wing, body, fin and engine to provide lift, volume, directional control and thrust. Studies have indicated the possible effects of viscosity on the aerodynamic characteristics, particularly the lift-drag ratio, for several idealised lifting re-entry vehicles. However, reports of viscous effects on the proposed Space Shuttle are sparse. Apart from statements that the Orbiter will be fitted with large aerodynamic surfaces for control throughout re-entry [70], no data is available in open publications. Boylan and Potter [71] have demonstrated important viscous effects at high altitude which reduce the cross-range performance compared with inviscid conditions. The quoted cross-range for the Space Shuttle is 1100 nautical miles [72], suggesting a lift-drag ratio of 1.3. The model tests described below suggest that this is a region where, for inviscid flow, the waverider demonstrates a clear advantage over a flat-bottom vehicle, increasing the lift coefficient from 0.6 to 0.7. Metcalf [36], from experiments with the same family of models, predicts that viscous effects could reduce the lift-drag ratio at zero incidence by one third at an altitude of 50 miles. However, the planned Space Shuttle mission would put the vehicle at 30° incidence at this altitude causing only a small decrease in aerodynamic performance by viscous interactions. It is, nevertheless, important that full account be taken of these phenomena and it is for this reason that measurements of surface pressure and heat transfer have been made in a hypersonic, viscous flow.

The basic requirement of the Space Shuttle vehicle is to reduce the cost of space transport by using a re-usable vehicle capable of operating from existing airport environments. Since the vehicle is to be prepared for its next flight in a relatively short time then the major part of the thermal protection system should be radiative rather than ablative. This design feature requires as low heat transfer rates as possible and so the first benefit of a lifting re-entry vehicle, where most deceleration takes place at high altitude, is attractive since the heat transfer is reduced. However, the time for deceleration is longer and the total heat load may not be significantly less. A vehicle with a significant lift to drag ratio will also possess a cross-range offering a choice of alternative landing sites. For the models described below, with a maximum lift at a lift to drag ratio of about 0.95, the cross-range would be 600 nautical miles. Townend [5] suggests that the requirement for minimum heat transfer can best be met by

i) operating at or near the incidence for maximum lift,
ii) designing for as high $C_{L_{MAX}}$ as possible,
iii) lift-drag ratio greater than unity to maximise cross-range performance.

He concludes that the Caret wing, or waverider, is the shape best suited to fulfill these requirements. This shape was originally suggested as a lifting re-entry body by Nonweiler [6] who proposed an infinite wedge as a known flow field from which to form a lifting body. The shape is a wedge of triangular planform with its leading edges in the plane of the shock wave produced by the wedge. The volume of the vehicle is fixed by the chosen wedge angle, the free stream Mach number and the required aspect ratio. If inviscid, the flow field is entirely known and contained by a plane shock wave. The upper surface is made parallel to the free stream flow and the generation of lift is dominated by pressures on the lower surface of the wing. The top surface of the vehicle has relatively little effect at hypersonic speeds when the underside is exposed to extremes of heat and high pressure. At subsonic speeds the major part of the lift force is generated by suction over the upper surface and the lower surface is then relatively unimportant. The low aspect ratio waverider with sharp leading edges supports a known separated flow field characterised by a pair of strong leading edge vortices above the wing surface. Viscosity is important in the initial formation of the vortex and the effects of viscosity become concentrated in the centre of the spiral, taking up only 5% of the diameter of the vortex. Effects of Reynolds number are small and cause only a small change in the position of the primary vortex; this leads to a small change in pressure distribution. The velocity is locally increased to several times the free stream value and the resulting pressure loss provides the lift force to support the slender delta wing when flying subsonically.

Disadvantages of the vehicle are its bluff base and large anhedral. The volume characteristics are not ideal with a very slender nose and thin wings, with sharp leading edges, projecting well below the centre line. However, the upper surface has been designed in the simple waverider assuming that all of the lift is produced by the lower wing surface. For attached leading edge flow, the design of the upper surface is an independent process and may be based on another known flow field for an expansion process. The design of the upper surface is important as it could reduce the vehicle base area and transfer lift from the bottom surface. An actual lifting body vehicle might incorporate an inverted "V" undersurface into a more realistic lifting body configuration. A suitable vehicle could be the Northrop HL-10 vehicle with integrated lift and volume but a large expanse of concave undersurface. From a stability point of view the aspect ratio of the vehicle should be at least 0.2. The damping derivative in pitch is then stabilising at angles of attack up to 45° but beyond this the vehicle is unstable in pitch. Figure 1 indicates some possible lifting body configurations, all based on the idea of a known two-dimensional flow field. Jones [7] has proposed similar vehicles based on the known three-dimensional flow-field of a cone.

Modifications proposed for the basic waverider, the name given to the family of Nonweiler wings since they are supported in flight, or ride, on a shock wave contained beneath the vehicle, include replacing the basic wedge by an isentropic compression surface. This has the potential advantage that three-dimensional intakes may be made a part of the compression surface to preserve two-dimensional flow for a combined lift and propulsion body. Two caret wings may be joined back to back to produce a "W" wing and the interference effect of the central wedge can enhance the performance of the basic waverider [8].

Much of the work done on waveriders to date has ignored viscous effects, which must be of importance for a waverider flying at very high altitude and very high Mach numbers. An understanding of the aerodynamics involved, including viscous effects, could mean that aerodynamically controlled manoeuvres might be possible even at the edge of the atmosphere. This would reduce the time for which reaction controls would be in use and decrease the power of such controls, both effects reducing the amount of control fuel carried. The purpose of this Thesis is the investigation of viscous effects on a possible space shuttle shape under low-density flow conditions at hypersonic speed. The work progresses in three distinct stages. In the first the rarefied flow over a flat plate at zero incidence is examined in order to add to our knowledge of the basic mechanisms of viscous interaction. This is extended to an investigation of a forward facing step on the flat plate and the separation effects in low-density flow resulting from, for example, a control surface or a badly fitted skin panel. Although relevant to the waverider problem these two fundamental flow fields were also studied as a part of a wider programme created around the wind tunnel facility used. In this a calculation method known as the Monte Carlo Direct Simulation technique is being developed to predict real rarefied flow fields in two and three dimensions. Hopefully this can be extended at some later time to include complex shapes such as the waveriders used in the present experimental work. Data from the present experiments are being used for a comparison with the flat plate and step theoretical predictions.

The second section of the Thesis deals with three possible waverider shapes in conditions of near-inviscid flow. This provides a comparison with the results from viscous flow and also measures their performance at very high angles of attack where viscous effects would certainly be small. These angles are typical of those used for aerodynamic braking on re-entry. The final section concerns the behaviour of the same three waverider shapes in a hypersonic, low-density viscous flow. Pressure and heat transfer distributions are measured and compared with simple inviscid theory.

The experiments were all carried out in two hypersonic wind tunnels at the Department of Aeronautics, Imperial College. The two facilities are complementary and between them cover a wide range of flow conditions. Figure 2 shows the operating ranges of the two facilities compared with a typical satellite re-entry profile. The space shuttle corridor may be taken as the lower quarter of the satellite profile and is covered by the lower edge of the Nitrogen Tunnel operating region. As explained [9], this lower line corresponds to a very low tunnel stagnation pressure and very high tunnel stagnation temperatures and is bounded at the high Mach number end by limitations of vacuum pump characteristics. This limit therefore corresponds to maximum heat transfer from the graphite resistance heater into the low pressure supply gas. Under these conditions of very high Mach number and very low Reynolds number viscous effects are of very great importance and it is for these reasons that the Nitrogen Tunnel was commissioned. The Gun Tunnel on the other hand is a high Reynolds number facility not suited to re-entry viscous effects but more concerned with sustained hypersonic flight within the atmosphere [10].

In any hypersonic facility the basic requirement is for gas at high temperature so that when the flow expands to high Mach number the test gas remains un-condensed. One way to avoid condensation has been to use a monatomic gas such as Helium. However, this is unrepresentative of flight in our atmosphere and a parallel theoretical study by Pullin [11] highlights the differences which may be expected by substituting monatomic for diatomic flow.

The two hypersonic facilities used for this work illustrate two basic techniques to obtain test conditions necessary to establish hypersonic flow. The Gun Tunnel uses a normal shock wave produced by a sudden release of high-pressure gas to heat the test gas ahead of a piston which maintains steady flow conditions for a very short time. The continuous running Nitrogen Tunnel uses a graphite resistance heater to heat the high-pressure test gas before it is expanded to a very high Mach number through a cooled nozzle. The same compressor plant is used by both facilities and the flow rates at high pressure are relatively low. The Nitrogen Tunnel operates at very high Mach numbers (~23), with very large expansion ratio, to give very low test section Reynolds numbers suitable for investigations of hypersonic low-density flows. The general layout of the laboratory is shown in Figure 3 and the photograph of Figure 4 shows the Nitrogen Tunnel, vacuum pumps and compressor plant.

2. FLAT PLATE THEORY

The hypersonic flow of a viscous fluid over a flat plate aligned with the flow has been studied theoretically and in experiments for some time past. The problem is one of an interaction due to viscosity, heat conduction and non-equilibrium effects within the test gas, since the potential flow solution for a sharp edged flat plate at zero incidence shows no disturbance at all over the top of the model. These viscous effects are particularly pronounced for a hypersonic low-density flow.

One of the first observations of this viscous interaction was an experiment by Becker at Langley Field Laboratory in 1949. A simple calculation showed that the thick boundary layer growing over the flat plate caused an apparent change in the body shape. The displacement effect was calculated and the pressure distribution over this effective body agreed with the experimental results.

Since then, attempts to explain viscous effects on the flow over a flat plate have fallen into two main groups. At the back of the model continuum flow may be established with a distinct shock, inviscid region and boundary layer. At the leading edge the explanation is based on kinetic theory and flow models attempt to represent the molecular collision processes. Between these two extremes is a transition region where the shock and boundary layer interact and neither kinetic theory nor continuum theory can fully explain the measured pressure distributions. Attempts to correlate results from different facilities have fallen into two main groups; extending continuum theory to the front of the model or kinetic theory back towards the region of continuum flow. A typical flat plate flow field is shown in Figure 5, the dimensions of the various zones being representative of a model in the Nitrogen Tunnel. At a Mach number of 22 the free stream density is 8.8×10^{-6} of the density in the stagnation chamber of the wind tunnel. Under these conditions of rarefied flow continuum theory no longer applies but the number density is such that assumptions of free molecular kinetic theory are not valid. The Knudsen number is defined as:

$$Kn = \lambda/d$$

and is a useful measure of the degree of rarefaction of a flow field. For $Kn \ll 1$, which characterises a continuum flow, inter molecular collisions determine the flow, since disturbances cannot travel out from the solid boundary any significant distance except through molecular collision processes. The gas is in near thermal equilibrium characterised by a Maxwellian distribution of velocities around some mean value. Viscous and heat conduction effects are explained by macroscopic transport coefficients in a continuum flow; the Navier Stokes equations.

When the Knudsen number is large collisions between molecules and the solid surface are the dominant feature. Molecules from the body travel far out before colliding with a free stream molecule. The effect of the re-emitted molecules on the incident stream may be neglected and because the incident stream is unaffected by the presence of the body, shock waves are not expected and the boundary layer is extremely diffuse. Incident and reflected molecules can be treated separately and in an extreme case the thermal energy may be neglected compared with the mean flow energy and there is a close resemblance with the Newtonian flow approximation. The free molecular flow can be treated mathematically since the basic kinetic theory assumptions are valid. The interaction between incident molecules and the surface must be specified by two parameters. The thermal accommodation coefficient defines the degree to which the incident molecules have their mean energy accommodated to an energy level appropriate to being re-emitted with a Maxwellian distribution corresponding to the surface temperature. Experiment suggests that energies associated with all degrees of freedom are accommodated to the same extent. The second parameter defines the type of reflection, specular or diffuse, at the surface. The incident distribution function may be non-Maxwellian but can, in any case, be obtained from the local conditions of the flow.

A rarefied flow is one in which the molecular mean free path is comparable to some significant dimension in the flow field, $Kn = O(1)$. Whether the flow is more like a continuum or is free molecular in nature depends on the geometry of the body. Neither solution can be applied rigourously since the solution falls between the two extreme cases. The characteristic time between molecular collisions is comparable with the transit time through some distance associated with the flow field. This may vary greatly through the flow field due to steep gradients of pressure, velocity or temperature and any theory which may be applied to the region must accommodate this as well as matching the free molecular limit upstream and the continuum limit downstream. Continuum theory is rejected in favour of a kinetic theory but the molecular collisions must be considered in detail. Non-Maxwellian velocity distribution and internal modes of polyatomic molecules complicate the simple theory. Inelastic collisions between polyatomic molecules involve the transfer of energy and the time taken for this energy transfer may be comparable to the time between collisions, or the transit time for a molecule. The relaxation time for a particular mode is a measure of the time taken for energy adjustment and each mode is considered separately, since there may be an order of magnitude difference between relaxation times of different modes.

Analyses of rarefied gas flows fall into two groups: methods which extend continuum theory towards the kinetic region and methods to extend kinetic theory to predict continuum flow. In continuum theory flat plate pressure distributions are explained in terms of the boundary layer which grows rapidly in low-density flows because of viscosity of the gas. For a flat plate at zero incidence the displacement thickness of a boundary layer, δ^*, is given by:

$$\delta^*/x \sim \mathrm{Re}_{\infty_x}^{-\frac{1}{2}}$$

for an incompressible flow. A relevant definition of the Knudsen number, associated with this boundary layer growth, might be:

$$\mathrm{Kn} = \frac{\lambda_\infty}{\delta^*} \sim M_\infty \, \mathrm{Re}_{\infty_x}^{-\frac{1}{2}} \; .$$

This will be seen to be a fundamental parameter related to the length scale of a rarefied gas flow. The pressure may be thought of as being due to an effective change in shape by the boundary layer displacement thickness. The tangent wedge approximation [37] for a body with surface angle θ predicts that:

$$\frac{p}{p_\infty} = 1 + \gamma K^2 \left[\left(\left(\frac{\gamma+1}{4} \right)^2 + \frac{1}{K^2} \right)^{\frac{1}{2}} + \frac{\gamma+1}{4} \right]$$

where K is the hypersonic similarity parameter for the effective shape and the surface angle for the plate, at zero incidence, is given by:

$$\theta = \frac{d\delta^*}{dx} \quad \text{and} \quad K = M_\infty \theta \; .$$

For laminar flow the displacement thickness is defined by:

$$\delta^* \sim x . (\mathrm{Re}_x)^{-\frac{1}{2}}$$

This can be re-written in terms of the basic flow properties as:

$$\frac{\delta^*}{x} \sim \left(\frac{c}{\mathrm{Re}_x} \right)^{\frac{1}{2}} \frac{M^2}{(p/p_\infty)^{\frac{1}{2}}}$$

In the strong interaction limit $K > 1$, $K^2 \gg 1$ and the tangent wedge approximation predicts that:

$$\frac{p}{p_\infty} \simeq \frac{\gamma(\gamma+1)}{2} K^2 = \frac{\gamma(\gamma+1)}{2} M_\infty^2 \theta^2 \ .$$

Substituting this expression for p/p_∞ above, and solving for δ^*:

$$\frac{\delta^*}{x} \sim \left(\frac{c}{Re_x} M_\infty^2\right)^{\frac{1}{4}} = \bar{V}^{\frac{1}{2}}$$

where $\bar{V}$ is defined as the rarefaction parameter and is directly related to the Knudsen number defined for an incompressible flow. The hypersonic similarity parameter for a laminar flow with strong interaction is given by:

$$K^2 = M_\infty^3 \cdot \left(\frac{c}{Re_x}\right)^{\frac{1}{2}} = \bar{\chi}$$

where $\bar{\chi}$ is the hypersonic viscous interaction parameter. So for strong interaction on a flat plate at zero incidence the pressure distribution due to viscous interaction may be written as:

$$\frac{p}{p_\infty} = a\bar{\chi} + b + 0\left(\frac{1}{\bar{\chi}}\right) \qquad \text{for} \quad \bar{\chi} \gg 1 \ .$$

For weak interaction with, $K < 1$ and $K^2 \ll 1$, the tangent wedge approximation may be written:

$$\frac{p}{p_\infty} = 1 + \gamma K + \frac{\gamma(\gamma+1)}{4} K^2 + \dots.$$

and $\qquad p/p_\infty \sim 1.$

So, immediately from the definition of δ^* we have:

$$\frac{\delta^*}{x} \sim M_\infty^2 \left(\frac{c}{Re_x}\right)^{\frac{1}{2}} \quad \text{and in this case} \quad K = \bar{\chi} \ .$$

So for a weak interaction flow field the pressure distribution is given by:

$$\frac{p}{p_\infty} \sim 1 + a\bar{\chi} \ .$$

The boundary layer displacement thickness grows as $x^{\frac{1}{2}}$ compared with $x^{\frac{3}{4}}$ for the strong interaction flowfield. For the present experiments the viscous interaction is strong and, in fact, for free stream Mach numbers greater than 8 the weak interaction region may not exist. The experimental results have been compared with predictions of strong interaction theory. The pressure distribution is described by:

$$\frac{p}{p_\infty} = a_1\bar{\chi} + a_2$$

where $a_1 = \frac{9}{32}\gamma(\gamma+1)\delta_0^2$

$$a_2 = \frac{10}{3}\delta_2 + \frac{32}{9}\frac{(3\gamma+1)}{\gamma(\gamma+1)^2}\frac{1}{\delta_0^2}$$

δ_0 and δ_2 are constants related to the strong interaction displacement thickness function, $G(g_b, Pr, \beta)$. The function is dependent on the wall temperature, the Prandtl number and the pressure gradient parameter. Li and Nagamatsu [40] tabulate the strong interaction displacement thickness function in terms of the ratio between wall and stagnation temperature. The effect of cooling the model is to reduce viscous interaction by thinning the boundary layer. In terms of parameters relevant to the present experiment the constant δ_0 is given by:

$$\delta_0^2 = -0.246(T_w/T_o)^2 + 0.539(T_w/T_o) + 0.397$$

and this analytic form is used to calculate the strong interaction flat plate pressure in the expression:

$$\frac{p}{p_\infty} \sim \frac{9}{32}\gamma(\gamma+1)\delta_0^2\,\bar{\chi}\ .$$

This gives the surface pressure to a first order approximation. In terms of the fundamental rarefied flow parameters, $\bar{V}$, $\bar{\chi}$, the pressure is dependent on the temperature ratio of the experiment.

Both strong interaction and weak interaction theory predict that surface pressure increases right up to the leading edge. Experiment shows a plateau region close to the leading edge and beyond this point, if the flow model is to hold, the surface pressure should fall towards the free molecular value at the leading edge. This transition from continuum to kinetic regimes corresponds to the merged layer region where the shock and boundary layer coalesce. This represents the extremes of both theoretical models. Becker [17], in an attempt to bridge between the two, suggests that the wall Knudsen number changes from the kinetic theory prediction to that for a merged flow. From his experimental results he justifies the use of the parameter:

$$M_\infty / Re_{w,x}$$

to correlate pressure measurements in this transition region and this, in turn, is related to the modified parameter:

$$\bar{V}_{\infty,x}\left(\frac{T_w}{T_o}\right)^{0.5} .$$

This is consistent with the results of his experiment and with other results which indicate, for $\bar{V}_x \sim O(1)$, there is a further dependence on the freestream-to-wall temperature ratio.

Either side of this merged layer are two clearly defined regions, one of kinetic flow, the other the beginnings of continuum flow. The downstream limit of strong and weak viscous interaction for continuum flow have already been described but the slip flow region represents the immediate boundary to the merged layer and is defined by:

$$0.01 < Kn = \frac{M}{\sqrt{Re}} < 0.1 , \quad Re > 1$$

Typically the mean free path (indicating the move towards kinetic theory) is less than 10% of the boundary layer thickness. Since either the Mach number must be large or the Reynolds number small, slip flow can only occur in coincidence with strong compressibility or viscous effects.

These phenomena may mask the rarefaction effects associated with the molecular structure and significant departures from continuum behaviour are not apparent until the transition region is reached. Because of the complexity of the situation in this and the transition regime there are few solutions for specific flow situations. Empirical solutions are based on experimental results but the general feature of velocity slip and temperature jump at the surface is to reduce skin friction and heat transfer, if other factors remain the same. However, the actual measurement of slip velocity and temperature jump is far from straightforward. Becker [17] in his paper proposing the modified rarefaction parameter for the merged layer includes data for slip velocity; this he calculates by extrapolating pitot pressure to the value at the wall and assumes zero temperature jump at the surface. He concludes that a typical value for the slip velocity would be 0.4 of the freestream velocity for $\bar{V}_x = 0.5$, under conditions of the present experiment. Pullin also presents calculations of the surface velocity based on his Monte Carlo technique for similar conditions and these are shown below.

One of the basic assumptions of kinetic theory is that molecules travel a long distance between collisions; another is that molecules are thought of as point molecules. Obviously both of these assumptions are invalid; at all times the molecules are diatomic and only very close to the leading edge is the physical scale such that molecules travel a relatively long distance between collisions. The free-molecular limit is not found at the leading edge; some molecules reflect forward from this edge and so the undisturbed flow is found some, molecular, distance in front of the sharp model.

A more detailed analysis of the collision process close to the leading edge indicates, for example, that the idea of a single mean free path within the flow is not valid. The flow around the leading edge is dominated by two streams of molecules, those in the free stream and those being re-emitted from the body. The probability of collision between two molecules is proportional to the relative velocity between free stream and body molecules. These collisions, as well as being the most probable, involve the largest energy transfer. So this type of collision will dominate the region in which they occur and a suitable length parameter would be the mean free path of a free stream molecule in collision with a body molecule, λ_{fb}.

A free stream molecule carries with it a sphere of influence with a diameter equal to the effective molecular diameter. Any other molecule within this diameter will be in collision with the free stream molecule travelling at its mean molecular speed, $\bar{c}$. All other molecules are considered to be stationary. The volume swept in unit time is $\pi d^2 \bar{c}$ and if n is the number of molecules per unit volume of gas, then the number of collisions in unit time is $n\pi d^2 \bar{c}$. During this time the molecule has travelled a distance $\bar{c}$ so the mean free path λ is given by:

$$\lambda = \frac{1}{n\pi d^2}$$

Obviously, this simple argument is only true if all other molecules are at rest. But it is sufficient to show that:

$$\lambda \propto \frac{1}{n\sigma}$$

where n is the number density and σ is a collision cross section. This is the basis for a mean free path definition for all molecular models. Dependent on the actual molecular model being used the definition of a collision cross section is of fundamental importance. This collision cross section should be appropriate to the relative velocity of free stream and body molecules and should be based on some macroscopic property of the gas; in our case viscosity with an inverse power law molecular model.

So the definition of an appropriate mean free path becomes

$$\lambda_{fb} = \frac{1}{n_B\,\Omega_{fb}} = \frac{1}{n_B\,\sigma_\mu}$$

where n_B is the number density of molecules from the body surface and Ω_{fb} is a collision cross-section, in this case the viscosity cross-section, σ_μ, where

$$\Omega_{fb} = \sigma_\mu = 2\pi\left(\frac{2\alpha a}{m}\right)^{2/\alpha} A_2(\alpha)\, g^{-4/\alpha}$$

and $$A_2(\alpha) = 5\sqrt{\frac{mKT}{\pi}}\left(\frac{2KT}{\alpha a}\right)^{2/\alpha}\left[8\mu\,\Gamma\left(4 - \frac{2}{\alpha}\right)\right]^{-1}$$

This definition, in turn, assumes an inverse power law molecular model where the intermolecular potential, V, is given by:

$$V = \frac{a}{r^\alpha}$$

The constants a, α are chosen to fit experimental data for a given gas over the temperature range in question. To allow for all molecular models to be covered by a single definition of λ_{fb} a slight modification is necessary. For rigid sphere molecules of radius σ the potential may be written

$$V = \lim_{\alpha\to\infty} c\left(\frac{\sigma}{r}\right)^\alpha \qquad \begin{array}{l} V=0;\ r>\sigma \\ V=\infty;\ r<\sigma \end{array}$$

For an equivalence between the two expressions for the intermolecular potential

$$a \equiv c\,\sigma^\alpha$$

substituting above:

$$\Omega_{fb} = \lim_{\alpha\to\infty}\left[2\pi\left(\frac{2c\sigma^\alpha\alpha}{m}\right)^{2/\alpha} A_2(\alpha)\, g^{-4/\alpha}\right]$$

$$= \lim_{\alpha\to\infty}\left[2\pi\left(\frac{2c}{m}\right)^{2/\alpha}\alpha^{2/\alpha}\sigma^2\, A_2(\alpha)\, g^{-4/\alpha}\right] .$$

It is shown [64] that:

$$\lim_{\alpha\to\infty} A_2(\alpha) = 1/3$$

$$\lim_{\alpha\to\infty} \alpha^{2/\alpha} = 1$$

$$\lim_{\alpha\to\infty} \left(\frac{2c}{m}\right)^{2/\alpha} g^{-4/\alpha} = 1 .$$

Hence, for hard sphere molecules,

$$\Omega_{fb} = \frac{2}{3}\pi\sigma^2 .$$

But the total cross-section of a hard sphere molecule of radius σ is $\pi\sigma^2$. So the original definition of Ω_{fb} should be modified to include hard sphere molecules and we have:

$$\Omega_{fb} = \frac{1}{1}\sigma_\mu\frac{3}{2} \quad \text{and} \quad \lambda_{fb} = \frac{1}{n_B\sigma_\mu}\frac{2}{3} .$$

The numerical values for α must be matched to the values for nitrogen under conditions appropriate to the present series of experiments in the Nitrogen Tunnel. Since the collision cross-section is based on the viscosity of nitrogen this matching should be with reliable experimental data. Furthermore, since the collision cross-section depends on the relative molecular velocity, the viscosity ~~data~~ should be calculated for a temperature corresponding to the ~~sum~~ relative velocity of stagnation and body molecules. ~~temperatures~~. Over the temperature range from 1500°K to 2500°K the viscosity of Nitrogen is given by [65]:

$$\mu(T) \propto T^{0.6476}$$

For the case of an inverse square law molecule the viscosity, in terms of α, is given by:

$$\mu(T) \propto T^{(1/2 + 2/\alpha)}$$

and a matching of the molecular model to the relevant experimental data gives a value 13.550 for α and σ_μ is given by:

$$\sigma_\mu = \frac{3}{2}\,\frac{5}{4}\,\frac{4^{2/\alpha}\pi^{1/2}}{\Gamma(4 - 2/\alpha)}\left(\frac{KT}{m}\right)^{2/\alpha + 1/2}\frac{m}{\mu}\,g^{-4/\alpha}$$

An alternative definition for λ_{fb} can be put forward to allow for more complicated molecular encounters:

$$\lambda_{fb} = \frac{1}{n_B\, A_{fg(g)}}$$

where $A_{fg(g)}$ is a collision cross-section at an appropriate relative velocity. This collision cross-section is defined as:

$$A_{fg(g)} = \pi\sigma^2\, Q^{(2)*}\, g^*$$

where $Q^{(2)*}$ and g^* are collision integrals relevant to the molecular model being used. Pullin [11] gives the reduced collision integrals for both Lennard Jones 6-12 and Morse potentials in which the molecular model allows for an attractive force between molecules when the separation is large compared with their molecular diameter.

Close to the leading edge of the flat plate model the surface pressure should very nearly equal the free molecular value, if the conditions of the experiment are such that free molecular conditions can exist over a measurable distance. The free molecular pressure is dependent on the molecular reflection from the surface. If the molecules are reflected specularly the normal velocity component is reversed but the tangential velocity remains unchanged. For diffuse reflection the molecule is momentarily trapped in the surface while the incident temperature adjusts towards that of the surface; the molecule is then re-emitted in a random direction with a Maxwellian velocity distribution corresponding to some temperature less than the wall temperature. The accommodation coefficient for the surface is the degree to which the molecules have their temperature adjusted to that of the surface and the numerical value lies between 0 and 1.

In a truly free molecular flow the molecules reflected from the body surface do not collide with the incoming molecules to any large extent so the velocity distribution remains Maxwellian. Molecules are reflected diffusely with a temperature T_r, different, in general, from that of the gas or the surface. Since incident and reflected molecules are independent their mass and momentum transfer may be treated separately. The molecular velocity is made up in part of the body velocity and the remainder is due to random molecular motion. The total number of incident molecules which collide with unit area of the surface in unit time is:

$$N_i = n_i\sqrt{\frac{RT_i}{2\pi}}\,[e^{-S_v^2} + S_v\sqrt{\pi}(1 + \mathrm{erf}\,S_v)]$$

where $S_v = \frac{\bar{v}}{C_i} = S \sin\theta$ where $S = \sqrt{\frac{\gamma}{2}}\,M$.

The reflected molecules are emitted from a gas at rest relative to the surface. These molecules have a random Maxwellian motion at a temperature T_r, dependent on the surface accommodation coefficient. Then

$$N_r = n_r\sqrt{\frac{RT_r}{2\pi}} \; .$$

If the number of molecules is conserved during the reflection process,

$$n_r = n_i\sqrt{\frac{T_i}{T_r}}\,[e^{-S_v^2} + S_v\sqrt{\pi}(1 + \mathrm{erf}\,S_v)] \; ,$$

and for a flat plate at zero incidence:

$$n_r = n_i\sqrt{\frac{T_i}{T_r}}$$

and the free molecular number flux for a flat plate at zero incidence is given by:

$$N_{fm} = n_i\sqrt{\frac{RT_i}{2\pi}} = n_\infty\sqrt{\frac{RT_\infty}{2\pi}} \; .$$

The free molecular pressure on the surface is the normal momentum exchanged at the surface by incident and reflected molecules. For incident molecules the normal momentum change gives:

$$C_{p_i} = \sin^2\theta \left[\frac{1}{\sqrt{\pi}\, S_v} e^{-S_v^2} + \left(1 + \frac{1}{2S_v^2}\right) (1 + \mathrm{erf}\ S_v) \right]$$

and for a flat plate at zero incidence this reduces to

$$C_{p_{i_o}} = \frac{1}{2S^2} .$$

For the reflected molecules:

$$C_{p_r} = \frac{\sin^2\theta}{2S_v^2} \sqrt{\frac{T_r}{T_i}} \left[e^{-S_v^2} + \sqrt{\pi}\, S_v (1 + \mathrm{erf}\ S_v) \right]$$

and, again, for a flat plate at zero incidence:

$$C_{p_{r_o}} = \frac{1}{2S^2} \sqrt{\frac{T_r}{T_i}} .$$

So the total pressure due to incident and reflected molecules is given by:

$$C_p = \frac{1}{2S^2}\left[1 + \sqrt{\frac{T_r}{T_i}}\right] \qquad \text{or} \qquad p_w = \frac{p_\infty}{2}\left\{1 + \sqrt{\frac{T_r}{T_i}}\right\}$$

In order to calculate the free molecular pressure at the leading edge the incident temperature is assumed to be the free stream temperature, T_∞, and the surface or reflected temperature assumed to be the wall temperature, T_w. Then

$$p_{w_{FM}} = \frac{p_\infty}{2}\left[1 + \left(\frac{T_w}{T_\infty}\right)^{\frac{1}{2}}\right]$$

In practice the extent of the free molecular region is small and analysis based on kinetic theory is used to predict surface properties away from the leading edge. Three distinct methods are used in kinetic theory methods:

i) The gas flow is treated as a number of separate but interacting streams. Hamel and Cooper [12] consider an incident free stream, a body reflected stream and a scattered stream made up of products of the first collision processes. The length scale associated with these techniques is λ_{fb}.

ii) The collision integral of the Boltzmann equation is simplified by linear approximations which allow for all the properties of the gas. Huang et al. [13] have presented solutions for the leading edge problem of a diatomic gas with internal energy. They found that the surface pressure is lower for a diatomic gas with internal degree of freedom than for a monatomic gas under similar conditions. Each linear approximation has its own relaxation parameter which is matched to experimental data giving the complete solution a response similar to the test gas.

iii) Under non-equilibrium conditions, such as exist over the flat plate, a solution of the Boltzmann equation is not possible by analytic or finite difference techniques because of the complicated collision integral. One method is to make linear approximations to this collision integral. Bird's [14] Direct Simulation Technique attempts to use Monte Carlo techniques to model the collision process and replace the collision integral by a simulation. He uses a sample of particles as a model of the gas dynamic system. Each particle is free to move in a random fashion and its movement is followed along with all the other particles. The collision integral can be computed from the model particles once an appropriate model for the collision process is introduced. The original work with this technique was confined to flows of monatomic gases with elastic spherical molecular models. This has recently been extended, notably by Pullin [11], to analysis of diatomic gases. He adopts an approximate form of a classical model used by Parker which has been successfully used to predict the temperature dependence of rotational collision numbers [15]. This gives an approximate analytical expression for energy exchange in a collision in terms of the conditions before the event. From this the post-collision parameters are determined from conservation equations. This model is used for high relative velocity collisions and retains the correlation between pre- and post-collision properties, particularly the directed velocity. He checked the collision model by simulating the rotational relaxation of Nitrogen and it was found necessary to introduce a weighting to ensure the equipartition of energy between rotational and translational modes. It was also necessary to introduce an elastic collision probability parameter to compensate for the behaviour at low collision energy and to drive the gas into a state of energy equipartition near to equilibrium. For low energy collisions he uses the model of Larson and Borganakke, a statistical model which gives the precise approach to equilibrium but does not correlate between pre- and post-collision properties. For low energy encounters this defect is not serious. Pullin's calculations have been based on Nitrogen Tunnel conditions with a diatomic test gas and so represent a unique comparison between theory and experiment.

It is in the merged layer regime that experiments provide the easiest way to investigate the flowfield over a sharp flat plate. But the rarefied flow over the model leads to errors in the measured surface pressure, which is usually measured through a small tapping in the model surface. In general the pressure at the model surface is not the same as the pressure measured in the cavity because of temperature jump at the surface. The wall pressure can be calculated from the cavity pressure if the shear stress and the heat transfer are known.

There are, however, two stages in the process to correct measured pressures to the true value. The first stage is to convert from the actual pressure tapping, shown in Figure 11, to the pressure which would have been measured in a sharp-edged, free molecular orifice. This is done using the theory of Hughes and De Leeuw [22] which is based on the work of Clausing (1932) for free molecular flow through cylindrical tubes. Having converted to a sharp-edged orifice the data is presented as the normal molecular number flux so that dubious corrections to the measured pressure, to allow for jump conditions at the surface, are avoided. The data is normalised by the free molecular number flux and provides a more reliable comparison of experimental data than does a straightforward comparison of measured surface pressure.

3. FLAT PLATE EXPERIMENTS

Experiments to measure the viscous effects of a rarefied hypersonic flow were conducted in the low-density facility at Imperial College. The model used was the same as the one used by Uppington [16]. The tunnel test section diameter, originally 6", has been increased to 8" since his experiments and the test section Mach number has increased from 19 to 23. Tunnel running conditions and the range of relevant parameters for a typical flat plate model are shown in Figure 5, for a Mach number of 23.

Pitot surveys were made by the author on a flat plate model in the original tunnel, with a 6" test section diameter. These measurements were made prior to Uppington's surface pressure experiments and indicate that the flowfield is typical of a merged layer flow. McCroskey [63] describes a series of tests to define a transitional flow over a sharp flat plate. One basic feature of such a merged flow is the change in structure close to the leading edge. In particular, when the viscous region and the shock wave merge, the shock wave thickness increases by a large amount and the ratio between this and the shock layer thickness provides a dramatic demonstration of the effects of merging. The pitot profiles measured in the small test section are shown in Figure 6. Using the same definition for shock wave and shock layer thickness as did McCroskey, the ratio between them is also shown in Figure 6. McCroskey's data is also shown, as is the continuum flow behaviour and the four points for the present experiment show a similar increase in shock thickness for $\bar{V} \sim 0.17$. In fact the merged layer seems to be well established by this point with a significant change between $\bar{V} = 0.1$ and 0.2, consistent with McCroskey's data. If $\bar{V} = 0.1$ be taken as the point of departure then the front $2\frac{1}{4}$" of the model represents a non-continuum flowfield. However, with the enlarged tunnel diameter this length of non-continuum flow extends up to 12" from the model leading edge, for the lowest Reynolds number condition, so the present results were made in a truly rarefied environment.

Uppington [16] made measurements of the flat plate surface pressure and these have been repeated by the author in the larger test section, where the static pressure was reduced by one order of magnitude. Pressures were measured on a bank of Barocel transducers but at these low pressures especial care was necessary to make reliable pressure calibrations of the instruments. The entire tunnel was used as a vacuum chamber to calibrate the pressure transducers. Dry nitrogen was leaked into the tunnel through a micrometer valve. The chamber was connected to a rotary vacuum pump and a series of steady pressure levels could be set up by adjusting the leak. In this steady state condition the pressure transducers were calibrated against a Mcleod gauge. The transducers, gauge and tunnel were outgassed at a pressure below 0.5 microns prior to calibration and the zero readings checked immediately after a run. Because of the time needed to out-gas the pressure tapping, the zero reading after the run did not return to the original calibration zero. However, the method did indicate any gross effect, for example a shift in the sensor datum during an experiment. When used on the flat plate models the Barocel gauges were accurate to ±1 micron over the range 0-100 micron.

At first the model was mounted $\frac{1}{4}$" below the tunnel centre line, to avoid any effects of shock focussing out of the conical nozzle, and the models were carefully aligned to be parallel with the tunnel axis. Pressure distributions measured in this way indicated a pressure peak at the front pressure hole. At first it seemed that the pressure tube was leaking and high-pressure gas from the region below the leading edge bevel was increasing the measured pressure to six times the free molecular value. However, tests with a yawmeter showed that the flow out of the nozzle was conical and 0.3° off-axis at a point $\frac{1}{4}$" below the centre line; the position of the flat plate leading edge. The front of the model was raised to match the conical flow and the experiment repeated. The pressure peak disappeared and the results are presented here. The response of a typical pressure hole to a change in static pressure is shown in Figure 7. The tunnel was allowed to stabilise for a period of ten minutes after a change in running conditions before data was recorded. From the lower graph of Figure 7 it can be seen that after ten minutes' settling time the rate of change per minute of the measured pressure is 0.2 times the change in pressure ~~per minute~~. For the flat plate the measured pressures changed only 5 microns from one condition to another. The error in the measurement corresponds to a change of 1 micron per minute which is well within the overall accuracy of the experiment.

Figure 8 shows the flat plate data presented in terms of parameters relating to low density flow of a continuum fluid. If the flow were truly continuum in nature then both the rarefaction parameter, $\bar{V}$, and the strong interaction parameter, $\bar{X}$, would correlate data from the different tunnel conditions. In fact there is a strong dependence on the stagnation temperature for both the rarefaction and the strong interaction parameters. Also shown is the pressure distribution due to strong interaction theory. This predicts a surface pressure which increases to infinite at the leading edge; the experimental data reaches a plateau value and then falls as the leading edge is approached. The data has been normalised by the free stream static pressure corresponding to the Mach number measured at the model leading edge. There is a significant Mach number gradient along the tunnel but no allowance has been made for the change in static pressure over the length of the model. If this were included the normalised pressures would increase with distance away from the leading edge. The results demonstrate that a viscous effect does exist; simple continuum ideas show a marked dependence on stagnation temperature and the surface pressures begin to fall at the front of the flat plate.

These results indicate that under the present free stream conditions the continuum models of a rarefied and viscous flow do not fully predict the surface properties and do not have the correct dependence on the ratio of wall to stagnation temperature. Becker [17] has also investigated this departure from continuum boundary layer flow in the region of transition from the free molecular leading edge flow. He proposes a form of the rarefaction parameter which depends on wall conditions and the stagnation temperature. Shorenstein and Probstein [18] suggest a similar length parameter defined as:

$$\bar{V}^2_{x_\infty}\left(\frac{T_w}{T_o}\right)^{\frac{1}{2}} \simeq \frac{M}{Re_{w,x}}\left(\frac{T_\infty}{T_w}\right)^{\frac{1}{2}}\left(\frac{2}{\gamma-1}\right)^{\frac{1}{2}}$$

The dependence on the temperature ratio and on wall conditions, expressed as a wall Reynolds number, is immediately obvious. Results are presented in Figure 9 in terms of this parameter. Data is seen to collapse, for eight different stagnation pressure, stagnation temperature conditions, if the measured surface pressure is normalised by the free molecular pressure. There is evidence of a trailing edge effect resulting from upstream propagation through the boundary layer of disturbances at the back of the model. A comparison with strong interaction theory is ~~also~~ not shown. since these points would lie outside the scale, the pressures being very much higher than were measured.

Although this modified rarefaction parameter is capable of correlating data over the entire flat plate the data is also presented in terms of kinetic theory parameters. The uncorrected data is shown in Figure 10 in terms of the mean free path of freestream molecules colliding with molecules from the body surface, λ_{fb}. ~~As a comparison~~ Again the results for strong interaction theory ~~are also~~ cannot be shown ~~and~~ on the same scale but it is noticeable that, in terms of free molecular kinetic theory parameters, there is still a strong dependence on wall to stagnation temperature ratio. The uncorrected surface pressure correlates well over the middle and front of the model but not so well at the back. Data taken at the front shows a definite plateau region and has a tendency to fall towards the free molecular value.

Uppington's previous experiments were made at higher static pressures and with a model having large diameter pressure tappings. Since the "rarefied flow" effects were significantly less than in the present experiment it was not necessary to correct the measured pressure data to convert from tube measurements to true orifice pressures. The flow conditions were such that the cavity pressure was little different from the surface pressure. It is interesting that Uppington's data for surface pressure, which is devoid of any correction technique because of the local conditions and hole size, is in very good agreement with the theoretical data of Pullin. However, the resolution with these large holes was poor and for the present experiments the hole size was reduced by bushes in the original holes. These bushes were cut away at the back to produce an orifice with only a short parallel neck, as shown in Figure 11. The tunnel static pressure is also reduced by an order of magnitude for these experiments and these two changes mean that pressure correction techniques are now important. To eliminate problems of relating surface pressure to cavity pressure under rarefied flow conditions, the measured cavity pressure was converted directly to number flux measurements knowing the temperature of the pressure tapping to be the same as the model wall temperature. This was compared with the theoretical data after the measurements had been corrected to true orifice values. Because sufficient parameters were not measured during the experiment, self-consistent corrections could not be made. Thus Pullin's theoretical values are substituted, as described below, in order to calculate the speed ratio for incident particles, necessary to correct the, albeit short, tube-measured number flux. If the theoretical data are consistent with the experimental data then, although the comparison cannot claim to be independent, the corrected number flux should be the same as the Monte Carlo predictions, if they are accurate.

Surface pressure distributions were measured through orifice gauges mounted in the top surface of the flat plate model. These orifices open out into a larger cavity and are connected by metal tubing to a bank of pressure sensors. The cavity is in a part of the model which is water cooled and, since the pressure transducers are also at room temperature, no correction for thermal transpiration is necessary. Figure 11 shows the geometry of a typical pressure port.

For free-molecular flow through the orifice and into the larger cavity the number flux is given by:

$$N = {}^{P}/_{m\sqrt{2\pi R T}}$$

If the mean free path of the gas in the cavity is larger than the orifice diameter the flux out of the cavity will be given by the same expression. In steady-state conditions the number flux in and out are the same and, if it is assumed that ingoing and outgoing molecules do not collide at the orifice, the above expression can be used with temperature equal to that in the cavity. Since any molecule leaving the cavity must collide with the wall many times this is a reasonable value for the temperature of the molecules leaving the cavity. In the present tests the mean free path of the gas within the pressure cavity is somewhat smaller than the freestream value so the cavity is not truly free molecular. The cavity Knudsen number is about 0.3. Horstmann [19] has shown that for air a variation in cavity Knudsen number from 1 to 30 had little effect on the normalised number flux and it is assumed that the present value is acceptable.

Because of the difficulty of machining a true sharp-lipped orifice the measured cavity pressures must be corrected for the effects of a blunt lip. The theory of Hughes and De Leeuw [22] predicts the behaviour of an impact tube in a rarefied gas flow, providing that the flow is sufficiently rarefied that the flow around the probe and in its interior is free molecular. In the present case the impact tube is normal to the free stream flow; the external flow and the internal flow are effectively free molecular. The response of a pressure tapping is expressed in terms of an ideal orifice and the number flux is calculated from this ideal orifice using the measured cavity pressure, corrected by the method of Hughes and De Leeuw. The correction factor is a function of the cavity aspect ratio, the tube incidence and the incident flow speed ratio. In the present experiment the aspect ratio is 1 and the incidence 90° and the correction factor depends only on the local speed ratio for the incident stream.

The speed ratio necessary to calculate the factor to correct measured surface pressure to that which would have been measured in a sharp-lipped orifice can be thought of as either the speed ratio of incident molecules or as the speed ratio of gas adjacent to the wall. The incident molecule speed ratio is in fact correct, but both incident and wall speed ratios were calculated to test the dependence of the correction technique on the molecular models used. No experimental measurements were made of incident molecular conditions nor of the conditions in the gas adjacent to the wall. The results of Pullin's Direct Simulation Experiment for an identical diatomic experiment were used. Corrections based on the theoretical model were used to correct the measured pressures which were then compared with Pullin's data. If the results agree then this would be a very strong indication that both the theoretical model and the experiment together with a correction technique are correct in themselves.

Pullin's data for the variation in gas temperature near to the model surface and for the variation in slip velocity are shown in Figure 12 as functions of the non-dimensional distance parameter x/λ_{fb}. The local speed ratio at the wall may be calculated from:

$$S_w = \frac{U_w}{\sqrt{2RT_g}} = \left(\frac{U_w}{U_\infty}\right) \frac{U_\infty}{\sqrt{2RT_\infty}} \left(\frac{T_\infty}{T_w}\ \frac{T_w}{T_g}\right)$$

$$= M_\infty \sqrt{\frac{\gamma}{2}\frac{T_\infty}{T_w}} \left(\frac{U_w}{U_\infty}\right) \left(\frac{T_g}{T_w}\right)^{-\frac{1}{2}}$$

The wall speed ratio calculated from Pullin's data is shown in Figure 13. Also shown is the speed ratio for an incident stream calculated by Lewis [23] and used in a similar correction technique applied to the correction of flat plate surface property measurements. The present data is seen to be considerably lower than that of Lewis. The speed ratio for incident particles is now calculated for the present experiment. It will be seen that the alternative speed ratio is very much different. The speed ratio based on incident properties is defined by:

$$S_i = M_\infty \sqrt{\frac{\gamma}{2}\frac{T_\infty}{T_w}} \left(\frac{U_i}{U_\infty}\right) \left(\frac{T_i}{T_w}\right)^{-\frac{1}{2}}$$

The temperature of the incident stream is the average thermal energy of incident molecules and can be written:

$$T_i = 1/5\ (T_{xx_i} + T_{yy_i} + T_{zz_i} + 2T_{R_i})$$

The gas temperature close to the wall is a complicated function of the incident temperature. The incident stream, unaffected by the presence of the model, is in thermal equilibrium, so that we have:

$$T_{xx_i} = T_{yy_i} = T_{zz_i} = T_{R_i}$$

and

$$T_i = T_{yy_i}$$

and the incident temperature may be calculated from:

$$\frac{T_i}{T_\infty} = \frac{T_{yy_i}}{T_\infty} = \frac{\frac{1}{2}\left(1 + \sqrt{T_w/T_\infty}\right)\left(p/p_{fm}\right) - \sqrt{T_w/T_\infty}\left(N/N_{fm}\right)^{\frac{1}{2}}}{n/n_\infty - \left(N/N_{fm}\right)\frac{1}{2}\sqrt{\frac{T_\infty}{T_w}}}$$

This reduces to the required value of $T_{yy_i}/T_\infty = 1$ for free molecular flow. The incident temperature is calculated from the results of Pullin. The incident molecule velocity is calculated in three stages. The first step is to calculate the wall number density from:

$$\frac{n}{n_{fm}} = \frac{n_w}{n_\infty}\left(\frac{T_w}{T_\infty}\right)^{\frac{1}{2}}$$

The second step is to calculate the incident molecule number density. This necessitates a guess for (n_t/n_∞); this is made from Pullin's data for density contours over the flat plate model. Substitution gives (n_i/n_∞) from:

$$\frac{n_t}{n_\infty} = \frac{1}{2}\left(\frac{n_i}{n_\infty} + \frac{n_w}{n_\infty}\right)$$

The final step is to calculate the incident molecular velocity from:

$$\frac{U_i}{U_\infty} = 2\,\frac{n_t}{n_i}\left(\frac{U_w}{U_\infty}\right)$$

This value for the velocity, together with the incident molecular temperature, is substituted in the expression for the incident molecule speed ratio above. The results are shown in Figure 13 where they are compared with the wall speed ratio and the data from Lewis. This value of the speed ratio is used to correct the measured pressures to the sharp orifice value and the results shown in Figure 14. The correction factor for perpendicular impact tubes, or surface gauges, indicates that the measured pressure will always be less in a blunt orifice than that measured in a sharp edged orifice. So, in general, experimental results will always be increased by correction techniques for measured pressures. The measured, corrected pressure is compared with the data of Pullin, Agreement is not too good for the surface pressure measurement, but it is difficult to relate cavity pressure to the actual surface pressure. ~~the agreement is seen to be reasonable, giving confidence in both the theoretical and experimental results~~. A more realistic comparison is to compare the number flux measurements from theory and experiment. The flux is expressed in terms of the free molecular number flux and is calculated from the corrected ~~surface~~ cavity pressure by:

$$N = p_c / m\sqrt{2\pi R T_c}$$

and the free molecular number flux is found from:

$$N_{fm} = n_\infty \sqrt{\frac{RT_\infty}{2\pi}}$$

The measured number flux is in better agreement with Pullin's data than is the surface pressure. However, considering the complexity of both the experimental and theoretical experiments the results are seen as encouraging. Figure 15 shows that the corrections are largest at the front of the model. The data of Lewis [23] is also shown and agreement is seen to be bad; although the overall magnitude of the plateau is of the right order its position is different by an order of magnitude. The correction technique used by Lewis is based on a fundamental assumption that the flow close to the surface is free molecular. He models the flow adjacent to the wall by a two stream, two sided distribution function. For a diffuse and fully accommodating surface the reflected stream is, by definition, half-Maxwellian and the incident stream is characterised by parameters to be determined from measured quantities. This model, applied to the number flux balance at the entrance plane of a near free molecular sharp lipped cavity, results in a simple relation between wall and cavity pressures. However, a comparison between the present data, the theoretical solution of Pullin (in which the molecular velocity distribution does not support the assumptions of Lewis for $\lambda_{fb} > 0.1$) and the data of Lewis shows marked differences in the results.

In order to try and explain the differences between Pullin's data and the present experiments, the effects of a conical flow and Mach number gradients have been calculated. The measured gradient was typically 0.2 Mach number per inch and the increase would be 1.2 over the length of the model. The freestream static pressure at the back of the model would be decreased by 50% relative to the front of the model as a result of this gradient. The number flux ratio, since the measured value is unchanged, would be increased by 50% bringing the experimental results closer to the theoretical value. This, however, is only an indication of the effect of a Mach number gradient. Pullin's results are limited to the region at the front of the model and, in any case, the Mach number away from the influence of the model may not have a direct effect on the static pressure at some distance back from the leading edge. It is more likely that surface pressure is influenced by the Mach number at the front of the Mach cone within which the point on the surface is contained. The effects of an axial gradient would, however, be to move the experimental results in the direction of the theoretical data. The best solution would be to calculate the theoretical distribution for a model in an appropriate conical flowfield, which is possible using a three-dimensional version of the computer program. In the present experiments no check has been made for the two-dimensionality of the flow. Measurements were taken on the model centre line and Uppington reports results for the step model in the small test section which show the flow to be basically two-dimensional.

In conjunction with Davis [24] the electron beam was used to probe the flow field away from the flat plate surface. The beam was traversed along the model a number of times and photographed with a long exposure as the beam moved across the plate. The light intensity at any point on the beam depends on the local gas density at that point. The flat plate photograph of Figure 16 is therefore a representation of the density profile over the model. The shock shows as an area of light and the model surface is just visible. The dark area below the model occurs because the beam was fired onto the model surface and no light is visible underneath. The pitot tube can be seen showing just ahead of the model. As described in Appendix A2, the surface is graphite coated, except for the front ¼". It is noticeable that the general light level is increased at the front of the model indicating the increased reflection from the uncoated metal. At other points on the model there is no evidence of surface reflection, indicating that secondary electrons were trapped within the surface. The features of a flat plate rarefied hypersonic flow can be seen; in particular the curved shock wave at the front of the model. Because of the limited distance of travel for the beam, the photograph is composed from three different exposures, the model being moved between each exposure (which accounts for the apparent sudden changes in the shock structure).

4. FORWARD FACING STEP

A second part to the flat plate experiment was to investigate a forward facing step in a merged layer flow. One single step, $\frac{1}{8}$" thick, was fixed to the flat plate model $1\frac{1}{2}$" back from the leading edge. In terms of kinetic theory parameters this meant that the step was either $1.3\lambda_{fb}$ or $2.5\lambda_{fb}$ from the leading edge under the two extreme running conditions. The slip velocity at this position was calculated to be $0.32U_{\infty}$ or $0.20U_{\infty}$ and the gas temperature adjacent to the model surface varied between $3.9T_w$ and $3.0T_w$, according to Pullin's results for the flat plate. The step was instrumented with pressure holes similar to those on the flat plate. The step pressures have not been corrected in any way since the levels are much higher than for the flat plate. The step experiment was also performed by Uppington, with higher static pressure and a lower Mach number. As in his experiment the step could be moved around a datum position so that one pressure hole at the foot of the step could be used to build up a detailed pressure distribution around the compression face.

The pressures measured around the step are shown in Figure 17. With the widely spaced set of pressure tappings it was difficult to locate the start of the separation region ahead of the step. As was found by Uppington and by Rogers, Berry and Davis [25], the separation is dominated by the step geometry and changes in free stream conditions have only a small effect. Surface pressures have been normalised by the free stream pressure ~~and the magnitude of the peak value just ahead of the step is an almost constant multiple of the free stream static pressure~~. It is impossible to define the separation region from measurements of the surface pressure distribution. Pullin's calculations show a very small region of separated flow ahead of the step. As is seen, the agreement between theory and experiment is reasonable supporting the suggestion that the flow is compressing into the corner rather than separating some distance ahead of the step as for a continuum flow, with a region of reversed flow just ahead of the step. The flow at the model surface is certainly slipping and this will delay separation in the merged layer flow.

Rogers, Berry and Davis [25] reported four basic results for a forward facing step in a low-density, supersonic flow:

i) as a given step approaches the leading edge there is a steady increase in the surface pressure just ahead of the step.

ii) the general shape of the pressure distribution does not alter greatly until the influence of the step reaches the leading edge.

iii) for a given step position there is a progressive increase in the corner pressure as the step height is increased; the interaction length also increases.

iv) the flow Reynolds number has only a small effect on the interaction mechanism.

In the present experiment only a single step height was used and this was at a fixed distance from the flat plate leading edge. These results do, however, show that Reynolds number has only a small effect. The other three conclusions listed above were borne out by Uppington's experiments and the present measurements of surface pressure have been compared with both his results and with the theoretical calculations by Pullin in Figure 17. In conjunction with Davis [24] the existing electron beam apparatus was used to measure density distributions over the step model. The beam could be continuously traversed over the model and measurements were made close to the front edge of the step. Typical electron beam density distributions are shown in Figure 18. Complete pressure distributions over the step and flat plate model are plotted, in Figure 19, as a function of Becker's modified rarefaction parameter. Only the pressures on top of the step are shown since the very high pressure in the corner, already shown in Figure 17, would shrink the pressure scale to such an extent that detail would be lost. Pressures a small distance upstream of the high pressure region are not affected by the presence of the step. Pressures on the step are increased over the flat plate value but, even so, they do not come up to the level predicted by strong interaction theory for a flat plate alone. Therefore, a step embedded within a merged layer flow does not increase the surface pressure to that predicted for a flat plate by a continuum theory extended forward to a region of rarefied flow.

5. WAVERIDERS IN LOW-DENSITY FLOW

One of the important reasons why the Waverider has been promoted as a possible second generation space shuttle vehicle is that it represents a concept based on simple, known flow fields; that of flow past an infinite wedge. The resulting flow is two-dimensional and completely contained by a shock wave which lies in the plane of the leading edges. However, this simple model is only true for a given incidence, a given free stream Mach number and an inviscid flow. At design point all the properties of the wing are known. The actual vehicle will have to fly through a range of speeds from subsonic to hypersonic and a range of altitude from sea level to orbital height. In order to manoeuvre within the atmosphere the vehicle should be controlled and the incidence will change. Viscous effects will become more pronounced as altitude increases. It is therefore important that viscous effects should be studied not only at the design point but also under off-design conditions.

Figure 20 shows the change in the angle between a wedge surface and its shock wave over a range of wedge angle and a range of Mach number. At low speeds this angle is relatively insensitive to changes in the wedge angle for a given Mach number. The angle is much more sensitive to changes in Mach number and as this increases the angle is progressively more sensitive to changes in incidence. However, the dependence on Mach number ~~vanishes~~ is much less for values greater than 15 and the shock stand-off angle varies almost linearly with increasing incidence. Thus, at low Mach numbers, the shock remains in the plane of the leading edges for a wide incidence range about the design point. Within this range the pressure across the span is approximately uniform and equal to the two-dimensional wedge value. At high Mach numbers the incidence range about the design point is very much less and the pressure distribution varies much more with changes in incidence. The dependence on Mach number vanishes and, for high free stream Mach numbers, a given model will operate over only a very narrow range of incidence but for a wide range of Mach number. This analysis assumes inviscid flow and in these conditions a vehicle could accelerate at constant incidence and maintain a constant pressure field below the wing.

Squire [26] has calculated the off-design behaviour of waveriders. He extended Messiter's [27] theory for the lift of slender wings according to Newtonian theory to the solution for off-design behaviour of waveriders. Squire lists solutions in terms of two parameters and the surface pressure and shock shape are given for diamond and caret wings. The two parameters are:

Sweep parameter $\Omega = {}^{b}/\epsilon^{\frac{1}{2}} \tan\alpha$

Thickness parameter $t_o = {}^{h}/\epsilon \tan\alpha$

and $C = {}^{t_o}/\Omega$

Here

$$\epsilon = \frac{\gamma-1}{\gamma+1} + \frac{2}{\gamma+1} \frac{1}{M_\infty^2 \sin^2\alpha}$$

is the density ratio through a shock wave in the plane of the wing leading edges and α is the incidence of those leading edges. A positive value for C corresponds to wings of diamond cross-section and a negative value corresponds to a waverider wing.

Pennelegion and Cash [28] measured the pressure on the undersurface of a waverider in the N.P.L. 6" shock tunnel. The vehicle was designed for a flight Mach number of 8 and was tested over a range of speeds from Mach 8 to Mach 9. Considerable thought went into the design of pressure transducers capable of accurately measuring the short duration pressure rise at a single pressure hole in the underside of the waverider. The results were compared with the value for a two-dimensional wedge at angles between −5.5° and +20°, referred to the inner ridge line of the waverider.

The shock remained attached over a wide range of incidence and stagnation temperature. The measured local pressures agreed reasonably well with theoretical pressures behind oblique shocks on a two-dimensional wedge, the experimental results being consistently higher than the theoretical values. The measured shock stand-off angles were consistently larger than predicted by theory. Since these were measured from flow photographs the tunnel flow may be the root cause of errors in both the measured surface pressure and the shock angle.

Crabtree and Treadgold [29] conducted wind tunnel tests over the complete speed range on a set of idealised waverider shapes. At low speeds a vortex flow will exist on the upper surface of a typical vehicle. A series of models were used to investigate the development of a separated flow field over the upper surfaces at high angles of attack. One of the important results of these experiments was that a progressive blunting of the apex reduces the pitch-up and the amount of the reduction in lift curve slope which accompanies vortex breakdown. There were no inherent problems in the low-speed handling characteristics of the representative waverider shape. The off-design behaviour of the caret wing was investigated in a supersonic tunnel. The undersurface pressure distribution was uniform but slightly higher than predicted by inviscid oblique shock equations. The uniform flow is maintained over a wide range of off-design incidence and Mach number but was sensitive to small angles of side-slip.

Pressure distributions for a caret wing at Mach 8.6 were compared with flat bottom delta wings with the same aspect ratio and volume coefficient. The delta wings show an increase in pressure towards the wing tips particularly at the higher angles of attack; the caret wing undersurface pressure distribution remained uniform over a range of incidence. Crabtree and Treadgold conclude by estimating the range performance of a long-range hypersonic aircraft using hydrogen fuel.

The hypersonic wind tunnel tests indicated that a lift to drag ratio of 4 can be achieved. This would give a range of the order of 10,000 miles with a fuel weight no more than 50% of the take-off weight at a cruising speed of Mach 8. If the lift to drag ratio be raised to 6 at the same speed the range is increased to 12,000 miles.

Greenwood [30] reports the results for the heat transfer and pressure distributions in two 90° corners inclined at 4.4° to the free stream flow. The tests were made using the RAE rocket-propelled free flight model. Data from on-board transducers is transmitted to the ground by radio telemetry and the flight takes place along an instrumented trials range. Heat transfer measurements were made using the thin shell technique with allowances for radiation losses and transverse conduction. Pressure measurements were made using a transducer with a self-contained reference level. Flights were confined within strict limits and the models were made non-lifting by mounting models back to back in the shape of a cruciform containing four 90° waveriders. Incidence was measured from the pressure differential between similar pressure holes in opposing surfaces of the model; the incidence history indicated that the model pitched up and was destroyed at Mach 4.31.

The measured pressures were normalised by the estimated inviscid two-dimensional wedge pressure; the basic wedge angle was 8.75° and the undercut 6.15°. Near to the corner, with $y/b < 0.2$, the measured pressures were close to the wedge value over the speed range up to Mach 4.3. The pressures near to the sharp leading edges were sensitive to small angles of sideslip. Because the complex model was made up of four waveriders there is spillage from one part of the model to another and spanwise pressure distributions are not representative of distributions found on caret wings in isolation.

Keldysh and Maikapar [31] have looked at a series of bodies which contain plane and conical shocks and are formed from stream surfaces of known two-dimensional and axisymmetric flows. They measured the pressure distribution on three waveriders based on a 31.5° wedge in a Mach 6 flow and each with a different wing span. The undercut in each case was the same but two of the models had subsonic leading edges and the third supersonic. The undersurface pressure was the same for all three models and equal to the wedge value. Their tests at a Mach number 3 show that as incidence is increased the shock remains plane and the pressure distribution gradually develops a peak towards the front of the model. The pressure level generally is that predicted by wedge theory. For Mach 6 flow the shock breaks down into two oblique shocks which intersect down in the corner of the model. The pressure distribution is drastically altered showing local pressure peaks corresponding to areas of local separation and the pressure measured in the vicinity of the corner is nearly twice the wedge value. At incidence close to design the plane shock is re-established.

Waveriders supporting a single plane shock have the same lift to drag ratio as a wedge. Keldysh and Maikapar propose more complicated shapes supporting two plane shocks on either side of a central body which has an improved lift to drag ratio.

Watson and Weinstein [32] have studied hypersonic corner flow interactions with Helium at a Mach number of 20 using two 10° wedges. They also give data for Nitrogen at Mach 8. The Helium data shows corner heating rates of six times that at the tips. The data for Nitrogen, at a lower Mach number, shows increased heating rates for $y/b < 0.1$ having a maximum value twice that at the edge. The heating rate actually in the corner was 0.4 of the edge value.

Stainback and Weinstein [33] give three flow phenomena for Mach 8 corner flow. The first is an interaction between boundary layers on the two surfaces forming the corner with a reduction of the heat transfer rate along the join. Second is a vortex system generated by the corner flow field causing increased heat transfer rates some small distance away from the corner. Typically this heating peak is at a position where $y/b \sim 0.2$. The third is a separation and re-attachment on one surface caused by strong shocks generated by the adjacent surface. From limited experimental data they predict that the increase in heating in the vicinity of the corner will not be so great for turbulent flow as it is for laminar flow. Nardo and Cresci [34] have also investigated the flow through a sharp-edged rectangular corner, aligned with the flow, at a Reynolds number of 1.8×10^5 ft^{-1}. They used a blowdown tunnel with test Mach number of 11.2 and measured heat transfer and surface pressure in the vicinity of the corner. The surface pressure showed a peak some distance out from the corner which was more pronounced as the corner angle closed down. With a corner angle of 90° the peak pressure was 1.5 times the undisturbed value but with a corner angle of 60° the pressure peak reached 2.5 times the flat plate value. The peak occurred around $y/b \sim 0.2$. Heat transfer also showed a peak some distance out from the corner. For a 120° corner the heat transfer reached 1.6 times the two-dimensional value but this soared to 5 times for the 60° corner. For both pressure and heat transfer the ratio between the local peak values and the two-dimensional value increased with downstream distance and the position of the peaks moved out from the corner.

The work of Greenwood also includes measurements of the heat transfer rates in a 90° corner at high Reynolds number with turbulent flow. He found a strong dependence of the heating rate on spanwise position and an increase in heating rate near to the centre line as the distance from the nose increased. Heat transfer in the corner was definitely reduced with a value of 30-40% of that measured close to the wing tips. He found that the heat transfer rates were predicted by flat plate theory based on the intermediate enthalpy method at positions away from the corner with $y/b > 0.1$.

East and Scott [35] have made measurements of the heat transfer to the lifting surface of a caret wing at Mach numbers of 8.4 and 9.7 in a gun tunnel with unit Reynolds number up to 1.01×10^7 ft^{-1}. The wedge angle of the waverider was 9° and the undercut angle 4.5° giving a design Mach number of 9.7. Incidence was changed ±10° about the design incidence and off-design conditions were investigated at free stream Mach number of 8.4. Heat transfer rates were measured with Platinum resistance gauges on a Borosilicate backing which was let in to the model undersurface. These panels gave heat transfer distributions parallel to the lower ridge line and across the model semi-span. Thermocouples give temperature information at a point; the panels used in this experiment gave heat transfer data averaged over the area of the gauge and therefore are not so accurate. Although the data is for a different Mach number, different model geometry and different free stream conditions, the results for the chordwise and spanwise heat transfer distribution at an incidence of 20° have been included. These results are compared, in Figure 21, with the closest data from the present experiment; the 5° waverider at 28° incidence. Since the supply conditions and the Mach number are completely different in the two experiments it is purely fortuitous that the numerical value for the heat transfer rates are the same. The comparison is, however, useful since it shows a fundamental difference in the centre line heat transfer distribution. The Reynolds number in the experiment of East and Scott is higher than in the present experiments and the chordwise distribution shows a transition to turbulent boundary layer, with much increased heating, for $x/c > 0.6$. The spanwise distribution at $x/c = 0.92$ shows a similar pattern to the present data, but since this relates to an area of turbulent flow the actual heat transfer rates are higher.

Metcalf [36] has made measurements of the total lift and drag forces on waverider shapes to assess the viscous effects and their dependence on the viscous interaction parameter. The tests were made in the RAE Low-Density Tunnel at Mach 6. The stagnation temperature was maintained at 700°K and the free stream Reynolds number varied between 89 and 454 cm^{-1}. The model geometry is identical to the models used in the present series of experiments.

Model size was found to influence the measured drag coefficient of a particular shape whereas the lift coefficient was independent of model length. At all angles of incidence the drag increases and the lift decreases for increasing rarefaction; these effects seem most pronounced at the higher angles of attack. The incidence at which $C_{L_{MAX}}$ occurs is reduced with increasing rarefaction. A comparison between the delta wing and the waverider is complicated by viscous effects on the leeward surface; at design incidence the upper ridge line of the model is aligned with the flow. A comparison between lift coefficient as a function of the lift to drag ratio indicates that the caret wing gives 10% more lift than does the delta wing at nearly all values of lift drag ratio. This could be due to the delta wings having a lower viscous effect on their forward surface due to a reduction in boundary layer thickness by flow spillage. Some difference may arise from the different base flow of the delta wing and waverider.

Metcalf also attempts to calculate the total drag and lift forces on the delta wing models. He uses data for flat plates with the local inviscid conditions and assumes the models are made up from a series of flat surfaces which do not interact. In calculating the normal force on surfaces of the delta wing body he uses the analysis of Hayes and Probstein [37] who give the pressure on an inclined plate as:

$$\frac{P_W}{P_2} = 1 + \gamma\left(\frac{M_\infty}{M_2}\right) J_1(K) d_2 \bar{\chi}_2$$

where, for Pr = 0.725,

$$d_2 = \frac{0.968}{M_2^2}\left(\frac{T_w}{T_2}\right) + 0.145(\gamma-1)$$

and

$$J_1(K) = \frac{p_\infty}{p_2}\left[\frac{\gamma+1}{2}K_b + \frac{1 + 2\left(\frac{\gamma+1}{4}\right)^2 K_b^2}{\left[1 + \left(\frac{\gamma+1}{4}\right)^2 K_b^2\right]^{\frac{1}{2}}}\right]$$

The surface pressure distribution was integrated over the area of the delta wing and the pressure-dependent lift and drag forces calculated. Metcalf also considers the problem of matching tunnel results to flight conditions. Flow régimes on the flat plate may be defined in terms of the strong interaction parameter and the viscous interaction parameter. Matching the viscous interaction parameter in tunnel test and flight will give a similar length of merged layer flow and of trailing edge interference, which is dependent on the boundary layer thickness. However, any difference between tunnel and flight Mach numbers could mean that the strong interaction region on the flight vehicle is non-existent on the model. Effects of incidence and of wall temperature ratio may also mean that the wind tunnel tests are not representative of flight. However, he suggests that a matching of the viscous interaction parameter is sufficient to model the effects of viscosity on overall forces. The flat plate results presented here demonstrate that temperature ratio is an important parameter and that results under different conditions are best correlated by Becker's parameter, $\overline{V}\sqrt{T_w/T_0}$. Since the extent of the merged layer is defined by $\overline{V}$, this should be matched at the back of the model to the value at the back of the flight vehicle. It would seem, therefore, that cooled models should be used and the wind tunnel Mach number reduced or the Reynolds number increased to preserve the value of rarefaction parameter between flight and experiment. For the case quoted by Metcalf, a 20 m vehicle flying at

Mach 25 and 300,000 ft altitude, the Nitrogen Tunnel could match the full-scale vehicle under the following running conditions: supply pressure 450 psi, stagnation temperature 1350°K. The model length would be 10" to preserve the value of $\bar{V}_L$ and the model would have to be cooled to 136°K. Under these conditions the parameter most relevant to merged layer flows would be the same in flight and experiment.

Hefer [38] made experiments to investigate the low Reynolds number effects on a waverider. The model was designed for Mach 8.5 constructed by electroforming Nickel and was uncooled. Pressure gauges and a force balance were used to investigate aerodynamic behaviour in the low-density wind tunnel at DFVLR at Göttingen, at Mach numbers 10.5 and 12.2. The free-stream Reynolds number varied between 2.5×10^4 and 2.5×10^5 m^{-1}. Pitot profiles showed that shock wave and boundary layer are merged except at the back of the model where there is a thin inviscid layer. Pressure distributions were measured over the incidence range from -5° to +8° and the measured values compared with the prediction for a sharp wedge in weak interaction, given by Creager [39] as:

$$\frac{p}{p_\infty} = \frac{p_1}{p_\infty}\left[1 + \gamma\left[\frac{0.865}{M_1^2}\ \frac{T_w}{T_1} + 0.166(\gamma-1)\right]\frac{M_1^3}{Re_{1_x}^{\frac{1}{2}}}\right]$$

The wall temperature was non-uniform over the surface of the model. No allowance was made for this nor for the change of wall temperature as the incidence increased. In all cases the wall temperature was assumed to be a uniform 420°K. The calculated values were compared with pressures measured in the corner and were in reasonable agreement except at the back of the model where measured pressures were lower than theory. This was attributed to the effects of the base of the model but could also include effects due to non-uniform temperature. Spanwise distributions showed the pressure to be increasing out towards the wing tips, consistent with a detached shock under the wing. Force measurements indicate that the lift is independent of Reynolds number and in agreement with inviscid theory, whereas drag is strongly dependent on flow viscosity. In low-density flow this increase in drag force causes a significant decrease in lift to drag ratio for the waverider model.

Previous work has concentrated, therefore, on measurements of surface pressure and heat transfer to waveriders but under normal hypersonic continuum conditions; theoretical methods are available to predict off-design behaviour. Viscous effects in rectangular corners are well established and only two authors, Metcalf and Hefer have investigated waveriders in hypersonic viscous flow. Of these, Metcalf measured only overall forces, on similar models to those used here and Hefer used uncooled thin sheet models in conditions of weak viscous interaction. The present results therefore represent the only data available for waverider vehicles under conditions of strong viscous interaction but, even so, cannot relate directly to a flight vehicle since the models were water-cooled to 288°K.

Schulz [48] has written extensively on different techniques which are available to measure heat transfer to bodies in short-duration, high Reynolds number facilities. These techniques are also applicable to low-density hypersonic flow and can be used to measure heat transfer in the Nitrogen tunnel, providing the model is injected into the established flow. The present experiments to measure heat transfer distributions on waverider shapes represent the first heat transfer measurements in the Nitrogen tunnel and were therefore designed to develop new techniques as well as to measure heat transfer distributions over lifting bodies in a rarefied hypersonic flow.

Metcalf [49] has used four different techniques to measure heat transfer rates on cylindrical models. The first of these is the steady state Gardon gauge. These are available, ready calibrated and are small enough that a local measurement of heat transfer can be made. The gauge consists of a thin metal foil supported around its edge by a holder which is maintained at constant temperature. A thermocouple measures the temperature at the centre of the foil and the temperature difference across the sensor is a measure of the heat transfer rate. Even though they represent one of the smaller commercial gauges the need for water cooling of the support and the fact that the sensor has a relatively large flat surface means that they are only really of use in blunt-faced models or models which have large areas of flat surface. They would certainly be of use in a calibration experiment for the waverider, providing the internal volume of the model were large enough. They could not be used near to the tip of a slender model nor close to the leading edge of a wing. One could be mounted as a reference but this would involve a local coolant supply and the bulk of the gauge could modify the heat transfer distribution measured over the remainder of the model. This technique could be used with an injected model, where the heat transfer would change as the wall temperature changed, or with a quick start tunnel. In such facilities a quick acting valve is used to divert a gas flow through a nozzle and past a model, the valve operating fast enough to produce a transient measurement of heat transfer.

The second technique is to measure the total heat transfer rate by measuring the temperature rise of a solid model. A variation is to mount a substantial copper plug into the model and measure the heat input, over a known area, by temperature rise of the calorimeter, after allowing for heat losses around the plug. This method was used to measure the stagnation point heat transfer on a hemisphere by making the model with a solid copper nose and, using an assumed distribution for heat transfer to a sphere, the overall heat transfer is used to calculate the stagnation point value.

The third technique, which is particularly useful for complex shapes, is to measure the surface temperature of a solid model made from an insulating material of known thermal properties using phase change paint. The surface temperature distribution may then be used to calculate the heat transfer rate; if several different temperature paints be used the technique gives qualitative heat transfer data which immediately locates regions of high heat transfer rate. With other techniques information is only available at the sensor locations; in this technique continuous temperature contours are known over the complete model and this is particularly useful for complex shapes with very local variations. The model is injected into the flow for a short duration then removed and the lines of constant temperature measured from the paint melt line. Alternatively the model may be left in the flow and temperature changes recorded using high-speed photography. Metcalf has used this technique to compare heat transfer to flat bottom and waverider type space shuttle vehicles.

The final technique is to use thin shell models of known thickness and thermal properties and to measure the transient temperature rise through the skin when the model is injected into the flow. The temperature rise is measured by a thermocouple on the back of the skin and the model must be exposed to the steady flow as fast as possible. Two methods are available. In the first the model is covered by a protective shield which is removed to expose the model then closed after a short time. Such shields may well be bulky and lead to tunnel blockage problems. The covers may be designed to spring apart quickly but this may mean slow closing to re-tension the unit and during this time the model may well reach a high temperature. The advantage of this method is that the model is stationary throughout and if a rigid mount is necessary in order to carry the model loads then this may be the only method. An alternative is to inject the model into a steady flow then retract it after a short time. The model is subjected to high acceleration forces which may well affect the delicate thermocouples inside the shell.

Also the model is injected through the nozzle boundary layer and evidence from the present experiments indicates that the initial temperature rise may well be affected by conditions in the nozzle shock wave. In the present experiment this problem was overcome by assuming an exponential temperature rise and, using a plotting table linked to an on-line computer, an exponential curve was fitted to data measured over a short time interval. This technique avoids conduction effects, providing the time interval is short, and the initial rate of rise of temperature may be calculated from the fitted exponential curve. This technique is particularly useful if the temperature rise information is recorded digitally this avoiding the tedious transfer of information from analogue chart into the computer.

The thin shell technique was chosen as being the most useful technique for the initial heat transfer experiments in the Nitrogen Tunnel using waverider and delta wing models. The injection rig developed for the experiment could have been used to carry solid thermographic paint models and it was hoped to include these measurements, but time did not allow this.

The thin shell technique is ideally suited to short duration facilities since the model may be fixed and the heat pulse provided by the tunnel firing. These tunnels tend to operate at higher stagnation temperatures than the continuous facilities and transient temperature rises can be very large indeed. Continuous tunnels, running at lower unit Reynolds number, have a slower response and temperature rises may well be small and heat conduction effects in the model skin and along the thermocouple wires can be important. One of the objects of the present experiments was to investigate the effects of model wall thickness on the measured heat transfer rates.

Thin shell techniques use a skin instrumented on the back with thermocouples which measure the rate of increase of temperature. The thin skin may be either the complete model or a piece of thin metal made as a part of a more solid piece. The thermal properties of the shell should be accurately known; in the present experiments the thin walled models were made by an electroforming process using Nickel, as described in the Appendix. A one-dimensional analysis of the heat transfer to an element of the shell gives:

$$\dot{q} = h(t_r - t_w) = \rho_w \ell_w c_w \left(\frac{dT}{dt}\right)_{t=o}$$

All of the properties of the material are temperature-dependent. As the model is injected into the flow its temperature rises and the wall properties change. The thermocouple calibration is also temperature-dependent and the temperature change during an experiment, which depends on the heat transfer rate and the skin thickness, determines the size of this error. Providing the rate of increase of temperature is taken immediately the model is injected these problems are avoided. Schulz gives the errors in thermal properties for a given rise in temperature. For a combination of chromel/alumel thermocouples and a copper shell, the most similar to the present case, there is not significant variation for temperatures up to 300°C. The maximum heat transfer rate measured during the present experiments, at the stagnation point of a hemisphere, corresponds to a temperature rise of 186°C/second and this gave almost 2 seconds soak in the free-stream before changes in thermal properties were noticeable. All of the temperature rise curves were fitted over the first 0.5 seconds, so errors due to changes in model temperature were not important. Between runs the models were cooled with a jet of Nitrogen; even so their temperatures at injection were different. But since the experiment is concerned with temperature differences the change in thermal properties were assumed to be negligible.

A second and possibly more important source of error is conduction within the shell and thermocouple leads. The measured heat transfer rate falls as the surface temperature increases because of conduction effects. If the temperature on the back face of the shell be used to calculate the heat transfer coefficient the expression for heat transfer is:

$$(T_r - T_B)h_B = \rho c \ell \, ({}^{dT_B}/dt)_{t=o}$$

This describes the conduction of heat normal to the surface. Naysmith [66] gives the error in using the back surface temperature to calculate the actual heat transfer rate as:

$$^{h}/_{h_B} = 1 + \frac{1}{3}(^{h\ell}/_{K}) \qquad \text{for} \quad t > \ell^2/\alpha_1$$

For a model with a 0.010" Nickel skin and a heating rate of 2.5×10^4 W/m^{-2} the error by measuring the rear face temperature is less than 2%. If there are temperature gradients along the model, as there always will be with a complex shape, then conduction along the skin may be important. George and Reinecke [67] show that conduction along the skin can be expressed as:

$$\frac{\text{conduction heat transfer}}{\text{surface heat transfer}} = \frac{\alpha \, t \nabla^2 \dot{q}_s}{\dot{q}_s}$$

The skin conduction error increases with time and is independent of the wall thickness. The heat transfer to a sphere of radius R close to the stagnation point has the form:

$$\dot{q}_s = \dot{q}_o(1 - 0.6 \, ^{x^2}/_{R^2})$$

and for this case the error due to skin conduction is:

$$\frac{\text{conduction heat transfer}}{\text{surface heat transfer}} \approx \frac{2.4 \alpha \, t}{R}$$

For a Nickel sphere with a diameter of 0.625", as was used in the present experiment, the time for a 5% error in the stagnation point heat transfer rate due to internal conduction is about 130 msec. It is therefore very important that the rate of increase of temperature should be measured as soon as possible after the model is injected into the flow and conditions are steady.

Chevallier and Leuchter [68] have calculated the conduction errors due to the thermocouple wires attached to the rear of the thin skin. In the present models the thermocouple wire has a diameter of 0.004" and the wall thickness is typically 0.010". At the time at which internal conduction becomes important the error in the measured back face temperature is less than 1% due to the presence of the thermocouple. If the thermocouple diameter were increased to 0.010" to make the final model more robust this error would be about 4%. It is therefore important to keep thermocouple size to a minimum consistent with mechanical reliability and ease of manufacture.

6. GUN TUNNEL TESTS

A set of three delta and caret wings were tested at high Reynolds number in a Mach 9 gun tunnel facility. Since any future vehicle, based on these simple shapes, will fly at both high and low altitude at hypersonic speed the models have been tested in both high- and low-density wind tunnels. The same models have also been tested by Metcalf [36] in the RAE Low Density Tunnel at a lower free stream Mach number. Data is therefore available for these models throughout the hypersonic speed range including the effects of viscosity.

The models were made from solid aluminium alloy and mounted on a three component strain gauge balance in the Imperial College No. 2 Gun Tunnel [10]. The models were only 3" long and therefore considerably smaller than other models tested in this facility. Force measurements were made at angles of attack up to 70° without any evidence of tunnel blockage from Schlieren photographs of the flow. Coleman reports previous work with caret wings in the same gun tunnel [41], also at high angles of attack. Other experiments by Rao [42] and by Carr [43] suffered from effects of tunnel blockage. The present experiments extend this earlier work by including a model considerably thicker than the others. Seen from the side all of present models have a similar 28° wedge angle. Differences from model to model are due to undercutting the basic delta wing by 5° and 8° to form caret wings. Hopefully these wings produce a more contained two-dimensional flow but with a penalty of reduced internal volume.

The models were not designed for an inviscid Mach number associated with either of the wind tunnels in which they have been tested. The design Mach number for the 8° waverider is 6.1; the 5° model does not correspond to a finite flight Mach number. In the present tests force measurements were made at a Mach number 9 and the test conditions are shown in Figure 5. Data is presented in terms of the effective wedge angle which is the angle between the wedge defining the flow field and the free stream. In terms of this angle the incidence of the three models when the top ridge line is parallel to the flow is 28°, 23° and 20°.

Figures 22 and 23 show the variation of lift coefficient and drag coefficient with effective wedge angle. Undercutting a delta wing is represented by moving to the left in Figures 22, 23, giving decreased lift and drag. Figures 24 and 25 show the variation of lift to drag ratio and shock wave stand-off angle as the effective wedge angle changes. The shock stand-off angle is compared with the shock shape predicted by the method of Squire [44]. Also shown are the shock angles for wedge and cone flow. The theory of Squire predicts the shock position for the delta wing very closely. The flow is seen to be similar to the cone value. As the lower surface is undercut the flow becomes more nearly two-dimensional, although the simple flow fields grossly over-predict the shock angles for incidence above 30°. Squire's theory predicts the delta wing shock accurately over the complete incidence range. However, his theory is not so good for the two caret wings. Typically the shock angle is in error by 2° but this error decreases with increased incidence. The flow remains attached to the slender wings at angles much above the shock detachment angles for similar wedges or cones at the same free stream Mach number.

The lift to drag ratio for the three models collapses to a unique curve, Figure 24, and aerodynamic performance may be estimated by Newtonian theory based on the effective wedge angle. Since the models are small, with a smooth surface and the Reynolds number is large, viscous effects are negligible. There is no obvious increase of lift for the caret wings when incidence is measured to the effective wedge surface, Figure 22. If the lift coefficient be plotted against the angle to the plane of the leading edge then the caret wing appears to have a superior performance. In comparing a delta wing with a caret wing it seems most useful to have a unique curve on which the benefits may be seen. Figure 24 indicates the increase in lift to drag ratio to be had if a delta wing is undercut. From a point on the curve representing the basic delta a move towards the origin through the number of degrees of undercut will give the increase in overall performance. Both the lift and the drag forces are reduced and the effect of the undercutting is simply to turn the force vector forwards by the amount of the undercutting. In this part of the experiment viscous effects must be small and the underwing pressure acts normal to the lower surface.

Figure 26 shows the normal force coefficient for the three models plotted against the effective wedge angle. Comparisons are shown for Newtonian theory and for the theory of Squire. In terms of this theory a model is described by two fundamental parameters which describe the sweep and the thickness as functions of free stream Mach number, leading edge incidence and model geometry. The Mach number and the incidence are used to calculate the ratio of upstream to downstream density across a shock wave inclined to the flow at an angle equal to the incidence of the plane containing the leading edge of the wing. The theory predicts closely the measured value of normal force for the delta and the caret wings. The comparison has been made between the calculated centre-line pressure and the coefficient calculated from the overall normal force. No allowance has been made for local pressure variations, for example in the corners of the caret wing models. This increased pressure appears to cancel the effects of the spanwise pressure decrease towards the wing tips. In later tests in the nitrogen tunnel actual pressure distributions are measured and compared with the theoretical distributions.

More realistically, comparisons between different wings should be based on the actual aerodynamic performance of the wings. Figure 26 shows that for a given wing incidence the caret wing develops a higher normal force than does the delta wing. Figure 26A shows the lift obtained for the same lift to drag ratio. The two caret wings develop more lift as incidence increases. The lift coefficient reaches a maximum value of 0.76 for the delta wing at L/D = 0.77 and 0.83 at L/D = 0.92 for the caret wings, which therefore develop more lift at lower incidence than the delta wing. Incidence for maximum lift is 52° for the delta wing and 47° for the caret wings. Thus the waverider could cruise at lower incidence, with lower heat transfer, at a maximum lift which would be greater than for a corresponding delta wing. Beyond this angle of maximum lift there is no obvious gain for the caret wing compared with the delta. The present models all develop greater lift than did those tested by Coleman [41] and the superiority of the caret wing is less marked for these models. Coleman measured a 17% increase in lift coefficient for the caret wing compared with a 10% increase in the present experiments.

7. NITROGEN TUNNEL: DELTA AND CARET WING STUDIES

7.1 PRESSURE DISTRIBUTIONS

A further series of three models were tested in the Nitrogen Tunnel to investigate low-density effects on a complicated vehicle. The model geometries are the same as those models used for the Gun Tunnel force measurements. In the present experiment, of a low-density flow past a delta shaped lifting re-entry vehicle, several flow parameters are important in defining the flow. The incidence and shape of the body produce a wedge-like flow field which is modified by the three-dimensionality of the model. Also, the effects of viscosity will further modify the pressure distribution away from that predicted by inviscid theory. Once the flow field for the flat bottom vehicle is known then the advantages of modifying the body, by undercutting into a waverider, may be measured.

Two previous pieces of work are of particular relevance to the present experiments. Vidal and Bartz [45] have measured the heat transfer and pressure distribution for low-density flow past a two-dimensional wedge. They measured the effects of viscosity by comparing experimental results with the viscous shock theory of Cheng [46]. A further comparison of the present results with this work, under similar viscous conditions, gives an immediate indication of the differences between two-dimensional and three-dimensional models, both of which are based on the same fundamental wedge cross section.

The pressure data measured on the wedge covers the transition régime of low-density flow. By changing the wedge incidence it is possible to change the flow structure from near continuum to nearly free molecular and to investigate the mechanisms which control the departure from continuum theory. Vidal and Bartz [45] have extended Cheng's thin boundary layer theory [46], for an inclined flat plate with boundary layer displacement, to compare with experimental results from hypersonic viscous flow past a wedge. In this the real flow is made up of an inviscid wedge flow together with an induced pressure due to the displacement effect of the substantial boundary layer, as was the case with the flat plate flow field. The surface pressure can be expressed in terms of these two parts by the expression

$$\frac{p}{p_\infty} \sim \left(\frac{2\gamma}{\gamma+1}\right) M^2 \sin^2\theta + \tfrac{1}{2}\sqrt{3}\,\chi_\epsilon$$

where

$$\chi_\epsilon = \frac{\gamma-1}{\gamma+1}\left[0.664 + 1.73\frac{T_w}{T_o}\right] M^3\left(\frac{c^*}{Re_x}\right)^{\frac{1}{2}}$$

and θ is the shock angle.

The pressures measured on the delta wing model have been compared with these viscous predictions for a wedge. Distances are measured from the leading edge, parallel to the model centre line.

This comparison between delta wing and wedge in a viscous flow is shown in Figure 27 for an angle of incidence of 20° and for four different tunnel stagnation conditions. The delta wing values are only one third of the wedge value. Whereas the wedge shows pressures which increase with increasing viscosity (as the leading edge is approached) the delta wing pressures drop towards the leading edge. Since the delta wing is so slender this indicates that flow spillage is particularly strong at the front of the model and, in any case, three-dimensional effects reduce the surface pressure well below the wedge value. Figure 27 shows that viscosity has some effect but three-dimensional effects are dominant for the flat delta wing.

The theory of Squire [44] may be used to predict the three-dimensional effects in an inviscid flow. A comparison of the present results with this theory will indicate how important are the effects of viscosity. It will also, and the two effects may be indistinguishable, test the validity of Squire's theory under extreme flow conditions. The theory extends Messiter's first order correction for Newtonian flow to the calculation of the off-design behaviour of waveriders. In the extension of Newtonian theory to the general conical case Messiter [47] studied the problem of flow over an infinite swept wing with an attached shock. He presented the solution in the form of a basic Newtonian solution with the shock lying in the wing surface together with a series solution in terms of the density ratio across the basic shock wave. Messiter obtained analytic solutions for the case of flat swept wings. Squire extended the theory to a numerical calculation for wings with some thickness. In particular the solution for diamond and caret wings can be presented in terms of two fundamental parameters. Squire presents results for a wide range of these parameters in the form of charts, which can be used to predict surface pressure distributions and shock shape for waverider vehicles. His theory has been used to predict the inviscid pressure distribution for the conditions of the present experiment. The measured pressure has been compared with the theoretical values computed according to [44] and these comparisons are shown on Figures 29, 33, 34 and 37. The difference between the calculated and measured pressures is an indication of the accuracy of the method and of the effects of viscosity. Unfortunately, no other data is available for pressure distributions on conical wings at such high Mach numbers and so there is no way of separating differences due to viscosity from basic inaccuracies of the theory under these extreme flow conditions.

The two parameters defining the flow are functions of the model geometry and of the density ratio across a shock wave lying in the plane of the wing leading edges. The two parameters, defined above, are:

$$c = \frac{h}{b\epsilon^{\frac{1}{2}}} \qquad \text{and} \qquad \Omega = \frac{b}{\epsilon^{\frac{1}{2}} \tan\alpha}$$

Ω is the transformed wing semi-span and a constant value for c corresponds to wings with constant body slope. These two parameters define the type of inviscid flow to be expected. The two lines $c\Omega = -1$ and $(\Omega - c) = 2$ divide the (c,Ω) plane into distinct regions each with a different type of flow field. Positive values for c correspond to conical wings with diamond cross-section, negative values of c with waveriders and zero values with flat bottom wings of delta planform. In the present experiment c has a zero or negative value in the range 0 to -1.5 and Ω lies in the range 1.0 to 5.0. These combinations are shown in Figure 28 which also indicates the flow types in each of the regions. The most reliable comparisons can be made in the region of detached shock wave solutions. This corresponds, in the present experiment, to the flat bottom delta at incidence greater than 15°. The delta wing pressures, at incidence greater than 15°, have been reduced to coefficient form and compared with Squire's theory in Figures 29. The pressure coefficients are shown as functions of the geometrical parameter ζ. Constant values for ζ represents moving out along a ray originating in the point of the model; $\zeta = 0$ being the centre line and $\zeta = 1$ the leading edge. The layout of pressure holes and the value of the parameter ζ for each hole is shown in Table 1 for the delta wing, Table 2 for the 5° waverider and Table 3 for the 8° wing. Data is presented for all running conditions of the experiment, sometimes four and sometimes eight combinations of stagnation conditions. The measured pressures are generally lower than is predicted by theory. Apart from the centre line the pressure is reasonably constant across the wing span. The position of the furthermost pressure tapping is within the linear portion of the theoretical profile and no pressure increase was measured in the experiment close to the leading edge. The spanwise variation of pressure increases with increased incidence.

Squire predicts constant pressure along the centre line. As can be seen the greatest scatter in the experimental data occurs along the centre line, the pressure at the back of the model being considerably lower than towards the front. Figures 30 show the variation of pressure with the viscous length parameter; both are normalised in the manner of Cheng's expression for viscous wedge flow. Figure 30A shows all pressure points for the delta wing; Figure 30B shows only points on the model centre line. The distance used to calculate the viscous parameter, χ_ϵ, is the distance behind the leading edge. This correlates all the delta wing pressures for a given angle and all stagnation conditions. The flat delta wing may, therefore, be thought of as a series of flat plates in a viscous flow defined by the flow conditions behind the shock front. The shape is similar to that of the flat plate but in the case of the delta wing the mechanism of the flow is much different. Viscous effects and spillage from the model combine to give a pressure distribution which exhibits a peak some distance behind the model leading edge.

In Figure 31 the flat delta wing pressure distributions have been plotted as functions of the rarefaction parameter, $\bar{V}_{x_{LE}}$. This parameter is calculated from the calculated inviscid conditions behind the wedge shock wave and the distance of the pressure hole behind the wing leading edge. The angle of incidence is 28° and the measured pressures have been normalised by the two-dimensional inviscid wedge pressure. Data is presented for two different values of Reynolds number in each of the two graphs. This shows the degree of correlation for a particular incidence and a particular Reynolds number. Graphs presented so far have given data for all stagnation conditions; this correlation is present in all delta wing results, though sometimes masked by variations in flow conditions. The pressure rises away from the point of the model to reach a peak value some distance downstream. The magnitude and the position of this peak, in terms of the present parameters, is Reynolds number dependent. An increase in Reynolds number causes the pressure peak to both move back and to decrease in magnitude for an incidence of 28°. This is consistent with the idea of a viscous interaction causing an effective change in body shape, since, at increased Reynolds number, this induced pressure would be less. However, these values of the rarefaction parameter are appropriate, on a flat plate model, to a strong interaction region in which the pressure data would be correlated by the rarefaction parameter. It would appear, therefore, that there is a Reynolds number effect present in the nature of the basic flow structure around a slender delta wing at incidence in a low-density hypersonic flow. It is not possible to predict the pressure forces over a flat delta wing by a strip theory in which each strip is thought of as an isolated flat plate at zero incidence in a viscous hypersonic flow defined by conditions behind an oblique shock wave. Some allowance must also be made for the additional effect of Reynolds number on the flow structure and its effect on flow spillage from under the model. A comparison of the two graphs of Figure 31B will show that the Reynolds number dependence is not straightforward; the highest Reynolds number does not give the lowest pressure peak nor does the lowest give the highest pressure peak. Figure 31B shows comparable pressure distributions at an angle of incidence of 20°. Scatter is due to variations across the span for holes at the same distance behind the leading edge.

The overall results of Figures 29, 30 and 31 show, between them, the data for flat delta wing pressure distributions at all angles of attack and all stagnation conditions. The large scatter is explained by the Reynolds number dependence at a given incidence, which also changes. However, the overall trend of a pressure peak downstream of the tip of the model is still discernible from the data.

The detailed pressure distributions for the three models have been tabulated in Tables 1-3. The positions of the pressure holes are given as points in a plane defined by the wing leading edges. Running conditions are the same for all three models; any slight difference in the free stream Reynolds number may be explained by the day to day variation in tunnel performance for the same, nominal, supply conditions. An added complication during the delta wing runs was that the model was mounted in the test section with the electron beam above. The model itself was at 45° to the vertical and the pitot tube mounted on the side of the test section. This meant that the free stream Mach number was measured some distance away from the point of the model. At the time of the first series of runs with the delta wing only two of the pressure channels were reliable and so the pressure distributions were built up from four or five separate tunnel runs. This, together with the difficulty in measuring free stream conditions, means that there may be errors in the pressure data. Holes 3 and 4 are mirrored in the model centre line and any difference in these two positions is an indication of the overall accuracy, since these two pressures were always measured during different runs. For later tests and for all tests with the two waverider models, more pressure sensors were available but the ideal situation where all pressures were measured during the same run was not achieved. The data in all cases is composed from at least two runs and the values for Reynolds number and free stream pressure are only indications of the measured values since they changed for each contributing run.

Figure 27 shows pressure data for the 5° waverider compared with data for the delta wing at an incidence of 20°. Data for the waverider, alone, at all incidences and for all Reynolds numbers is shown in Figure 32. The pressure level is much higher than the delta wing and much closer to the two-dimensional value. Also shown is the inviscid pressure. The general shape of the pressure distribution, which includes all the pressure holes on and off the model centre line, is similar to that for the wedge and rises above the inviscid value. The general scatter of the data is much less, since it is possible to show all angles of attack and all running conditions on the one graph. This tends to confirm that the undercut wing is behaving much more like a wedge; the spillage of the delta wing being more contained by the waverider. This is better illustrated when actual values are quoted. For the 5° waverider, with a 23° equivalent wedge at 28° incidence, the calculated inviscid pressure on the lower surface is ~~0.22~~ 0·36 mm Hg. The pressure measured under the waverider was approximately equal to this value. For the delta wing the underside pressure is only 0.6 of the theoretical value of 0.49 mm. So the actual pressure levels under the two wings, both in a similar attitude and identical flow conditions, is ~~0.22~~ 0·34 mm Hg for the waverider and 0.29 mm Hg for the delta wing. In one case the delta wing is spilling the flow produced by a 28° wedge and in the other the waverider contains the flow from a 23° wedge. The pressure over the lee surface is the same for both models. Assuming that the pressure acts normal to the undersurface the waverider operates at an increased lift to drag ratio, since there will be only a small change in drag, but with the penalty of reduced internal volume.

The delta wing pressure distribution was approximately constant across the span, in agreement with the theory of Squire. There was, however, a pressure gradient along the model centre line. The 5° waverider distributions are shown in Figure 33 for three angles of incidence. The data is more constant, one data point being sufficient to cover all four running conditions at 20° incidence and the variation along the centre line much less than for the delta. At all three angles of attack the corner pressure is higher than further out on the wing. The spacing of the pressure holes was such that information is not available for the area between the centre line and a ray at 9° to it. The presence of a pressure peak along the corner is consistent with a rectangular corner in low-density hypersonic flow [33]. The present model has a corner angle of 106° but is slender, rather than rectangular.

It appears that corner effects are still present. The pressure coefficients are comparable with those for the delta wing indicating, again, an improved lift to drag ratio for the waverider vehicle.

As is shown by Figure 28 the theory of Squire cannot be applied to the present waverider models under Nitrogen tunnel flow conditions. The work of Keldysh and Maikapar [31] at low hypersonic Mach numbers for waveriders at off-design conditions also shows a corner pressure peak. The centre line pressure is certainly higher than at the leading edge but there is a further, higher, peak between the centre and the ray $\zeta = 0.3$. These peaks are due to an intersection of oblique shocks from the leading edges causing inner shocks in the corner of the model. These inner shocks may well cause local separations at the front of the model. The presence of these separations may well explain the increased scatter at higher incidence, Figure 33.

The waverider pressure distribution is shown as a function of distance behind the leading edge in Figure 34. The centre line pressure is seen to be higher than measured out on the wing panels. The data taken at 20° shows a quicker drop in pressure towards the back of the wing panels. The centre line pressures appear to be linear with distance from the front of the model.

The effect of viscosity is shown in Figure 35, where the pressure distribution is shown as a function of the rarefaction parameter based on distance behind the leading edge. Only the centre line pressures are shown to avoid confusions with variations out on the wing panels. Inviscid theory would predict that the centre line pressure remains constant over the length of the model. Data for the 5° waverider does not show variation due to spillage, as did the flat wing. Rather, the rarefaction parameter appears to correlate the pressure data and, further, pressure appears to increase with increases in the rarefaction parameter. This is typical of a merged layer flow over a flat plate. It is interesting to note that at 20° incidence viscous effects raise the pressure above the inviscid level. At higher incidence, 28°, the effect is to increase centre line pressures up to the inviscid level.

The data for the 8° waverider is generally similar to that of the 5° model. A comparison of centre line pressures with the theoretical values for a viscous wedge is shown in Figure 36 and, as with the 5° model there is a viscous effect. The pressures are still lower than the wedge values but the viscous effects are stronger at the front than for the other waverider model. This is reasonable since the inclination of the bottom face to the free stream is less for the 8° model. The pressure levels are considerably higher than for an inviscid wedge flow.

The variation of pressure coefficient across the span, Figure 37, is similar to the 5° model except the values are lower, since the model has a smaller effective wedge angle. The centre line pressure peak increases with increased incidence. This corner effect is also shown in Figure 38. Compared with the 5° waverider the difference on and off the centre line is greater and the pressure rises more quickly at the front of the model. Measured in terms of the inviscid wedge the pressures are slightly lower on the 8° model.

The viscous effects are also similar for the two models. Figure 39 shows the pressure normalised by the inviscid wedge value as a function of the "flat plate" rarefaction parameter. The pressure increase is greater on the 8° waverider since viscous effects are more pronounced at the smaller wedge angle. These results are consistent with the work of Hefer [38] who investigated an uncooled caret wing with a design Mach number of 8.5, at Reynolds numbers between 2.5×10^4 and 2.5×10^5 per metre. He found the pressure distributions comparable to two-dimensional viscous theories. Force measurements suggested that inviscid wedge theory is capable of giving lift coefficients but the drag coefficient is considerably increased by Reynolds number effect. This reduces the lift to drag ratio of the vehicle to such an extent that under rarefied flow conditions the value is only one quarter the inviscid value. It is noticeable that Hefer found no increase of pressure along the corner of his model, which had a corner angle of 138° and is considerably more than the corner angle of the present series of models.

7.2 HEAT TRANSFER DISTRIBUTION

As described above and in Appendix A2 a series of thin shell delta wing and waverider models were used to measure heat transfer rates. All of the criteria mentioned have been incorporated in the design of the models. For example, thermocouple wires were laid side by side on the thin shell material to avoid local thickening of the model during welding. The thermocouples were individually calibrated by two methods. The models were held in the free stream with very low heater power setting and the steady state signal recorded on an ultra-violet recorder and then on an electronic thermometer. Selected models were immersed in oil in a water bath and steady state signals measured on the recorder and with a thermometer. Both methods gave equal calibrations. The overall accuracy of the models was considered to be good and by fitting temperature rise information over a period of time and calculating the initial rate of increase errors due to conduction were also small.

Thin shell hemispherical models were used to calibrate and check the heat transfer experiment. A series of hemispheres with a diameter of $\frac{5}{8}$" were mounted on the injection ram and heat transfer rates at the stagnation point and at six other positions were measured for eight different free-stream conditions. These measurements allowed a comparison with other published work [49] for both the absolute heat transfer and the distribution over the surface. Since these experiments represent the first heat transfer measurements in the facility it was necessary to make these checks. The sphere results are also used to normalise heat transfer measurements made on the underside of waverider and delta wings under similar free-stream conditions.

Figure 40 shows the stagnation point heat transfer rate expressed as a Stanton number based on the model wall temperature. As with Metcalf's results the experiments were made with uncooled models with cold walled conditions. Since the recovery temperature was not measured the heat transfer coefficient in all the present results is defined as:

$$C_H = \dot{q}/\rho_\infty U_\infty (H_o - H_w) \ .$$

Cheng's thin shock theory predicts that the Stanton number is a function of the parameter K^2, where

$$K^2 = \frac{1}{2}\left(\frac{\gamma-1}{2\gamma}\right)\left(\frac{T_2 + T_w}{2T_o}\right)^{0.25} Re_{2_D} \qquad \text{for } K^2 \geqslant O(1) \ .$$

Results in terms of these parameters are shown in Figure 40 and they indicate that the present data for a hemisphere are in reasonable agreement with the results of Metcalf for a hemisphere at a Mach number 10. Variations may well be due to errors in measurement of the tunnel free stream conditions, since these are used to calculate both the Stanton number and Cheng's parameter. Figure 41 shows the same data as a function of the Reynolds number behind a normal shock and it is obvious that the use of Cheng's parameter correlates data over a wide range of tunnel conditions.

The heat transfer distribution around the hemisphere for four of the eight different free stream conditions is shown in Figure 42. The overall shape of the curve is similar for all running conditions; the two high pressure conditions giving heat transfer rates lower than the other six more rarefied conditions. Theoretical curves for continuum and free molecular flow are shown and it is seen that the move towards continuum flow is accompanied by a reduction in heat transfer rates away from the stagnation point. The results appear to be slightly higher than predicted by theory but results by Metcalf for a hemisphere under rarefied flow conditions are also higher than the theoretical value.

This preliminary experiment indicates that heat transfer experiments are possible in the Nitrogen tunnel. The results are in reasonable agreement with other published work. The major difficulty in the experiment is in the making of thin shell models and instrumenting them with fine thermocouples. Gauges which appear to be working perfectly when calibrated are unreliable when subjected to the high acceleration loads during injection. Quite often this type of failure affects two channels since wires move and touch. It is therefore difficult to build up a detailed picture of the heat transfer distribution. Typically, on a model with twelve channels, seven would give reliable temperature histories. If the distribution be built up using a series of models then it is important that models with different wall thickness should give the same heat transfer rate. As with the pressure models there is a problem of reproducing tunnel conditions from run to run over an elapsed time of several weeks.

A series of four delta wing and waverider models were constructed, each carrying a pattern of up to eight thermocouples on the lower surface. One shape was made with two different wall thicknesses to investigate the effect of skin thickness. The measured heat transfer rates have been compared with results from high Reynolds number flow and have also been normalised by the stagnation point heat transfer rate for a 0.625" diameter sphere under similar tunnel conditions. The results are given for the four models over a range of incidence in Tables 4-7. Since there are variations in tunnel conditions from run to run the quoted value is a useful indication of the repeatability of the runs. No allowance is made for the effects of varying tunnel blockage, as the model incidence is changed. This is because the free stream conditions are measured with the test section empty before the model is injected. Comparison of the results for the 5° waverider with two wall thicknesses is an indication of both the effects of skin thickness and of the general accuracy of the experiment.

The results for the delta and caret wings are given in Tables 4-7, expressed as a fraction of the stagnation point heat transfer rate for a $\frac{5}{8}$" sphere under similar flow conditions. It appears that a particular model has a certain heat transfer distribution. As the tunnel conditions change the pattern and the fraction of the stagnation point value are unchanged. Increasing the incidence increases the heat transfer rate but the distribution of heat transfer remains unchanged.

As with the pressure measurements for the slender delta and caret wings, a useful comparison is with viscous theory for a wedge at incidence. In the case of the two waveriders the wedge angle along the bottom ridge line is used to define incidence, since this centre line wedge defines the flow. Cheng's theory [46] also predicts the heat transfer rate to a wedge in viscous hypersonic flow. He writes a general relation between the heat transfer to the surface and the local pressure on the surface of the wedge:

$$M^3 C_H = 0.332\, M^3 \left(\frac{c^*}{Re_L}\right)^{\frac{1}{2}} \frac{p/p_\infty}{\left[\int_0^x \left(\frac{p}{p_\infty}\right) \frac{dx}{L}\right]^{\frac{1}{2}}}$$

Substituting the previously used expression for the surface pressure the heat transfer can be written as:

$$M^3 C_H = 0.166(3)^{\frac{1}{4}}\, \bar{\chi}(\lambda \bar{\chi}_\epsilon)^{\frac{1}{2}} \frac{\left[1 + \frac{4}{\sqrt{3}(\gamma+1)} \frac{M^2 \sin^2\theta}{\bar{\chi}_\epsilon}\right]}{\left[1 + \frac{2}{\sqrt{3}(\gamma+1)} \frac{M^2 \sin^2\theta}{\bar{\chi}_\epsilon}\right]^{\frac{1}{2}}}$$

where, again, θ is the shock wave angle and is related to the wedge angle, α, through the oblique shock relations.

The heat transfer measured on the wings has been compared with Cheng's theoretical value for a similar wedge. In making the comparison the data have been normalised in a similar way to the data presented by Vidal and Bartz [45] in their comparison with Cheng's theory. The measured heat transfer rates have firstly been reduced to coefficient form in the same way as for the hemisphere:

$$C_H = \dot{q}/\rho_\infty U_\infty (H_o - H_{Aw})$$

and the data has been plotted in terms of the following two parameters:

$$\frac{C_H \, \epsilon \, (1.73 \, {}^{T}w/_{T_o} + 0.664)}{\sqrt{\gamma} \, \sin^3\theta} \quad ; \quad \frac{\bar{\chi}_\epsilon}{M^2 \, \sin^2\theta}$$

ϵ and χ_ϵ are as used in the pressure comparison. Vidal and Bartz found very close agreement between theory and experiment for a wedge, allowing for the combined effects of boundary layer displacement and wedge angle.

Figure 43 shows the data for the delta wing. Data is for four different running conditions and at four angles of attack, 10°, 20°, 28°, 35°. It is clear that the wedge theory is sufficient to collapse all of the data and that the measured heat transfer is the same as would be measured on a wedge in similar flow conditions. It is interesting that over the bottom surface of the slender delta wing there is but little variation from the wedge value, although data was only measured at 7 positions and there may have been local hot spots.

Data for the 5° waverider shows more scatter, Figure 44, but the overall values are of the same order as the wedge values. There is no obvious region of low or of high heating. Figure 45 shows a sample of the data measured on the second 5° waverider model, which has a different wall thickness. The scatter appears less, but fewer data points are presented; the heat transfer rates for this model are the same as for the first 5° waverider. The benefit of the thinner shells lies mainly in a faster temperature rise, which is easier to measure rather than increased accuracy due to reduced conduction errors. This is countered by the difficulty of making heat transfer models with very thin shells.

Figure 46 shows the data for the 8° waverider. For this model there are definite points with high and with low heat transfer. High heat transfer is measured at point number 11, a position on the lower ridge line at the back of the model. The low heat transfer point is number 6, close to the leading edge about the middle of the wing span.

The spanwise distribution of heat transfer is also shown. The Stanton number is shown as a function of position across the span, ζ. As with the pressure data $\zeta = 0$ corresponds to the model centre line and $\zeta = 1$ to the leading edge. Each model has a characteristic distribution at each of the four angles of incidence which were tested.

The delta wing, Figure 47, has a distribution which rises steadily with distance away from the centre line. The two waveriders have greater variations along the centre line and show a peak heating rate along the ray $\zeta = 0.33$. The heat transfer rate also rises sharply at $\zeta = 0.75$ and these effects are found on both of the waverider models. On the 5° models the thermocouples cover the region around the ray $\zeta = 0.33$ in reasonable detail. This indicates that the area represents a localised area of high heat transfer which is consistent with heat transfer measurements for viscous corner flows at hypersonic speeds.

The heat transfer data for the three models is summarised in Table 8. This shows the heat transfer as a fraction of the wedge value, allowing for the effects of wedge angle and viscosity, at different positions across the model. Significant departures from wedge theory have been underlined and are summarised below:

i) The delta wing model shows higher heat transfer at points 7 and 11, which are on the centre line at the back of the model.

ii) 5° waverider: the two models are in agreement. Two points, one on each model, are close together ($8,8^*$) and show very different heat transfer rates indicating a corner flow effect. The heat transfer rate is low on the centre line at the back of the model.

iii) 8° waverider: a heat transfer rate peak on the centre line at the back of the model and low heat transfer rates just behind the leading edge.

8. CONCLUSIONS

Measurements have been made using simple and complicated shapes in a hypersonic, low-density flow where even a model 12" long would be covered by non-continuum fluid. Measurements on a flat plate model under a range of low-density free stream conditions show the relevant length scaling parameters to be a modified rarefaction parameter or a mean free path associated with free stream molecules colliding with others emitted from the surface of the model. Measured surface pressures are strongly dependent on the nature of the pressure tapping holes and reliable comparisons can only be made using the measured, normalised number flux. Reasonable agreement was found between experiment and the Monte Carlo calculation by Pullin for an identical, diatomic flow over a flat plate. This agreement was also confirmed for a forward facing step (in this case the measured pressure was significantly higher and a direct comparison of pressure data was possible since the corrections were negligible). An electron beam probe was used to visualise the flow over the flat plate and to measure the density distribution around the forward facing step.

A series of waverider models were tested in both high and low Reynolds number facilities. Force measurements at Mach 9 in the Gun Tunnel, at angles of incidence up to 70°, showed that the caret wing develops a higher normal force than a flat delta wing giving increased aerodynamic performance. In the low-density facility surface pressure and heat transfer distributions were measured. The surface pressure data was compared with the inviscid prediction of Squire. The results demonstrate the ability of the Waverider to contain a two-dimensional flow. Features of hypersonic corner flow and the effects of viscosity were measured for these lifting shapes in a rarefied hypersonic flow. The heat transfer apparatus was calibrated using a series of hemispherical models and the data compared with results from other experiments. Finally, the heat transfer to the same family of Waveriders was measured and compared with the results for a two-dimensional wedge in similar merged-layer flow.

Details of modifications made to the Nitrogen Tunnel to decrease the static pressure by an order of magnitude, the techniques used to make the models and pieces of apparatus needed for the tests are described in an Appendix. The tunnel instrumentation is also described along with the real gas theoretical model which was used to calculate the tunnel stagnation temperature.

ACKNOWLEDGEMENTS

It is a real pleasure to record my thanks to all the many people connected with the work just described. Particular thanks are due to Dr. John Harvey for supervising the work and to Jim Cunningham for keeping the machinery working and for helping to translate ideas into the final, useful hardware.

A special thanks to the laboratory staff, Jim Gibb, Ernie Turner, Geoff Corey, Nick Middleton for keeping the tunnels running and to Bill McGee and Ken Sage for making those tedious models. To my colleagues at Imperial College and now those at RAE Farnborough for many helpful discussions over the last five years. And, of course, to Sue for keeping me going through it all.

The work was sponsored by the Ministry of Defence, Procurement Executive, and monitored by Steve Metcalf under Contract AT 2037 084, Separated Flows At Very High Mach Numbers.

APPENDIX A

A1 TUNNEL MODIFICATIONS AND DEVELOPMENTS

The basic details of the wind tunnel remain very much as used by Uppington [16] and described by Harvey, Jeffery and Uppington [9]. The basic change has been that the test section diameter has been increased from 6" to 8", giving a change in Mach number from 19 to 23 and an order of magnitude decrease in the free stream density.

To keep the axial gradients as small as possible the original conical nozzle was replaced by a contoured version, designed with an exit diameter of 6". A straight sided, conical extension piece increased the exit diameter to 8". Tests were made to determine the influence of nozzle geometry, stagnation conditions and the distribution of nozzle coolant and diffuser geometry on the axial flow gradients. A centre-body diffuser, together with the contoured nozzle, only ran over a limited range of stagnation conditions. Below a Reynolds number of 3.5×10^5 ft^{-1} the nozzle flow was stalled. A disturbance appears to travel upstream from the diffuser through the thick boundary layer and separates the flow in the nozzle. The diffuser acts as a link to match the nozzle exit pressure to the inlet pressure for the vacuum pump system for the particular mass flow. The pressure at the nozzle exit is fixed for a given Mach number by the stagnation temperature of the flow. This pressure is the inlet pressure to the diffuser and the test section static pressure. The vacuum pumps operate on a performance curve such that the pump inlet pressure is a function of the mass flow rate. The diffuser slows down the flow through a complicated shock pattern set up with or without a centre body in place and recovers pressure up to the inlet pressure for the vacuum pump. The contoured nozzle is particularly prone to separations. The boundary layer displacement effect and the very small divergence at the end of the nozzle produce a very nearly parallel flow into the test section without any lip shocks. At low Reynolds numbers it would appear that the nozzle flow can be separated by even a very slight mis-matching of pressure by the diffuser. This was made in several distinct parts so that the front cone angle, the second throat area, the position of the centre-body could be changed along with flow Reynolds number to investigate the overall performance. It was found that, providing there was a model in the test section, the shock pattern from the model, reflected along the length of the tunnel, acted as a very good diffuser. To this end the tunnel was made as long as possible and the centre-body removed to produce the optimum unit.

Even with this "optimised" diffuser the flow in the contoured nozzle separated when the stagnation temperature was increased. Since the disturbances which induced this separation travelled upstream from the diffuser a barrier in the form of a jet was tried between the nozzle and diffuser. McDevitt [50] has used a gas injection device to extend the operating range of a low-density Helium facility. Operating Mach numbers varied between 10 and 25 and wihtout injection impact pressures varied during the duration of the test run, approximately 2 minutes. With the injection scheme the flow conditions were invariant up to a sudden flow breakdown. Force measurements on a blunt model indicate that the injection system improved the reliability of data by reducing the interference between the model flow field and the tunnel boundary layer. Figure 50 shows a schematic of the injection rig. An annular nozzle around the upstream end exhausts into the test section. The annulus is designed so that the jet blowing along the tunnel walls is underexpanded; the jet is supersonic and further expansion occurs within the tunnel boundary layer. In McDevitt's work this was found to be the most effective barrier to prevent disturbances travelling upstream from the diffuser and separating the flow in the nozzle.

For use in the Nitrogen tunnel the basic change is in the area ratio between the annulus throat and the exit area to achieve a given exit Mach number in nitrogen compared with Helium. The actual throat area must be made very small so that the exit slot should not reduce the test section diameter too much. The practical difficulty of making a useful injector means that if an annulus be used then parts of the blowing rig must be located to a very high accuracy; a typical width for the annular throat would be 0.002" to give an exit Mach number of 8. In the present design, shown in Figure 50, the annular throat was replaced by 16 half-round "scratches" on the sharp edge of one part of the assembly. When the rig is assembled these sharp edges locate on an inner nozzle to give the required expansion ratio, as shown. Although not a continuous ring the spread of each jet needs be only about 10° to give complete blowing around the whole of the test section wall. The supply pressure in the injector rig could be controlled by a pressure regulator.

The blowing unit was mounted on the contoured nozzle, the inside of the injection unit being a conical approximation to continue the nozzle profile. The unit extended the range of the contoured nozzle down to a lower Reynolds number but, because the blowing rigs fit inside the test section the useful core was reduced by about an inch.

Tests were also conducted to investigate the effects of nozzle cooling on tunnel performance. Cooling controls the growth of the boundary layer along the length of the nozzle and variations in coolant flow can cause large changes in static pressure for, supposedly, identical stagnation conditions. Because of the problems with flow separations in the contoured nozzle, the conical nozzle was used for this investigation. The initial part of the nozzle is water cooled but further downstream liquid nitrogen is used. With the conical nozzle there was evidence that a reduced coolant flow through the final nozzle section encouraged the boundary layer to thicken and produce a more parallel flow into the test section giving an improved Mach number gradient.

One further attempt to improve the nozzle flow and test section gradients was based on the original conical nozzle. At Mach numbers of order 20 the method of characteristics for an inviscid gas indicates that the major part of the flow is formed in the first 2" of the nozzle. Figure 51 shows the original design of the nozzle. The initial nozzle section, made of Beryllium Copper, was replaced by a contoured insert. The contour was initially that of the contoured nozzle but then was blended to the straight sided conical nozzle. This hybrid nozzle had much improved axial gradients; the initial contouring meant that the flow was more like that from a true contoured nozzle while the conical profile downstream of the contoured insert meant the flow was no longer prone to separation. This hybrid nozzle ran over the entire range of tunnel running conditions. Figure 52 shows the improvement in test section conditions due to this modified nozzle. One unusual feature of the new nozzle is that the tunnel flow is stalled under cold flow conditions. As the stagnation temperature increases and the Reynolds number decreases, the flow suddenly starts. It appears that the nozzle has two stable running conditions. At the end of a test run the flow suddenly stalls again as the heater power is reduced and it would seem that there is a change from one stable condition to another at a definite value of Reynolds number. It is interesting to note that Lewis [23] retracts his flat plate models to start the tunnel flow then lowers the models down into the stream. This enabled him to attach larger tubes to his models and achieve shorter response times for pressure measurements. This could mean that during the starting process, when a normal shock moves along the tunnel, the model shocks are sufficient to separate the flow in the test section. However, once the flow is established and the model introduced, the shock interactions are less and the flow remains attached.

Other items were built for some particular part of the experimental program. A quadrant was designed so that waverider and delta wing pressure models could be set at incidence in the tunnel test section. The assembly is pictured in Figure 53. The outer box was fabricated from Aluminium alloy and the model incidence could be changed after removing two cover plates. A carriage ran round the quadrant and could be set at 2½° intervals using jig-bored holes and dowel pins. The sting and model were water cooled and the pressure tubes were taken out through the oval section sting. From there on the tubes were contained in a recess in the front of the quadrant arm and covered by leading edge "bricks" (sharp-edged pieces of copper alloy which slid around the quadrant arm as the incidence changed and kept the pressure tubes covered and streamlined the front of the quadrant). The arm ran on two rails so that the model could be moved over a distance of 6" along the test section. The unit was originally designed for use with the traversing electron beam. So that the traverse was unobstructed the quadrant was mounted with its axis at 45° to the vertical. Waverider models were mounted on the quadrant axis so, when used with the electron beam, it was possible to see into the undersurface without the forward edge obscuring the point where the beam hit the model surface.

The original electron beam unit, as used by both Uppington and Lillicrap [69], was modified so that the beam could be traversed over the surface of a model which was insulated from the rest of the tunnel. Current passed to earth through a resistor and the voltage drop was used to monitor the beam current. This, in turn, was used to normalise density profiles against an unsteady beam current. The beam fired directly onto the model surface. When the electron beam hits the surface of the model secondary electrons are emitted. Thus the area near the point on the surface is lit up and no measurements are possible, since density is proportional to light intensity. Experiments with several graphite compounds showed that these secondary electrons could be trapped in the surface cutting down the general light level close to the model. The best material found was a thin sheet of graphite paper stuck onto a recessed model. As is seen in Figure 16 the light emitted at the coated model surface is very much less than the light in high intensity regions. Because the beam fired onto the model surface this eliminates the need for any holes through the model and so the drift tube, needed to balance the gun pressure with the surface pressure, was no longer necessary. Thus, the difficult job of lining up the drift tube, model and beam was avoided and the model was held at a fixed distance from the nozzle while the beam moved. Surface pressure measurements indicate that for a fixed position the local pressure could change by as much as 25% from day to day, due to changes in nozzle Mach number, in turn due to changes in nozzle cooling. This means that any pressure balancing should be done during the actual experiment and there should be some method of measuring the absolute surface pressure. This could be done using a pair of pressure tappings on either side of the model centre line; but, bearing in mind the difficulties of interpretation of surface pressure data using holes with different L/D ratio, this may not be possible. The alternative method of firing the beam directly onto the model surface means that reflection and scattering from the copper surface may mean that detailed measurements cannot be made close to the surface as described above. This problem was overcome by covering the model with some material which does not reflect electrons. Preliminary experiments by Davis [24] showed that a film of graphite paper 0.5 mm thick would trap electrons and effectively eliminate the reflection problem. To try and maintain a flat model surface, since the paper was slightly uneven, the model surface was undercut by 0.5 mm and the hole filled with an Araldite/carbon mixture which was machined flat.

Although this alternative method gave an ideal model surface, the intense local heating melted the film where the electron beam hit the surface, even though the model was water cooled. This technique was abandonned in favour of a layer of pyrolitic graphite, 0.5 mm thick and stuck down with the same Araldite/carbon mixture. Although the surface was not affected by the beam, the finish was not so smooth as the machined araldite layer.

The electron gun was mounted on a traverse above the test section. This traverse box carried a large glass window on each side so that the beam could be seen over most of the test section. The unit could also be used to photograph flow over a model using a flow visualisation technique. The traverse could be mounted at 45° intervals to the tunnel axis. This meant that traverses could be made parallel, perpendicular or diagonally across the test section. When used in conjunction with the quadrant the traverses were made across the tunnel; since the model could be moved along the axis a complete three-dimensional flow field could be explored. The moving traverse carried an optical traverse on which were mounted the optics necessary to traverse along the beam through a boundary layer. The optics were therefore at a fixed distance from the beam axis. The test section carried a removable tunnel liner which could be changed to give a field of view appropriate to the experiment.

For the heat transfer experiments a pneumatic injection system could be mounted in place of the electron gun above the test section. A rigid, hollow rod carried the model mounted on a short sting. At the other end the thermocouples were terminated by vacuum lead-throughs and the thermocouples passed from the model to the terminations through the hollow rod. Provision was made for 12 thermocouple channels. The top end of the ram ran in a guide which was bolted on to a top hat section mounted on the test section box. The incidence of the model could be changed by rotating the top hat section past a graduated scale to set a given angle. The injection time was timed as 140 msecs and Figure 54 shows the injection assembly with a waverider model in a partly retracted position.

A2 MODEL DESIGN

The two models used for flat plate measurements were inherited from Uppington. The pressure model carried ten pressure holes, closely spaced at the front of the model and more spread out towards the back. The size of the pressure tapping holes was reduced to 0.020" so that cavity correction techniques based on ideas of free molecular holes were applicable. The electron beam model was modified, as described in the previous section, so that the beam could be traversed across the model surface. This technique meant that it was no longer necessary to control expansion of the sting as the stagnation temperature increased. Previously this had meant filling the sting with Woods metal to act as a heat sink. With the new technique alignment of the beam was straightforward; the deflection coils at the top of the drift tube to compensate for the field from the heater were also not needed.

A yawmeter was made to measure the flow angularity in the tunnel test section. This took the form of a 15° wedge which spanned the tunnel. It was water cooled and had a pressure tapping mirrored in the top and bottom surface. To measure the flow angle at a given distance from the centre line the wedge was set at a known angle, relative to horizontal, and the pressure difference measured. The angle was changed and a plot of pressure difference as a function of angle of incidence was drawn. Since the yawmeter was not exactly symmetrical, due to tolerances in manufacture, the wedge was turned over and the experiment repeated.

Figure 55 shows a typical result at a distance of $\frac{1}{4}$" below the centre line and at a stagnation temperature of 2000°K. This is the normal position for the flat plate model. The yawmeter could be set at different distances from the centre line to build up the variation of flow angularity across the test section.

Before final designs for the waverider models were drawn, a series of experiments were conducted in the small tunnel test section to check that a 3" long model could be tested at incidence. With the 6" test section a three-dimensional traverse is available and a pitot tube was used to give a representation of the model flow field. Results of the tests suggested that a model designed for high Reynolds number conditions would also perform in the more viscous Nitrogen tunnel flow at a high Mach number.

The first tests involved two caret wing models designed for Mach 20 and Mach 9 inviscid flows. These models were made from thin sheet steel and were uncooled. The lower surface was continuous and their incidence could be varied 17°. The lower surface of the wing was $\frac{1}{4}$" below the centre line to avoid shock focussing effects. The Mach 9 design had an underside included angle of 135°. Rectangular corner models with interior angles of 90° and 135° were checked for tunnel blockage so that the flow over the underside of the waverider could be compared with the flow in a rectangular corner with the same included angle. All of the models ran over the full Reynolds number range and the waverider models ran over the full range of incidence without any obvious blockage effects. A pitot tube was used to probe the shock wave from the caret wing models. The shock position is dependent on the stagnation temperature but the dependence decreases as the incidence increases but in all cases the shock wave lies further out than the plane of the leading edges. Using a glow visualisation unit the curved shock wave could be seen standing off from the model and wrapping around the leading edges.

Some preliminary calculations of the boundary layer growth on the two inviscid design models were made, assuming the caret wing to be made up from flat plates. The displacement thickness of the boundary layer was calculated from Cheng's thin shock layer theory, as used above to calculate the pressure on an inclined flat plate:

$$\delta^* = \frac{\gamma-1}{\gamma+1}\left(0.664 + 1.73\,\frac{T_w}{T_o}\right) M_\infty^2 \left(\frac{C_S x}{U_\infty/\nu_\infty}\right)^{\frac{1}{2}}$$

The boundary layer calculations were made for the Mach 9 design. Boundary layer effects modify the inviscid shape; the viscous shape of the Mach 9 model in a flow similar to that in the low-density facility is very nearly the same as a model which ran as a test model in the Nitrogen tunnel. So, it appears that an inviscid model designed for Mach 9 conditions would run successfully in a Mach 20 viscous flow. This was the first indication that a single model shape could be tested in the two hypersonic facilities to simulate flight at low and high altitudes.

At about this time, after discussions with Davies and Townend, [51], it was suggested that models should be made the same as a series of models which had already been tested on a force balance in the RAE Low Density Tunnel. To this end representative uncooled models made of sheet steel were mounted on a sting carried on the three-dimensional traverse. They could then be moved around the test section while the tunnel was running to find the optimum mounting position to avoid tunnel blockage. In all cases the best position was in the centre of the tunnel, in the middle of the test section. As the tunnel flow started the shock patterns travelling down the tunnel set the model vibrating strongly. The actual models were therefore mounted on a rigid sting and no further problems were encountered. A pitot tube traverse across the test section was sufficient to show whether the tunnel was stalled.

The maximum incidence before the tunnel stalled was found to be 50°, providing that the stagnation pressure was increased to 2500 psi to start the tunnel flow.

At first it was hoped that the delta wing and waverider models could be made by an electroforming technique using pure copper. A delta wing model was successfully electroformed, from copper, with a finished wall thickness of 0.050". The major difficulty with this method was to build the tip of the model out far enough; the current concentration around the sharp point meant that the model had to be shielded during deposition to give an even growth over the whole surface. The electroformed shell was keyed onto a mandrel which could be accurately located in a jig so that the outside of the model could be machined down to the finished dimensions. The shell was pushed off the mandrel without difficulty and the next step was to fix pressure tubes in the thin shell. Bushes were shaped to fit inside the model and soldered into holes accurately drilled in the shell using a medium temperature solder. Prior to fitting in the model the bushes had been soldered onto annealed stainless steel hypodermic tubes. The final step was to solder a backplate, which carried the model sting, onto the shell and pressure tube assembly using a low temperature solder. The finished model was non-porous and mechanically strong. The model was water cooled by water passing into the model just behind the tip. This circulated around the inside of the delta wing and passed out along the sting and then collected at the backplate to pass out of the tunnel through a tube in the quadrant arm leading edge space.

The major problem in making models by this technique was that space inside the model is very limited. This made it extremely difficult to insert the pressure tappings. The problem was more serious for the waverider models where the underside is undercut by a substantial amount. The two waverider pressure models were therefore constructed by a fabrication technique. The stages in the construction are shown in Figure 56. Starting with a block of copper alloy, the undersurface corner angle is machined into the block. This is then soldered onto a mating support while metal is cut away to leave the lower skin and the backplate as an integral piece. Holes are drilled to take the pressure tappings; on the centre line the ridge is relieved to give a flat surface on which to mount the bushes. Bushes are soldered onto pressure tubing and then shaped to fit within the model shell at a particular location. The tubes and bushes are much more accessible at this stage than they were with the electroforming technique, even though the internal volume is less. The model sting is soldered into the back plate and the pressure tappings soldered onto the bottom surface after the model is removed from the support piece. The large tube in Figure 56 is the tube which carries the incoming cooling water; the individual bushes may be seen, as is the way in which the pressure tubes are carried out of the model inside the sting. The final step is to machine a top cover which is soldered into place with a low-temperature solder so as not to melt the pressure tubes, bushes or sting mounting. The models were pressure tested with water to 25 psia with no signs of leaks nor any sign of deflection in the unsupported sides. The complete model is mounted on a quadrant arm as shown in Figure 53.

Heat transfer measurements were made by a thin shell technique in which thermocouples on the back of a thin piece of metal are used to measure the rate of increase of temperature due to heat transfer from the free stream. To reduce errors due to conduction through the shell from areas of high heat transfer, the models must be extremely thin. They must also be made from a material with accurately known thermal properties and should have a high melting temperature. For these reasons the heat transfer models were electroformed in Nickel using the mandrels originally made for the pressure models. From experience with the delta wing pressure model it was decided to make the models with an open back to facilitate installation of the thermocouples. The nickel shells were deposited on the mandrels; again building up the tips of the models was found to be extremely difficult. The rough models were machined with a single-point cutter and then ground to the finished dimensions. The shell was then cut away, as in Figure 57, leaving the back of the model exposed. The models were mounted on a dural carrier. They were locked in place by sliding the tapered shells back onto the carrier and were anchored by araldite along the edges.

The metal at the sides of the shell was left relatively thick to support the thin undersurface against aerodynamic loads. There was no evidence of flexing of the models during the experiment. The limit on skin thickness was that the models began to lift under the grinding wheel if the wall were too thin. If the model were left too thick then the thermocouple response was slow and difficult to interpret. So the process was one of compromise between a thin but distorted shell and a thick model with a slow response. The over-riding consideration was the heat load to a particular model. For the hemisphere tests the model wall thickness was 0.004"; for the waveriders the thickness was 0.010". (The galvonometers used in the hemisphere experiment were very much less sensitive to compensate for the thinner wall thickness.)

Thermocouples were made from Chromel/Alumel wire with a diameter of 0.004". The small diameter meant that heat losses down the wire were kept to a minimum. The first inch or so of the thermocouples was coated with a varnish, then the wires were insulated by a PTFE sleeve. Welding the wires onto the surface of the model was difficult. A technique was developed in which the wires were welded onto the nickel shell side by side. This meant that the shell thickness was not altered by a local thermocouple bead which would act as a heat sink. The welding was done in air and when fixed onto the surface the thermocouples were extremely fragile. So, once the welds were made the pair of wires were covered with candle wax which held the wires in place while the two parts of the model were assembled. Once mounted on the injection ram the model was heated with a flame until the melted candle wax ran out. A new model was injected into the flow two or three times before measurements were taken; the combined effect of heat and vacuum ensured that when the models were stripped after the experiment there was no sign of any wax remaining inside the shell. On the best of the models 12 thermocouples were attempted and of these 9 worked satisfactorily throughout the experiment.

A series of hemispheres were used as calibration models. These were made from sheets of pure nickel 0.004" thick. The model was formed by pressing a steel ball into an accurately machined cup. A parallel shoulder, 0.015" wide, was left on the model and used to mount the model on its dural support.

The gun tunnel models were machined from solid dural rod and bored to mount on the standard balance sting. The position of the load shoulder was fixed by photographing the sting alone then making a second exposure with the model mounted on the sting. In all cases the shoulder was close to the centre of pressure of the model. The overall dimensions of the models were the same as the nitrogen tunnel pressure and heat transfer models. The wings were mounted upside down on the balance so that the aerodynamic loads were in the same direction as the static calibrations. This led to the discovery of a cracked and suspect strain gauge in the lift channel of the balance.

A3 INSTRUMENTATION

Data collection from the nitrogen tunnel was based on a Hewlett Packard Coupler Controller. This accepted data in digital form from several input devices and output the data onto paper tape for computer analysis. One of the input devices was a 16 channel multiplexer used to collect data from analogue sources, usually the pressure transducers. The input and output devices were under the control of the Coupler and the data collection cycle could be programmed, on boards within the instrument, and measurements taken at selected time intervals.

Thermocouple outputs from the heat transfer experiment were recorded on a 12 channel ultra-violet recorder. The heat transfer rates were calculated from the temperature response of the gauges on the back of the shell. An exponential temperature rise was assumed and curves fitted to the experimental data using a Cadmac plotting table linked to a PDP-8 computer. The curves were fitted over a one second interval and from the entire curve the initial temperature rise was calculated. This technique reduces possible errors due to injection through the nozzle shock wave; traces showed a slight peak just after the ram began to move that was consistent with an increased heat transfer rate while passing through the shock.

For the gun tunnel force measurements the balance designed by Opatowski [52] was used. The original amplifier and filter units were replaced by modular bridge balance and amplifier units. Signals were recorded on Tektronix 502A oscilloscopes and the traces photographed; the measurement was triggered by a pressure diaphragm on the barrel close to the downstream diaphragm. Earlier experiments had shown that the balance in its original form gave unreliable results. The electronics were replaced so that half bridges were used in the drag and moment channels and external resistors were used to balance an offset voltage.

This method was also tried with the lift channel but unless a full bridge were used the lift response, allowing for the contribution due to pitching moment, was non-linear with load. It is possible that one of the lift channel gauges was damaged during previous high incidence tests using the balance. The offset of the full bridge lift channel was balanced with a variable voltage supply so that voltage variations due to load were about a null point to avoid over-loading of the amplifiers. External filters were used in a band-reject mode to suppress the strong component due to the balance natural frequency on both the lift and moment channels. The drag channel had a high frequency signal content which was removed with a low-pass filter. The time response on all channels was consistent with the stable running time of the tunnel. Schlieren photographs were taken to record flow field effects and to check there is no evidence of tunnel blockage.

A4 CALCULATION OF STAGNATION TEMPERATURE

Because of the high total temperature of the gas in the small stagnation chamber of the nitrogen tunnel, it is not possible to make a direct measurement of total temperature – for example, by using a thermocouple. Any transducer output would have to be fed through the walls of the pressure vessels and measurement of elevated temperature is, in any case, difficult. The stagnation temperature is therefore calculated from a knowledge of the mass flow rate, stagnation pressure and the nozzle throat diameter using a real gas calculation. It is assumed that the effects of compressibility and vibrational relaxation, while not negligible, are sufficiently small for their effects to be treated separately. The following method for the calculation of stagnation temperature has been suggested by Vincenti and Kruger [53].

The adiabatic flow of a real gas, in equilibrium, through a nozzle is represented by the following five equations:

Nozzle geometry	$A = A(x)$
Conservation of mass	$\dot{m} = \rho A U$
Energy equation	$h_o = h + \frac{1}{2}U^2$
Isentropic process	$s = \text{constant}$
Equation of state	$p = Z \rho R T$

The unknown quantity of the equation set is $\rho(h,s)$, which may be represented by the Mollier Diagram for nitrogen.

An initial guess for the stagnation temperature is based on the perfect gas equation for mass flow through an ideal nozzle when the stagnation pressure is known. The entropy and enthalpy for the real gas are calculated using the method of Woolley [54]. At the nozzle throat the cross section area is a minimum so the product of density and velocity must, since the mass flow is constant, be at a maximum. Knowing the entropy and stagnation enthalpy of the flow, the problem is one of moving along a line of constant entropy in the Mollier Diagram by varying the enthalpy. This corresponds to stepping towards the throat from the stagnation chamber. For each value of enthalpy the product of density and velocity is calculated. When this product reaches a maximum the mass flow through the nozzle is known at the assumed stagnation temperature. This mass flow is corrected for vibrational effects as described below and compared with actual mass flow during a particular test run. If the two mass flow rates are different the assumed value of stagnation temperature is modified — so moving to a different constant entropy line — and the mass flow re-calculated. This process is continued until the difference in mass flow ratio is such that the correction needed to update the stagnation temperature is less than 1°K.

At this time stagnation conditions, mass flow and the thermodynamic properties of the real gas are known. Using the method of Wilson and Regan [55] or that of Culotta and Richards [56], an equivalent perfect gas is calculated from the real gas properties. The equivalent perfect gas pressure and temperature and the measured test section pitot pressure are used in the equations for the isentropic flow of a perfect gas to calculate the test section Mach number. The measured pitot pressure is corrected for viscosity effects using the method of Schaaf [57] based on the Reynolds number of the pitot tube behind a normal shock. The test section Mach number is re-calculated until the changes in test section conditions are less than 0.01%. The parameters relevant to hypersonic rarefied flow are calculated from the known test section conditions. A listing of the program is attached at the end of the Figures in the Thesis.

The effect of vibrational relaxation on the mass flow through a hypersonic nozzle can be examined by comparison with the quasi one-dimensional flow of a vibrationally non-equilibrium gas in a converging diverging nozzle, as suggested by Petty [58]. The equations for such a flow may be written:

$$\rho T^{-1/\gamma-1} = \exp \int_{\sigma_\infty}^{\sigma} \frac{d\sigma}{dT}$$

$$\rho U A = \dot{m}$$

$$\frac{\gamma}{\gamma-1} T + \sigma + \frac{U^2}{2} = \frac{\gamma}{\gamma+1} + \bar{\sigma}_\infty$$

$$\frac{d\sigma}{dx} = \frac{\Lambda \rho\, \Omega(T)}{U} [\bar{\sigma} - \sigma]$$

$$\bar{\sigma} = \frac{\theta_v}{\exp\,(\theta_v/T) - 1}$$

$$p = \rho R T \quad .$$

$\Omega(T)$ is the relaxation frequency and is given by some empirical fit to experimental data. Widom [59] shows that:

$$\Omega = T^{\delta_1} \exp\left[D_o\left(\frac{T}{\theta_v}\right)^{1/3}\right] .$$

The rate parameter is defined by

$$\Lambda = \frac{\rho_\infty \Omega'_\infty h}{\sqrt{RT_\infty}} = \frac{\sqrt{\gamma}\, h'}{a'_\infty\, \tau_\infty}$$

where τ_∞ is the relaxation time and a' is the frozen sound speed. The two limiting cases are

fully frozen flow $\Lambda \to 0$

equilibrium flow $\Lambda \to \infty$.

The mass flow for these two extreme cases may be calculated. For the fully frozen flow the mass flow is given by:

$$m_o = \sqrt{\gamma}\left(\frac{2}{\gamma+1}\right)^{\frac{\gamma+1}{2(\gamma-1)}}$$

and for the equilibrium case by:

$$m_e = U_* \, T_*^{1/\gamma-1} \frac{(1 - \exp(-\theta_v))}{\left(1 - \exp\left(-\frac{\theta_v}{T_*}\right)\right)} \exp\left(\frac{\bar{\sigma}_*}{T_*} - \frac{\bar{\sigma}_\infty}{\theta_v}\right)$$

The maximum change in mass flow between these two limiting cases is, at most, 3%.

Since the present flow is neither fully frozen nor in equilibrium an attempt is made to allow for a finite value of the rate parameter. To examine the effect of rate parameter the flow through a hyperbolic nozzle with a 45° semi-angle was computed by Schofield and Wilson [60] at the National Physical Laboratory, using data given by Sebacher [61]. This was for various stagnation conditions and the results are shown in

Figure 58 as a plot of a mass flow ratio, $\bar{m}$, which is dependent on the rate parameter. A curve has been fitted to this data so that the mass flow correction is given by:

$$\bar{m} = \tfrac{1}{2}(1 + \tanh(\log_{10}(\Lambda/\Lambda_o))$$

The calculation of stagnation temperature, allowing for both real gas effects and the effect of vibrational relaxation, has been checked against data provided by the Gas Dynamics Laboratory at Princeton University. Their work was based on a comparison of measured stagnation temperature against the temperature calculated from the ratio of mass flow rates where

$$\dot{m} = \bar{\Gamma}\, p_o \frac{A^*}{\sqrt{RT_o}}$$

and $\bar{\Gamma}$, a real gas correction factor, is given by:

$$\bar{\Gamma} = \bar{\Gamma}(\gamma) = \sqrt{\gamma}\left(\frac{2}{\gamma+1}\right)^{\frac{1}{2}\left(\frac{\gamma+1}{\gamma-1}\right)}$$

Figure 59 shows the comparison between measured temperature, the perfect gas calculation, the Princeton method and the present results. Ideal gas calculations over-estimate the stagnation temperature by 400°K at 2000°K. The present method gives better agreement with the measured temperatures than the other methods. Even so, for stagnation temperatures above 2000°K there is an increasing error. This may be due to several effects; thermodynamic data at elevated temperature may be unreliable or the thermocouple measurements may be in error due to conduction or radiation effects, remembering that the reading is taken inside a very small high pressure region where the gas is certainly not stationary.

REFERENCES

1. D.E. BOYLAN, B.J. GRIFFITH.
   Simulation of the Apollo Command Module aerodynamics at high altitudes.
   J. Spacecraft & Rockets, 6, 334.

2. D.E. BOYLAN, J.L. POTTER.
   Aerodynamics of typical lifting bodies under conditions simulating very high altitudes.
   AIAA 5, 226.

3. D.B. WILKINSON, S.A. HARRINGTON.
   Hypersonic force, pressure and heat transfer investigations of sharp and blunt slender cones.
   AEDC TDR 63-177.

4. D. KUCHEMANN.
   Hypersonic aircraft and their aerodynamic problems.
   Progress in Aeronautical Science, 6, 271.

5. L.H. TOWNEND.
   Some design aspects of space shuttle orbiters.
   Progress in Aeronautical Science, 13, 81.

6. T.R.F. NONWEILER.
   Aerodynamic problems of manned space vehicles.
   J.R.Ae.S. 63, 521.

7. J.G. JONES.
   A method for designing lifting configurations for high supersonic speeds using the known flow fields of non-lifting cones.
   RAE Report Aero 2674.

8. J. SEDDON, A. SPENCE.
   The use of known flow fields as an approach to the design of high speed aircraft.
   AGARD CP30.

9. J.K. HARVEY, R.W. JEFFERY, D.C.UPPINGTON.
The Imperial College graphite heated hypersonic wind tunnel.
British A.R.C., R & M 3701.

10. D.A. NEEDHAM, G.M. ELFSTROM, J.L. STOLLERY.
Design and operation of the Imperial College number 2 hypersonic gun tunnel.
I.C. Aero Report 70-04.

11. D.I. PULLIN.
Rarefied leading edge flow of a diatomic gas.
Ph.D. Thesis, University of London, March 1974.

12. B.B. HAMEL, A.L. COPPER.
A first collision theory of the hyperthermal leading edge problem.
Rarefied Gas Dynamics, 6th Symposium, Academic Press, New York, 1969.

13. A.B. HUANG, P.F. HWANG, P.F. GIDDENS, R. STRINIVANAN.
High speed leading edge problem.
Preprint, School of Aerospace Engineering, Georgia Institute of Technology, Atlanta.

14. G.A. BIRD.
Direct simulation of the Boltzmann equation.
Physics of Fluids, 13, 2676.

15. J.G. PARKER.
Rotational and vibrational relaxation in diatomic gases.
Physics of Fluids, 2, 449.

16. D.C. UPPINGTON.
A study of laminar separation in a rarefied hypersonic flow.
Ph.D. Thesis, University of London, 1972.

17. M. BECKER.
Flat plate flow field and surface measurements from merged layer into transition regime.
Rarefied Gas Dynamics 6th Symposium, Academic Press, New York, 1969.

18. M.L. SHORENSTEIN, R.F. PROBSTEIN.
The hypersonic leading edge problem.
AIAA Paper 68-4.

19. C.C. HORSTMANN.
Number flux measurements on sharp plates and wedges in the kinetic flow regime.
Rarefied Gas Dynamics 7th Symposium, Pisa, 1970.

20. F.C. HURLBURT.
Studies of molecular scattering at the solid surface.
J. App. Physics, 28, 844.

22. P.C. HUGHES, J.H. DE LEEUW.
Theory for the free molecular impact probe at an angle of attack.
Rarefied Gas Dynamics 4th Symposium, Toronto, 1964, Academic Press, New York, 1965.

23. J.H. LEWIS.
An experimentally determined model for the noncontinuum flow at the leading edge in a high speed ratio stream.
Princeton University, Department of Aerospace and Mechanical Sciences, Report No. 954, February 1971.

24. J. DAVIS.
Private Communication, Imperial College.

25. E.W.E. ROGERS, C.J. BERRY, B.M. DAVIS.
Experimental investigation of the interaction between a forward facing step and a laminar boundary layer in supersonic, low-density flow.
British A.R.C., R & M 3506.

26. L.C. SQUIRE.
Calculations of the pressure distribution on lifting conical wings with applications to the off-design behaviour of waveriders.
AGARD CP30, May 1968.

27. A.F. MESSITER.
Lift of slender wings according to Newtonian theory.
AIAA, 1, 794.

28. L. PENNELEGION, R.F. CASH.
Preliminary measurements in a shock tunnel of shock angle and undersurface pressure related to a Nonweiler wing.
NPL Aero Report 1037.

29. L.F. CRABTREE, D.A. TREADGOLD.
Experiments on hypersonic lifting bodies.
RAE TR67004.

30. G.H. GREENWOOD.
Free-flight measurements at supersonic speeds of pressure and heat transfer in an inclined 90 degree corner having sharp, swept leading edges.
RAE TR 73161.

31. V.W. KELDYSH, G.I. MAIKAPAR.
Aerodynamics and heat transfer of waveriders.
ICAS PAPER 70-18.

32. R.D. WATSON, L.M. WEINSTEIN.
A study of hypersonic corner flow interactions.
AIAA PAPER 70-227.

33. P.C. STAINBACK, L.M. WEINSTEIN.
Aerodynamic heating in the vicinity of corners at hypersonic speeds.
NASA TN D-4130.

34. C.T. NARDO, R.J. CRESCI.
Experimental measurements of hypersonic corner flow.
Polytechnic Institute of Brooklyn, PIBAL Report 69-1.

35. R.A. EAST, D.J.G. SCOTT.
An experimental determination of the heat transfer rates to a caret wing at hypersonic speeds.
University of Southampton, AASU Report 273.

36. S.C. METCALF, C.J. BERRY.
Force measurements on a family of caret and delta wings in low-density flow.
RAE Unpublished.

37. W.D. HAYES, R.F. PROBSTEIN.
Hypersonic flow theory.
Academic Press, New York, 1966.

38. G. HEFER.
An investigation of a waverider at low Reynolds number.
XXI International Astronautical Congress, North Holland, 1971.

39. M.O. CREAGER.
The effects of leading edge sweep and surface inclination on the hypersonic flow field over a blunt flat plate.
NASA Memo 12-26-58A (1959).

40. T.Y. LI, H.T. NAGAMATSU.
Similar solutions of compressible boundary layer equations.
J. Aeronautical Sciences, <u>22</u>, 607.

41. G.T. COLEMAN.
Force measurements on caret and delta wings at high incidence.
I.C. Aero Report 72-16.

42. D.M. RAO.
Hypersonic aerodynamic characteristics of flat delta and caret wings at high incidence angles.
J. Spacecraft and Rockets, <u>7</u>, 1475.

43. C.J. CARR.
Force measurements on caret and delta wings over the incidence range $27° \leqslant \alpha \leqslant 55°$ at $M = 12.2$.
I.C. Aero Report 71.22.

44. L.C. SQUIRE.
Calculations of the pressure distribution on lifting conical wings with applications to the off-design behaviour of waveriders.
AGARD CP30.

45. R.J. VIDAL, J.A. BARTZ.
Experimental studies of low-density effects in hypersonic wedge flows.
Rarefied Gas Dynamics 4th Symposium, Toronto, 1964.
Academic Press, New York, 1965.

46. H.K. CHENG, ET AL.
Boundary layer displacement and leading-edge bluntness effects in high temperature hypersonic flow.
J. Aerospace Sciences, 28, 353.

47. A.F. MESSITER.
Lift of slender delta wings according to Newtonian theory.
AIAA J. 1, 794.

48. D.L. SCHULZ, T.V. JONES.
Heat transfer measurements in short-duration hypersonic facilities.
AGARDograph 165.

49. S.C. METCALF, G.T. COLEMAN, C.J. BERRY.
Heat transfer to bluff faced and hemispherical faced cylinders between continuum and free molecular flow limits.
9th Rarefied Gas Dynamics Symposium, Göttingen, 1974.

50. J.B. McDEVITT.
A study of gas injection in the boundary layer of a hypersonic wind tunnel to extend the operating range.
NASA TN D 2935.

51. L. DAVIES, L.H. TOWNEND.
Private Communication, 1971, Imperial College.

52. T. OPATOWSKI.
An experimental study of the flow around and the forces developed by hypersonic lifting vehicles.
Ph.D. Thesis, University of London, 1967.

53. W.G. VINCENTI, C.H. KRUGER.
Introduction to Physical Gas Dynamics.
Wiley, 1965.

54. H.W. WOOLLEY.
Thermodynamic properties of gaseous Nitrogen.
NACA TN 3271.

55. J.L. WILSON, J.D. REGAN.
A simple method for real gas flow calculations.
British ARC CP772.

56. S. CULOTTA, B.E. RICHARDS.
Methods for determining conditions in real Nitrogen expanding flows.
Von Karmann Institute, TN 58, 1970.

57. S,A. SCHAAF.
The pitot tube in low density flow.
AGARD Report 525.

58. D.G. PETTY.
Private Communication, Imperial College.

59. B. WIDOM.
Mean-first-passage times and the collision theory of bimolecular reactions.
J. Chem. Phys. 31, 1387.

60. D. SCHOFIELD, J.L. WILSON.
Private Communication, NPL.

61. D.I. SEBACHER.
A correlation of N_2 vibrational translational relaxation times.
AIAA J., 5, 819.

62. I.E. VAS, G. KOPPENWALLNER.
The Princeton University high pressure hypersonic Nitrogen tunnel N-3.
Princeton University Report 690, July 1964.

63. W.J. McCROSKEY, S.M. BOGDONOFF, J.G. McDOUGALL.
An experimental model for the sharp flat plate in rarefied hypersonic flow.
AIAA J, 4, 1580.

64. S. CHAPMAN, T.G. COWLING.
The mathematical theory of non-uniform gases.
Cambridge University Press, 1970.

65. I.E. VAS, G. KOPPENWALLNER.
The Princeton University high pressure hypersonic Nitrogen tunnel N-3.
Princeton University Report 690, July 1964.

66. A. NAYSMITH.
Measurements of aerodynamic heat transfer in intermittent wind tunnels.
RAE TN Aero 2942.

67. A.R. GEORGE, W.G. REINECKE.
Conduction in thin skinned heat transfer and recovery temperature models.
AIAA J., 1, 8.

68. J.P-. CHEVALLIER, O. LEUCHTER.
Mesures dans la souffleries hypersoniques à rafales brèves.
ONERA TP. 823, 1970.

69. D.C. LILLICRAP.
A study of rarefied flows using an electron beam.
Ph.D. Thesis, University of London, 1969.

70. J. PETER REDING, LARS. E. ERICSSON.
Effects of delta wing separation on shuttle dynamics.
J. Spacecraft and Rockets, 10, 421.

71. D.E. BOYLAN, J.L. POTTER.
Aerodynamics of typical lifting bodies under conditions simulating very high altitudes.
AIAA J. 5, 226.

72. AVIATION WEEK AND SPACE TECHNOLOGY
June 3, 1974, 12.

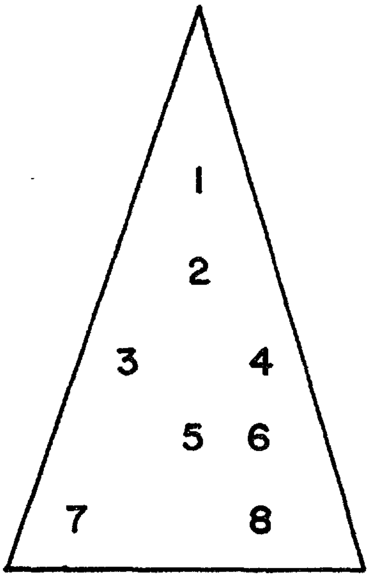

HOLE	X "	Y "	ζ
1	1.000	0	0.0
2	1.500	0	0.0
3	2.000	+0.236	0.500
4	2.000	−0.236	0.500
5	2.500	0	0.0
6	2.500	−0.236	0.400
7	3.000	+0.472	0.667
8	3.000	−0.236	0.333

SURFACE PRESSURE AS A FRACTION OF INVISCID WEDGE PRESSURE (P2)

α °	Re_∞ m^{-1}	P_2 mm Hg	1	2	3	4	5	6	7	8
3	1.04 5	.011	1.87	2.24	1.96	2.24	3.45	2.49	1.59	2.24
	1.23 5	.011	1.98	2.44	2.14	2.36	3.89	2.36	1.75	2.36
	7.84 4	.013	2.38	2.58	2.52	2.52	5.45	2.31	1.90	2.72
	9.29 4	.015	2.80	3.15	2.98	3.16	6.49	4.03	2.54	3.77
13	1.04 5	.130	0.60	0.67	0.52	0.58	0.50	0.60	0.56	0.56
	1.23 5	.143	0.59	0.71	0.55	0.57	0.55	0.52	0.55	0.59
	7.84 4	.160	0.60	0.72	0.57	0.58	0.55	0.52	0.57	0.60
	9.29 4	.181	0.67	0.96	0.84	0.72	0.87	0.66	0.77	0.78
20	1.04 5	.328	0.47	0.44	0.45	0.37	0.26	0.40	0.39	0.36
	1.27 5	.334	0.52	0.51	0.53	0.47	0.36	0.46	0.45	0.41
	7.29 4	.358	0.50	0.48	0.48	0.45	0.30	0.44	0.43	0.40
	9.39 4	.420	0.48	0.46	0.46	0.44	0.34	0.42	0.42	0.38
23	1.04 5	.356	0.64	0.60	0.57	0.65	0.35	0.62	0.62	0.66
	1.23 5	.390	0.74	0.67	0.59	0.76	0.40	0.70	0.67	0.73
	7.84 4	.438	0.83	0.74	0.64	0.88	0.40	0.76	0.75	0.79
	9.29 4	.497	0.84	0.74	0.64	0.88	0.43	0.77	0.75	0.81
28	1.04 5	.492	0.55	0.61	0.56	0.56	0.31	0.62	0.56	0.60
	1.23 5	.539	0.60	0.64	0.60	0.60	0.35	0.68	0.61	0.68
	7.84 4	.605	0.66	0.69	0.65	0.65	0.41	0.70	0.65	0.69
	9.29 4	.685	0.71	0.72	0.66	0.69	0.41	0.73	0.68	0.71
33	1.04 5	.636	0.57	0.65	0.60	0.55	0.34	0.76	0.67	0.60
	1.23 5	.697	0.64	0.68	0.67	0.61	0.36	0.79	0.72	0.67
	7.84 4	.782	0.68	0.74	0.74	0.63	0.40	0.81	0.76	0.70
	9.29 4	.887	0.71	0.77	0.73	0.65	0.40	0.82	0.78	0.71

TABLE 1: DELTA WING PRESSURE DISTRIBUTION

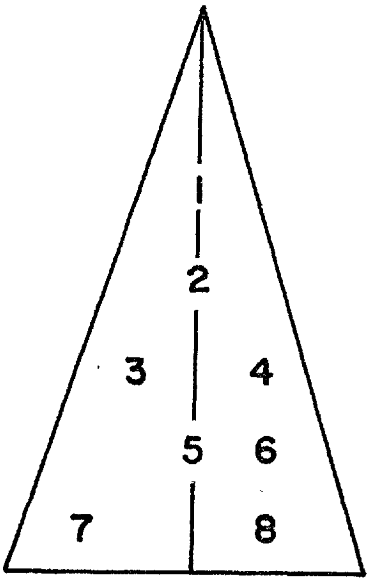

HOLE	X "	Y "	ζ
1	0.954	0	0.0
2	1.431	0	0.0
3	1.920	0.234	0.518
4	1.920	-0.234	0.518
5	2.385	0	0.0
6	2.397	-0.234	0.414
7	2.883	0.470	0.692
8	2.873	-0.234	0.345

SURFACE PRESSURE AS A FRACTION OF INVISCID WEDGE PRESSURE (p_2)

α °	Re_{∞} m^{-1}	p_2 mm Hg	1	2	3	4	5	6	7	8
20	9.96 4	.165	1.14	1.09	1.02	0.99	0.95	1.04	0.97	0.81
	1.31 5	.195	1.13	1.11	1.08	1.05	1.00	1.03	0.96	0.82
	7.73 4	.210	1.14	1.09	1.01	0.98	0.96	1.01	0.94	0.79
	1.03 5	.255	1.11	1.06	1.00	0.97	0.94	0.97	0.90	0.77
23	9.84 4	.224	0.80	0.77	0.69	0.68	0.73	0.69	0.70	0.63
	1.22 5	.258	1.00	0.98	0.91	0.86	0.90	0.90	0.86	0.77
	7.70 4	.289	0.94	0.86	0.77	0.82	0.87	0.77	0.83	0.75
	9.90 4	.338	0.97	0.93	0.87	0.82	0.88	0.84	0.83	0.76
28	1.04 5	.356	0.97	0.95	0.81	0.76	0.81	0.78	0.77	0.72
	1.23 5	.390	0.99	0.99	0.88	0.92	0.90	0.83	0.85	0.81
	7.84 4	.438	1.02	0.98	0.87	0.84	0.87	0.81	0.82	0.78
	7.74 4	.497	0.99	0.98	0.90	0.85	0.89	0.83	0.84	0.79

TABLE 2: 5° WAVERIDER PRESSURE DISTRIBUTION

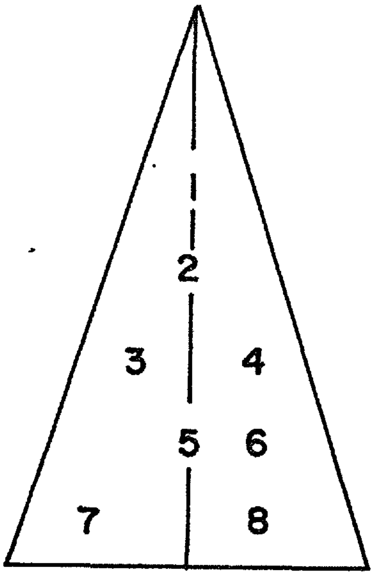

HOLE	X "	Y "	ζ
1	0.918	0	0.0
2	1.380	0	0.0
3	1.870	0.255	0.568
4	1.865	−0.253	0.575
5	2.312	0	0.0
6	2.331	−0.253	0.461
7	2.777	0.410	0.627
8	2.795	−0.253	0.384

SURFACE PRESSURE AS A FRACTION OF INVISCID WEDGE PRESSURE (p_2)

α°	Re_∞ m^{-1}	P_2 mm Hg	1	2	3	4	5	6	7	8
20	1.01 5	.108	1.17	1.05	0.91	0.85	0.98	0.88	0.81	0.84
	1.16 5	.110	1.25	1.15	1.05	0.96	1.10	1.04	0.94	0.93
	7.72 4	.138	1.33	1.11	0.93	0.99	1.03	1.02	0.94	0.90
	1.01 5	.169	1.30	1.04	0.90	0.98	0.99	1.02	0.92	0.89
23	9.69 4	.153	1.00	0.89	0.73	0.73	0.80	0.71	0.69	0.66
	1.03 5	.142	1.24	1.10	0.95	0.96	0.97	0.90	0.88	0.83
	7.32 4	.185	1.04	0.97	0.79	0.77	0.88	0.75	0.72	0.71
	8.07 4	.196	1.14	0.97	0.79	0.83	0.87	0.80	0.76	0.72
28	1.06 5	.275	0.94	0.86	0.75	0.72	0.81	0.70	0.70	0.66
	9.93 4	.240	1.17	0.97	0.89	0.93	0.92	0.87	0.90	0.81
	6.79 4	.293	1.03	0.93	0.80	0.79	0.88	0.77	0.75	0.73
	7.99 4	.331	1.05	0.97	0.84	0.80	0.92	0.79	0.76	0.74

TABLE 3: 8° WAVERIDER PRESSURE DISTRIBUTION

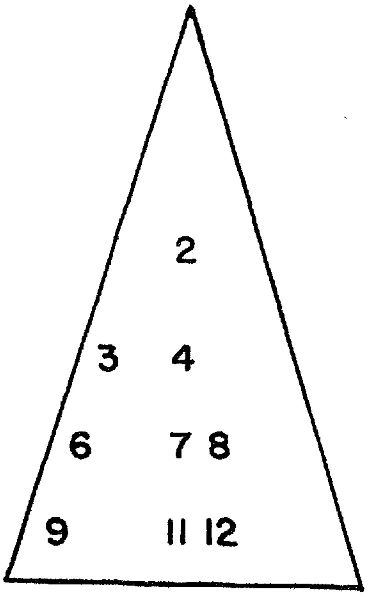

POSITION	X "	Y "	ζ
2	1.577	0.0	0.0
3	2.078	0.347	0.63
4	2.078	0.0	0.0
6	2.537	0.470	0.69
7	2.537	0.0	0.0
8	2.537	0.200	0.30
9	3.017	0.598	0.74
11	3.017	0.0	0.0
12	3.017	0.200	0.25

SURFACE HEAT TRANSFER AS
A FRACTION OF SPHERE
STAGNATION POINT ($\dot{q}_o$)

Re_∞	$\dot{q}_o$	α	THERMOCOUPLE POSITION								
m^{-1}	W m^{-2}	°	2	3	4	6	7	8	9	11	12
1.01 5	2.61 4	10	0.10	0.16		0.15	0.13	0.09	0.14	0.11	0.14
1.31 5	2.65 4		0.14	0.18		0.15	0.14	0.11	0.16	0.12	0.17
8.01 4	4.14 4		0.14	0.17		0.15	0.14	0.11	0.16	0.11	0.15
9.63 4	4.78 4		0.12	0.16		0.15	0.13	0.10	0.14	0.11	0.13
9.81 4	2.61 4	20	0.22	0.31		0.30	0.24	0.19	0.29	0.21	0.22
1.35 5	2.65 4		0.25	0.33		0.29	0.26	0.21	0.30	0.23	0.25
7.94 4	4.14 4		0.28	0.37		0.32	0.29	0.23	0.36	0.25	0.26
1.02 5	4.78 4		0.23	0.33		0.27	0.24	0.20	0.29	0.22	0.24
9.69 4	2.61 4	28	0.28	0.44	0.30	0.40	0.34	0.26	0.39	0.29	0.30
1.38 5	2.65 4		0.36	0.54	0.33	0.50	0.43	0.36	0.48	0.36	0.41
8.16 4	4.14 4		0.37	0.54	0.34	0.53	0.42	0.35	0.50	0.37	0.39
1.06 5	4.78 4		0.37	0.55	0.36	0.48	0.44	0.34	0.49	0.37	0.39
9.70 4	2.61 4	35	0.34	0.52		0.44	0.40	0.33	0.51	0.33	0.38
1.37 5	2.65 4		0.37	0.54		0.51	0.44	0.39	0.52	0.36	0.42
7.87 4	4.14 4		0.45	0.59		0.55	0.50	0.43	0.60	0.44	0.48
9.77 4	4.78 4		0.39	0.56		0.49	0.44	0.39	0.52	0.38	0.42

TABLE 4: DELTA WING HEAT TRANSFER DISTRIBUTION

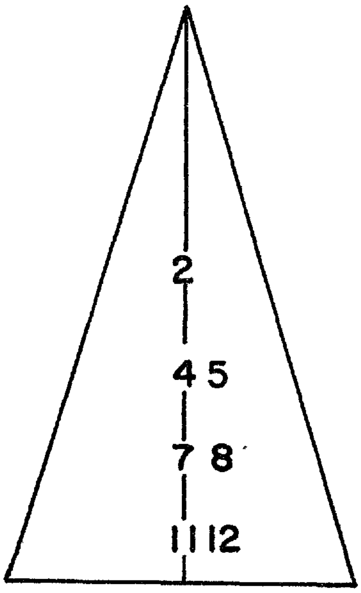

POSITION	X''	Y''	ζ
2	1.577	0.0	0.0
4	2.058	0.0	0.0
5	2.058	0.200	0.36
7	2.537	0.0	0.0
8	2.537	0.200	0.30
11	3.017	0.0	0.0
12	3.017	0.200	0.25

SURFACE HEAT TRANSFER AS A FRACTION OF SPHERE STAGNATION POINT ($\dot{q}_o$)

MODEL THICKNESS = 0.009"

Re_∞	$\dot{q}_o$	α	THERMOCOUPLE POSITION						
m^{-1}	W m^{-2}	°	2	4	5	7	8	11	12
1.02 5	2.61 4	10	0.09	0.10	0.07	0.07	0.14	0.06	0.10
1.44 5	2.65 4		0.09	0.10	0.09	0.10	0.15	0.07	0.11
8.16 4	4.14 4		0.14	0.10	0.08	0.08	0.13	0.07	0.10
1.06 5	4.78 4		0.12	0.09	0.08	0.07	0.13	0.05	0.12
9.93 4	2.61 4	20	0.26	0.18	0.16	0.17	0.26	0.12	0.19
1.43 5	2.65 4		0.23	0.20	0.14	0.17	0.26	0.11	0.18
8.27 4	4.14 4		0.27	0.19	0.16	0.17	0.28	0.12	0.21
9.78 4	4.78 4		0.17	0.18	0.15	0.15	0.26	0.10	0.19
1.05 5	2.61 4	28	0.48	0.32	0.30	0.24	0.49	0.20	0.33
1.45 5	2.65 4		0.33	0.32	0.16	0.24	0.48	0.17	0.34
1.68 5	3.31 4		0.34	0.20	0.18	0.15	0.33	0.12	0.22
1.86 5	5.00 4		0.23	0.24	0.21	0.20	0.33	0.13	0.23
8.57 4	4.14 4		0.32	0.29	0.23	0.32	0.38	0.15	0.27
1.02 5	4.78 4		0.35	0.28	0.21	0.23	0.38	0.14	0.27
1.25 5	8.08 4		0.27	0.19	0.13	0.15	0.24	0.09	0.17
1.03 5	2.61 4	35	0.47	0.36		0.27	0.50	0.19	0.33
1.39 5	2.65 4		0.36	0.38	0.23	0.29	0.54	0.21	0.39
8.27 4	4.14 4		0.36	0.33	0.18	0.26	0.50	0.18	0.35
1.02 5	4.78 4		0.39	0.29		0.22	0.46	0.16	0.31

TABLE 5: 5° WAVERIDER HEAT TRANSFER DISTRIBUTION

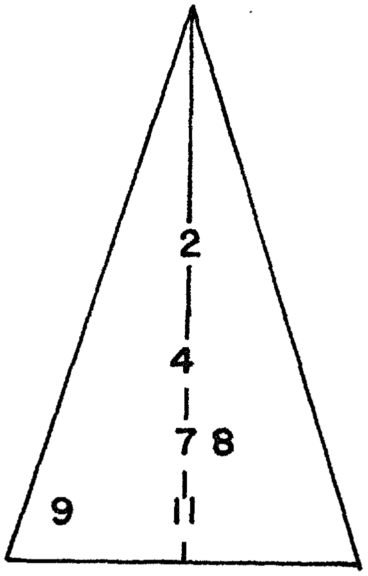

POSITION	X "	Y "	ζ
2	1.577	0.0	0.0
4	2.058	0.0	0.0
7	2.537	0.0	0.0
8	2.537	0.270	0.40
9	3.018	0.598	0.74
11	3.018	0.0	0.0

SURFACE HEAT TRANSFER AS A FRACTION OF SPHERE STAGNATION POINT ($\dot{q}_0$)

MODEL THICKNESS = 0.015"

Re_∞ m^{-1}	$\dot{q}_o$ W m^{-2}	α °	THERMOCOUPLE POSITION					
			2	4	7	8	9	11
1.01 5	2.61 4	10	0.12	0.11	0.06	0.09	0.14	0.07
1.42 5	2.65 4		0.15	0.14	0.07	0.09	0.17	0.07
8.07 4	4.14 4		0.16	0.12	0.07	0.10	0.17	0.08
1.04 5	4.78 4		0.14	0.13	0.06	0.09	0.17	0.07
9.34 4	2.61 4	20	0.22	0.20	0.11	0.14	0.22	0.13
1.36 5	2.65 4		0.26	0.22	0.12	0.17	0.24	0.16
8.18 4	4.14 4		0.29	0.25	0.12	0.18	0.32	0.18
1.03 5	4.78 4		0.30	0.24	0.12	0.18	0.32	0.17
1.09 5	2.61 4	28	0.32		0.12	0.20	0.36	0.14
1.34 5	2.65 4		0.35		0.09	0.20	0.38	0.14
8.39 4	4.14 4		0.38		0.13	0.23	0.44	0.18
1.05 5	4.78 4		0.43		0.15	0.24	0.47	0.19
1.08 5	2.61 4	35	0.45	0.36	0.17	0.27	0.48	0.19
1.46 5	2.65 4		0.54	0.40	0.22	0.33	0.56	0.28
8.30 4	4.14 4		0.50	0.31	0.18	0.30	0.62	0.25
1.06 5	4.78 4		0.49	0.34	0.17	0.27	0.55	0.22

TABLE 6: 5° WAVERIDER HEAT TRANSFER DISTRIBUTION

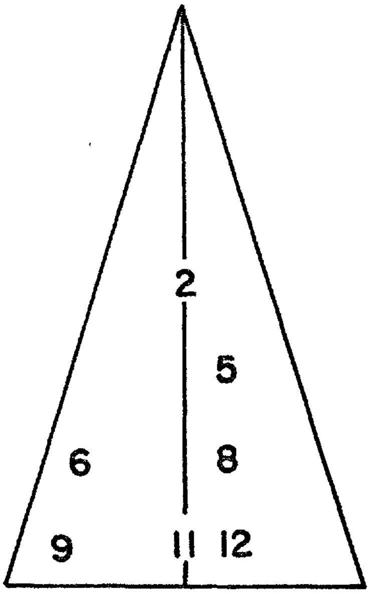

POSITION	X "	Y "	ζ
2	1.578	0.0	0.0
5	2.058	0.200	0.36
6	2.538	0.485	0.72
8	2.538	0.200	0.30
9	3.018	0.613	0.76
11	3.018	0.0	0.0
12	3.018	0.200	0.25

SURFACE HEAT TRANSFER AS A FRACTION OF SPHERE STAGNATION POINT ($\dot{q}_o$)

Re_∞ m^{-1}	$\dot{q}_o$ W m^{-2}	α °	THERMOCOUPLE POSITION						
			2	5	6	8	9	11	12
9.52 4	2.61 4	10	0.09	0.08	0.05	0.08	0.10	0.11	0.09
1.38 5	2.65 4		0.11	0.13	0.07	0.10	0.14	0.16	0.10
8.15 4	4.14 4		0.10	0.11	0.06	0.10	0.13	0.16	0.11
1.03 5	4.78 4		0.08	0.11	0.06	0.11	0.13	0.15	0.10
9.76 4	2.61 4	20	0.17	0.18	0.12	0.16	0.23	0.26	0.19
1.38 5	2.65 4		0.19	0.20	0.12	0.19	0.25	0.27	0.19
8.04 4	4.14 4		0.18	0.21	0.13	0.18	0.27	0.26	0.18
1.01 5	4.78 4		0.17	0.19	0.12	0.17	0.25	0.26	0.17
9.77 4	2.61 4	28	0.16	0.21	0.13	0.21	0.20	0.31	0.19
1.38 5	2.65 4		0.21	0.25	0.15	0.21	0.25	0.35	0.25
7.98 4	4.14 4		0.24	0.28	0.16	0.26	0.33	0.38	0.25
1.05 5	4.78 4		0.27	0.29	0.16	0.25	0.37	0.40	0.22
1.04 5	2.61 4	35	0.37	0.36	0.23	0.32	0.48	0.52	0.27
1.34 5	2.65 4		0.41	0.38	0.26	0.38	0.51	0.61	0.32
8.31 4	4.14 4		0.40	0.44	0.24	0.43	0.54	0.58	0.32
1.00 5	4.78 4		0.38	0.39	0.22	0.36	0.49	0.54	0.32

TABLE 7: 8° WAVERIDER HEAT TRANSFER DISTRIBUTION

MODEL	α°	THERMOCOUPLE POSITION										
		2	3	4	5	6	7	8	8*	9	11	12
DELTA	28	0.92	1.04			0.96	1.39	0.90		0.93	1.29	1.17
5°1		1.08		0.98	0.58		0.91	1.26			0.64	1.00
5°2		1.14							0.63	0.94	0.69	
8°		0.79			0.81	0.39		0.88		0.75	1.83	0.98
DELTA	35	0.86	0.93			0.83	1.26	0.88		0.90	1.16	1.11
5°1		1.01		0.99	0.52		0.84	1.32			0.65	1.03
5°2		1.19		0.98					0.66	0.99	0.78	
8°		1.10			0.97	0.49		1.09		1.04	2.21	1.02
DELTA	20	0.87	0.88			0.78	1.16	0.76		0.81	1.12	1.01
5°1		1.02		0.96	0.58		0.94	1.21			0.70	1.00
5°2		1.12		1.13					0.67	0.83	0.86	
8°		0.94			0.89	0.46		0.97		0.93	1.99	1.16
DELTA	10	0.74	0.71			0.64	1.06	0.64		0.84	0.97	1.06
5°1		0.88		0.94	0.55		0.89	1.17			0.77	1.08
5°2		1.14		1.20					0.69	0.89	0.88	
8°		0.92			0.86	0.37		0.98		0.77	2.20	1.21

Data shows average heat transfer rate for all stagnation conditions normalised by the viscous wedge value.

TABLE 8: SUMMARISED HEAT TRANSFER DATA

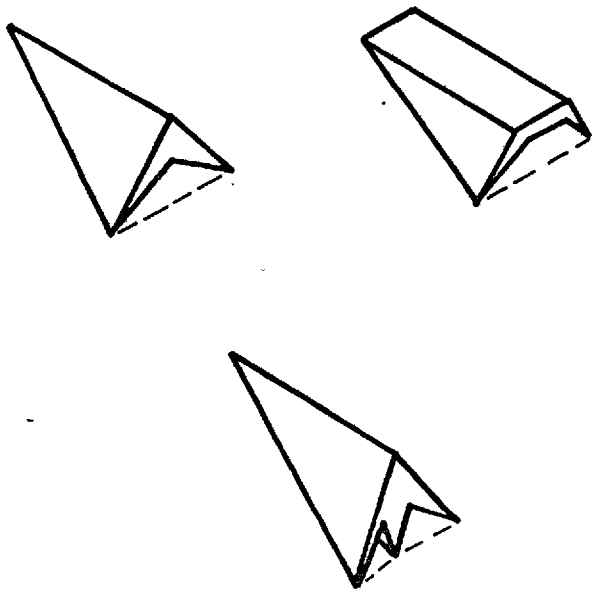

POSSIBLE WAVERIDER VEHICLE SHAPES.

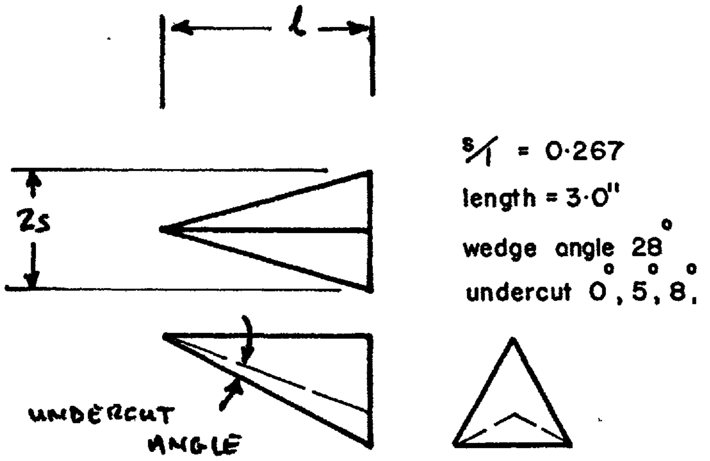

s/l = 0·267

length = 3·0"

wedge angle 28°

undercut 0°, 5°, 8°,

ACTUAL MODEL GEOMETRY.

FIGURE 1 POSSIBLE LIFTING BODY CONFIGURATIONS.

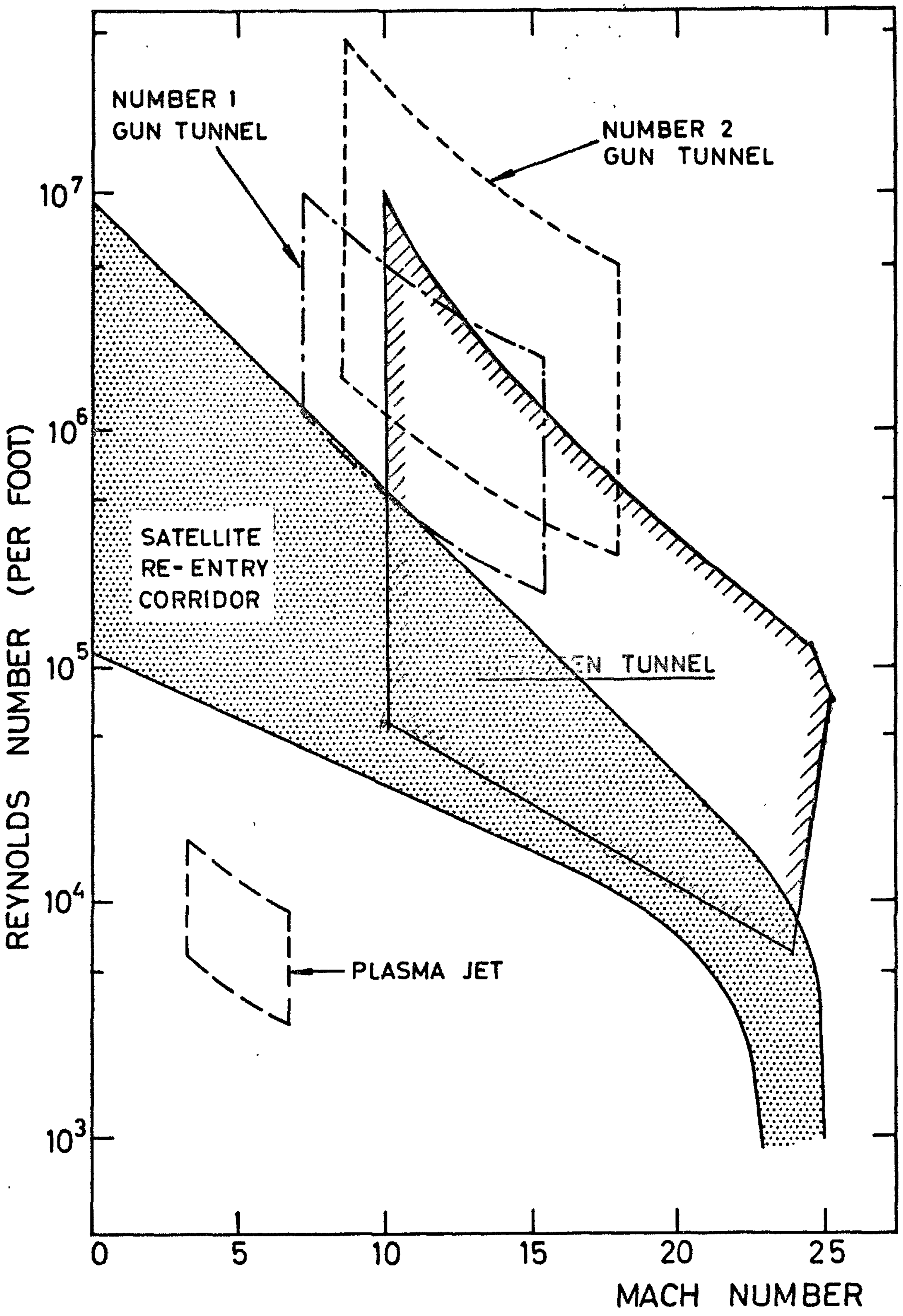

FIGURE 2 COMPARISON OF HYPERSONIC TUNNELS.

1	LIQUID NITROGEN STORE.
2	S 800 VACUUM PUMPS.
3	RUVAC 46 VACUUM PUMP.
4 5	RUVAC 59 VACUUM PUMPS.
6	STAGE 1 & 2 COMPRESSOR.
7	STAGE 3 COMPRESSOR.
8	HEATER POWER SUPPLY.
9	CONTROL ROOM.
10	CONTROL PANEL.
11	HEAT EXCHANGER.
12	DIFFUSER.
13	TEST SECTION.
14	NOZZLE.
15	DATA ACQUISITION.
16	SPECTROMETER.
17	ELECTRON BEAM LAB.
18	GUN TUNNEL DRIVER.
19	GUN TUNNEL TEST SECTION.

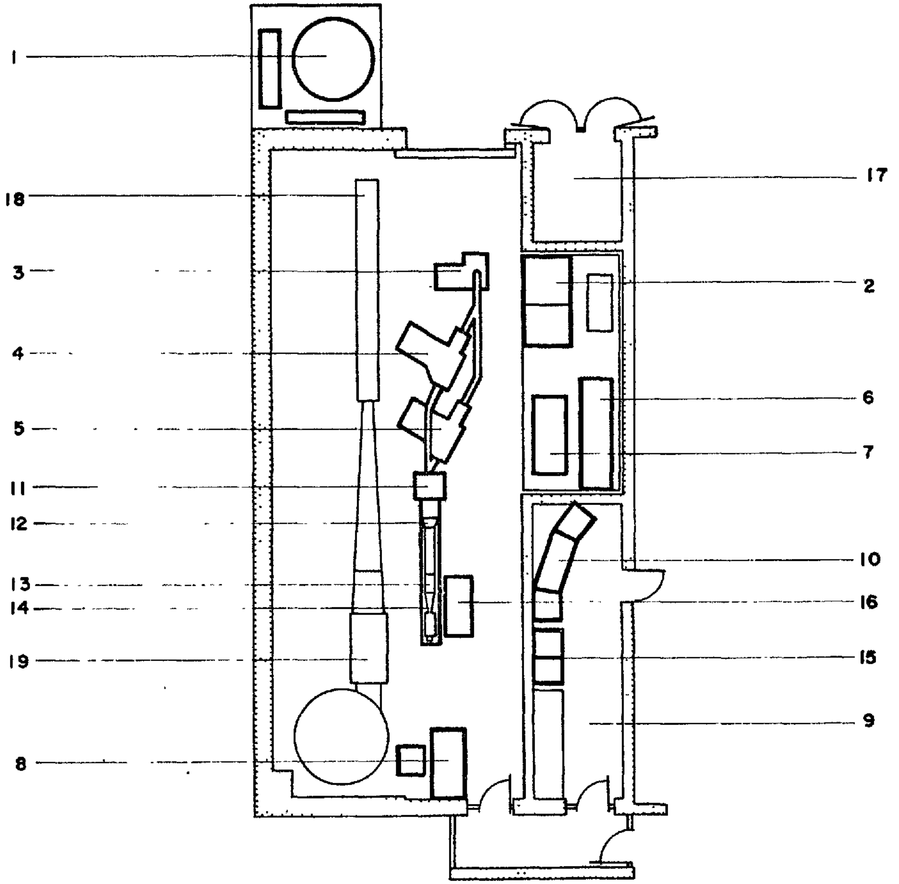

FIGURE 3 GENERAL LAYOUT OF HYPERSONICS LABORATORY.

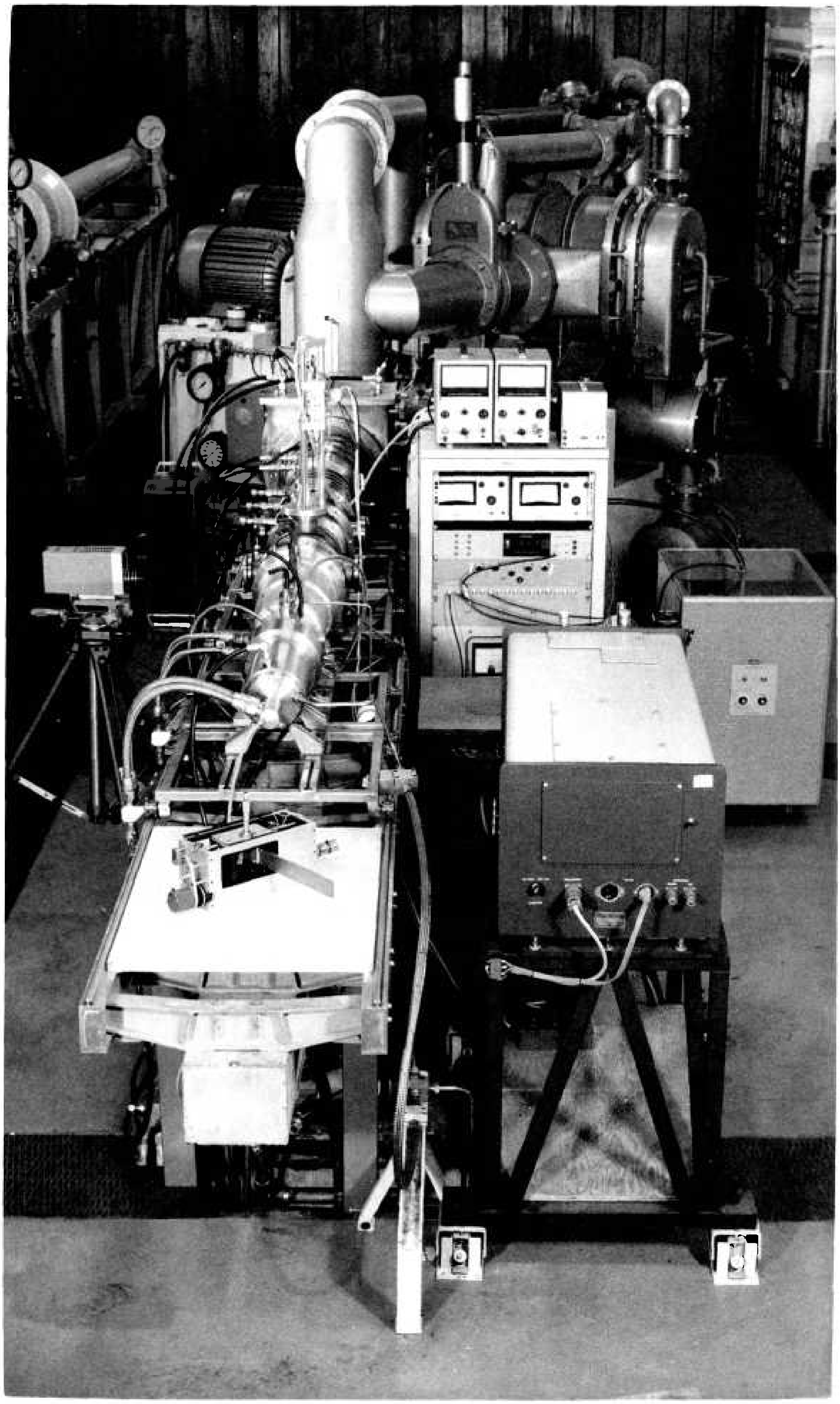

FIGURE 4 NITROGEN TUNNEL GENERAL VIEW

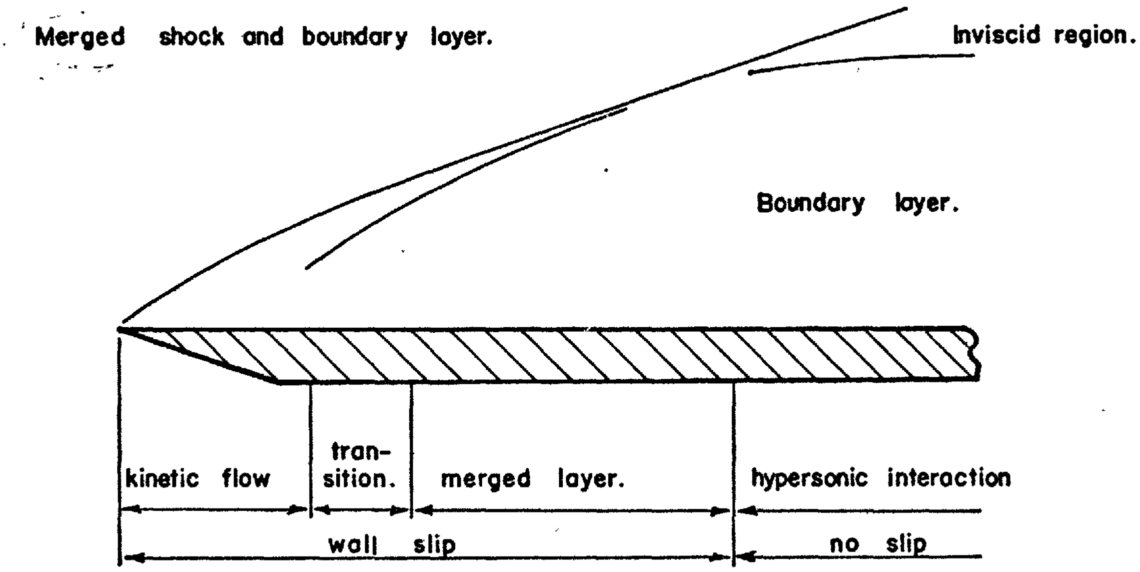

$\bar{V}\ \infty$	0·5	0·15
$X/\lambda_{fb}O$	1·5	20·0

FLAT PLATE CONDITIONS AT MACH 23, P_o = 600 psi, T_o = 2000 °K.

X (ins)	0·27	0·57	0·75	1·00	2·00	4·05
$\bar{V}$	0·987	0·679	0·592	0·507	0·361	0·255
X/λ_{fb}	0·434	0·917	1·205	1·644	3·251	6·509

TUNNEL CONDITIONS (NITROGEN TUNNEL AND GUN TUNNEL)

P_o (psia)	T_o (°K)	P_∞ (mm Hg)	M_∞	Re_∞ (m^{-1})
450	1350	2·42 -3	22	9·96 4
600	1350	3·04 -3	22	1·32 5
600	2000	3·47 -3	21	7·97 4~~5~~
750	2000	4·09 -3	21	9·47 4
2100	1070	5·30 0	8·96	1·22 7

FIGURE 5 TUNNEL CONDITIONS AND FLAT PLATE FLOW.

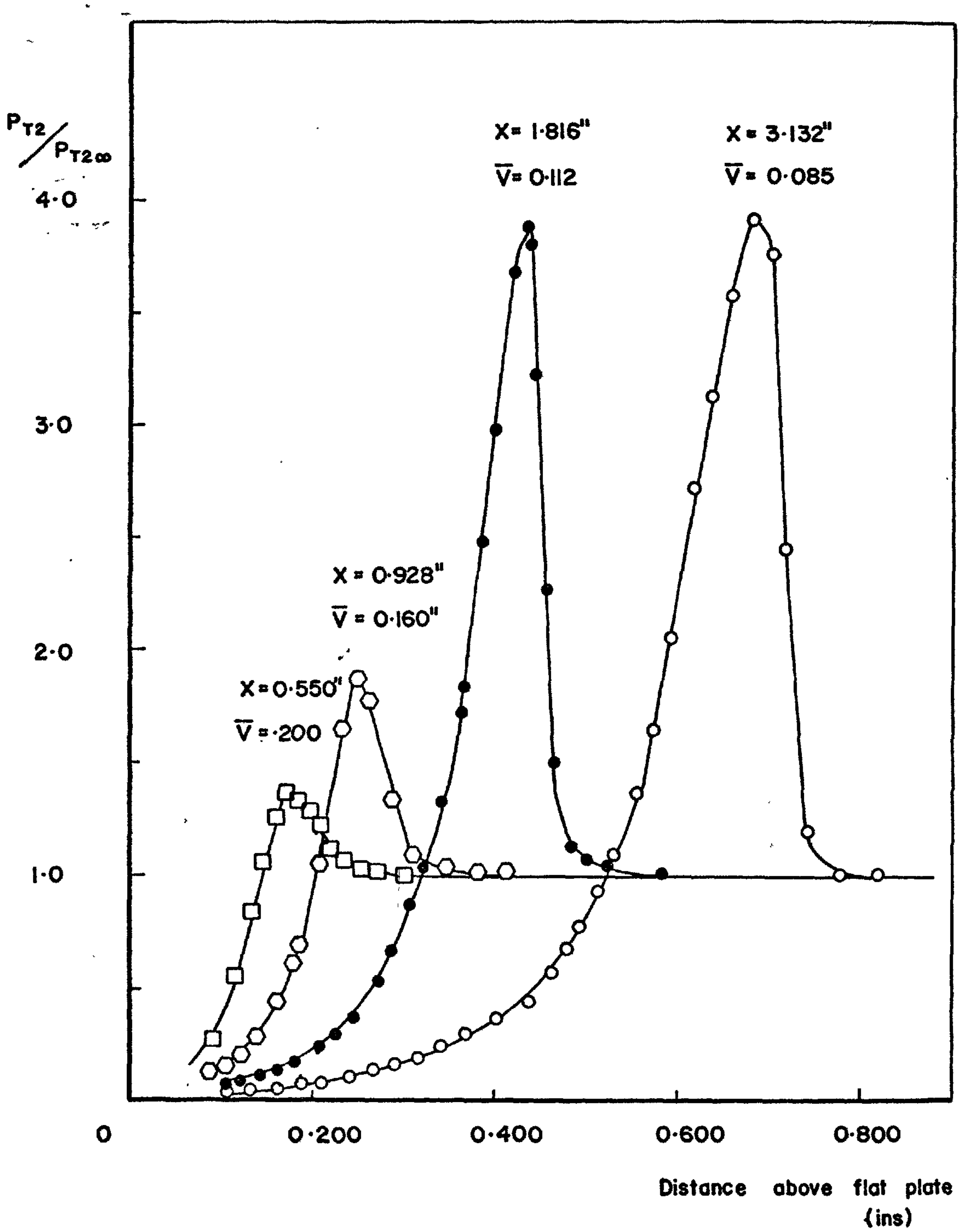

FIGURE 6a FLAT PLATE PITOT PROFILES.

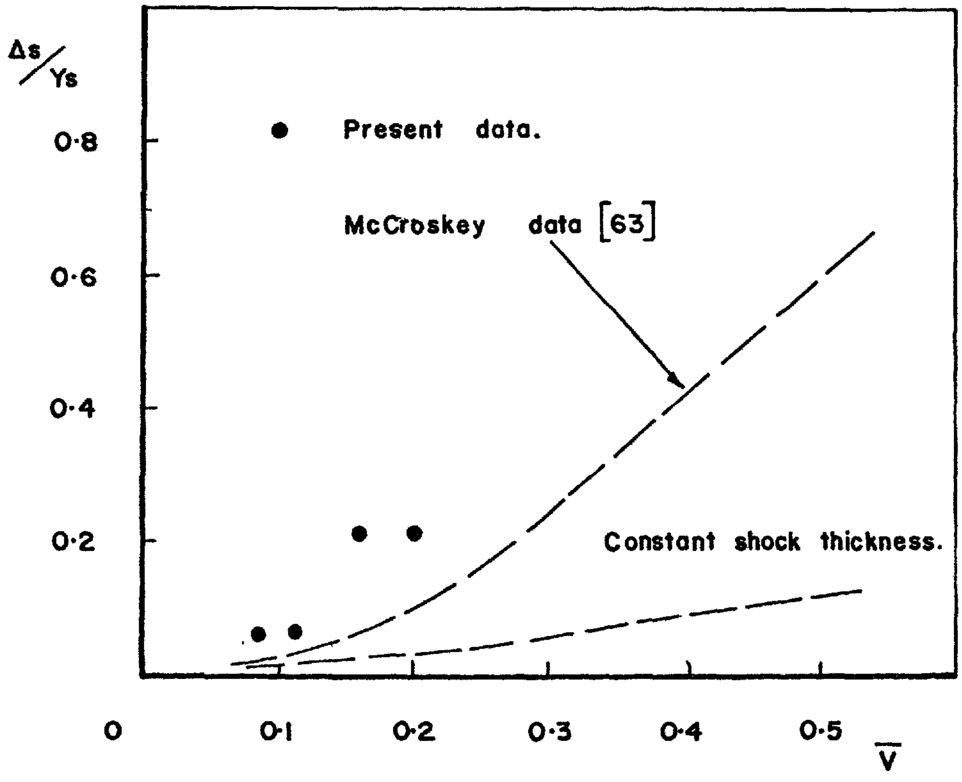

FIGURE 6b RATIO OF SHOCK WAVE THICKNESS TO SHOCK LAYER THICKNESS.

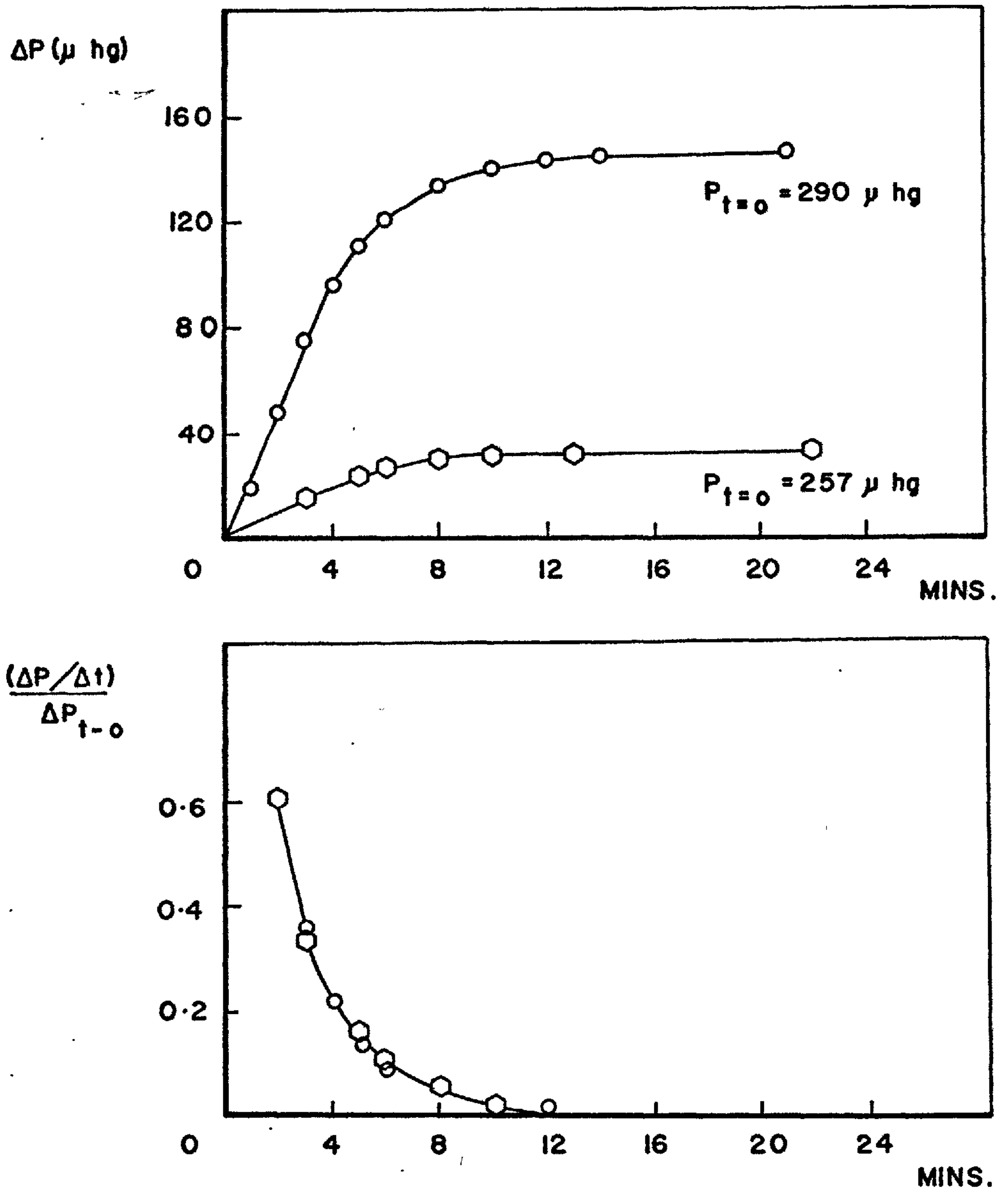

<u>FIGURE 7</u> PRESSURE TAPPING RESPONSE.

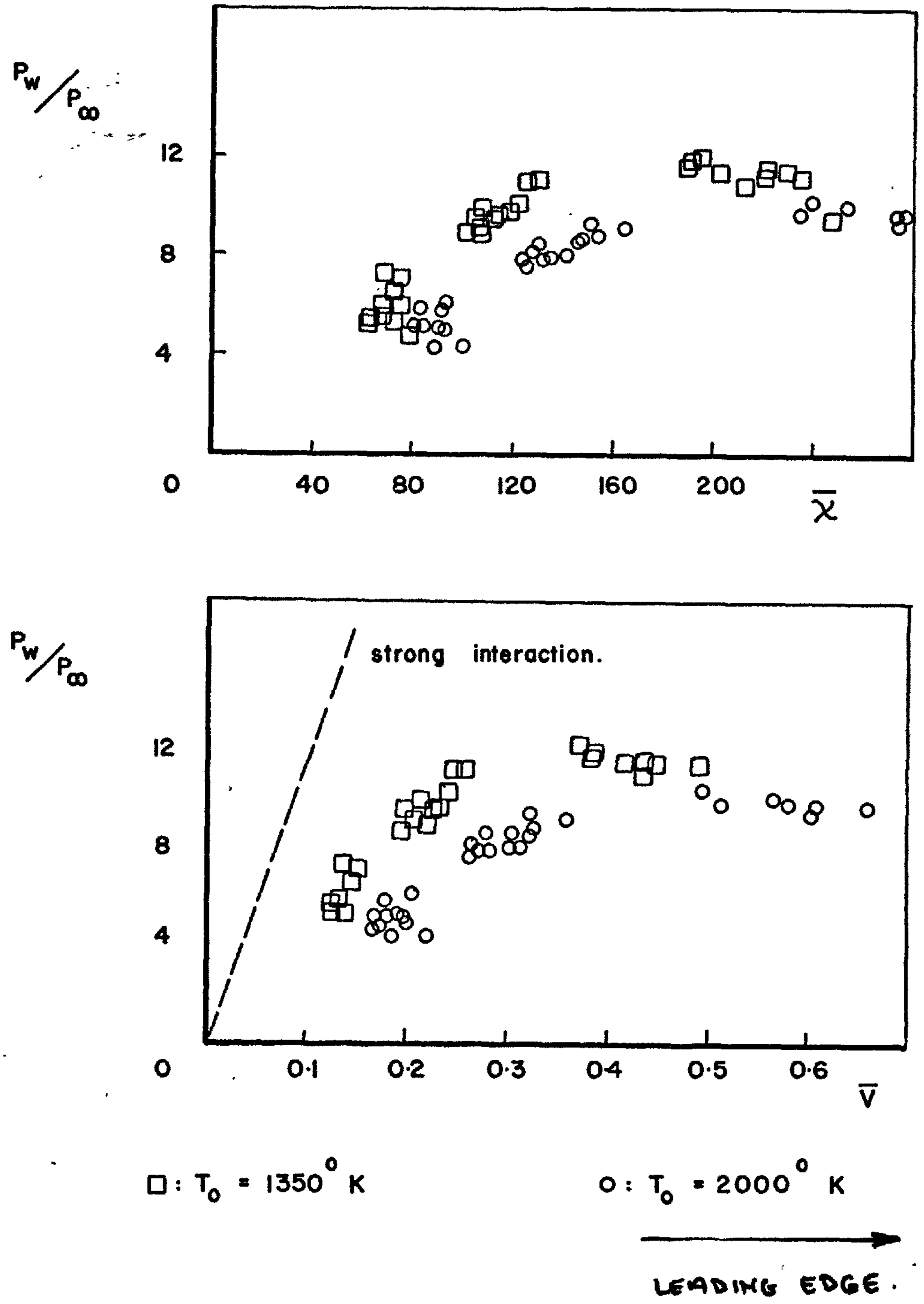

FIGURE 8 FLAT PLATE PRESSURE DISTRIBUTION.

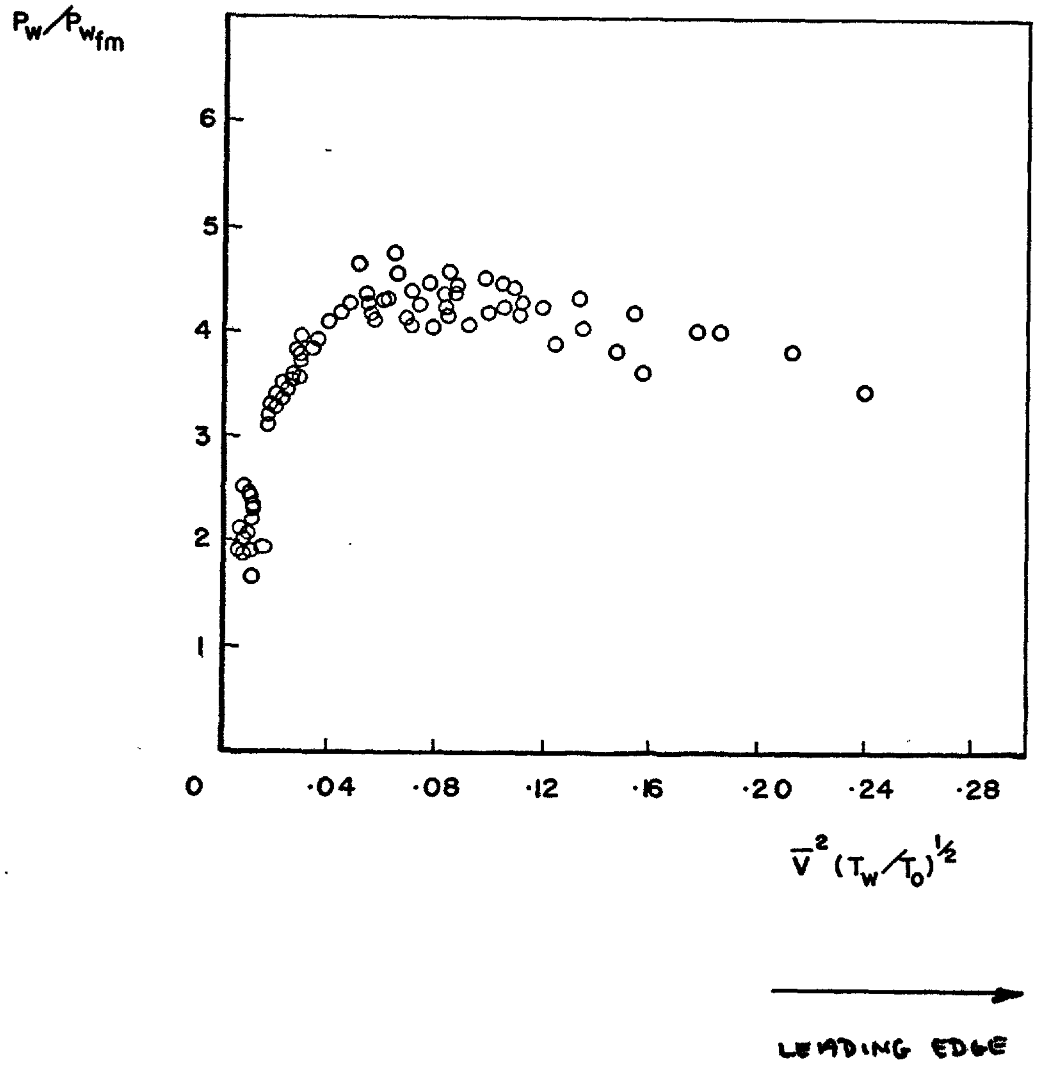

FIGURE 9 FLAT PLATE PRESSURE DISTRIBUTION.

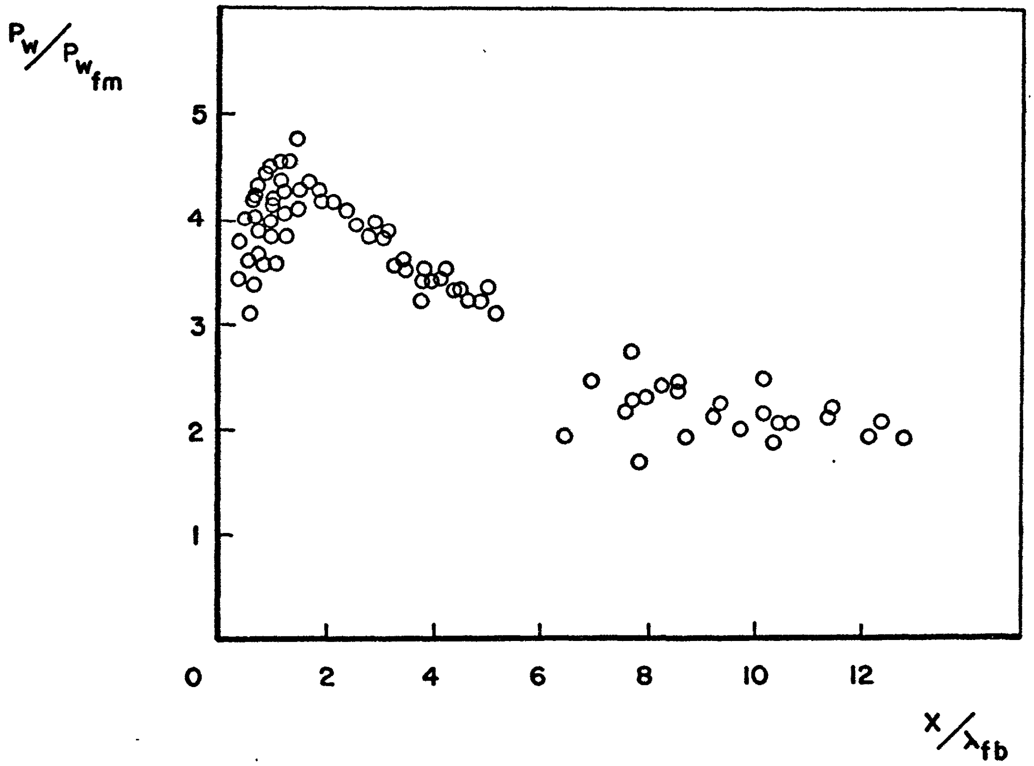

LEADING EDGE.

FIGURE 10 UNCORRECTED PRESSURE DISTRIBUTION.

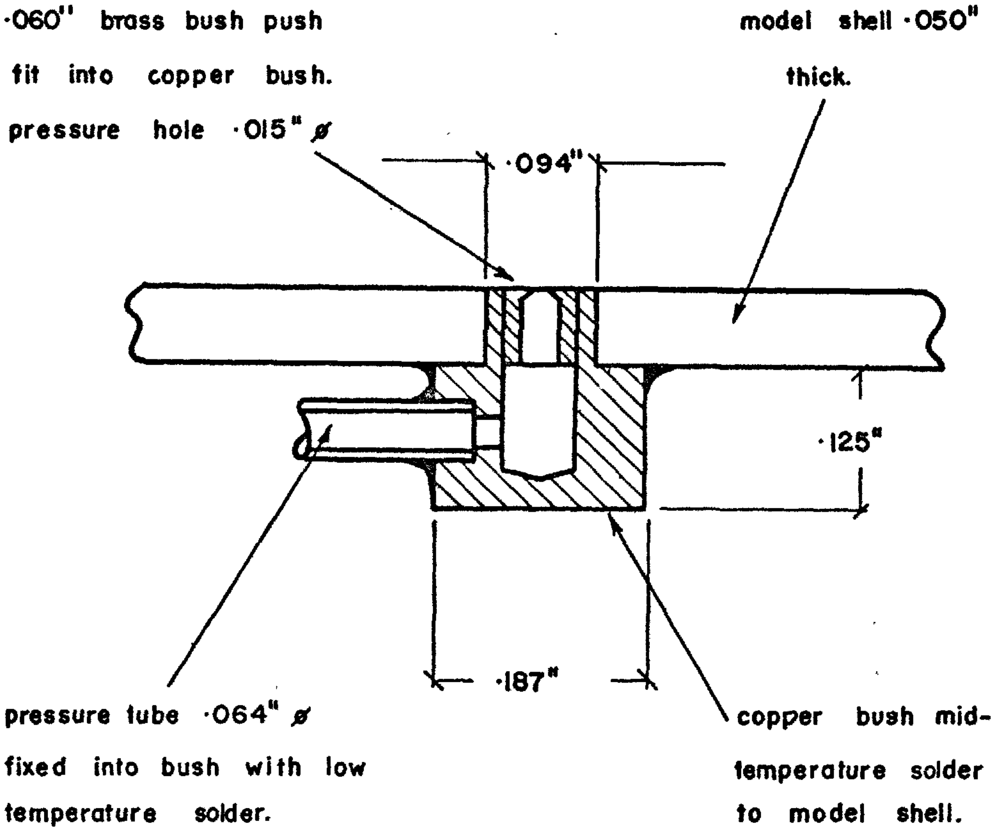

FIGURE 11 TYPICAL PRESSURE TAPPING.

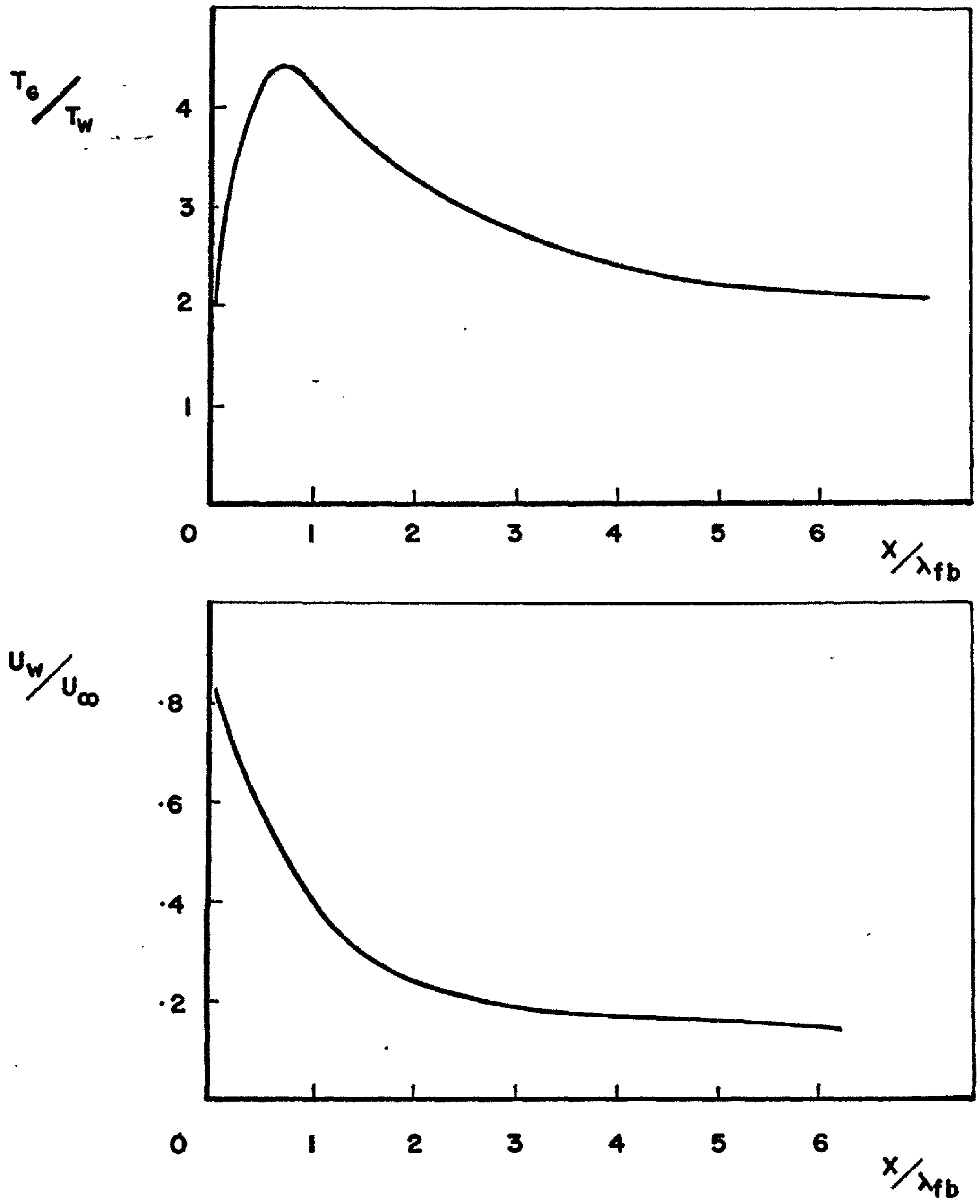

FIGURE 12 GAS TEMPERATURE AT THE WALL AND SLIP VELOCITY.

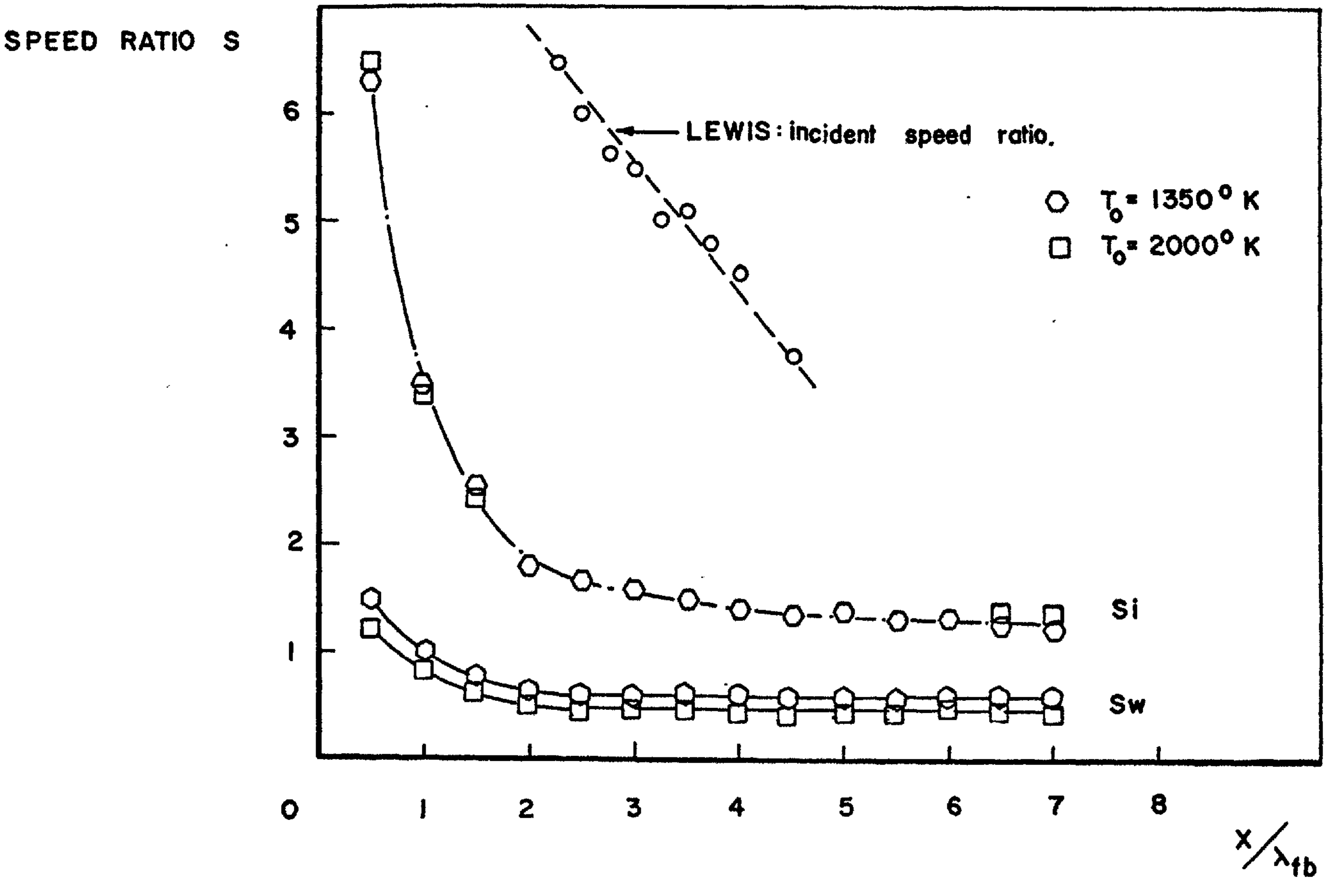

FIGURE 13 WALL AND INCIDENT SPEED RATIO.

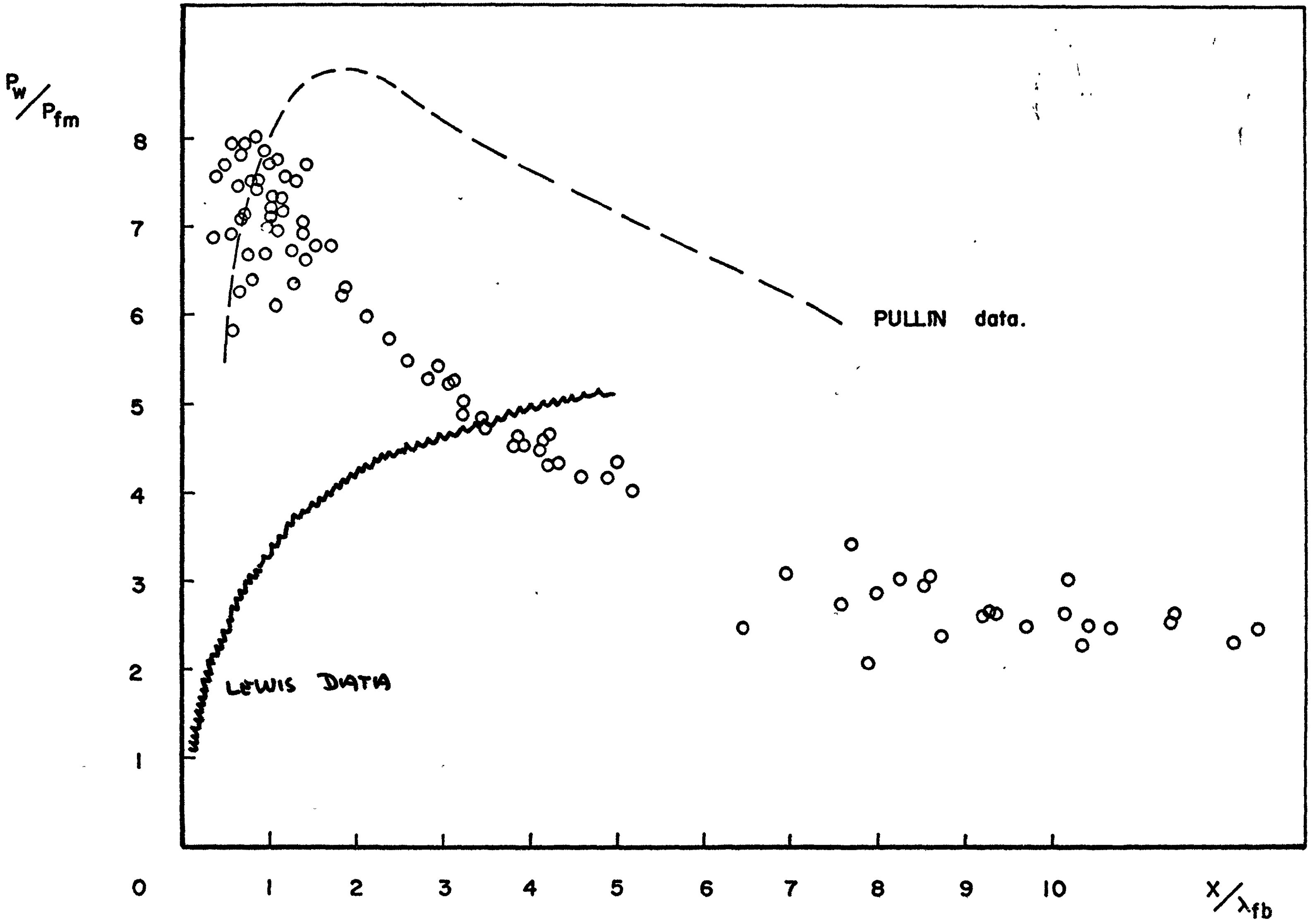

FIGURE 14 CORRECTED PRESSURE DISTRIBUTION.

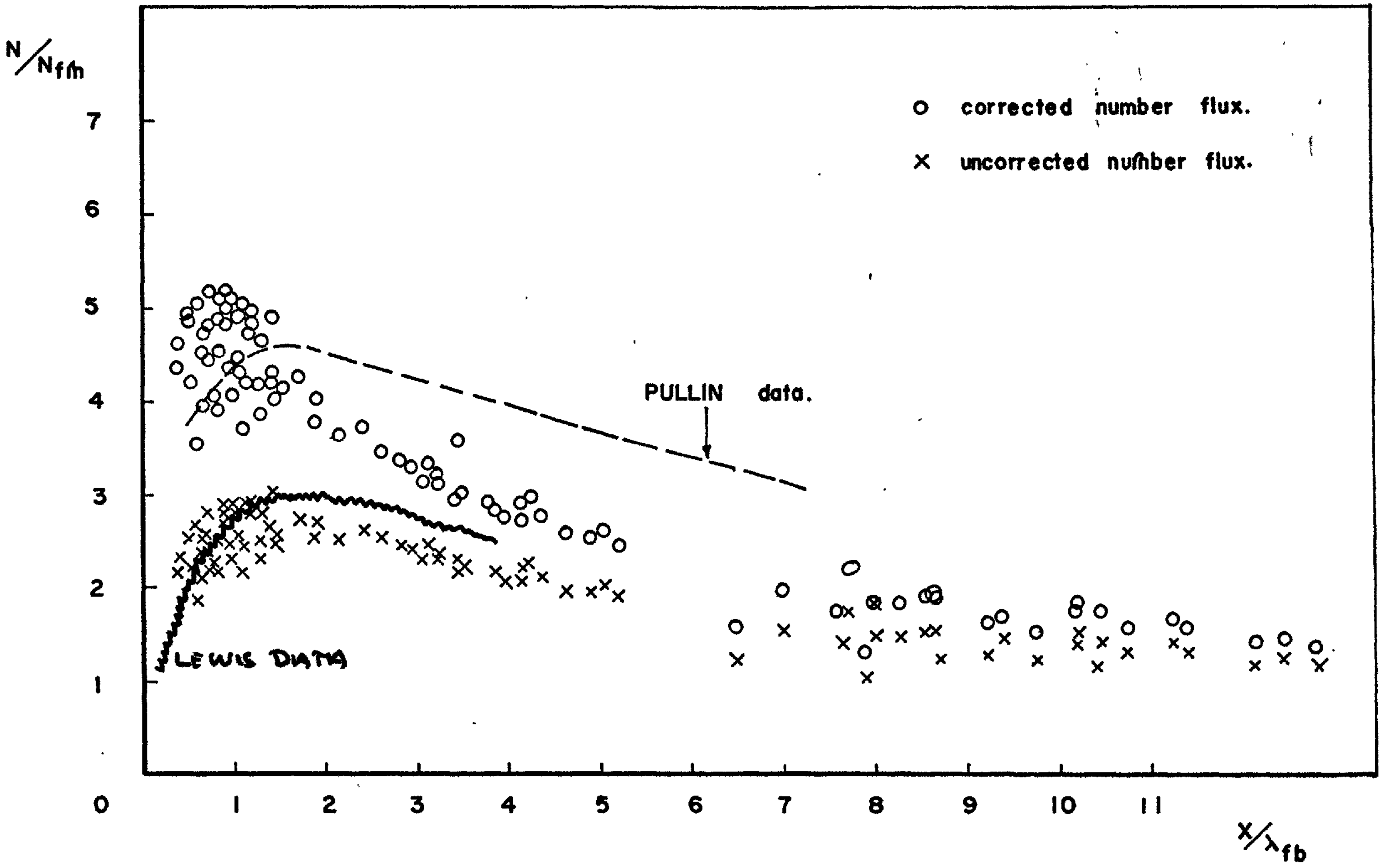

FIGURE 15 NUMBER FLUX DISTRIBUTION.

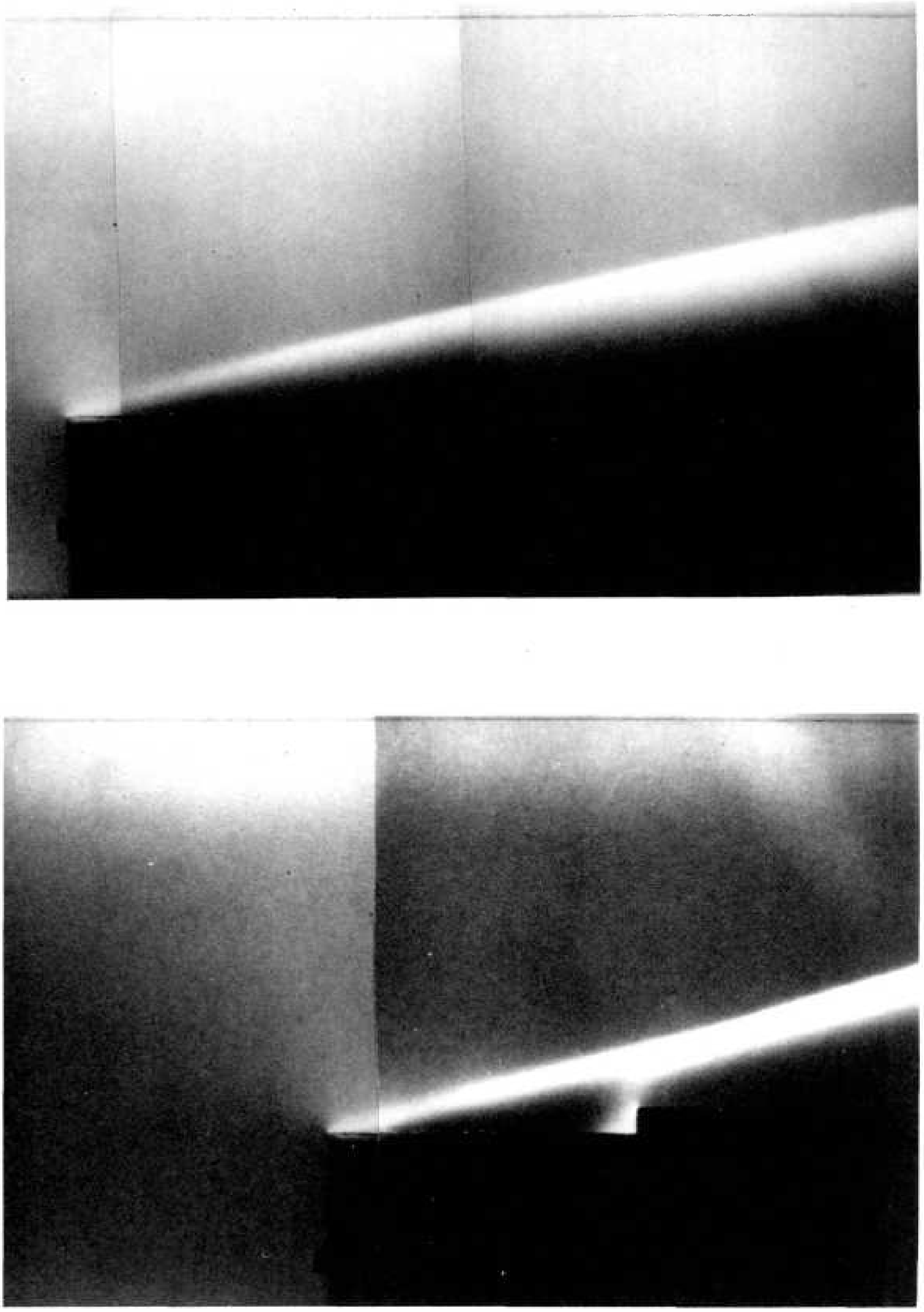

FIGURE 16   FLOW FIELD VISUALISATION

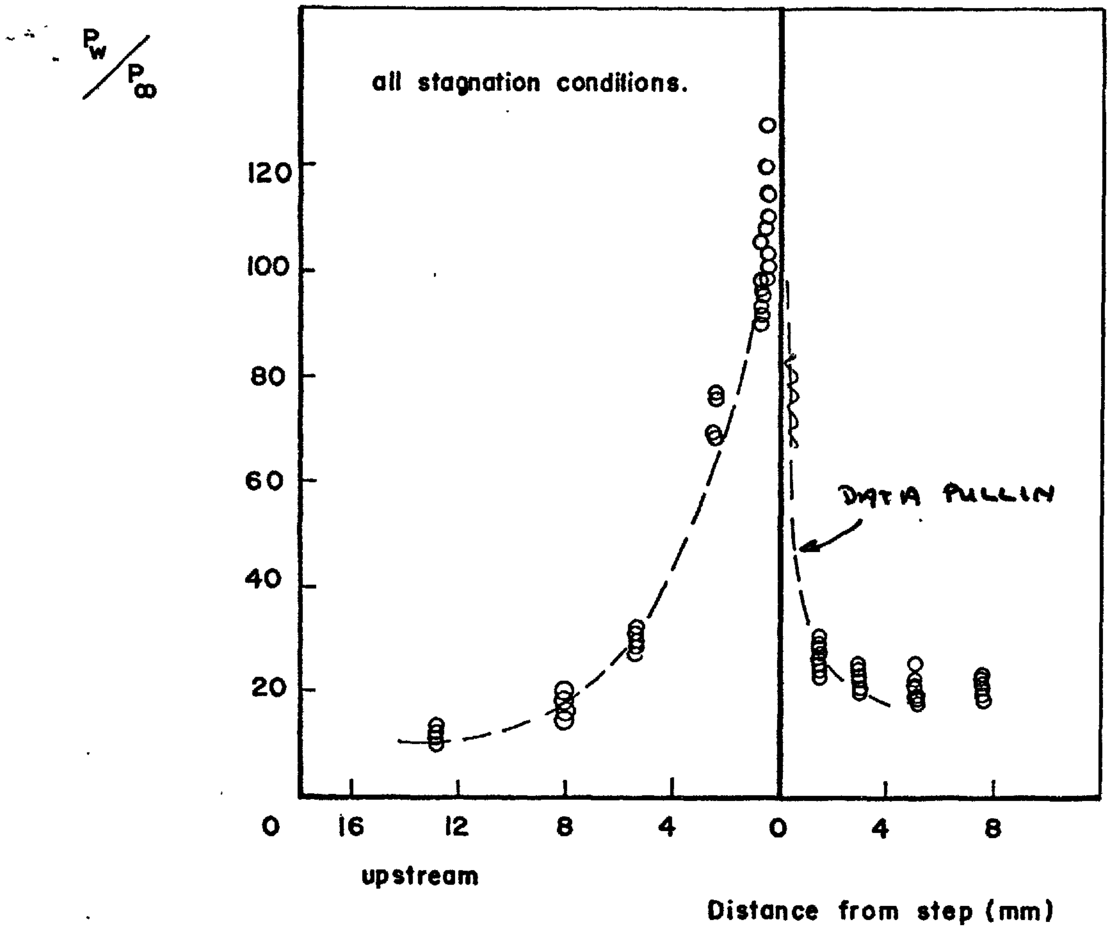

FIGURE 17 PRESSURES AROUND THE STEP.

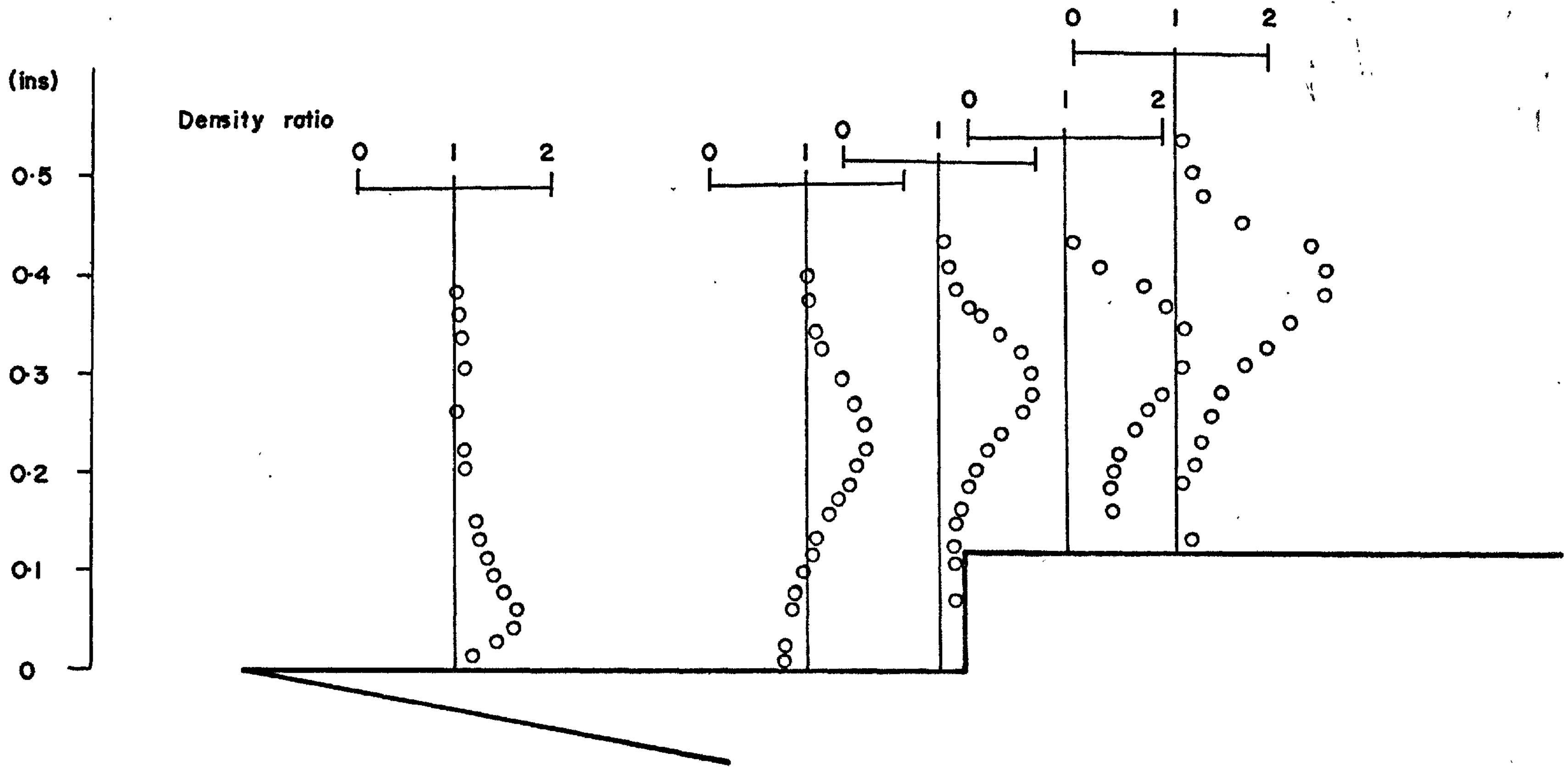

FIGURE 18 STEP DENSITY PROFILES (Davis preliminary data).

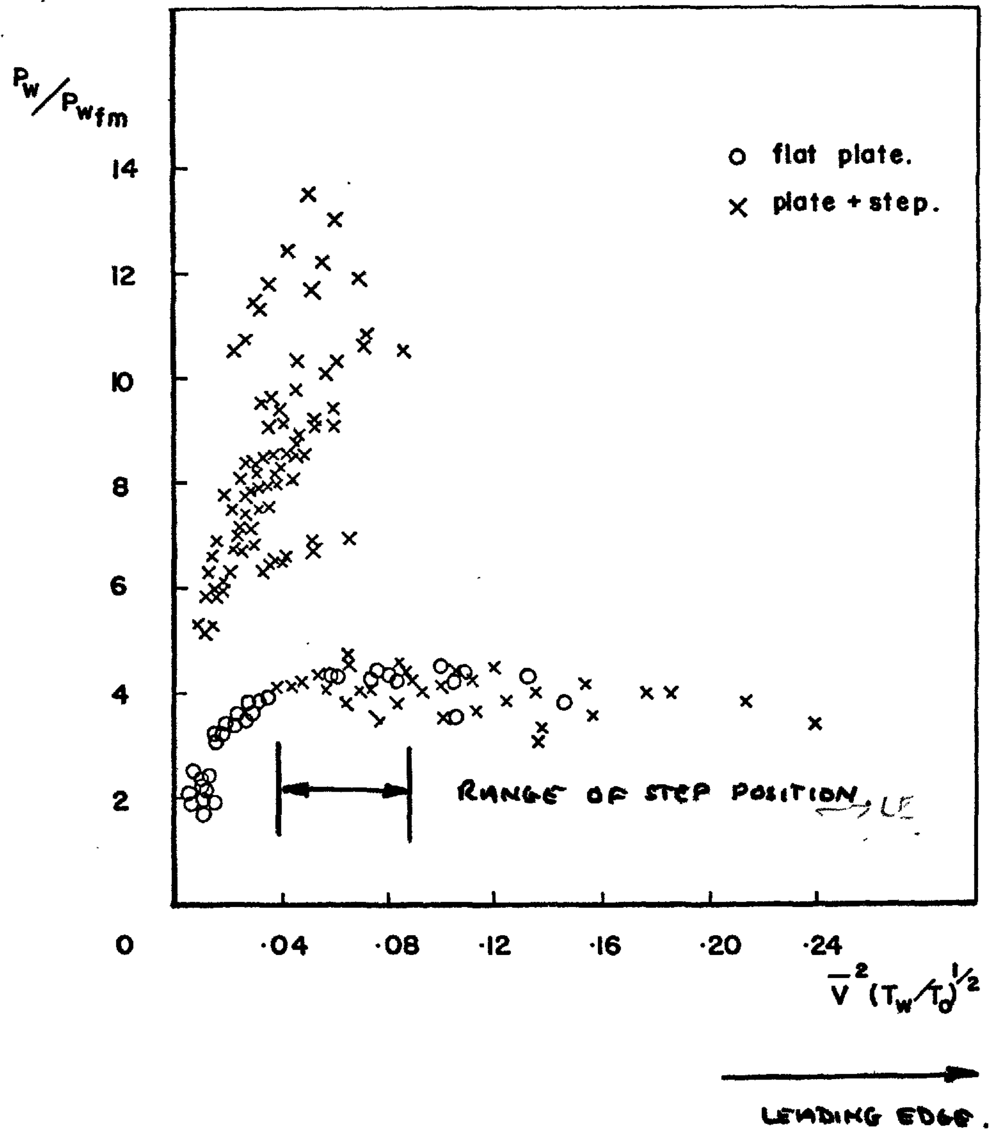

FIGURE 19 STEP PRESSURE DISTRIBUTION.

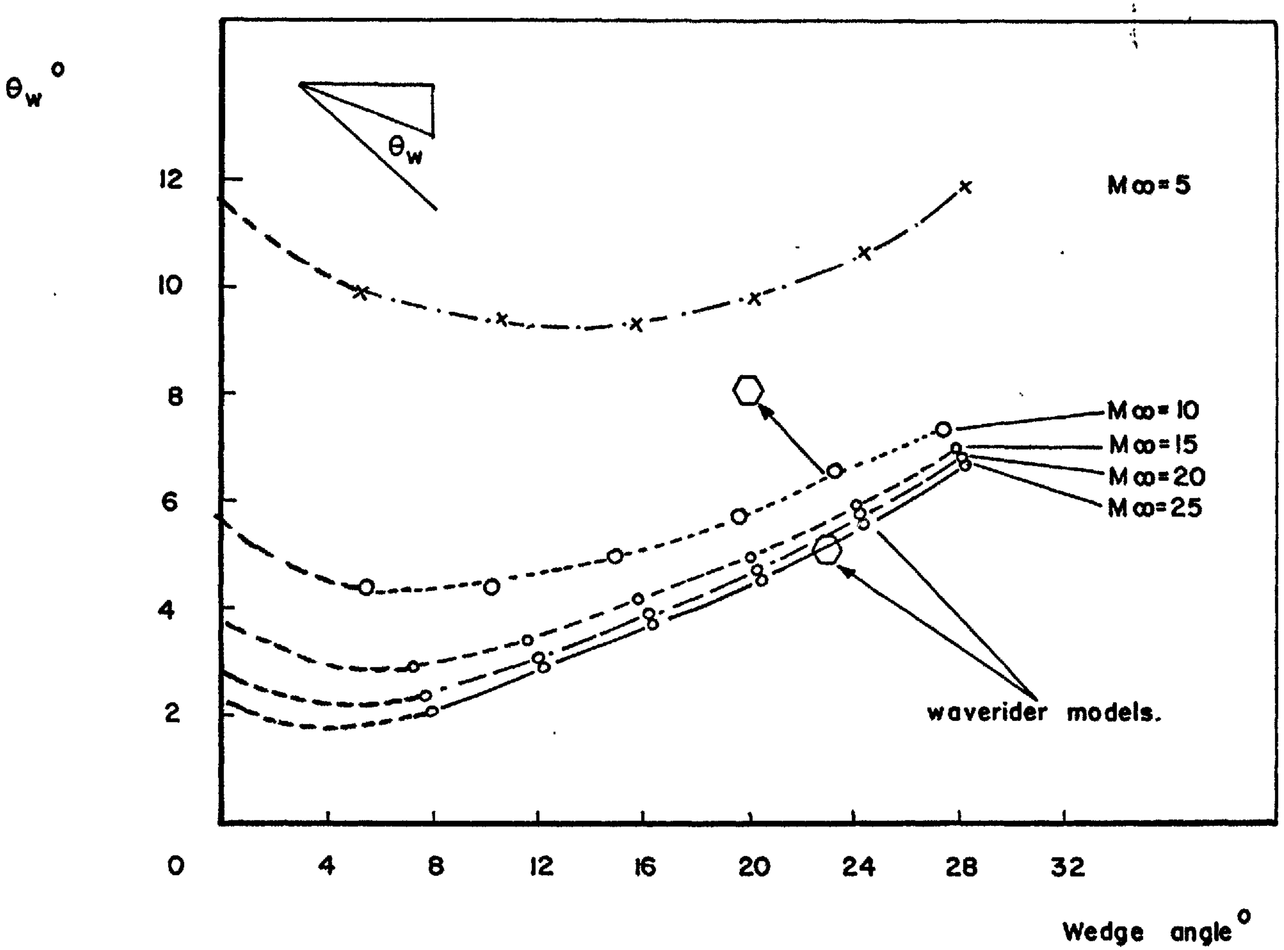

FIGURE 20 SHOCK STAND-OFF DISTANCE.

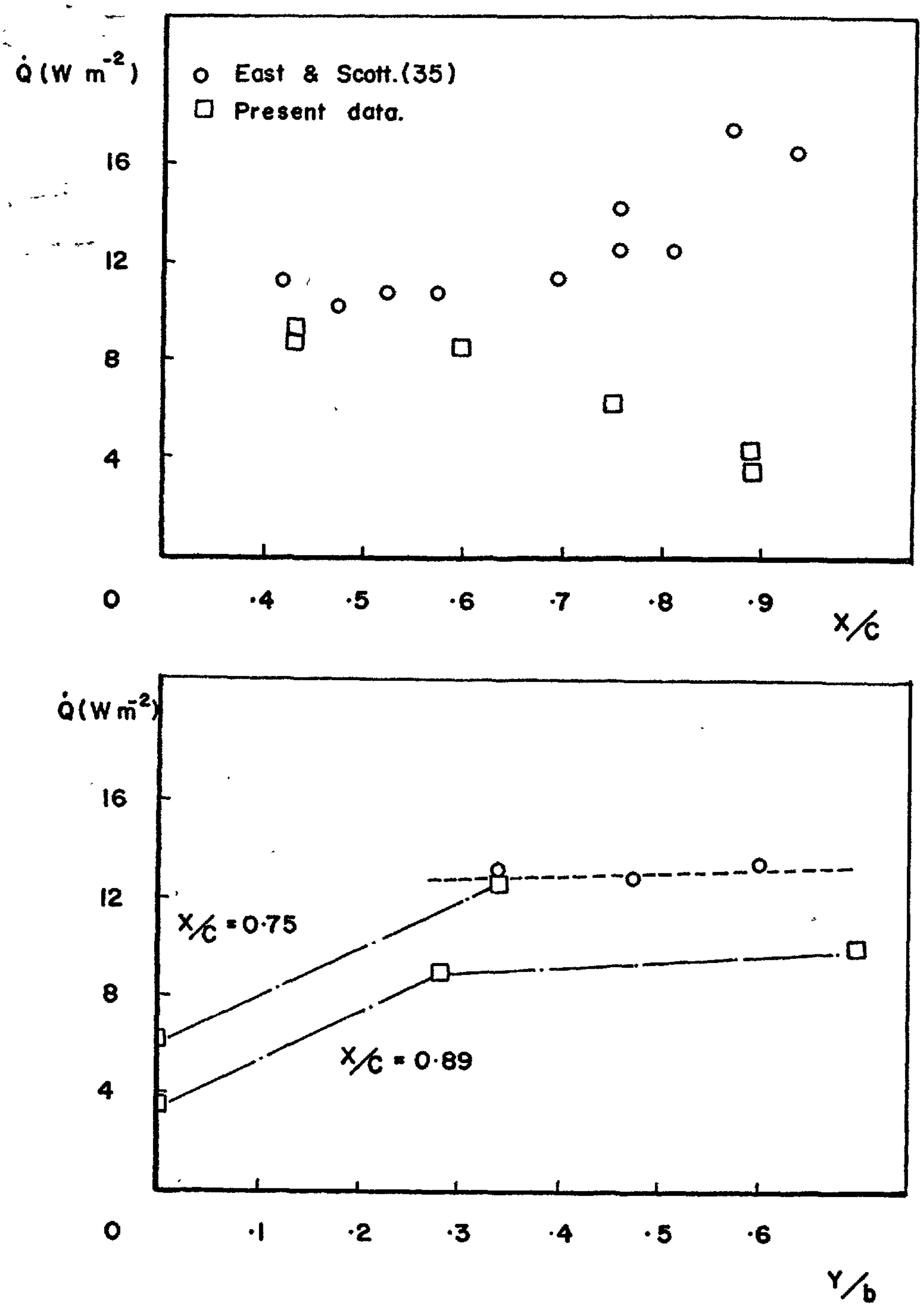

FIGURE 21 COMPARISON OF HEAT TRANSFER DATA

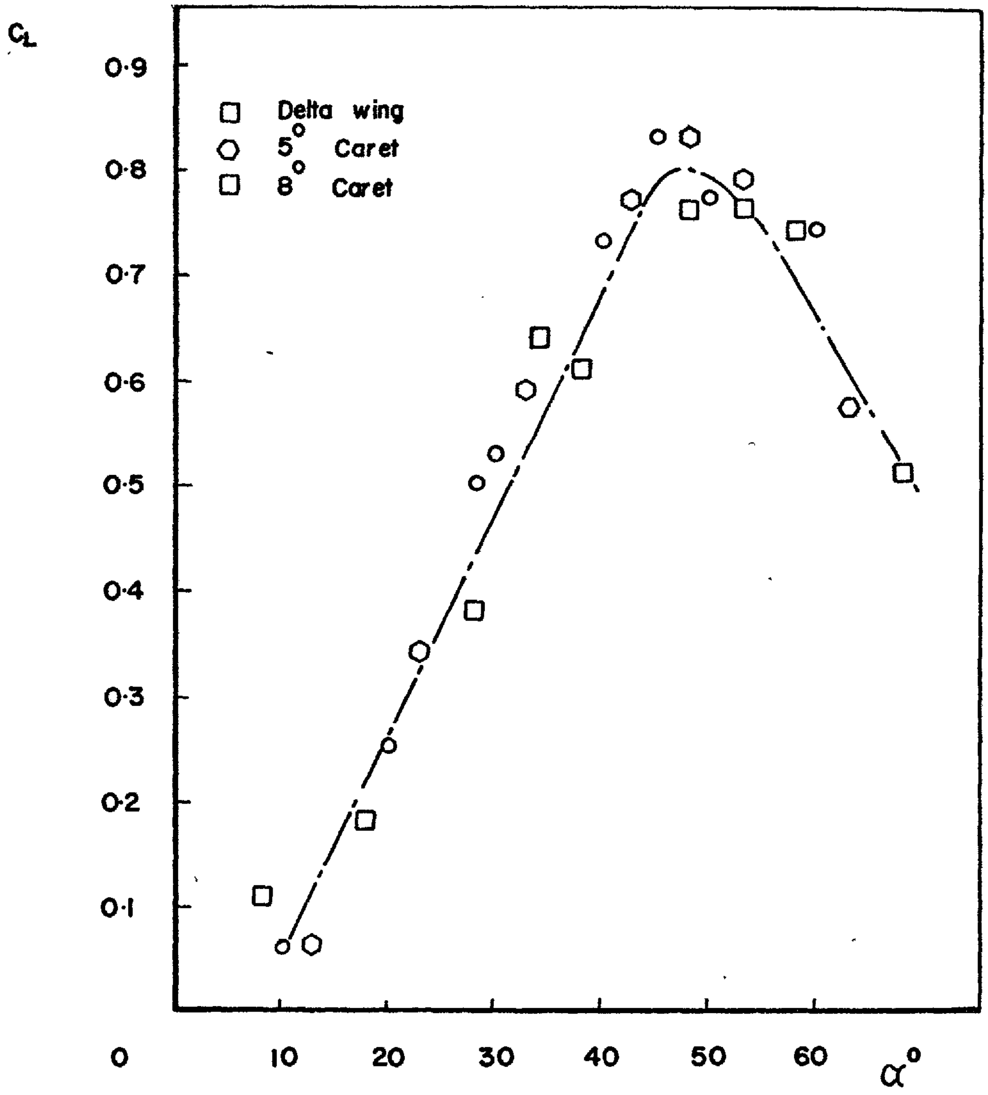

FIGURE 22 LIFT COEFFICIENT VARIATION WITH INCIDENCE

Gun Tunnel $M_\infty = 9$

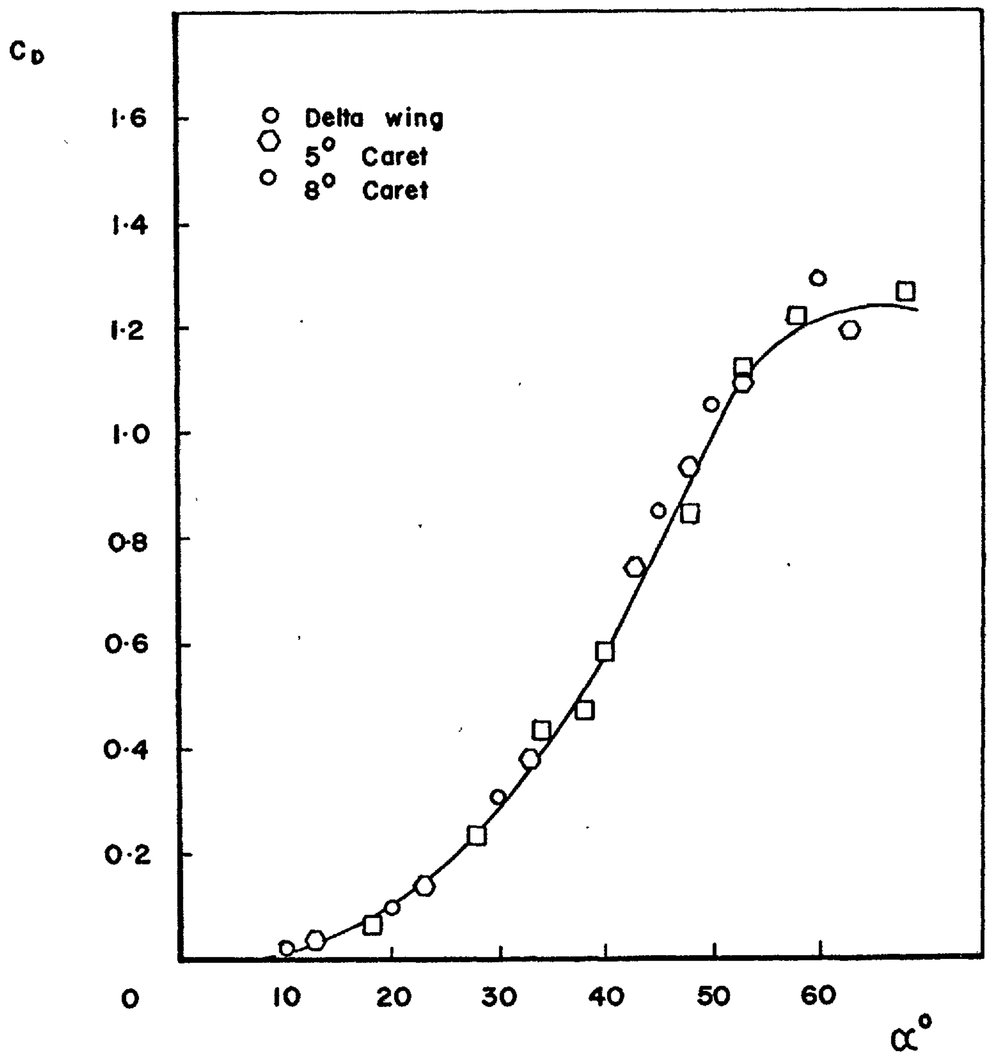

FIGURE 23 DRAG COEFFICIENT VARIATION.

GUN TUNNEL $M_\infty = 9$

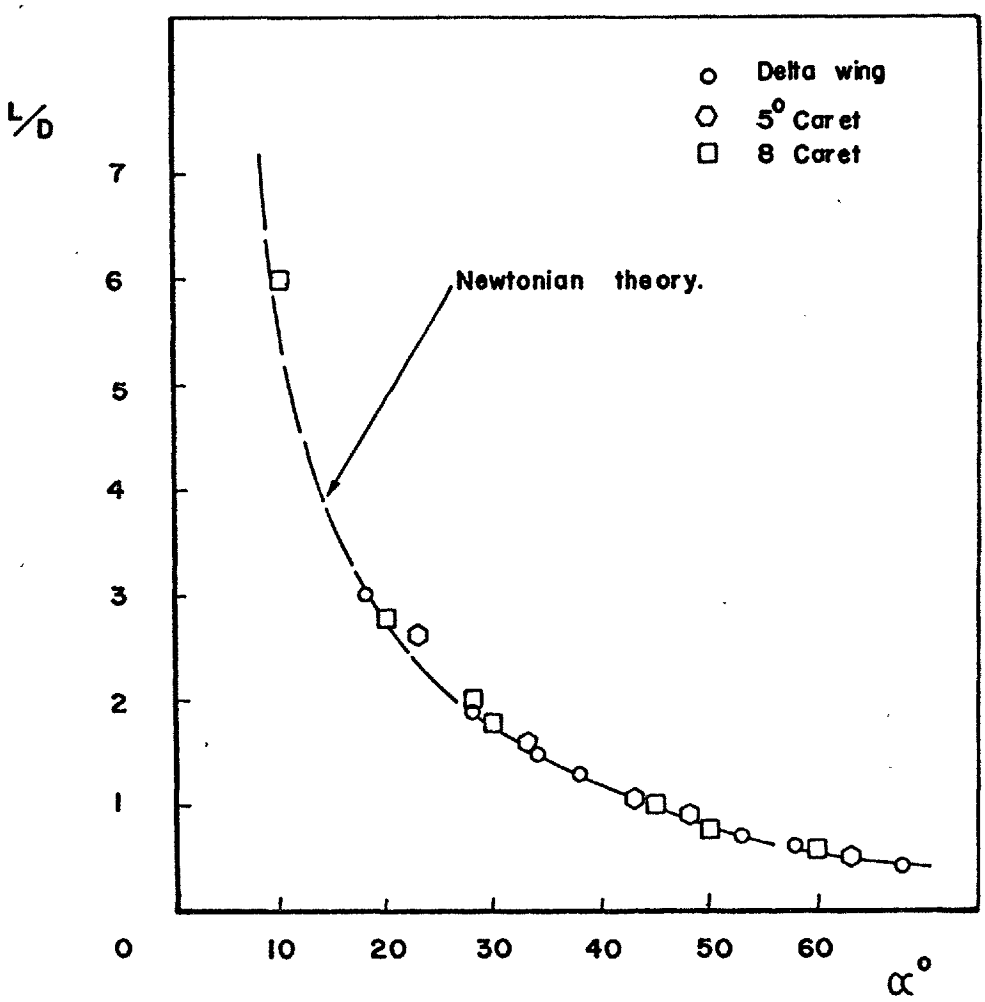

FIGURE 24 LIFT/DRAG RATIO VARIATION.

Gun Tunnel $M_\infty = 9$

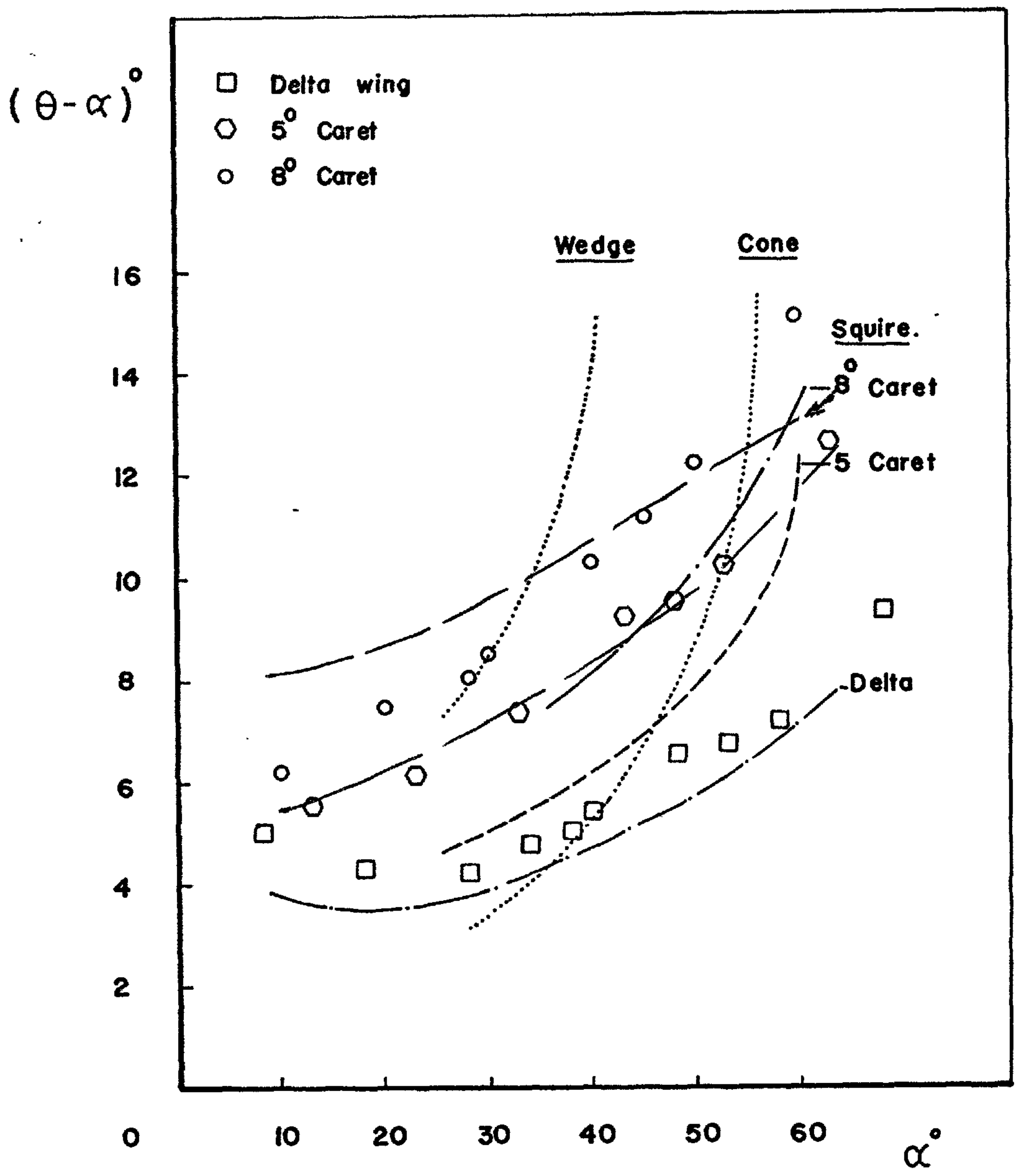

CORRECTED THEORY.

FIGURE 25 SHOCK STAND-OFF ANGLE.

GUN TUNNEL $M_\infty = 9$

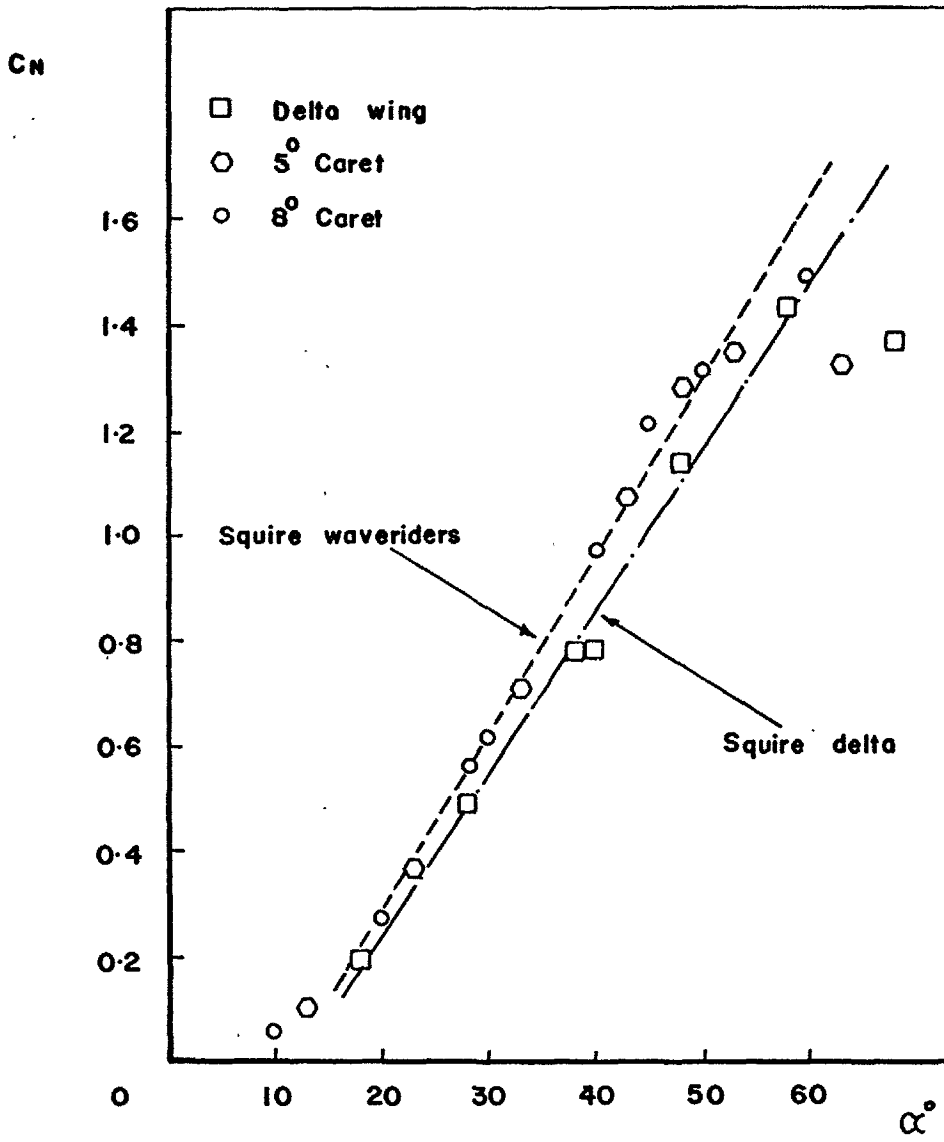

FIGURE 26 NORMAL FORCE COEFFICIENT.

Gun Tunnel $M_\infty = 9$

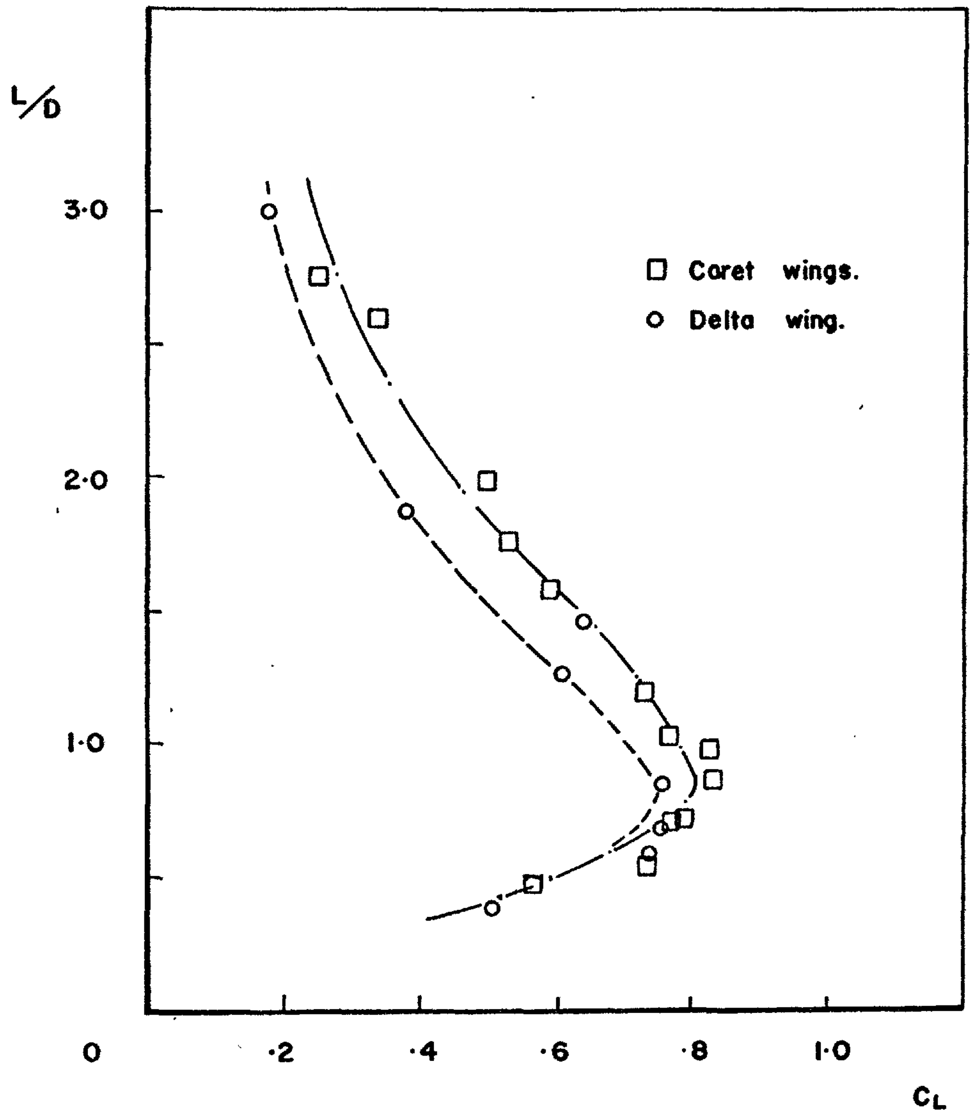

FIGURE 26A WING AERODYNAMIC PERFORMANCE.

Gun Tunnel $M_\infty = 9$.

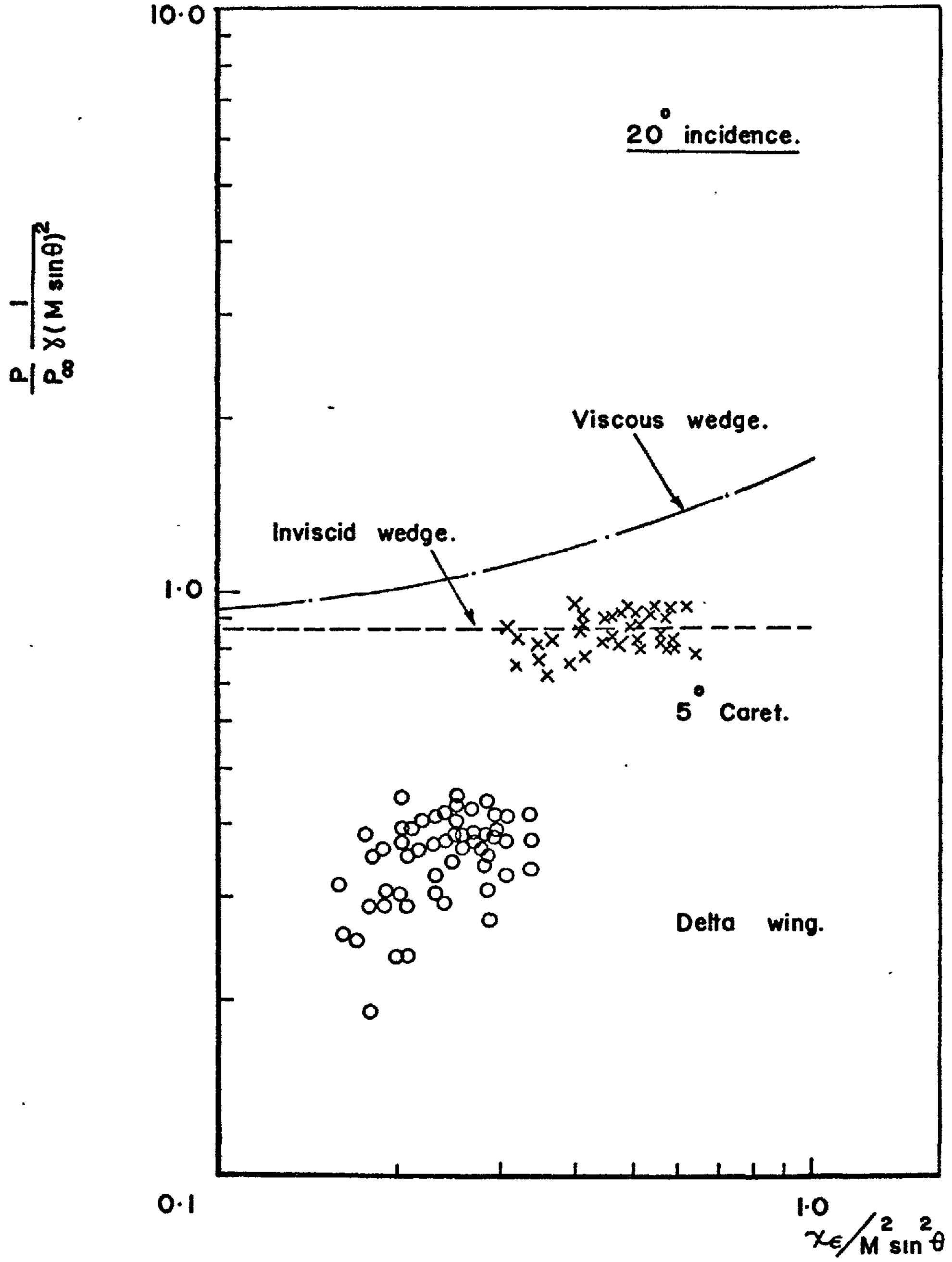

FIGURE 27 COMPARISON BETWEEN WEDGE & WING.

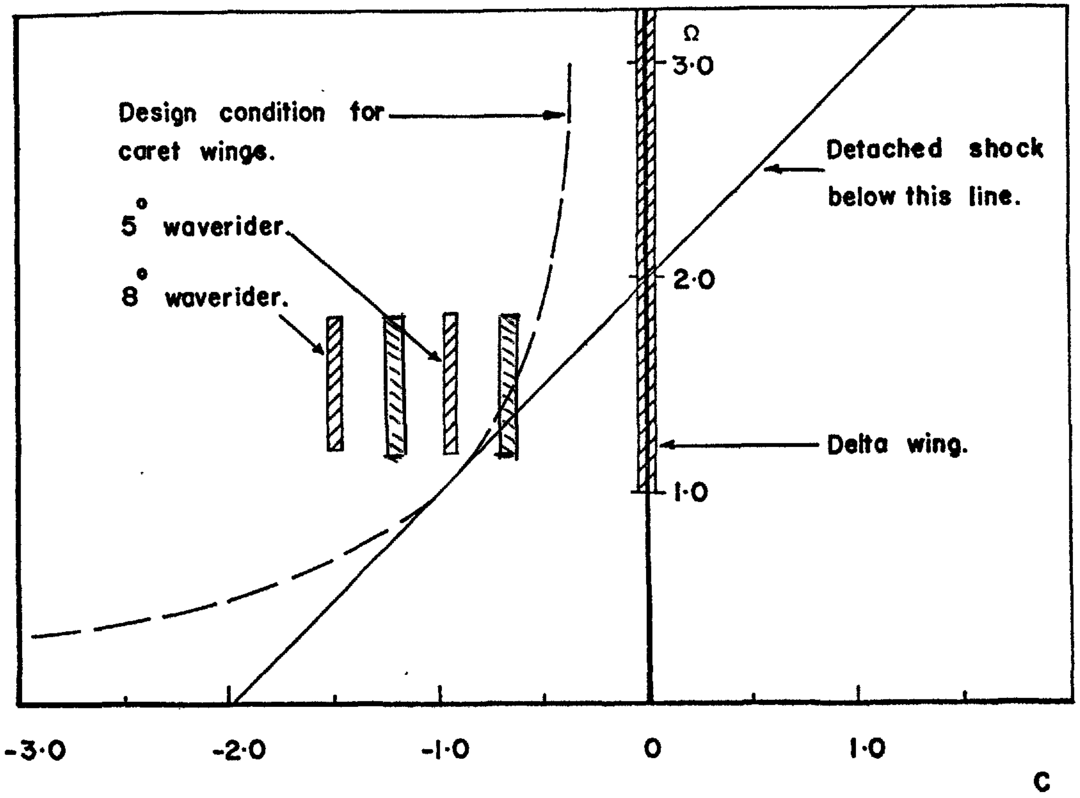

CORRECTED THEORY.

FIGURE 28 SQUIRE'S THEORY PARAMETERS.

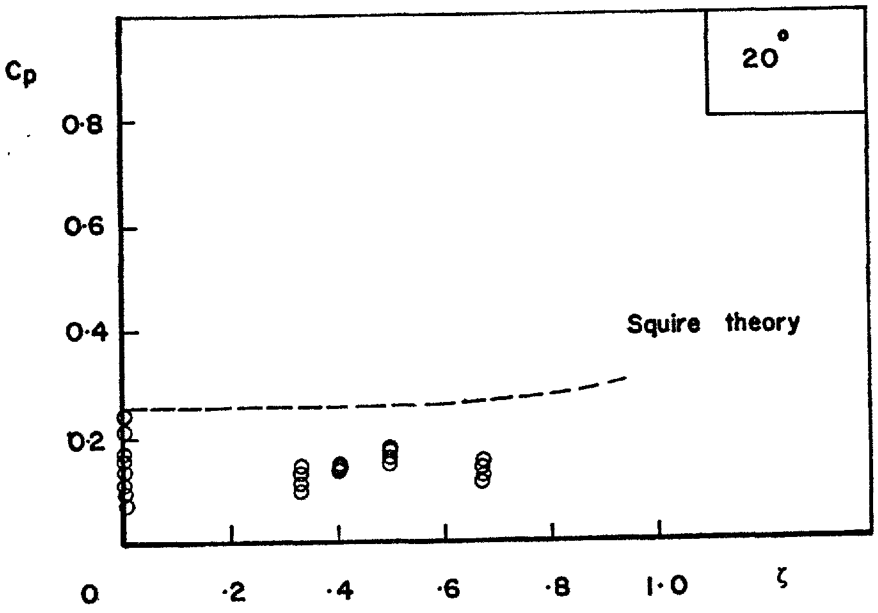

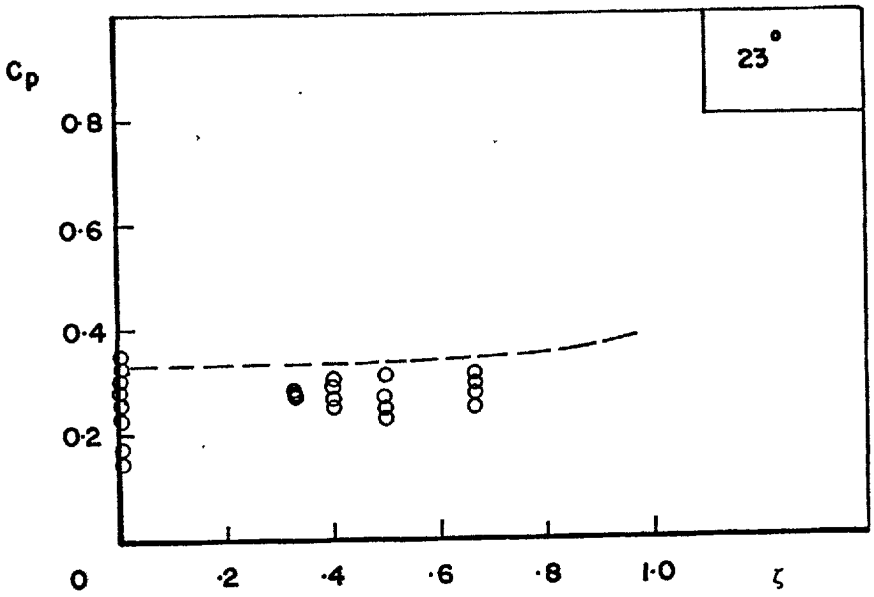

FIGURE 29a DELTA WING COMPARISON WITH THEORY.

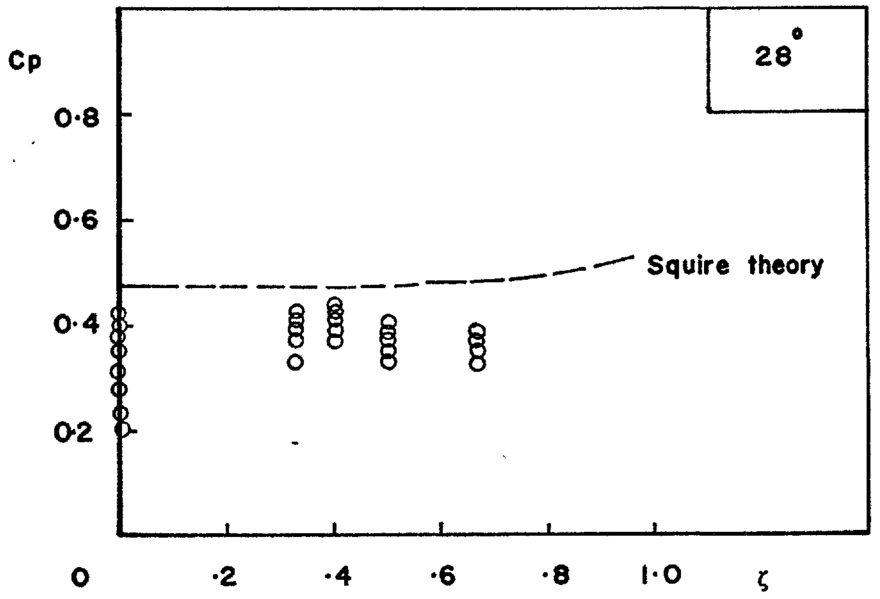
Cp
0·8
0·6
0·4
0·2
0
·2
·4
·6
·8
1·0
ζ
28°
Squire theory

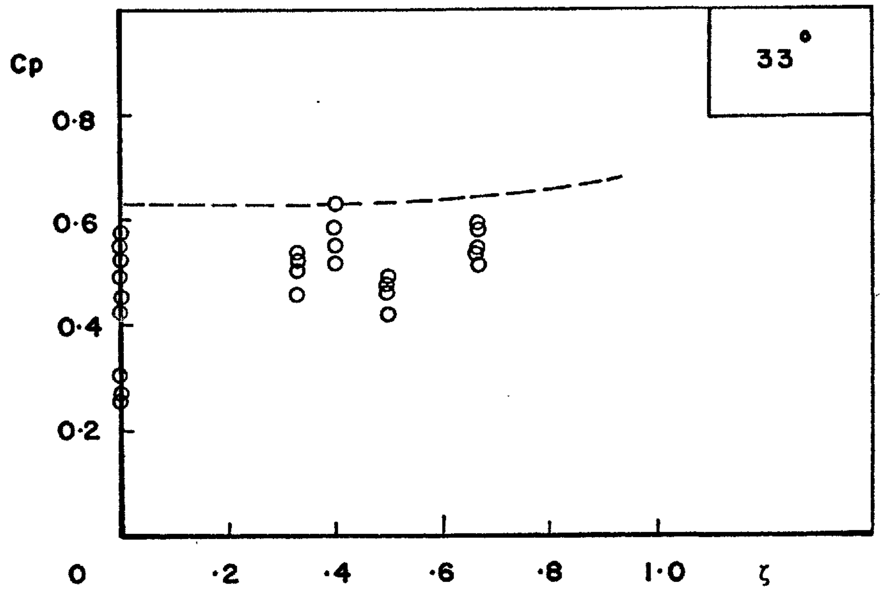
Cp
0·8
0·6
0·4
0·2
0
·2
·4
·6
·8
1·0
ζ
33°

FIGURE 29b.

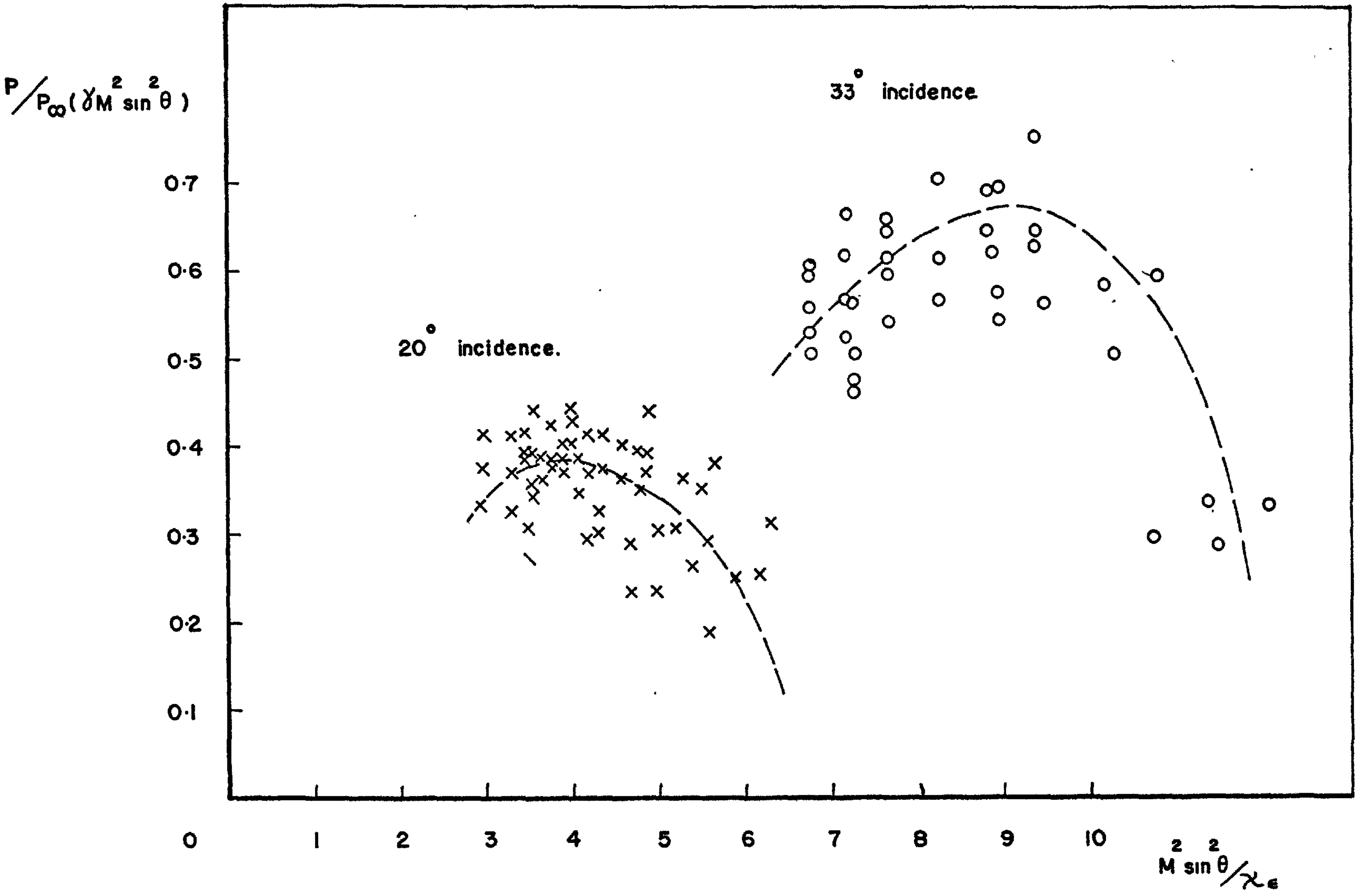

FIGURE 30a PRESSURE DISTRIBUTION FOR DELTA WING.

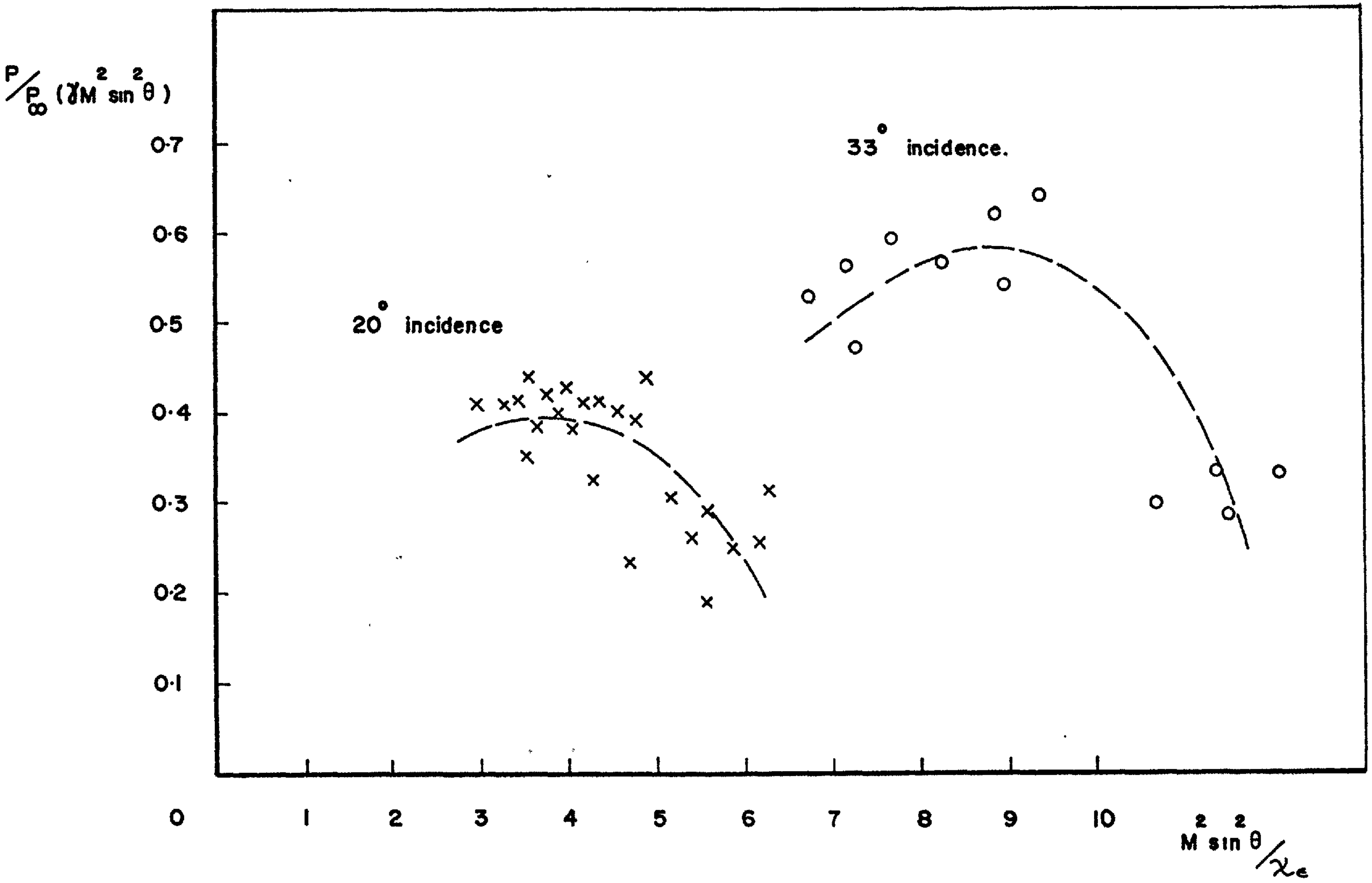

FIGURE 30b DELTA WING CENTRE LINE PRESSURE.

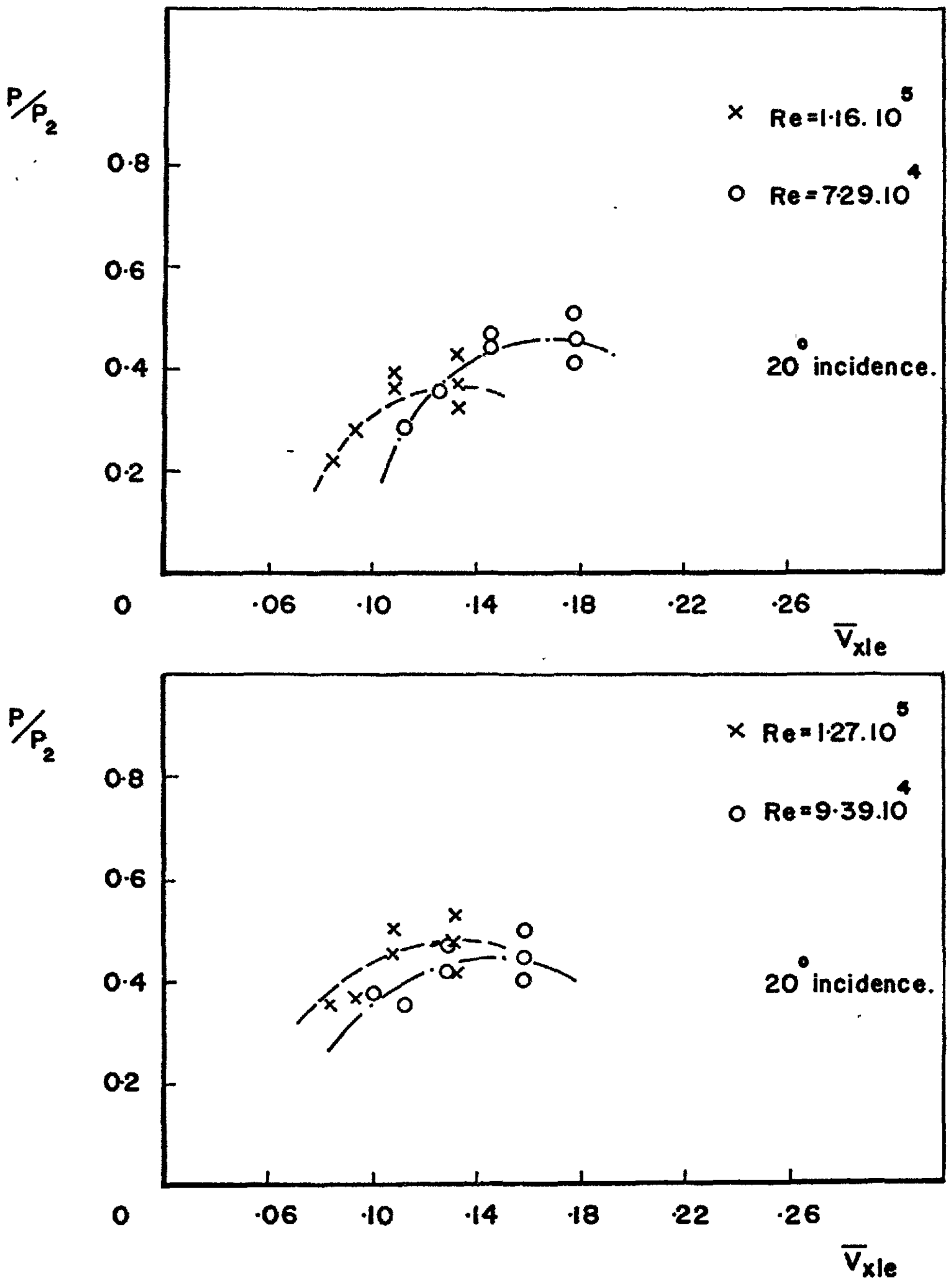

FIGURE 31a DELTA WING PRESSURE.

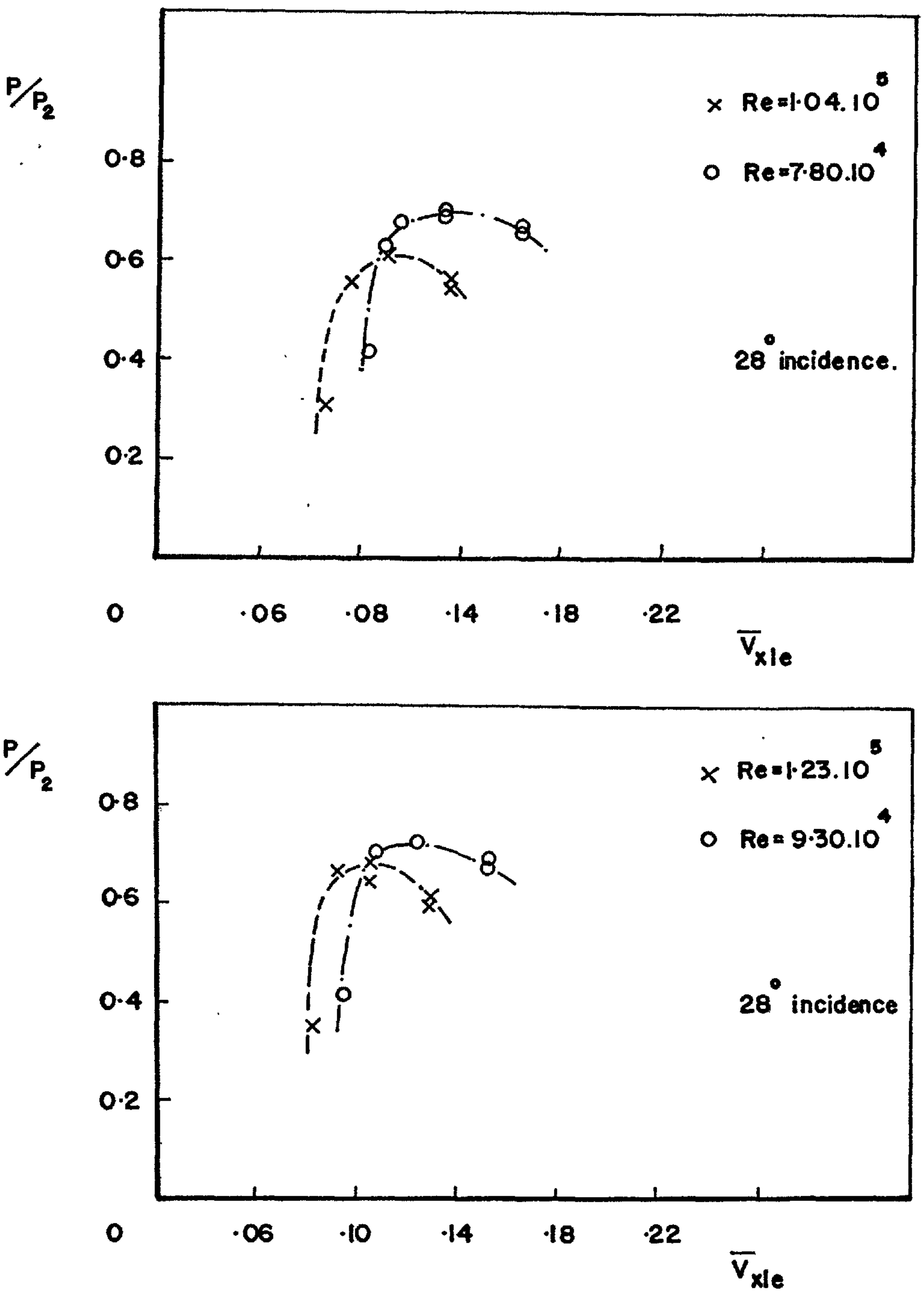

FIGURE 31b DELTA WING PRESSURE.

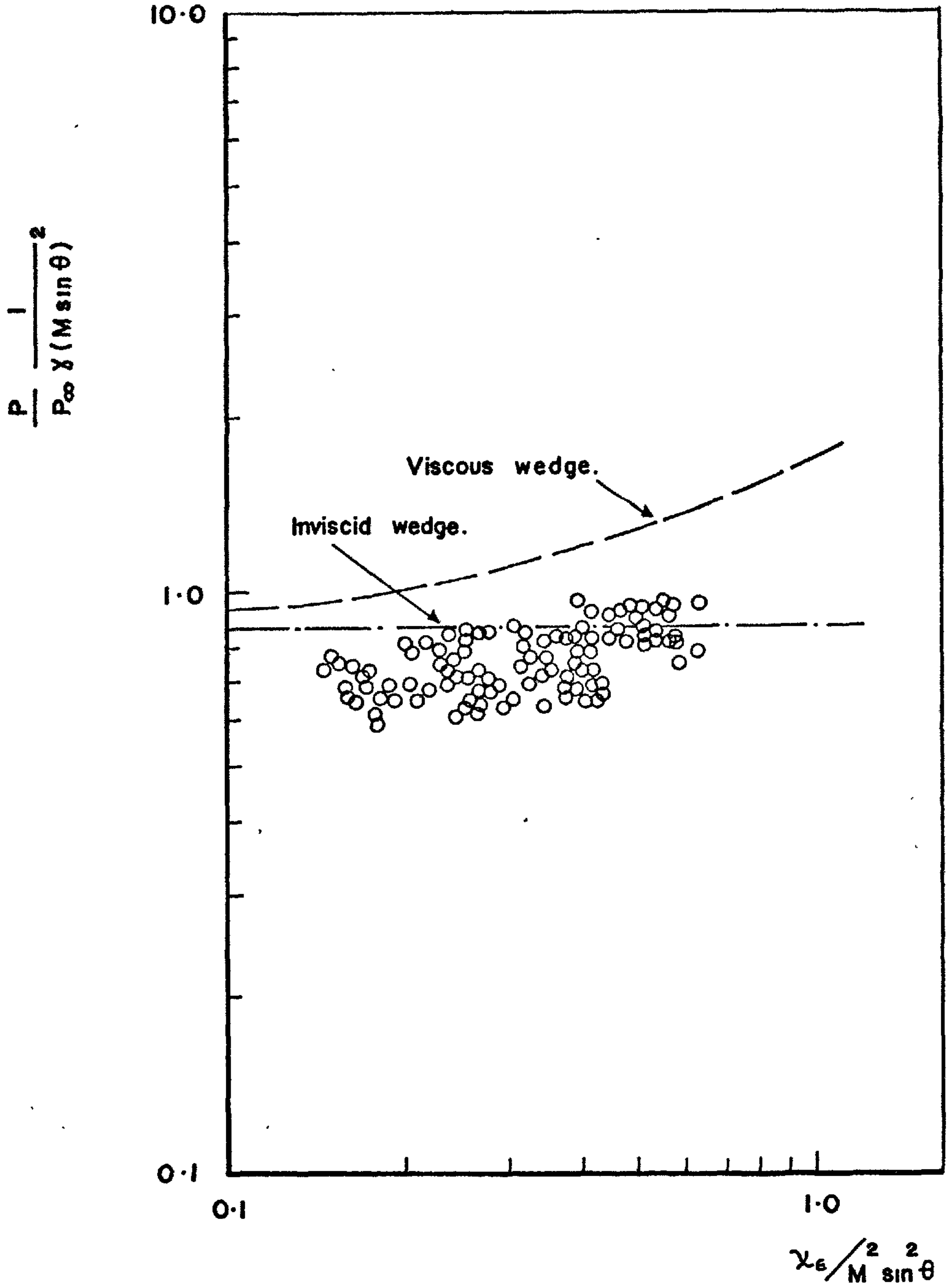

FIGURE 32 5° WAVERIDER PRESSURE DISTRIBUTION.

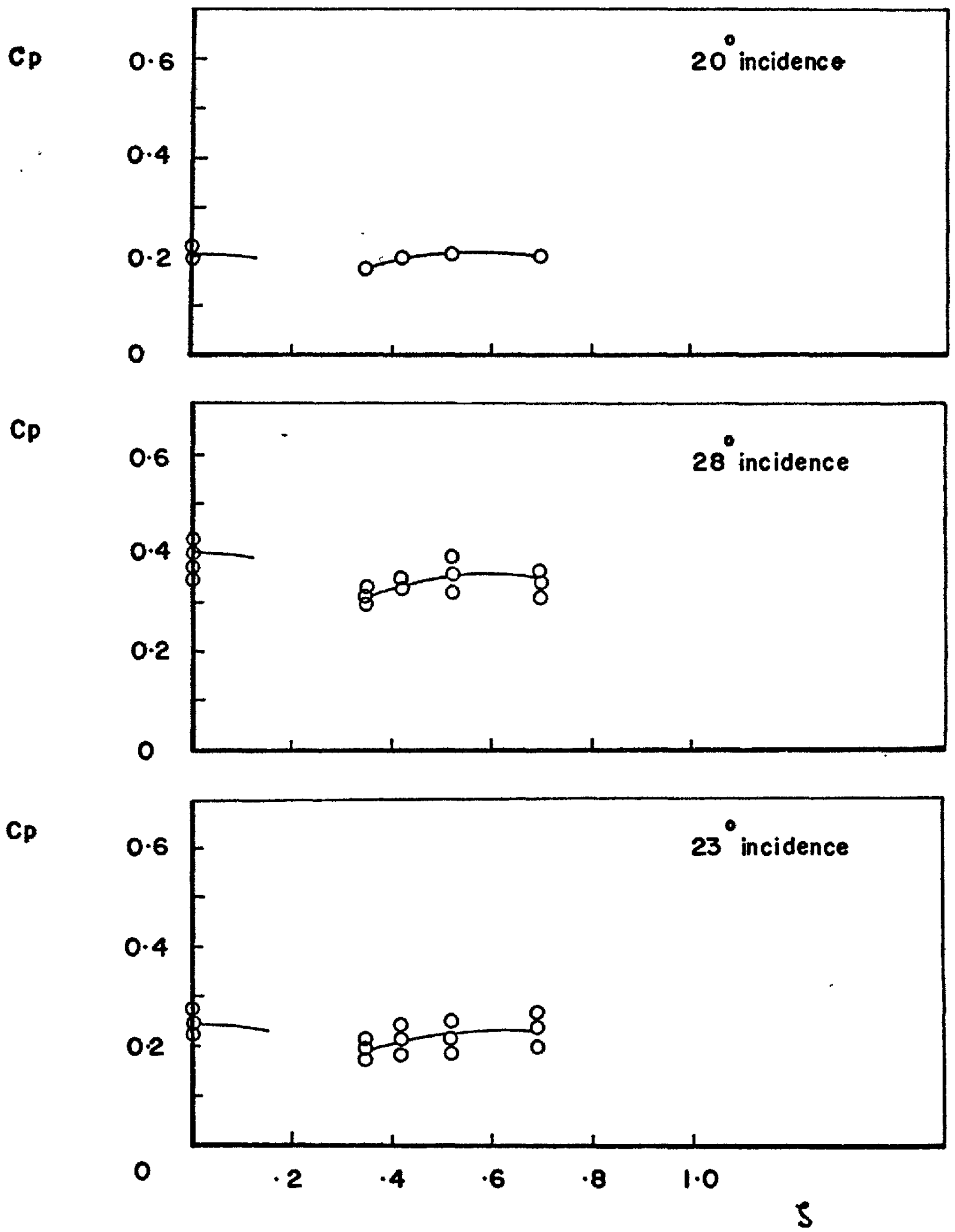

FIGURE 33 5° WAVERIDER SPANWISE PRESSURE.

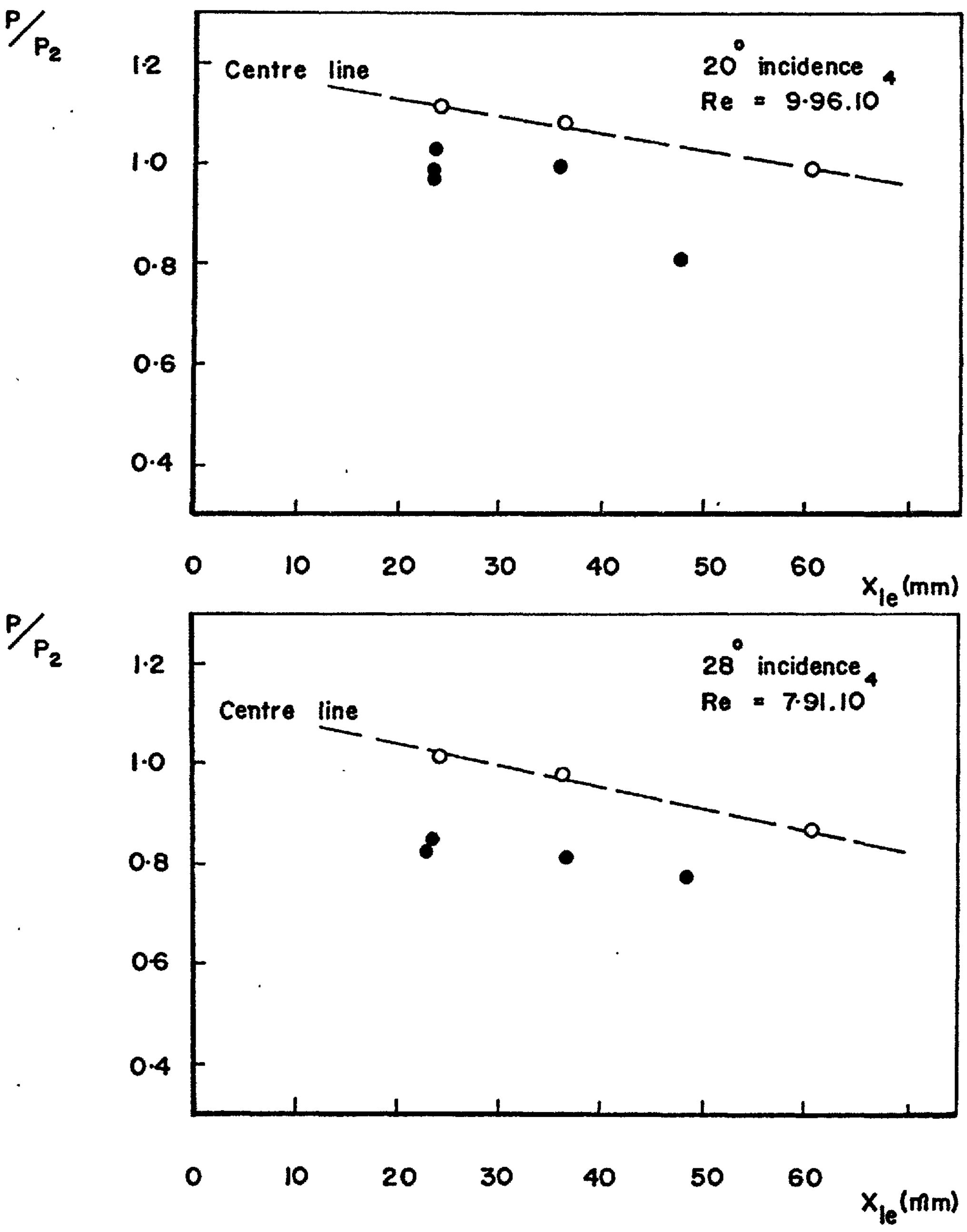

FIGURE 34 5° WAVERIDER PRESSURE DISTRIBUTION.

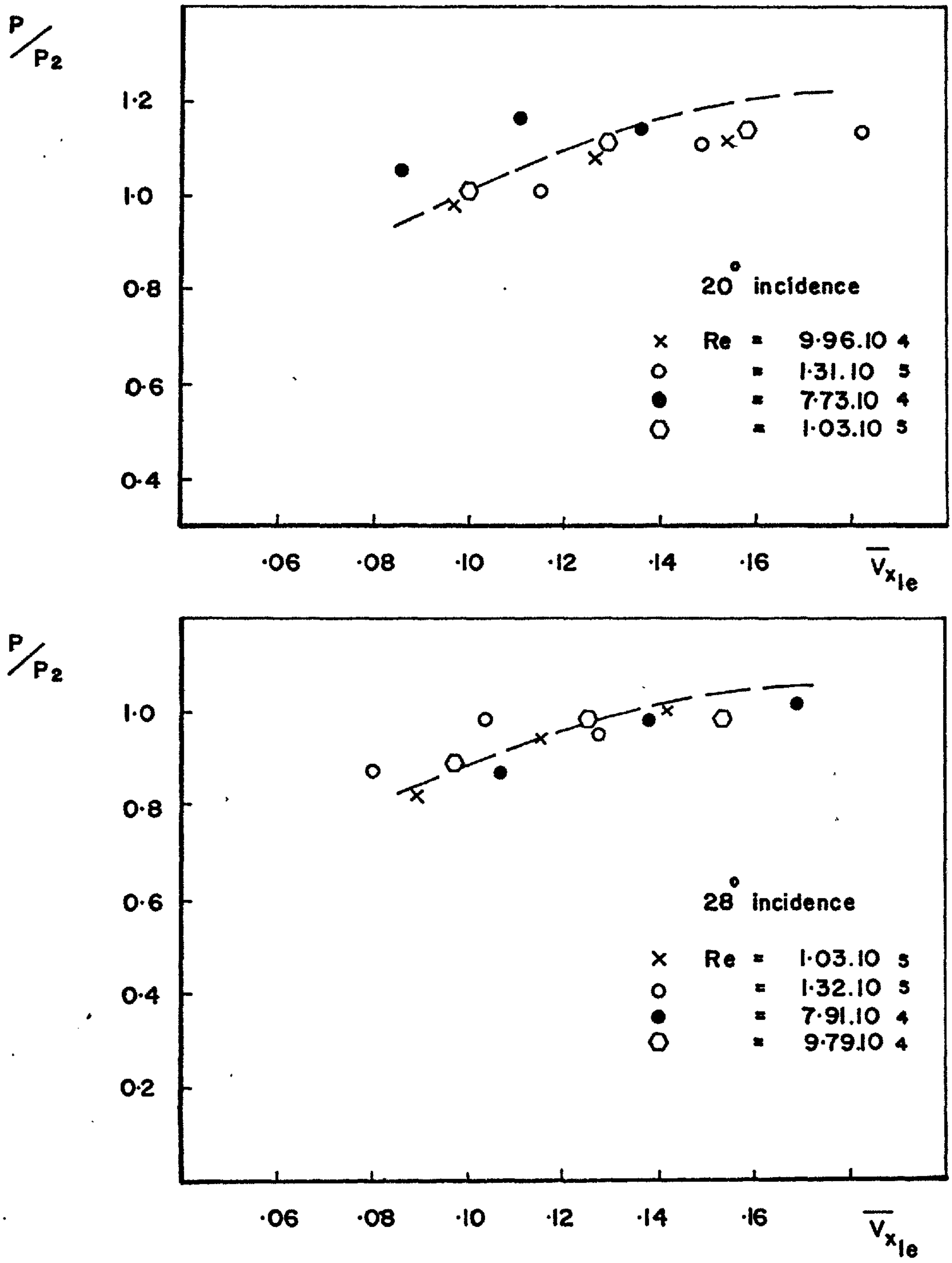

FIGURE 35 RAREFACTION EFFECTS ON 5° WAVERIDER.

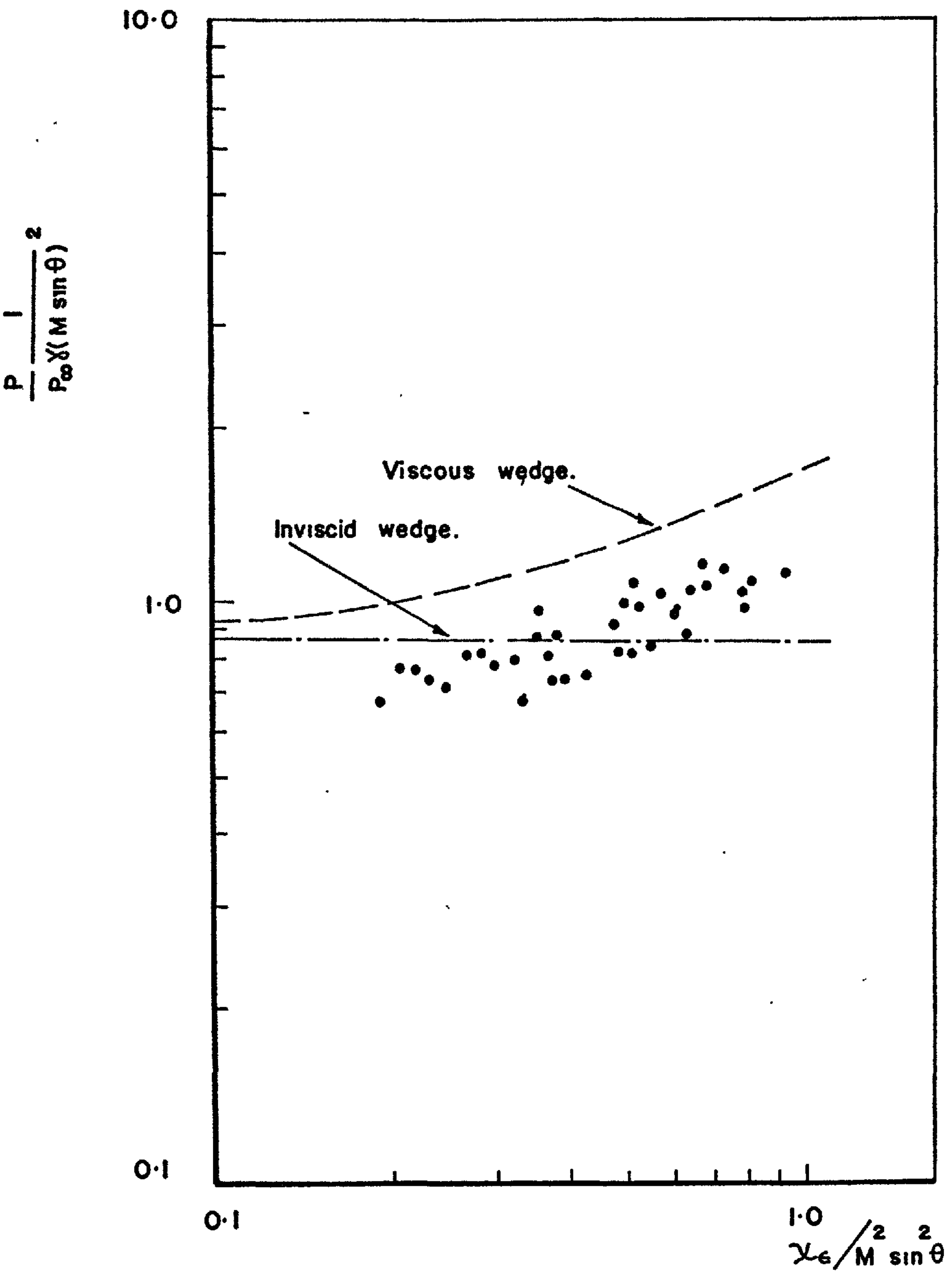

FIGURE 36 8° WAVERIDER CENTRE LINE PRESSURE.

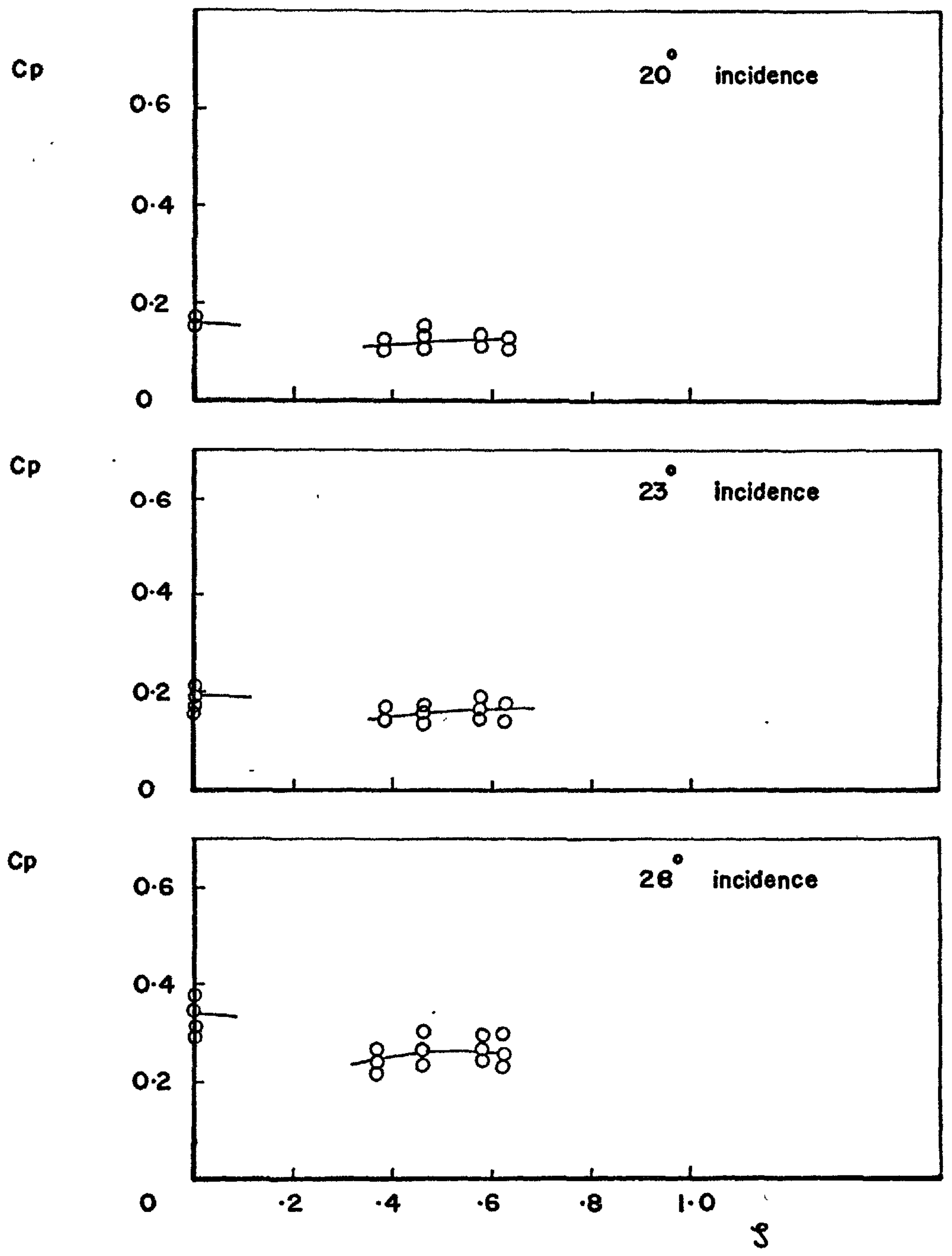

FIGURE 37 8° WAVERIDER SPANWISE PRESSURE.

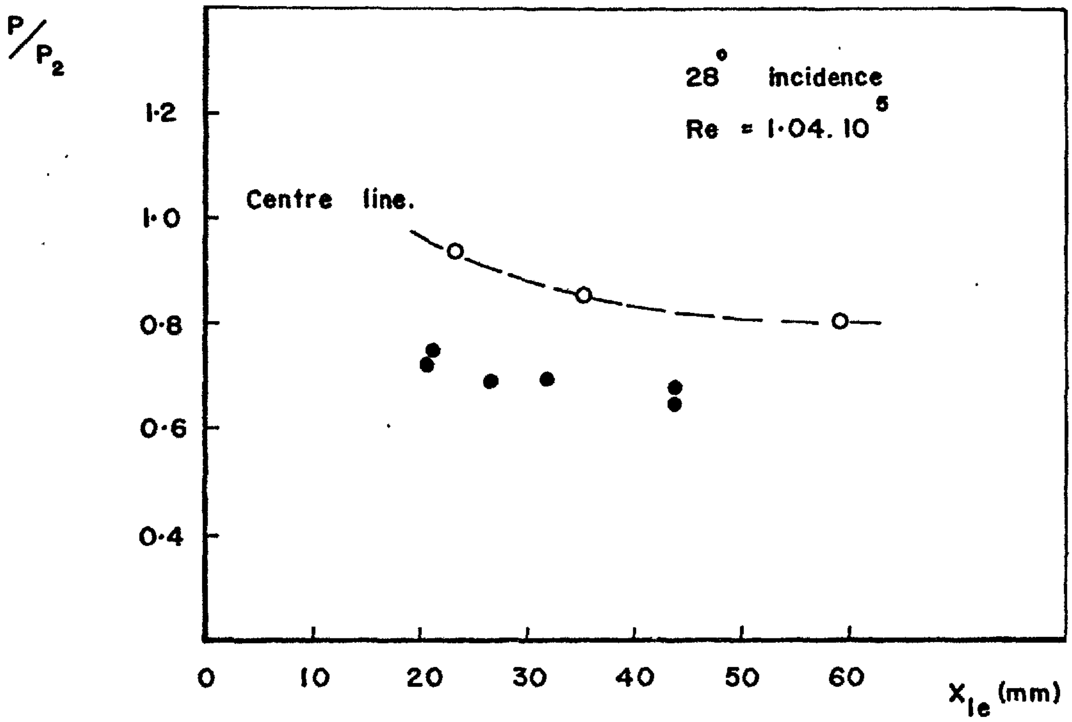

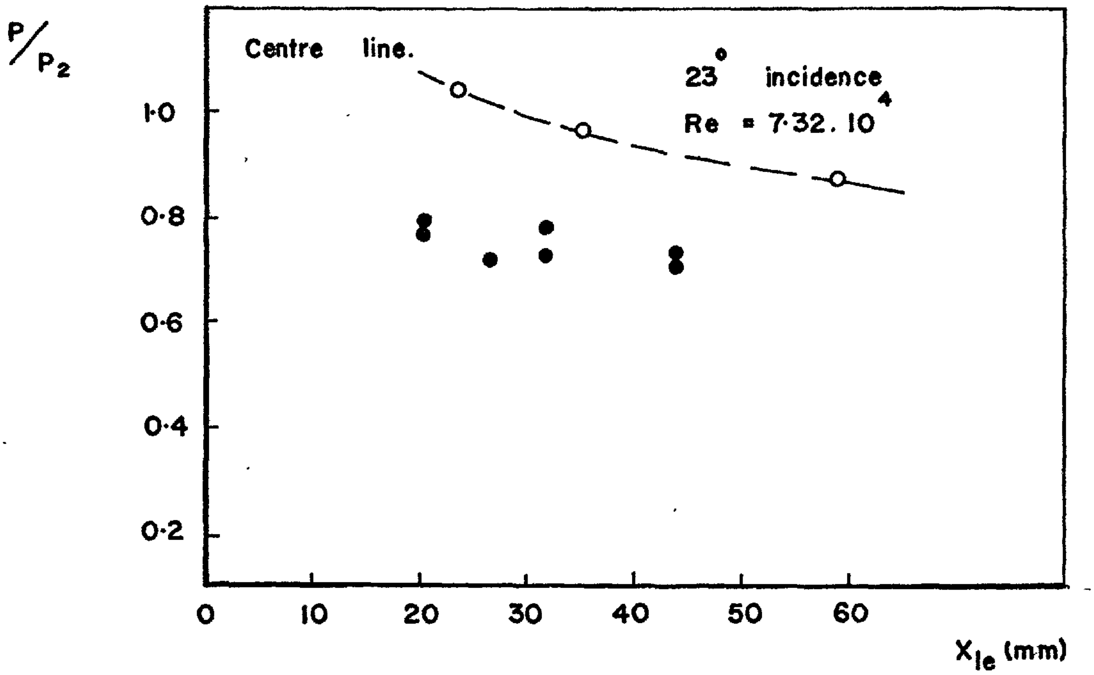

FIGURE 38 8° WAVERIDER PRESSURE DISTRIBUTION.

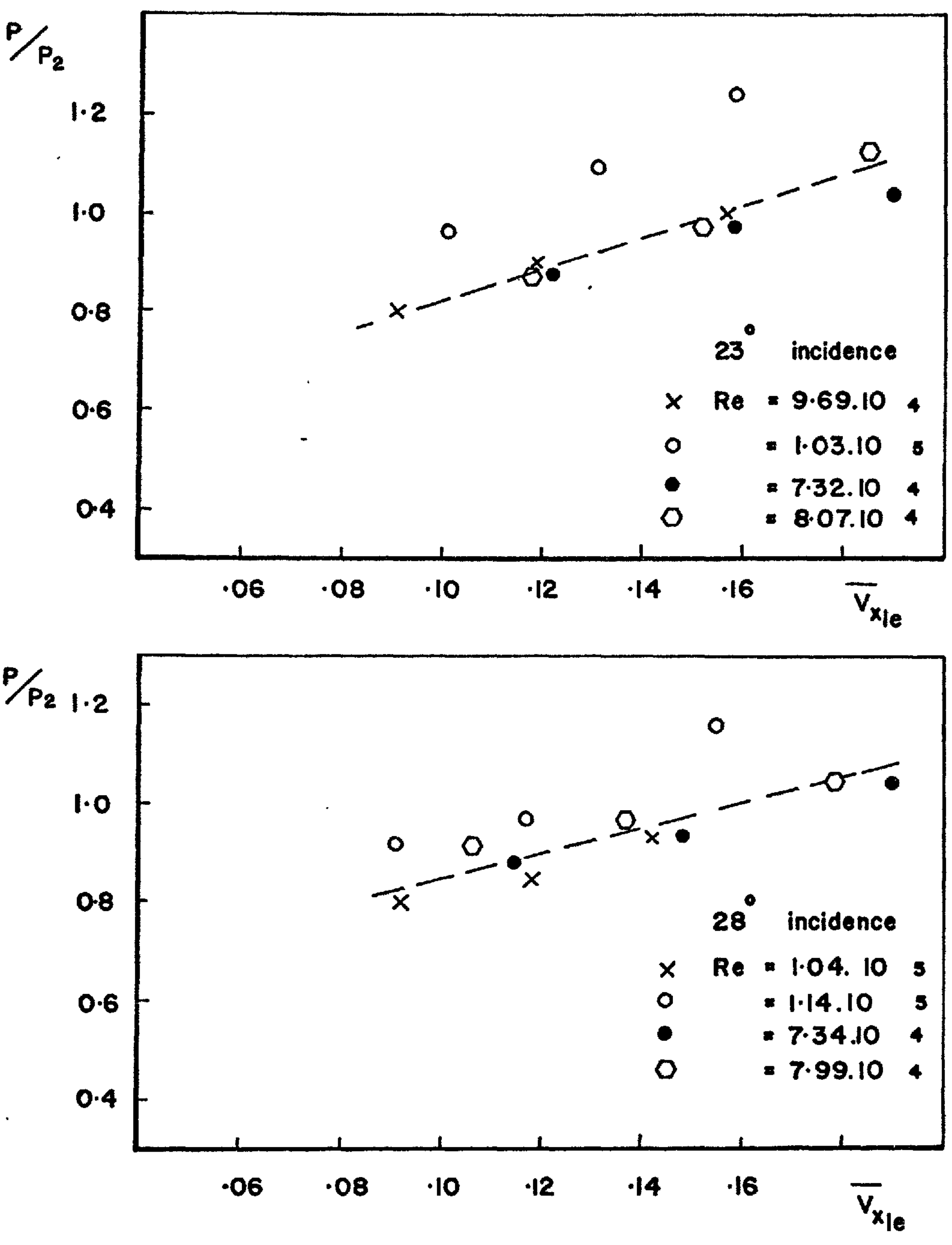

FIGURE 39 RAREFACTION EFFECTS ON 8° WAVERIDER.

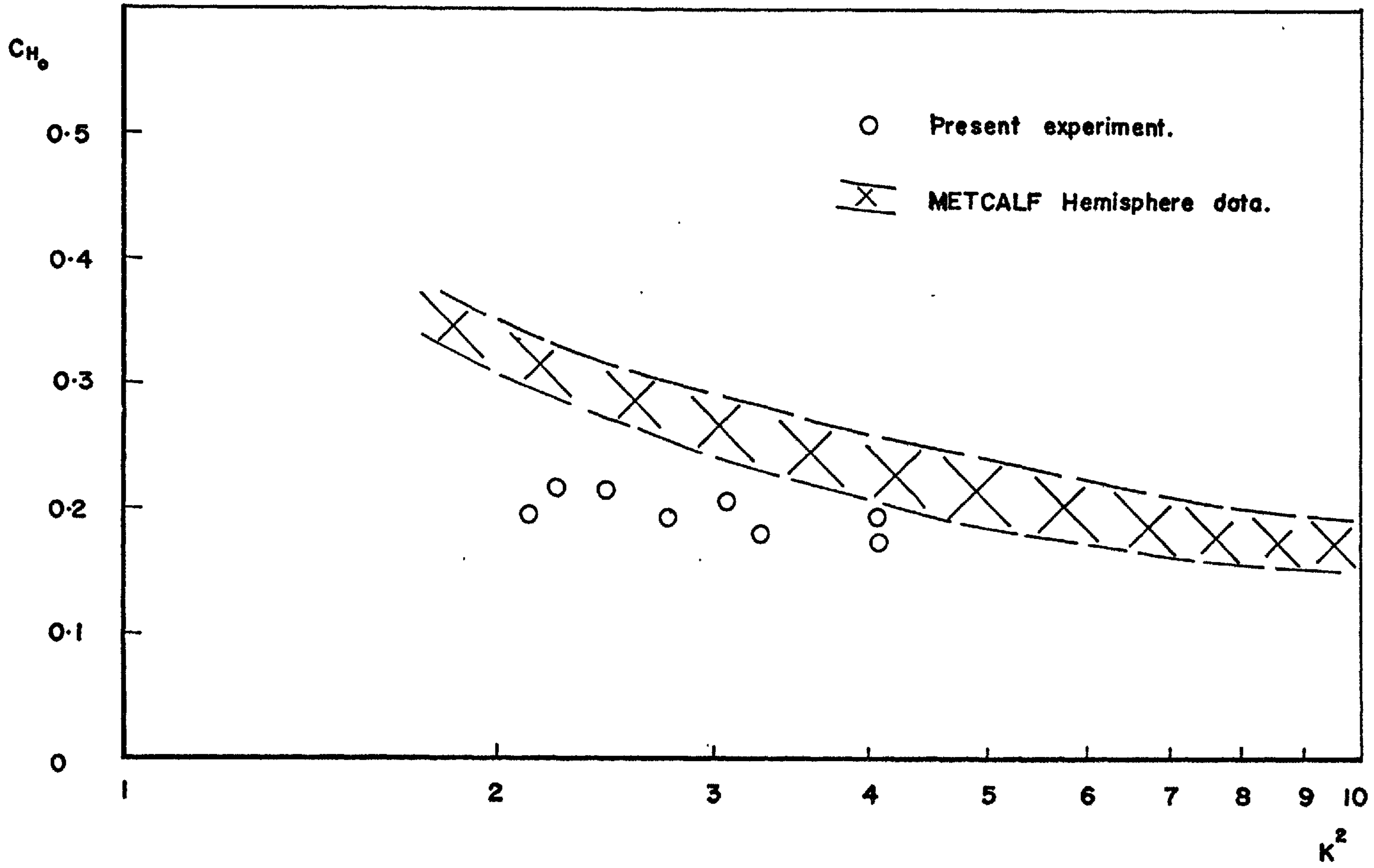

FIGURE 40 HEMISPHERE HEAT TRANSFER (stagnation point)

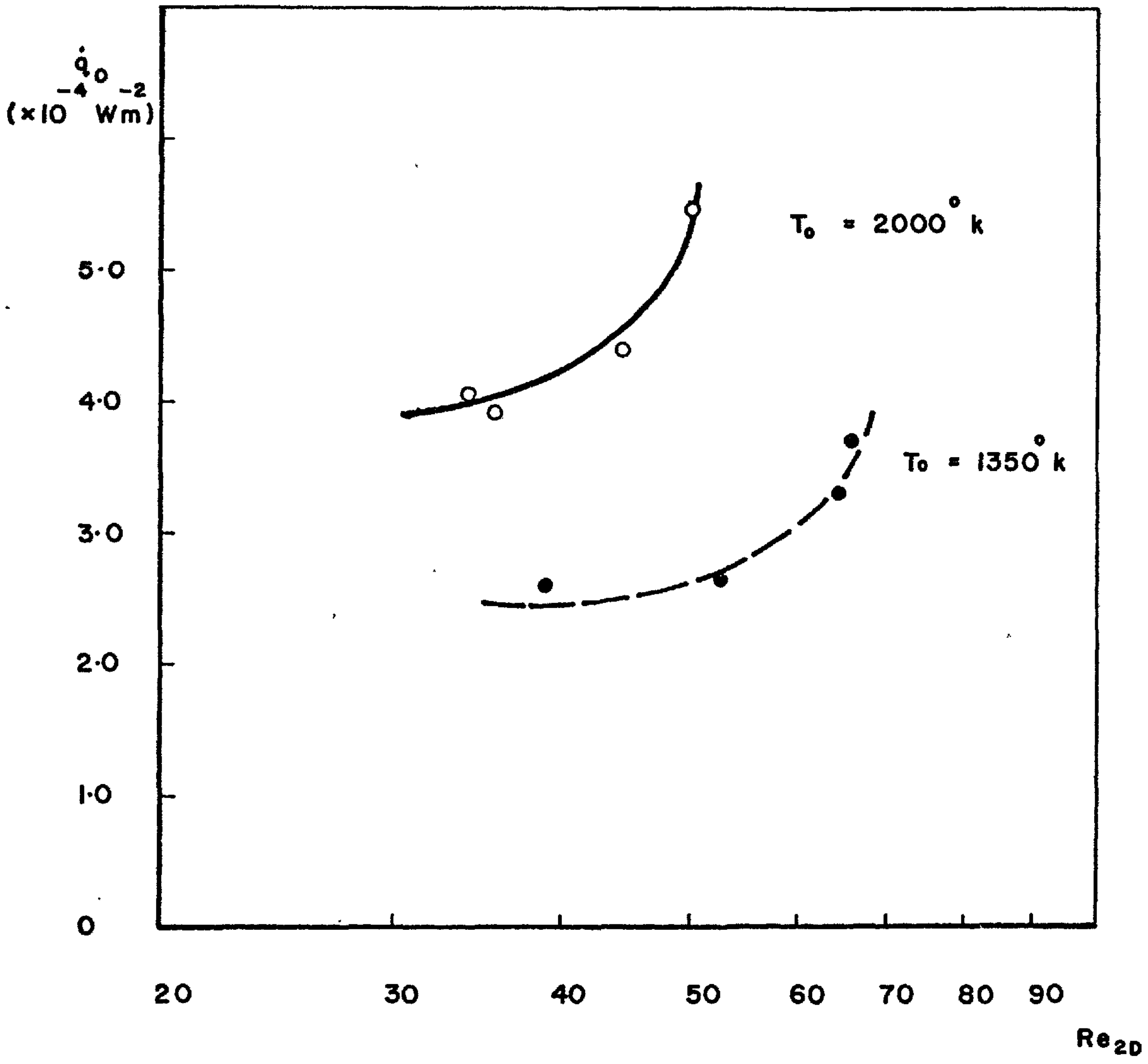

FIGURE 41 HEMISPHERE HEAT TRANSFER (stagnation point)

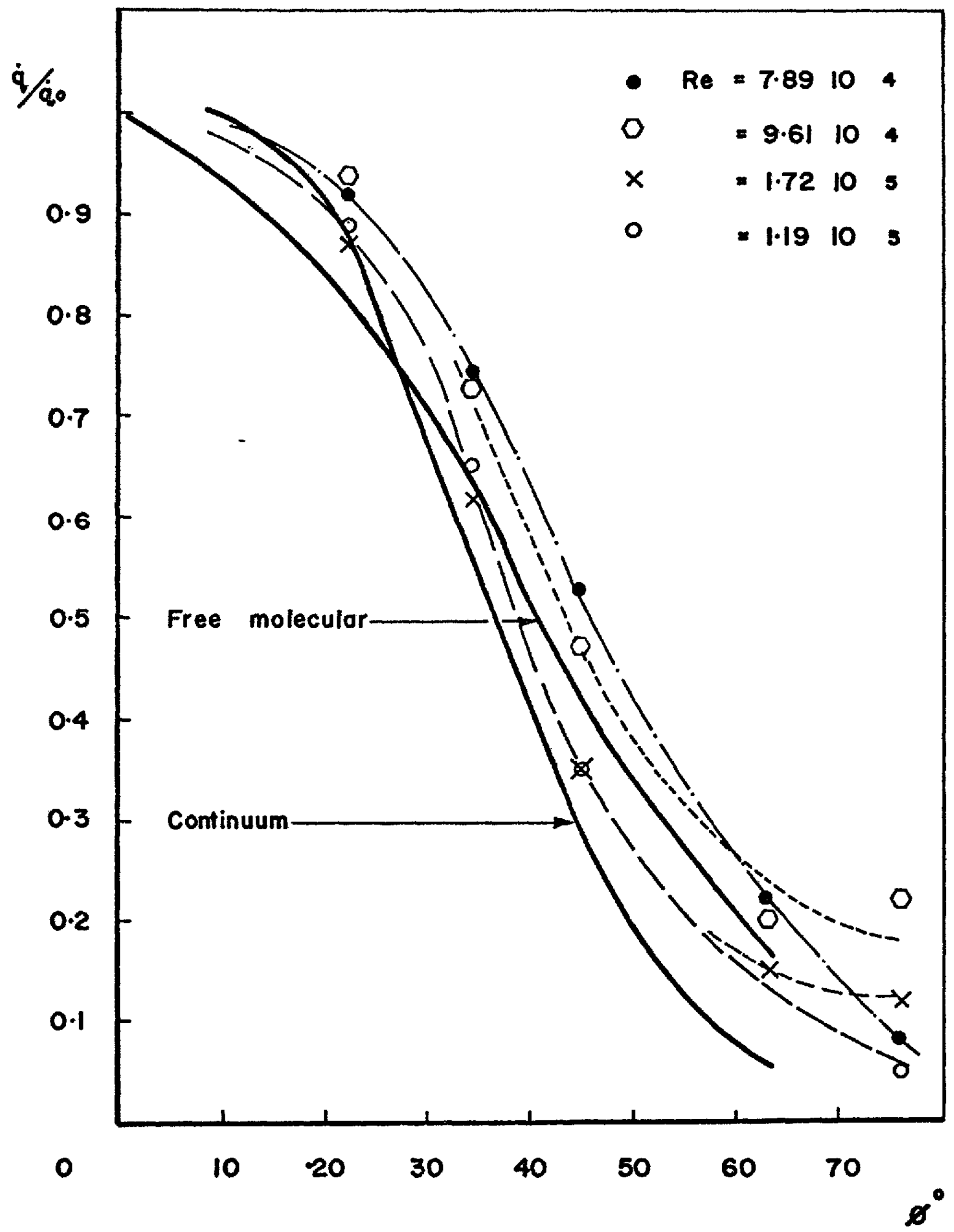

FIGURE 42 SPHERE HEAT TRANSFER DISTRIBUTION.

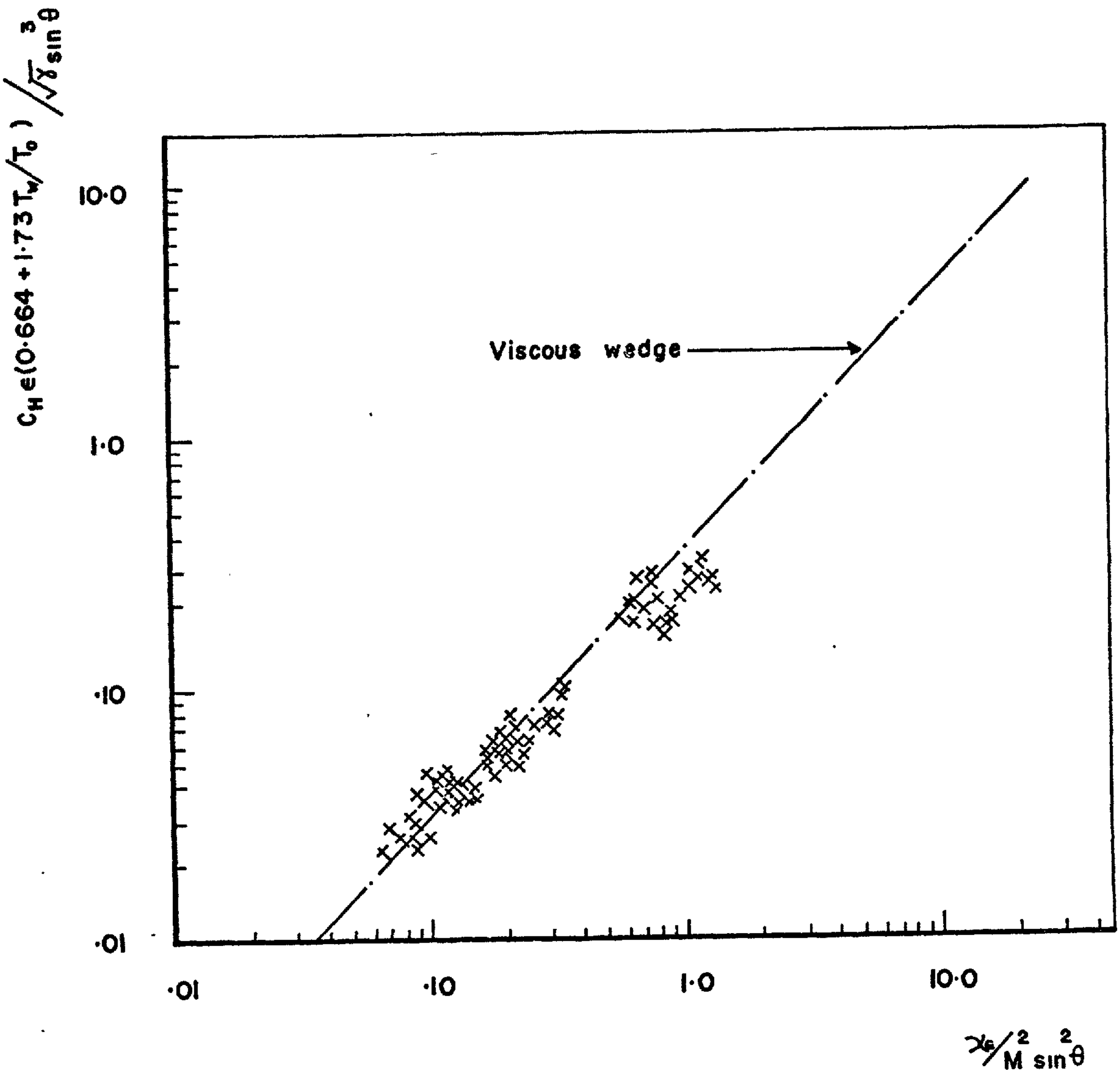

FIGURE 43 DELTA WING HEAT TRANSFER DISTRIBUTION.

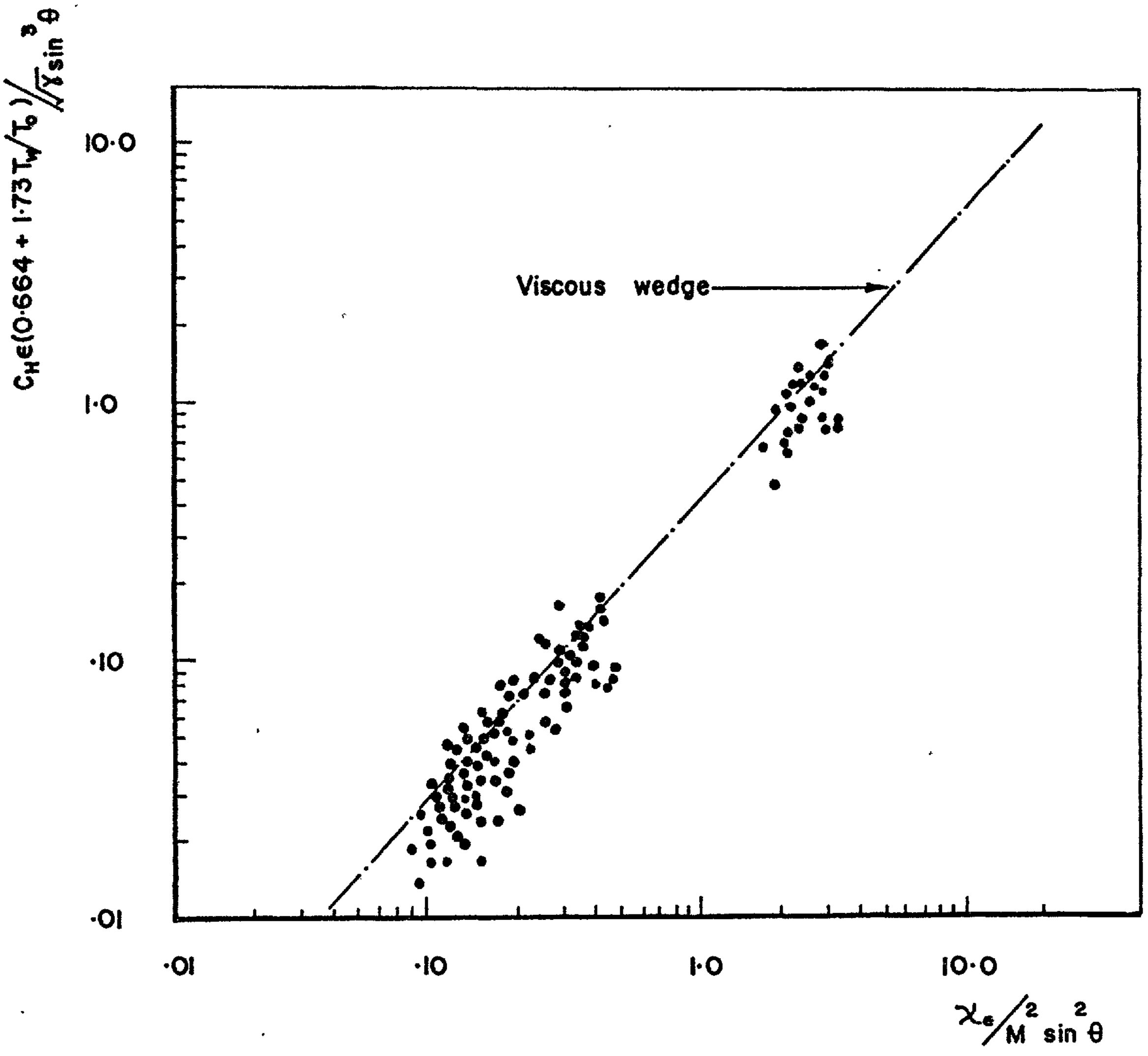

FIGURE 44 5°_{1} WAVERIDER HEAT TRANSFER DISTRIBUTION.

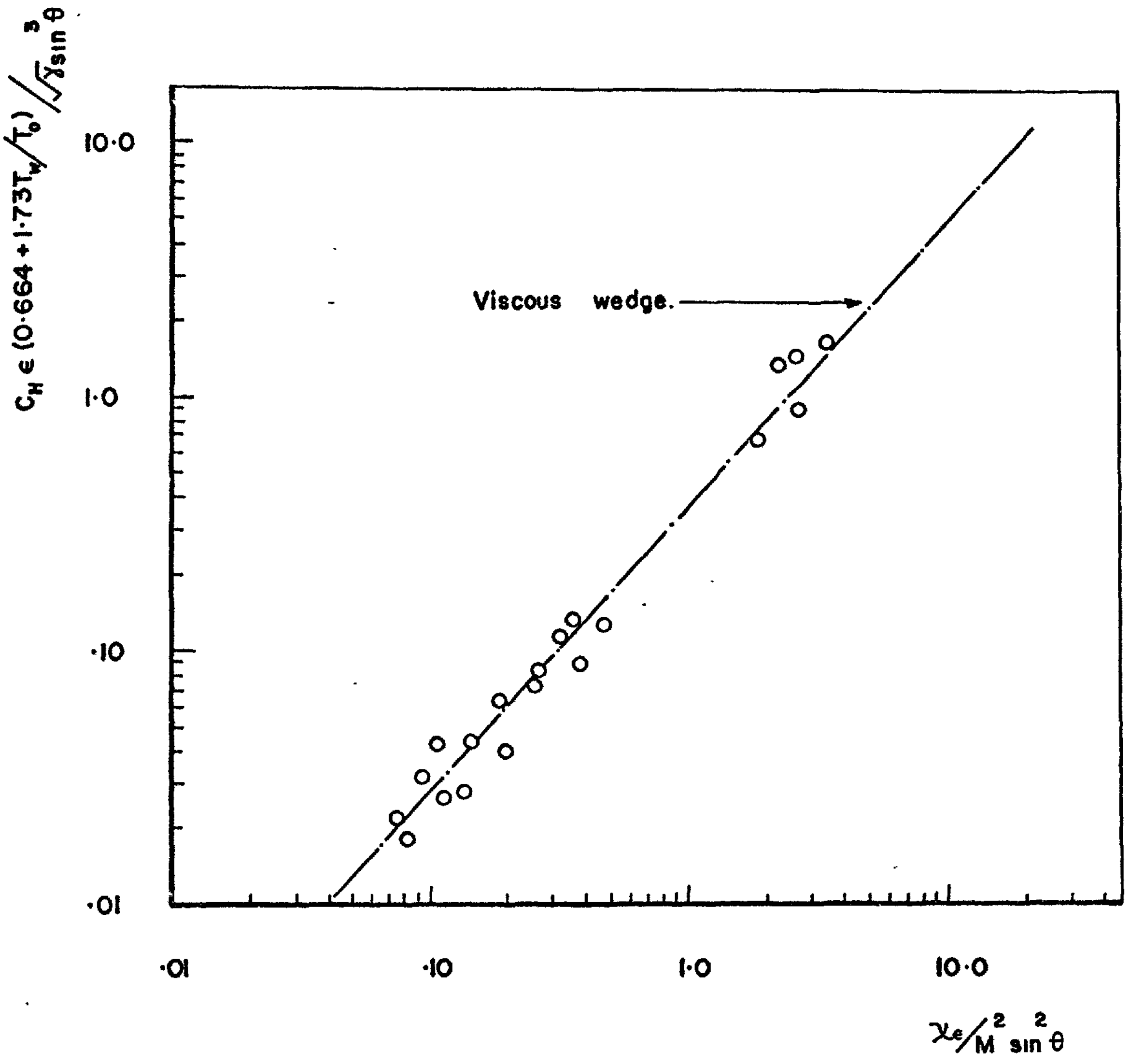

FIGURE 45 5_2° WAVERIDER HEAT TRANSFER DISTRIBUTION.

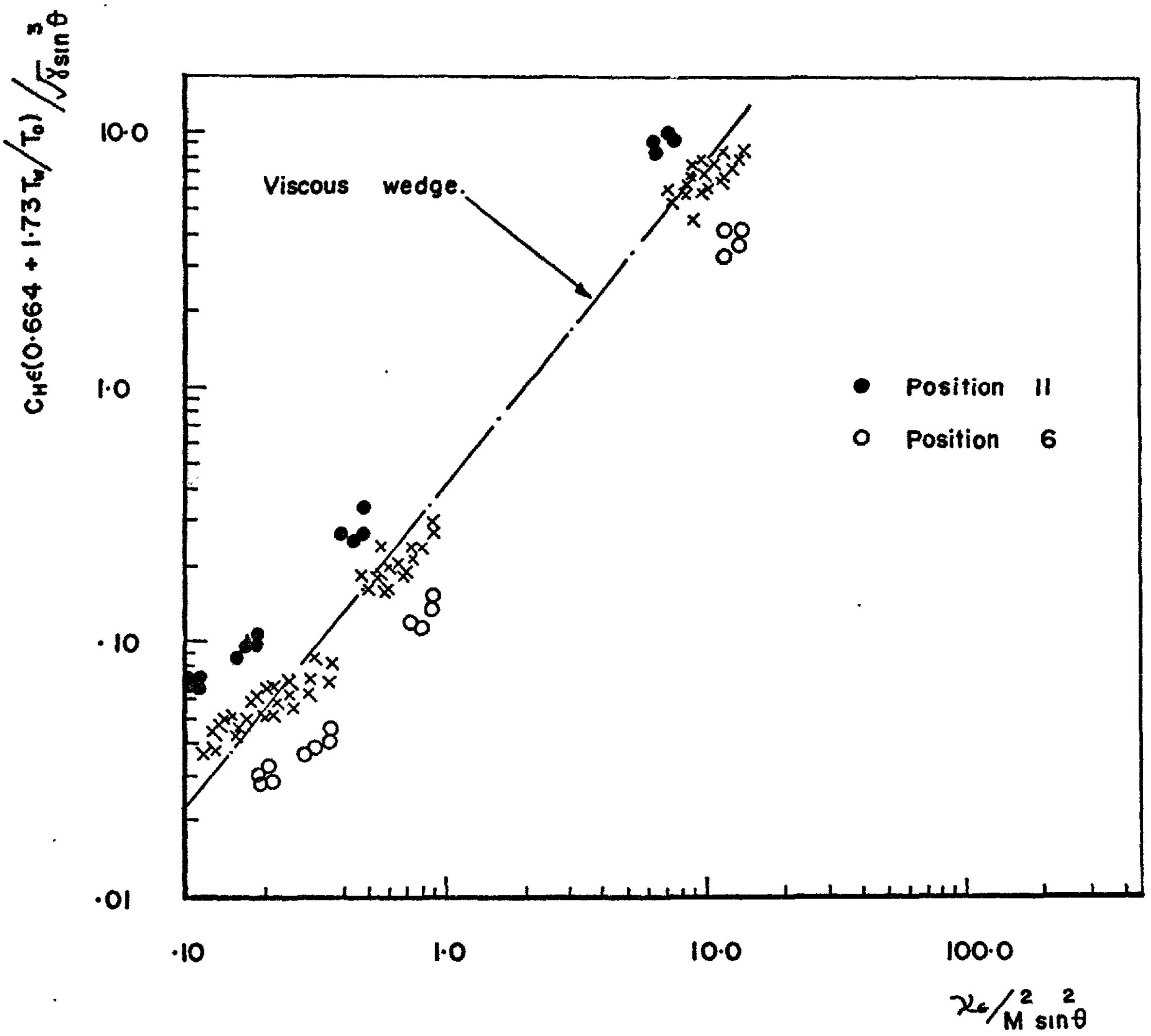

FIGURE 46 8° WAVERIDER HEAT TRANSFER DISTRIBUTION.

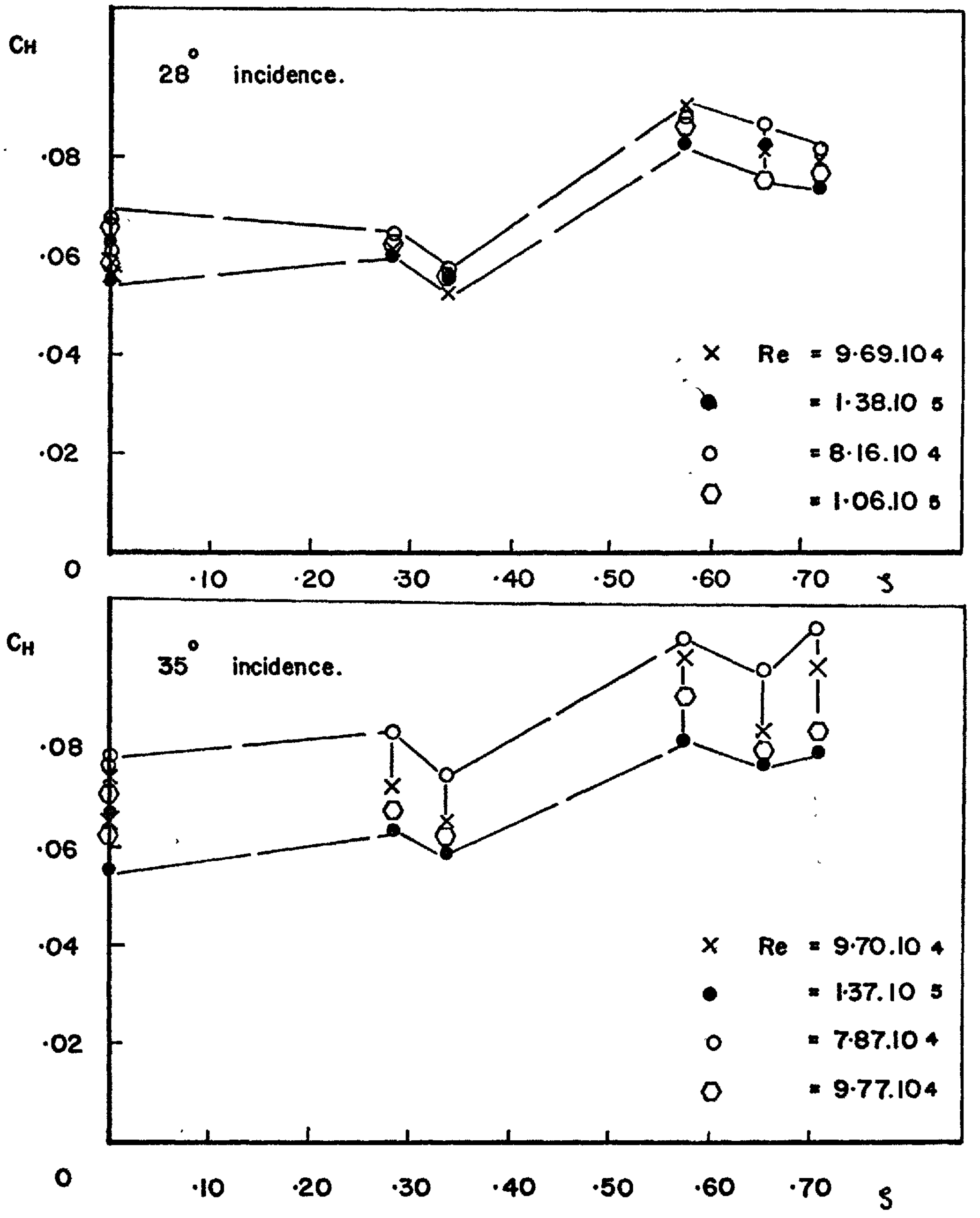

FIGURE 47 DELTA WING SPANWISE HEAT TRANSFER.

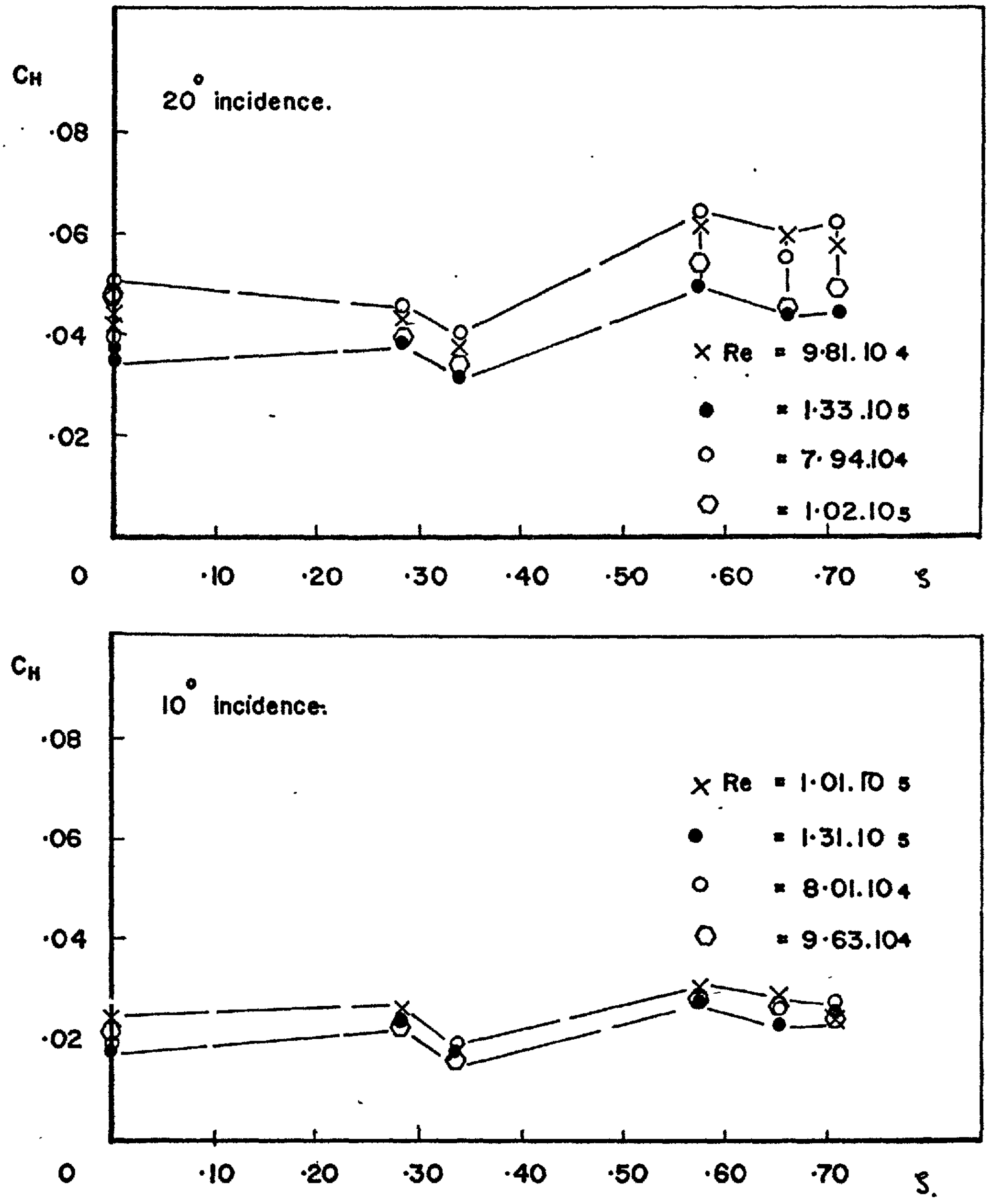

FIGURE 47 Continued.

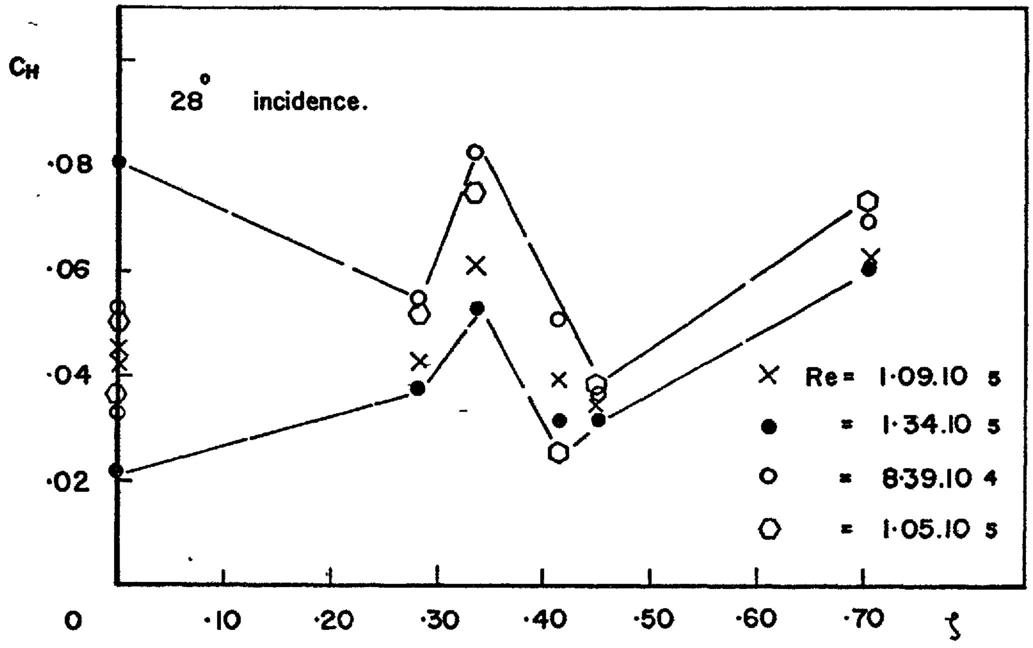

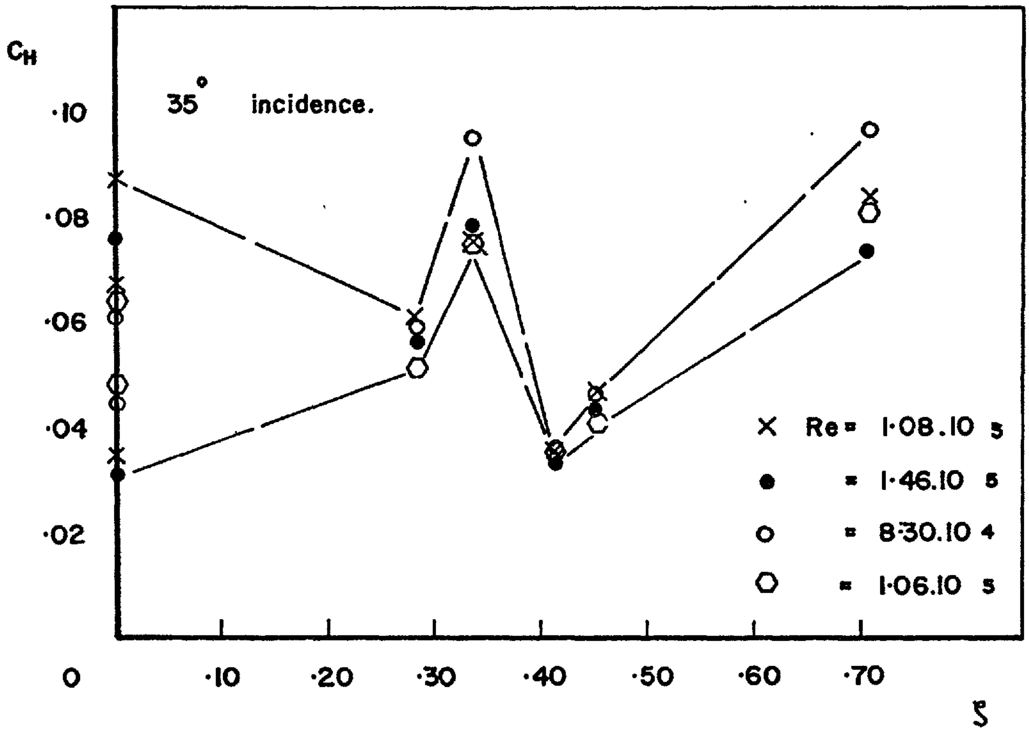

FIGURE 48 5° WAVERIDER SPANWISE HEAT TRANSFER.

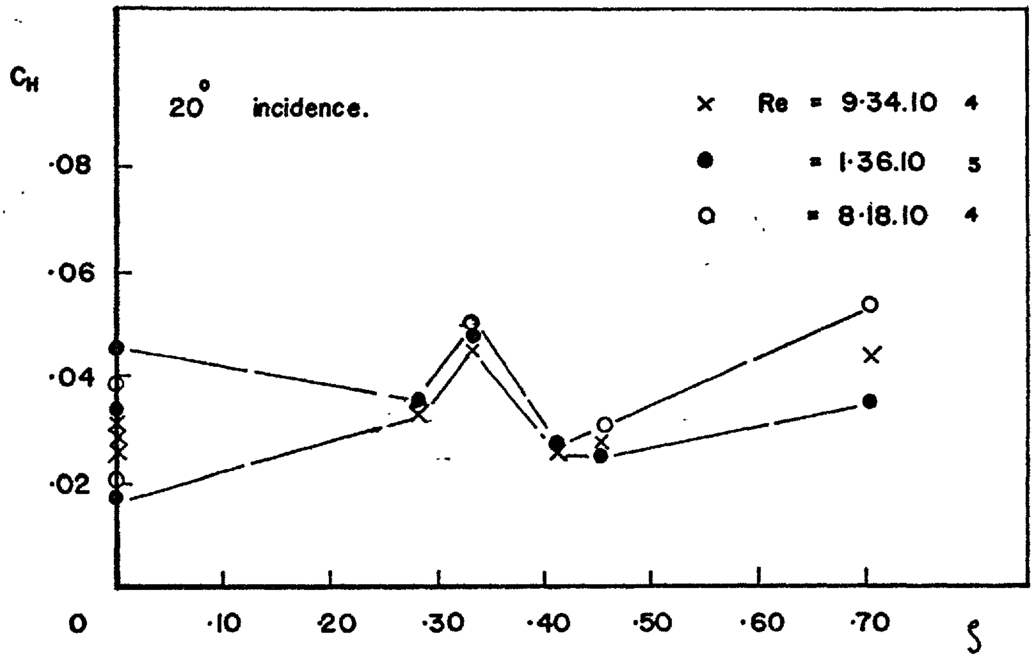

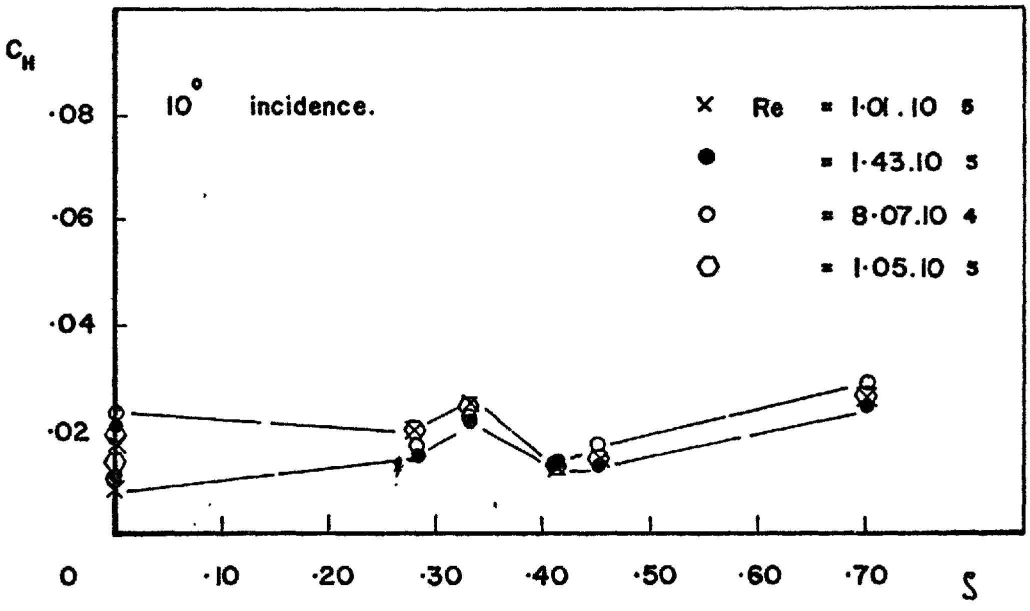

FIGURE 48 Continued.

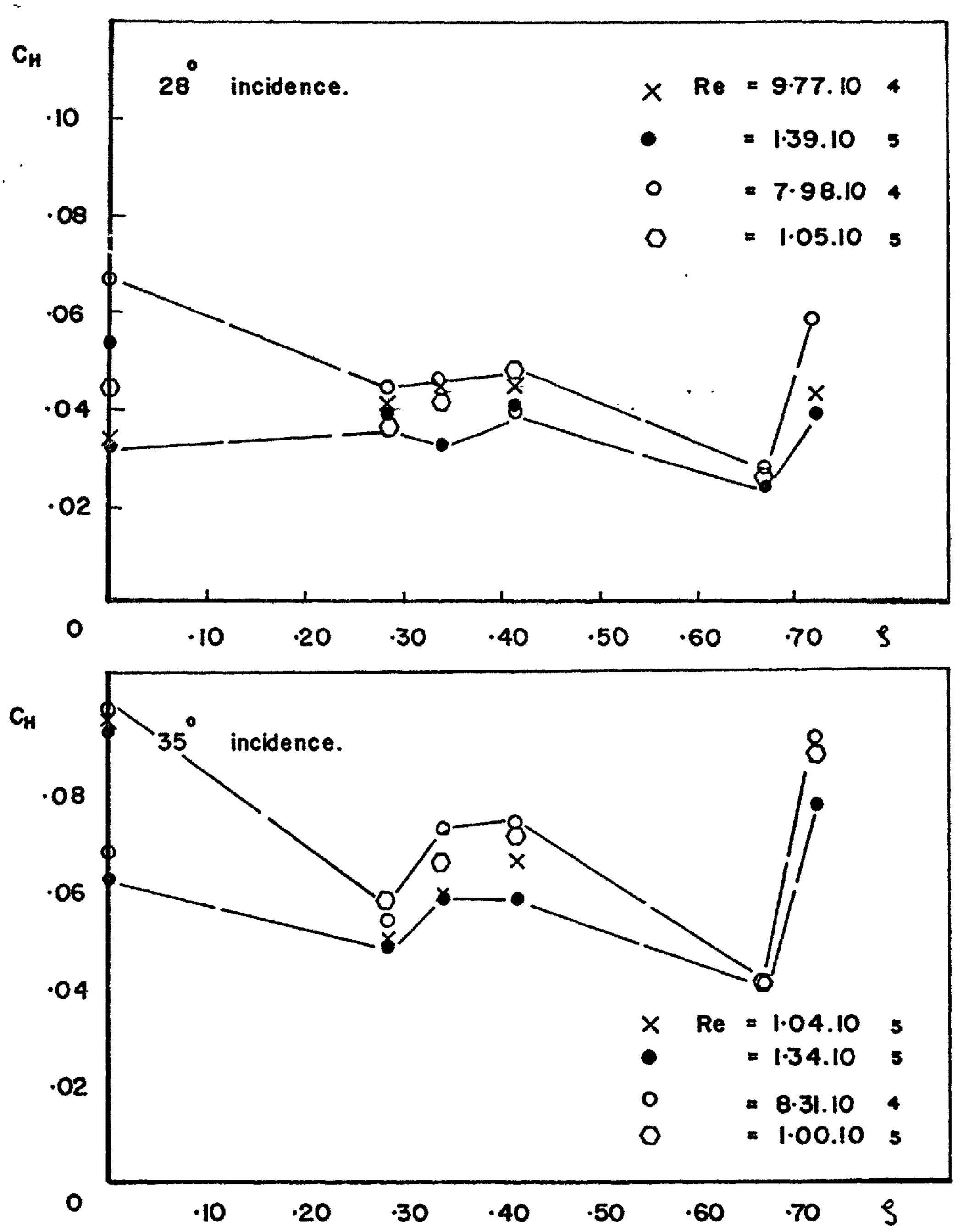

FIGURE 49 8° WAVERIDER SPANWISE HEAT TRANSFER.

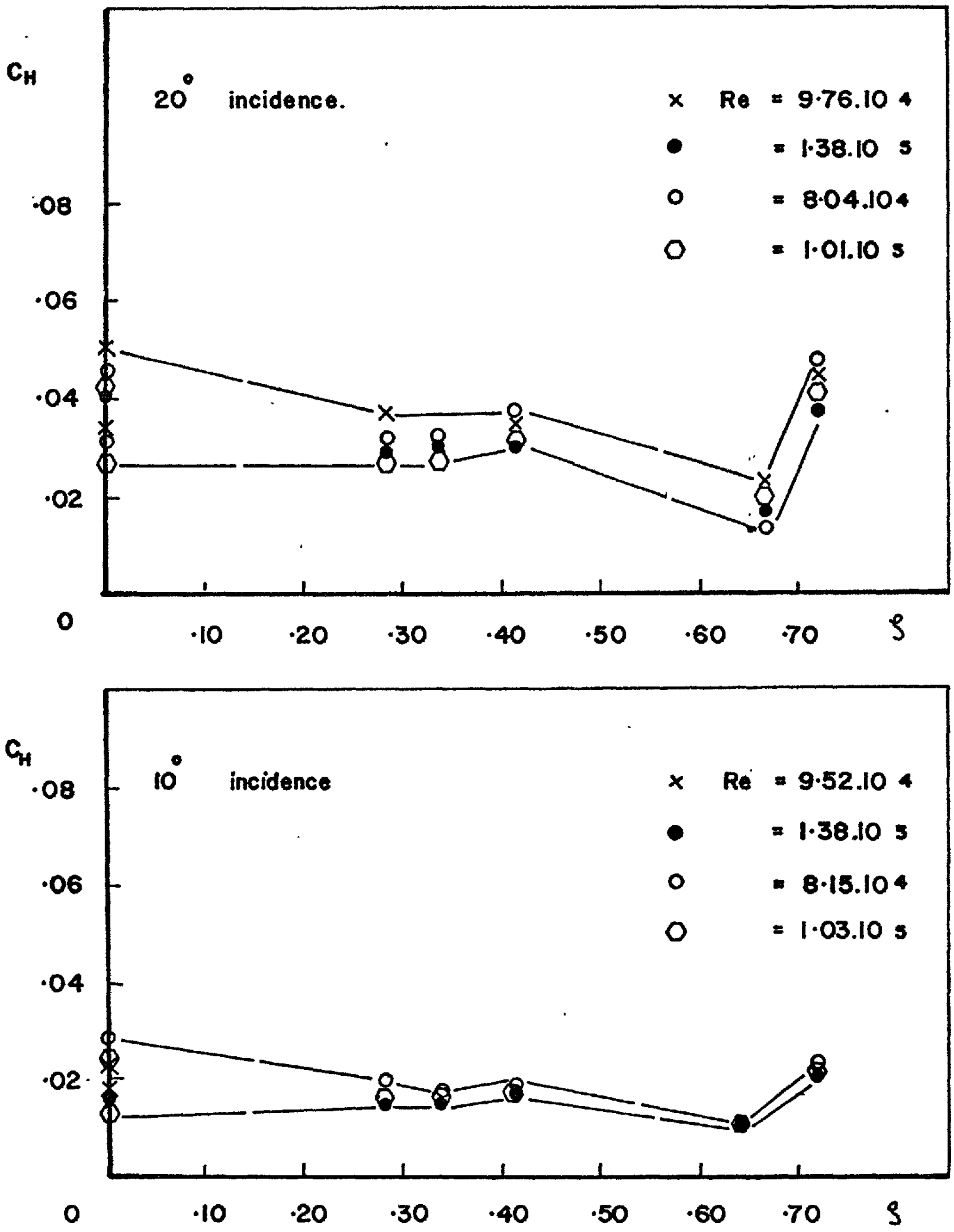

FIGURE 49 Continued.

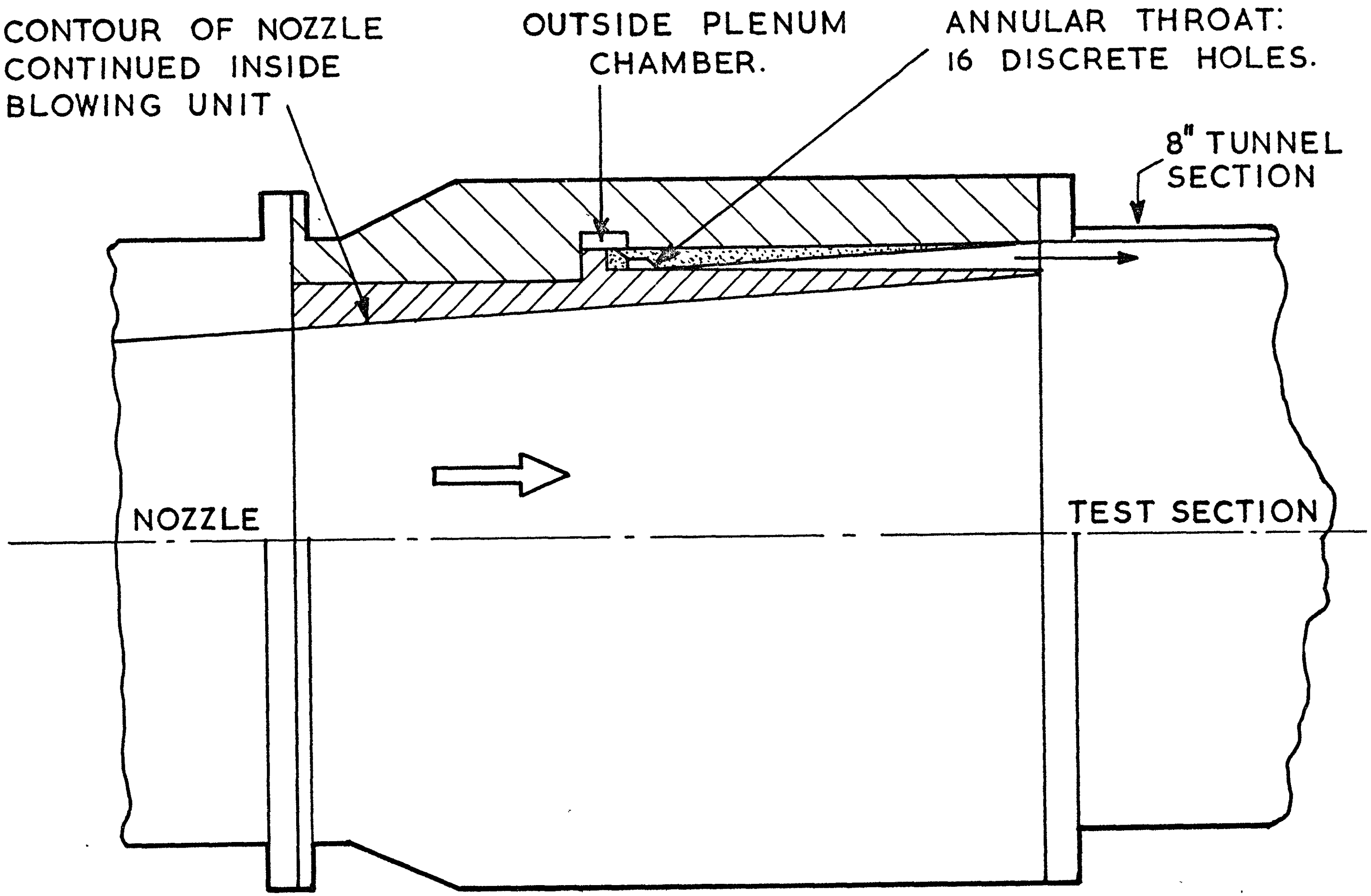

FIGURE 50 NOZZLE BLOWING UNIT (schematic)

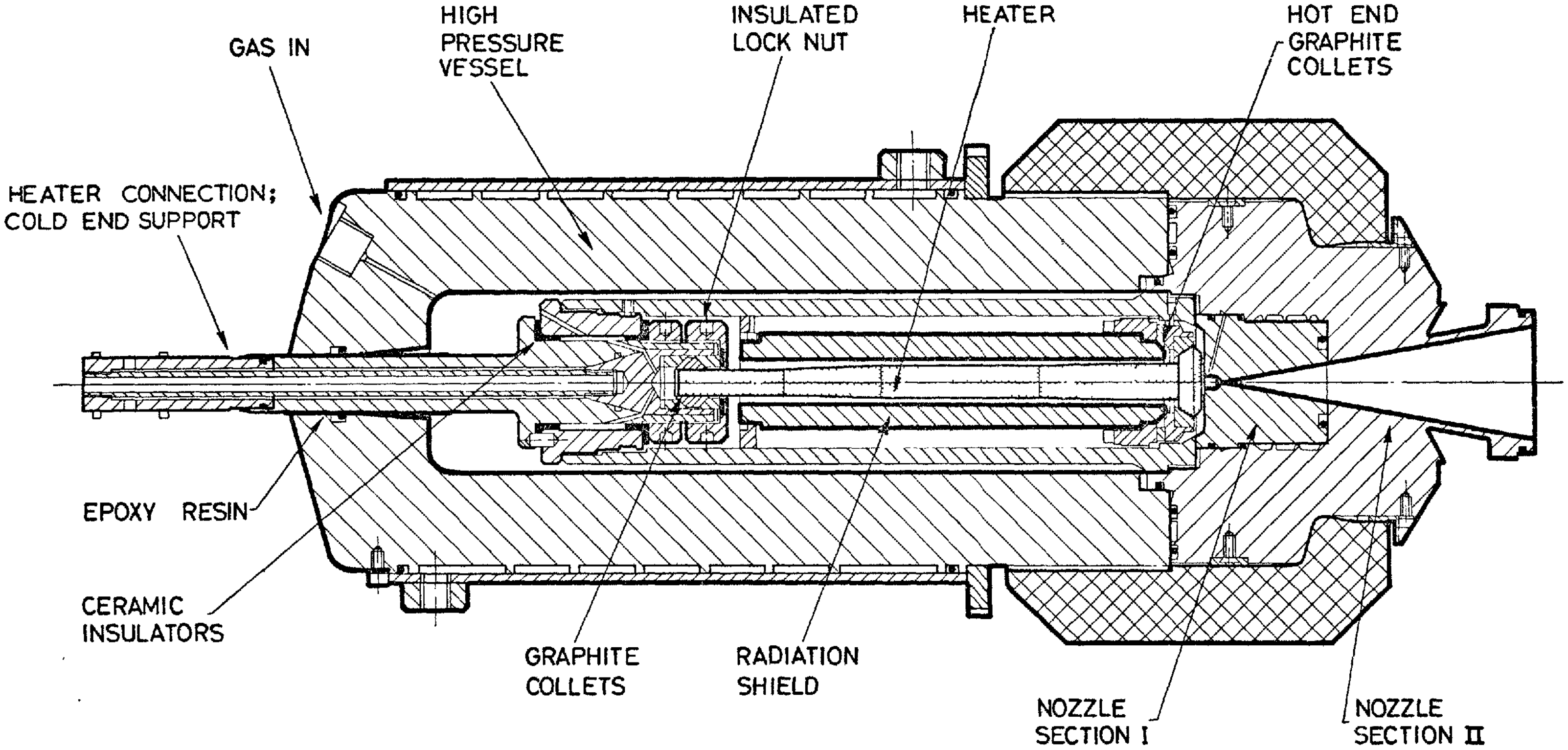

FIGURE 51 ORIGINAL NOZZLE AND HEATER ASSEMBLY.

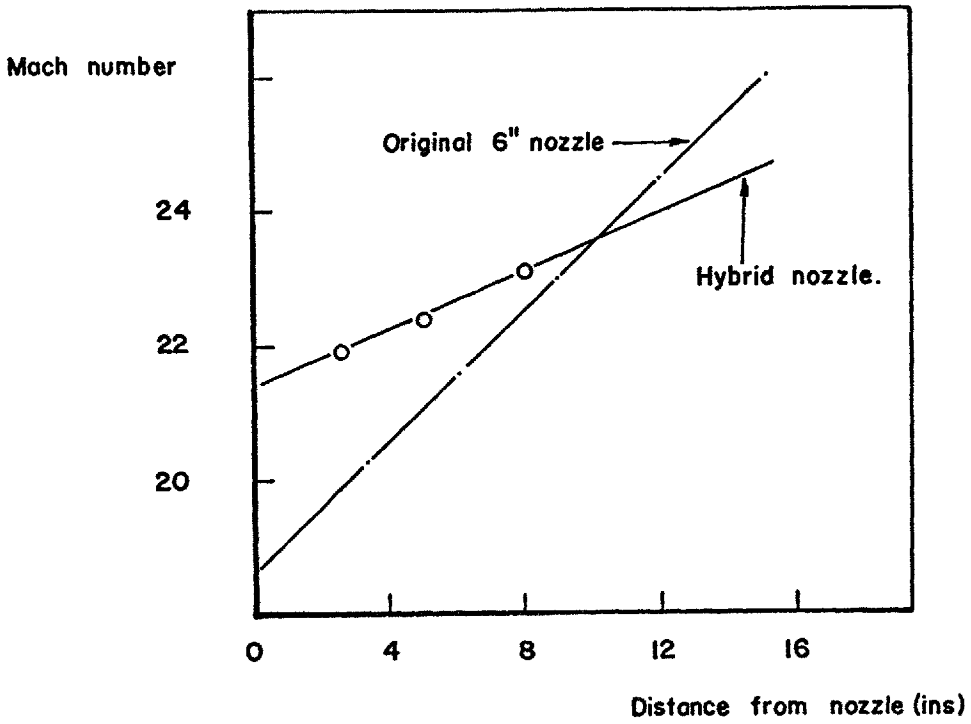

a) Mach number gradient.

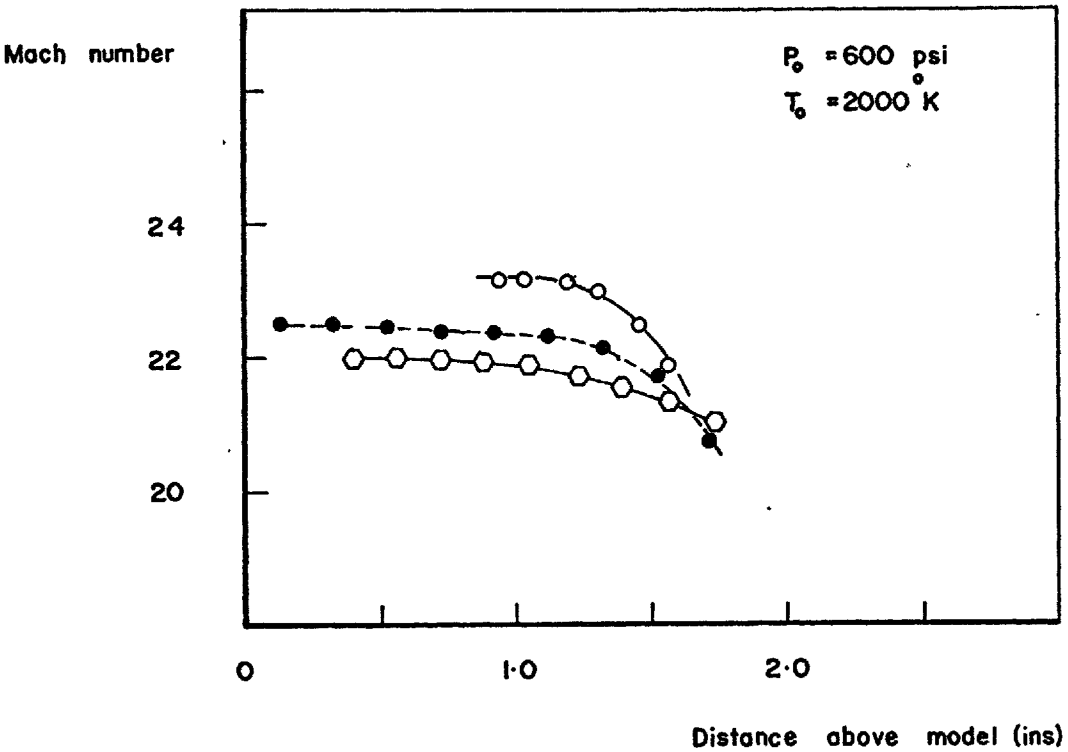

b) Test section profile.

FIGURE 52 FEATURES OF NOZZLE FLOW.

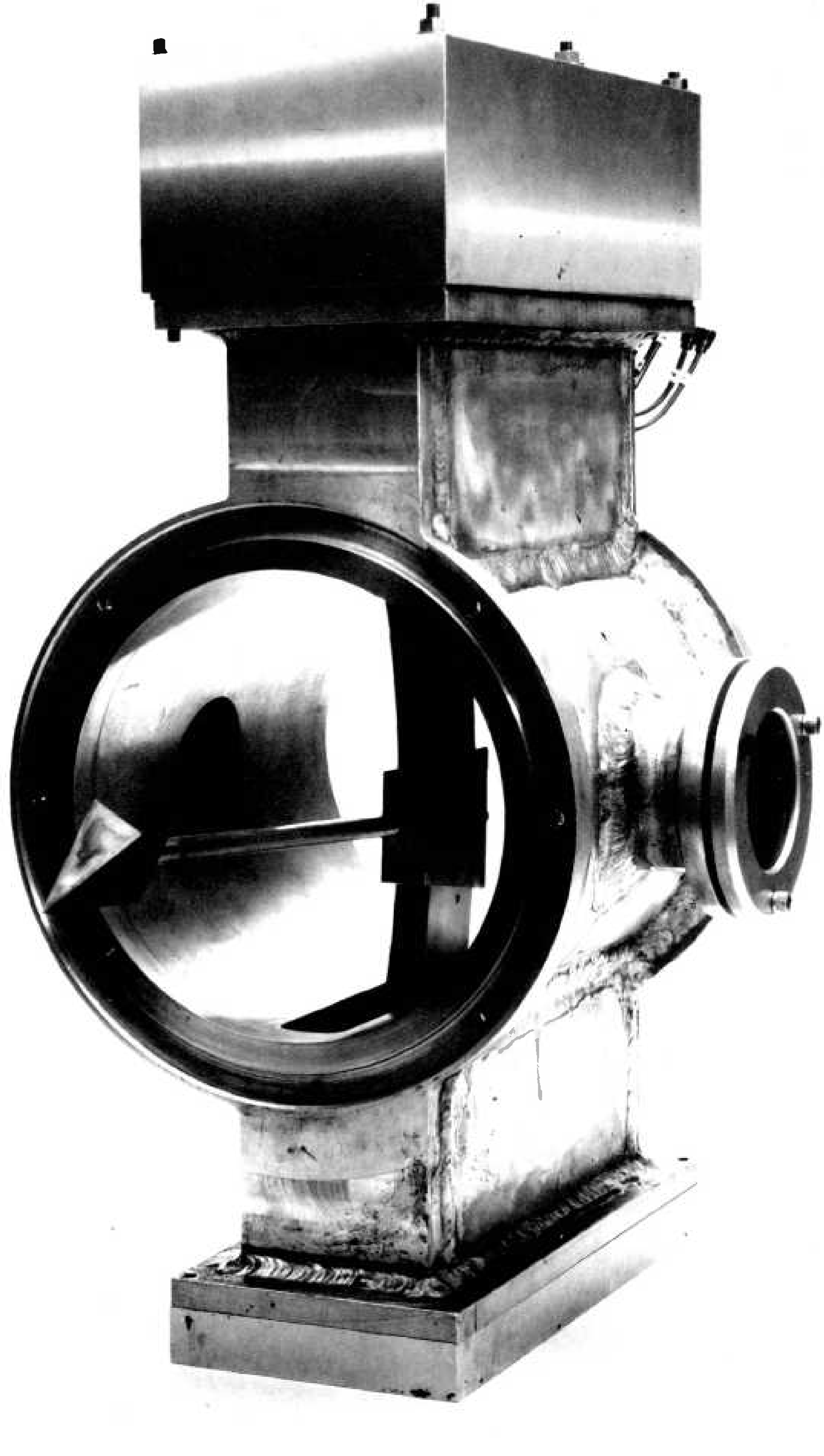

FIGURE 53 PRESSURE MODEL QUADRANT

FIGURE 54 HEAT TRANSFER INJECTION UNIT

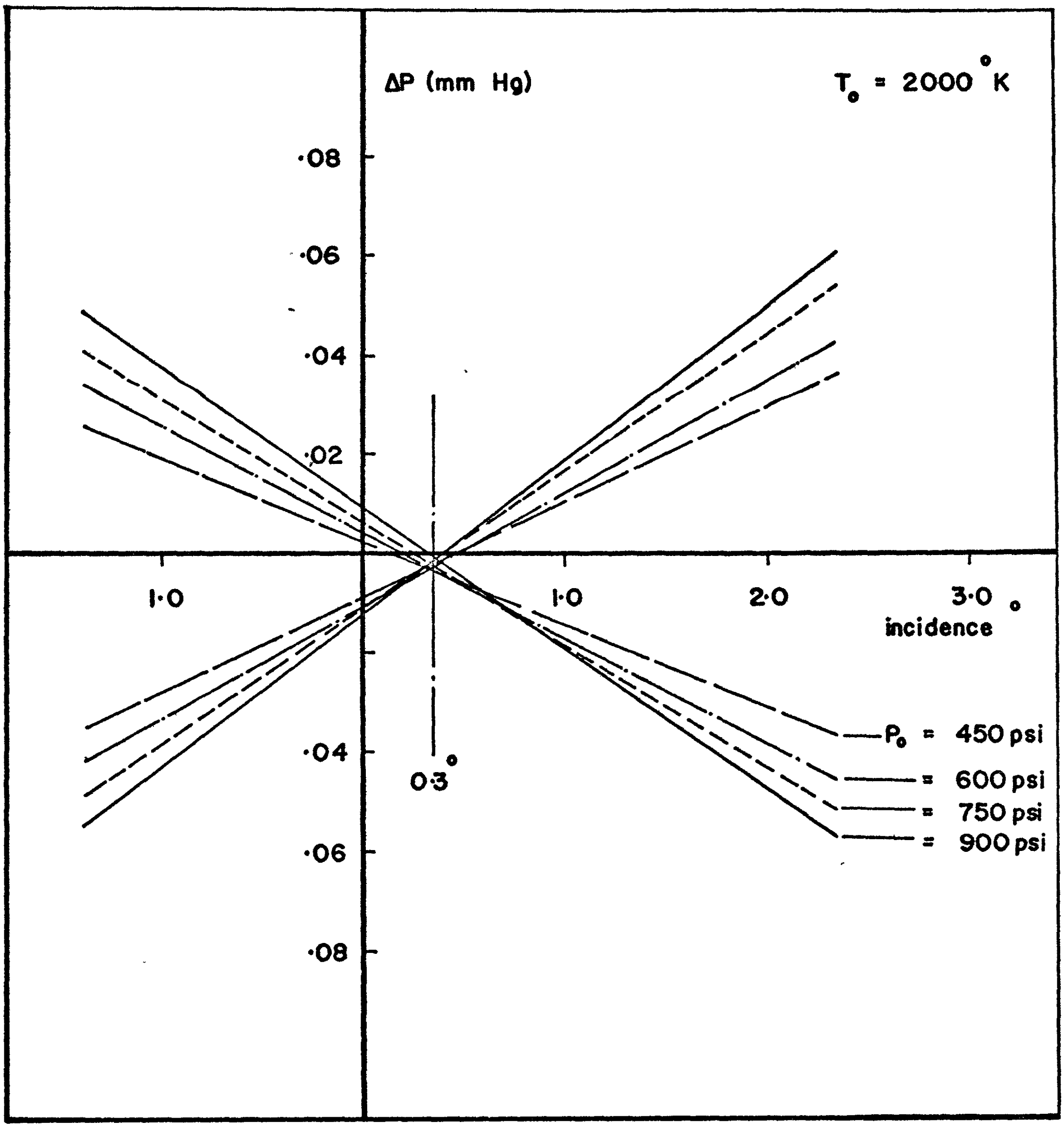

FIGURE 55 MEASURED FLOW ANGULARITY.

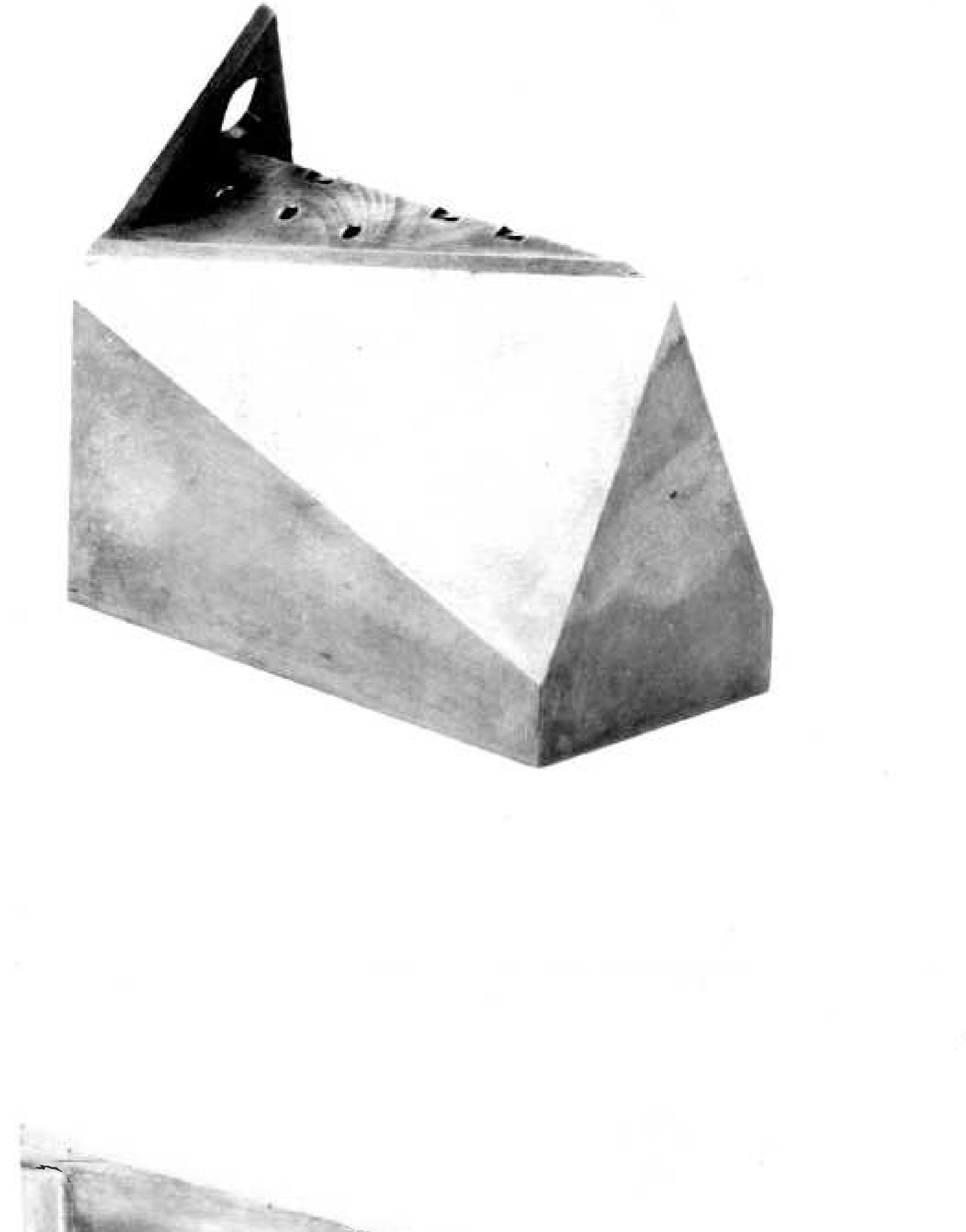

FIGURE 56 WAVERIDER PRESSURE MODEL

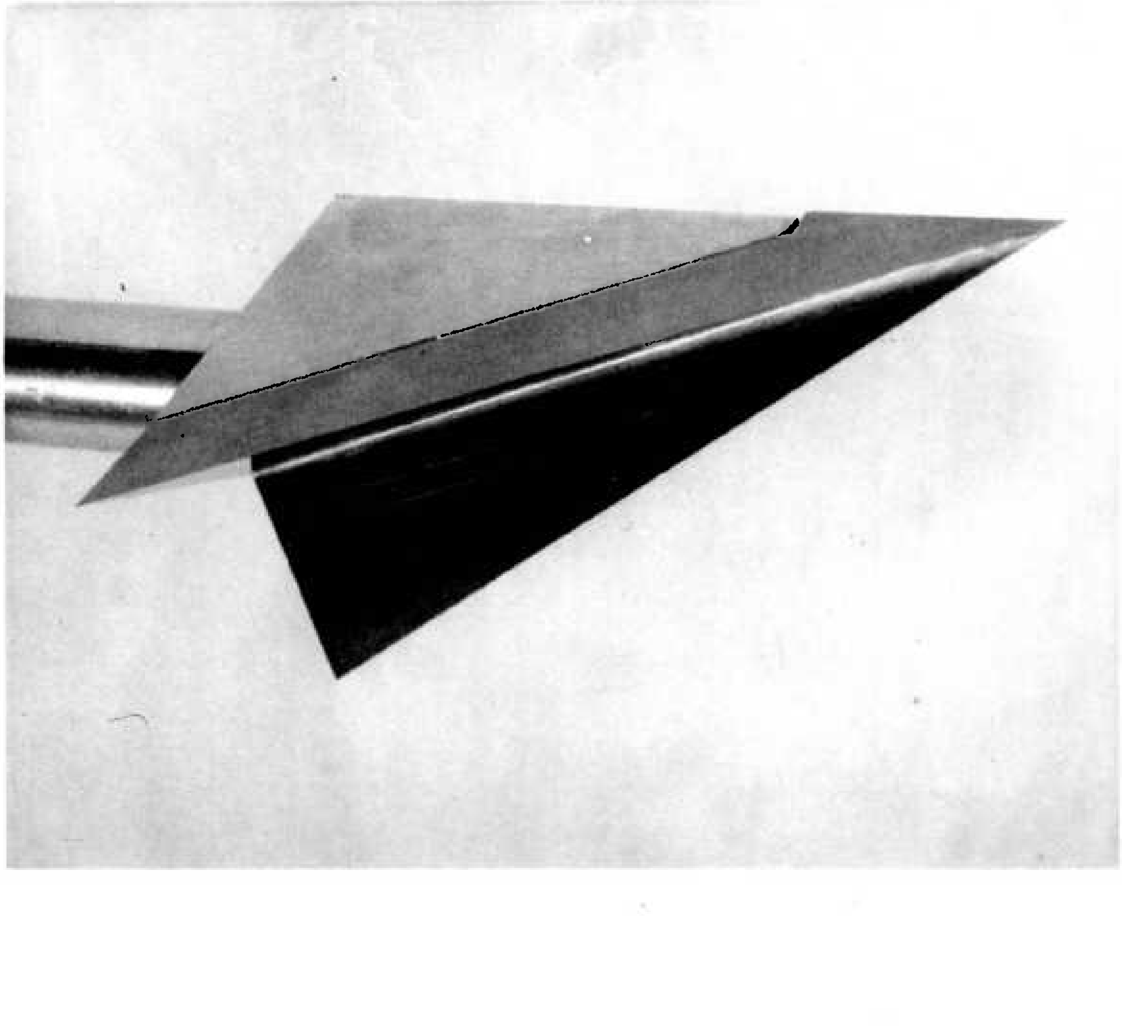

FIGURE 57 HEAT TRANSFER MODEL

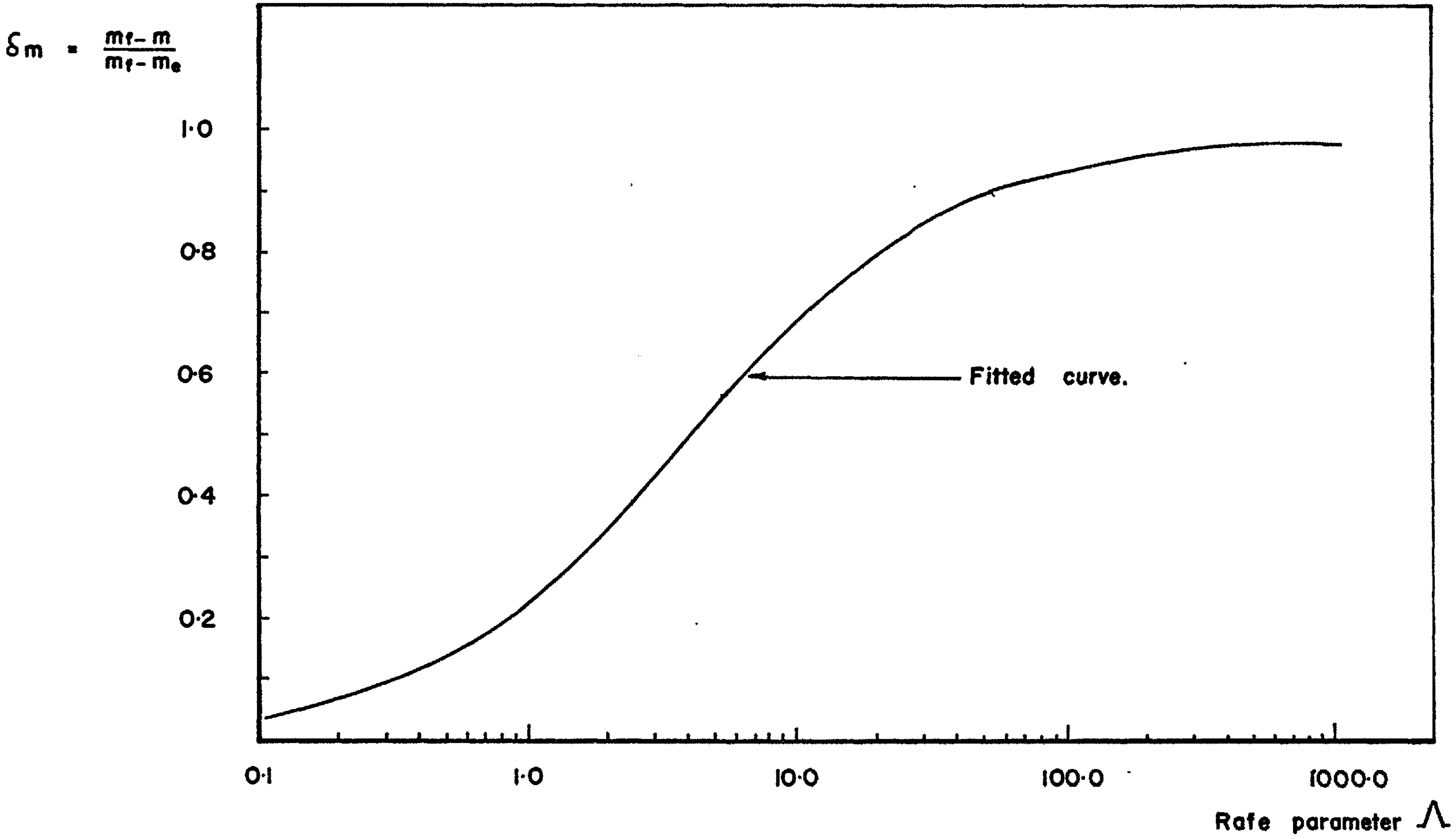

FIGURE 58 MASS FLOW WITH FINITE RATE PARAMETER.

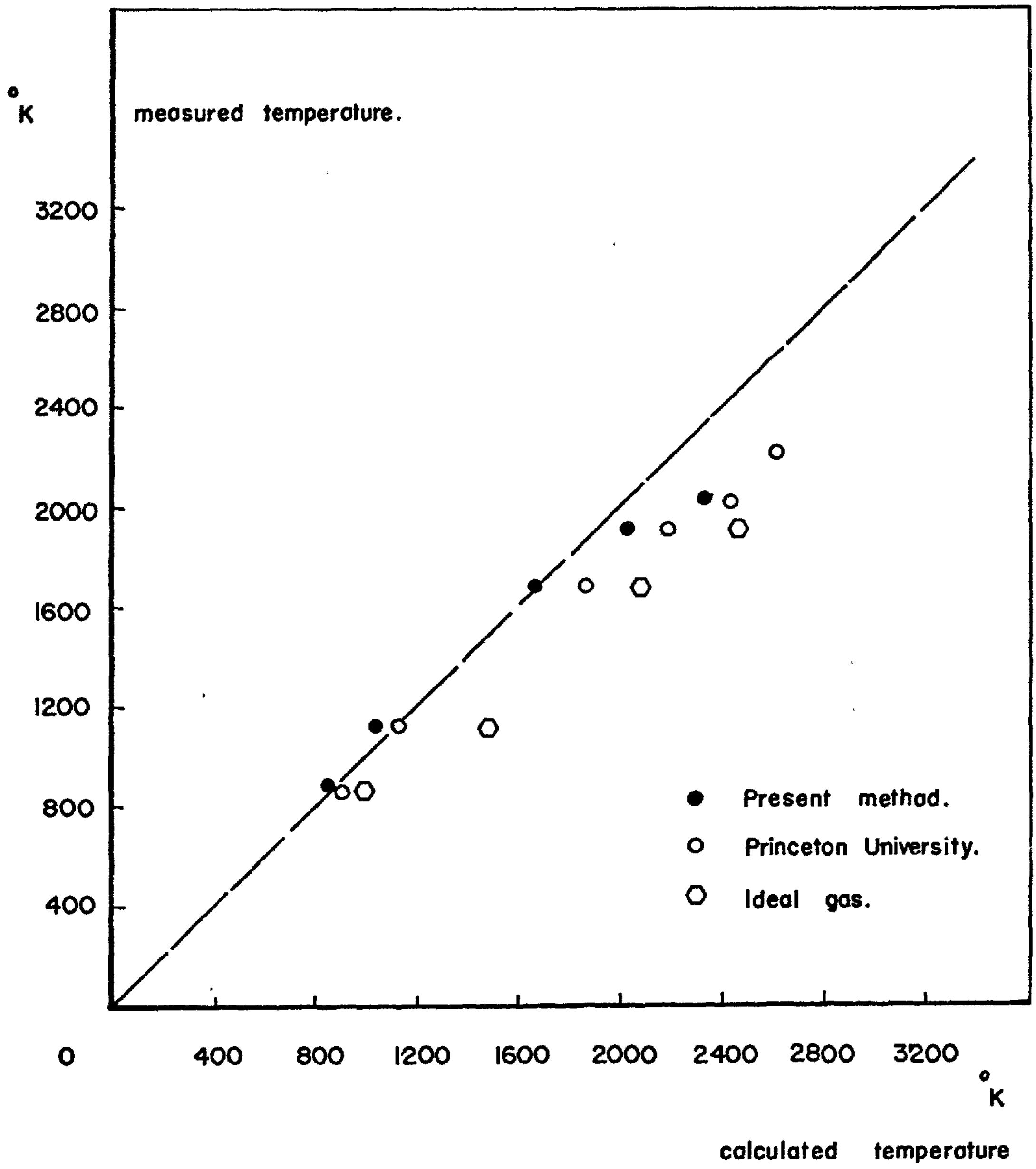

FIGURE 59 STAGNATION TEMPERATURE CALCULATION.

```
      REAL LB,LC,LD,MHOT,MCOLD,MRATIO,MRAT,MACH,MNEW,LMINF1,LMINF2,MACH2
     1,ME,MF,LAMBDA,MOLWT,NODENS
      DIMENSION LB(21),LC(21),LD(21),VIS(6),POLY(11),HOLE(18),X(18),VBM(
     118),VBMST(18),XIM(18),XIMST(18),XFB(18),XBF(18),BECKER(18),SI(18),
     2SIFM(18),PW(18)
      COMMON LB,LC,LD,SO,TO,PO,R,B,C,D,CB,DC,DD,D2B,D2C,D2D,PATM,Z,RHO,H
     1F,SF,B1,A11,A12,A21,A22,B2,TVIB,P1,FLOW,T1,S1F,H1F,Z1,VEL,NO1,NO2,
     2GAMMA,V1,V2,V3,CAL,CONST,RHO1,VIS,TDASH,ETA0,ETA1,TWALL,TO1,TO2,PI
     3,PITDIA,POLY,TGASCO,VIBCON,TVICON,FACTOR,THROAT,TAU,LAMBDA,ME,HOLE
     4,SIGMU,ALPCON,BOLTZ,MOLWT
      READ (5,100) R,TVIB,GAMMA,PI,VIBCON,TVICON
  100 FORMAT (F8.3,5X,F6.1,5X,F4.2,5X,F5.3,F8.1,F5.1)
      READ (5,101) (LB(I),LC(I),LD(I),I=1,21)
  101 FORMAT (3(E15.8,5X))
      READ (5,107) (POLY(I),I=1,11)
  107 FORMAT (E15.8)
      READ (5,102) SO,TO,PO
  102 FORMAT (F7.4,5X,F6.2,5X,F4.1)
      READ (5,108) (HOLE(I),I=1,10)
  108 FORMAT (F6.2)
      READ (5,111) (HOLE(I),I=11,18)
  111 FORMAT (F6.2)
      WRITE (6,150) (LB(I),LC(I),LD(I),I=1,21)
  150 FORMAT (1H1,19HVIRIAL POLYNOMIALS.//3(4X,E15.8))
      WRITE (6,161) (HOLE(I),I=1,18)
  161 FORMAT (1H0,26HFLAT PLATE HOLE POSITIONS./10(3X,F6.2)//20HSTEP HOL
     1E POSITIONS./8(3X,F6.2))
      READ (5,104) (VIS(I),I=1,6)
  104 FORMAT (E15.8)
      READ (5,105) ETA0,ETA1,TDASH,TO1,TO2
  105 FORMAT (E11.4,F11.4,F4.1,F4.1,F6.1)
      WRITE (6,154) (VIS(I),I=1,4)
  154 FORMAT (1H0,20HVISCOSITY CONSTANTS./1X,16HLOW TEMPERATURE./4(5X,E1
     14.7))
      WRITE (6,155) (VIS(I),I=5,6)
  155 FORMAT (1H0,17HHIGH TEMPERATURE./2(5X,E14.7))
      WRITE (6,156) ETA0,ETA1,TDASH
  156 FORMAT (1H0,10HCONSTANTS./3(5X,E10.3))
      WRITE (6,157) SO,TO,PO,R,TVIB,GAMMA
  157 FORMAT (1H0,5HSO = ,F7.4,5X,5HTO = ,F6.2,5X,5HPO = ,F4.1/1X,4HR =
     1,F8.3,5X,7HTVIB = ,F6.1,5X,8HGAMMA = ,F4.2)
      WRITE (6,160) VIBCON,TVICON
  160 FORMAT (1H0,33HVIBRATIONAL RELAXATION CONSTANTS./5X,F8.1,5X,F5.1)
      WRITE (6,153)
  153 FORMAT (1H0,18HPOLLARD CONSTANTS.)
      WRITE (6,158) (POLY(I),I=1,11)
  158 FORMAT (4X,F15.8)
      READ (5,109) SIGMU,ALPCON,BOLTZ,MOLWT
  109 FORMAT (E11.4,F6.3,E13.6,F11.4)
      ICOUNT=1
      READ (5,106) TWALL,N,PITDIA
  106 FORMAT (F5.1,I2,F5.3)
      READ (5,110) PCAL,CAL,CONST
  110 FORMAT (F6.1,F5.3,F5.2)
   10 READ (5,103)NO1,NO2,TIME,PVOLTS,MHOT,MCOLD,TGAS,TGASCO,V1,V2,V3
  103 FORMAT (I3,I2,F5.2,F6.1,F5.1,F5.1,F4.1,F4.1,F6.4,F6.4,F6.4 )
      P=PVOLTS*(1630.0/PCAL)
      WRITE (6,151) ICOUNT,NO1,NO2,TIME
  151 FORMAT (1H1,12HCASE NUMBER ,I2//1X,7HRUN NO.,I3,5X,10HDATA POINT,I
     13,5X,6HTIME  ,F5.2)
      WRITE (6,152) MCOLD,TGASCO,MHOT,TGAS,CAL,CONST,V1,V2,V3,PITDIA
  152 FORMAT (1H0,10HINPUT DATA//1X,9HM COLD = ,F5.1,7H C.P.S.,5X,18HGAS
     1 TEMPERATURE = ,F4.1,7H DEG.C.//1X,9HM HOT  = ,F5.1,7H C.P.S.,5X,1
     28HGAS TEMPERATURE = ,F4.1,7H DEG.C./60X,14HCALIBRATION = ,F5.2,9H
     3MM/VOLT.,5X,16HCAL. CONSTANT = ,F4.2,7H TORR. //60X,5HV1 = ,F7.5,5
     4X,5HV2 = ,F7.5,5X,5HV3 = ,F7.5,7H VOLTS.//60X,22HPITOT TUBE DIAMET
     5ER = ,F5.3,5H INS.///)
      MRATIO=MHOT/MCOLD
      CHECK1=V1/V2
      CHECK2=V3/V1
      CHECK3=V2/V3
      IF (CHECK1.LT.0.975.OR.CHECK1.GT.1.025) GO TO 50
      IF (CHECK2.LT.0.975.OR.CHECK2.GT.1.025) GO TO 50
      IF (CHECK3.LT.0.975.OR.CHECK3.GT.1.025) GO TO 50
      GO TO 30
   50 WRITE (6,159)
  159 FORMAT (1H0,60X,39HINACCURATE VOLTAGE DATA RUN IS IGNORED.)
      GO TO 40
   30 CALL FIRST (MRATIO,P,TGAS)
   40 ICOUNT=ICOUNT+1
      IF (ICOUNT.GT.N) GO TO 20
      GO TO 10
   20 STOP
      END
```

STAGNATION TEMPERATURE COMPUTER PROGRAM.

```
      SUBROUTINE FIRST (MRATIO,P,TGAS)
      REAL LB,LC,LD,MHOT,MCOLD,VRATIO,MRAT,MACH,MNEW,LMINF1,LMINF2,MACH2
     1,ME,MF,LAMBDA,MOLWT,NODENS
      DIMENSION LB(21),LC(21),LD(21),VIS(6),POLY(11),HOLE(19),X(18),VBM(
     119),VBMST(18),XIM(18),XIMST(18),XFB(18),XBF(18),BECKER(18),SI(18),
     2SIEM(18),PW(18),WAVANG(100)
      COMMON LB,LC,LD,SO,TO,PO,P,B,C,D,DB,DC,DD,D2B,D2C,D2D,PATM,Z,RHO,H
     1F,SF,B1,A11,A12,A21,A22,B2,TVIB,P1,FLOW,T1,S1F,H1F,Z1,VEL,NO1,NO2,
     2GAMMA,V1,V2,V3,CAL,CONST,RHO1,VIS,TDASH,ETA0,ETA1,TWALL,TO1,TO2,PI
     3,PITDIA,POLY,TGASCO,VIBCON,TVICON,FACTOR,THROAT,TAU,LAMBDA,ME,HOLE
     4,SIGMU,ALPCON,BOLTZ,MOLWT,ALPHA,DELTA
      MRATIO=(MRATIO*(TO+TGASCO)/(TO+TGAS))
      CALL MDOT (MRATIO,P)
      IF (FACTOR.GT.1.000) GO TO 910
      WRITE (6,953)
  953 FORMAT (1H0,58HNO VIBRATIONAL RELAXATION CORRECTIONS-TEMPERATURE T
     100 LOW.)
      GO TO 920
  910 WRITE (6,952) TAU,LAMBDA,ME,FACTOR
  952 FORMAT (1H0,31HVIBRATIONAL RELAXATION EFFECTS.//20X,18HRELAXATION
     1TIME = E10.3,6H SECS.,12X,23HRELAXATION PARAMETER = ,F5.2//14X,24H
     2EQUILIBRIUM MASS FLOW = ,F6.4,15X,30HMASS FLOW CORRECTION FACTOR =
     3 ,F5.3/)
  920 IF(T1.EQ.3000.0)GO TO 1972
      VOLTS=(V1+V2+V3)/3.0
      PT2=((VOLTS*CAL)+CONST)/51.71
      TEQ=(H1F*TO/3.50)
      PEQ=PO*(EXP((3.5*ALOG(TEQ/TO))+(SO-S1F)))
      IJ=1
      PITCOR=1.00
      WRITE (6,950) P1,PEQ,T1,TEQ,H1F,S1F,Z1,MRATIO,FLOW
  950 FORMAT (1H0,30HSTAGNATION CHAMBER CONDITIONS.//4X,17HTOTAL PRESSUR
     1E = ,F7.1,7H P.S.I.,4X,6HPEQ = ,F7.1,7H P.S.I.//1X,20HTOTAL TEMPER
     2ATURE = ,F6.1,7H DEG.K.,5X,6HTEQ = ,F6.1,7H DEG.K.//10X,11HENTHALP
     3Y = ,F8.4,6X,10HENTROPY = ,F8.4,5X,4HZ = ,F6.4//3X,19HMASS FLOW RA
     4TIO = ,F6.3,6X,12HMASS FLOW = ,F6.3,9H LBM/HR.///)
  980 RATIO=PT2/(PEQ*PITCOR)
      CALL PITOT (RATIO,MACH)
      III=1
      TINFIN=TEQ/(1.0+(((GAMMA-1.0)/2.0)*(MACH**2)))
      PINFIN = PEQ/((1.0+(((GAMMA-1.0)/2.0)*(MACH**2)))**(GAMMA/(GAMMA-1
     1.0)))
      RHOINF=(PEQ/(R*TEQ))/((1.0+(((GAMMA-1.0)/2.0)*(MACH**2)))**(1.0/(G
     1AMMA-1.0)))
      RHOINF=RHOINF*144.0
 1995 UINF=(MACH*(SQRT(R*GAMMA*TINFIN)))
      IF (TINFIN.LT.120.0) GO TO 1962
      F24=VIS(5)*((TINFIN/TDASH)**VIS(6))
      ETAINF=ETA1*F24/F23
      GO TO 1963
 1962 F11=(VIS(1)+(VIS(2)*(TINFIN/TDASH))+(VIS(3)*((TINFIN/TDASH)**2))+(
     1VIS(4)*((TINFIN/TDASH)**3)))
      F12=(VIS(1)+(VIS(2)*(TO1/TDASH))+(VIS(3)*((TO1/TDASH)**2))+(VIS(4)
     1*((TO1/TDASH)**3)))
      ETAINF=(ETA0*F11/F12)
 1963 RE=(RHOINF*UINF)/ETAINF
      IF (III.NE.1) GO TO 990
      RHO2=RHOINF*((1.0+GAMMA)*(MACH**2))/(2.0+((GAMMA-1.0)*(MACH**2)))
      RHORAT=SQRT(RHO2/RHOINF)
      T2=(TINFIN*(1.0+(((GAMMA-1.0)/2.0)*(MACH**2)))*(((2.0*GAMMA*(MACH*
     1*2))/(GAMMA-1.0))-1.0))/((((GAMMA+1.0)**2)*(MACH**2))/(2.0*(GAMMA-
     21.0)))
      MACH2=SQRT(((2.0/(GAMMA-1.0))+(MACH**2))/(((2.0*GAMMA*(MACH**2))/(
     1GAMMA-1.0))-1.0))
      U2=(MACH2*SQRT(GAMMA*R*T2))
      F24=VIS(5)*((T2/TDASH)**VIS(6))
      F25=VIS(5)*((TO2/TDASH)**VIS(6))
      ETA2=ETA1*F24/F25
      RE2=(RHO2*U2*(PITDIA/12.0))/ETA2
      RE2PIT=(RE2*RHORAT)
      IF (RE2PIT.GT.10.0.AND.RE2PIT.LT.1000.0) GO TO 935
      WRITE (6,962) RE2PIT
  962 FORMAT (1H0,60X,59HWARNING.PITOT TUBE CORRECTION OUT OF RANGE.RE 2
     1*(RHO)1/2 = ,F6.1)
  935 PITCOR=POLY(1)
      DO 945 I=2,11
  945 PITCOR = PITCOR+POLY(I)*RE2PIT**(I-1)
      IF (IJ.EQ.2) GO TO 970
      IJ=2
      OLDMAC=MACH
      GO TO 980
  970 IF (ABS(MACH-OLDMAC).LT.0.1) GO TO 990
```

```
      OLDMAC=MACH
      GO TO 980
  990 TSTAR=((1.0+(3.0*TWALL/T1))/6.0)*T1
      F21=VIS(5)*((TWALL/TDASH)**VIS(6))
      F22=VIS(5)*((TSTAR/TDASH)**VIS(6))
      F23=VIS(5)*((TO2/TDASH)**VIS(6))
      PINFMI=PINFIN*51.71*1000.0
      ETAWAL=ETA1*F21/F23
      ETASTA=ETA1*F22/F23
      CINFIN=((ETAWAL/ETAINF)*(TINFIN/TWALL))
      CSTAR=((ETASTA/ETAINF)*(TINFIN/TSTAR))
      REM=RE*3.0/0.914399
      VBAR=(MACH*SQRT(CINFIN/REM))
      VSTAR=(MACH*SQRT(CSTAR/REM))
      XIBAR=(VBAR*(MACH**2))
      XISTAR=(VSTAR*(MACH**2))
      PINFIN=PINFIN*144.0
      LMINF1=((ETAINF/PINFIN)*SQRT(PI*R*TINFIN/2.0))
      LMINF2=((16.0*ETAINF*SQRT(R*TINFIN))/(5.0*PINFIN*SQRT(2.0*PI)))
      LMINF1=LMINF1*12.0*25.4
      LMINF2=LMINF2*12.0*25.4
      RHOM=RHOINF/RHO1
      IF (TINFIN.LT.120.0) GO TO 1964
      VISCOS=ETAINF/ETA1
      GO TO 1965
 1964 VISCOS=ETAINF/ETA0
 1965 UINFME=UINF*0.914399/3.0
      PT2=PT2/PITCOR
      PT2MET=PT2*51.71
      CB=(SQRT(2.0*BOLTZ*TWALL/MOLWT))/100.0
      RELVEL=SQRT((UINFME**2)+(CB**2))*100.0
      CSAREA=SIGMU*(RELVEL**(-4.0/ALPCON))
      PWFM=PINFMI*((1.0+SQRT(TWALL/TINFIN))/2.0)
      NODENS=((RHOINF*0.016018369)/MOLWT)*32.2
      NODENS=NODENS*SQRT(TINFIN/TWALL)
      RE2=(RE2*12.0/PITDIA)*(3.0/0.914399)
      CHENG=((GAMMA-1.0)/(4.0*GAMMA))*(((T2+TWALL)/(2.0*TEQ))**0.25)*RE2
      FREEFB=(UINFME*1000.0)/(NODENS*RELVEL*CSAREA)
      FREEBF=(CB*1000.0)/(NODENS*RELVEL*CSAREA)
      FREEBF=FREEBF*SQRT(TINFIN/TWALL)
      WRITE (6,951) PT2MET,MACH,PINFMI,TINFIN,RHOM,VISCOS,UINFME,REM,PIT
     1COR,VBAR,VSTAR,XIBAR,XISTAR,TWALL,TSTAR,CINFIN,LMINF1,CSTAR,LMINF2
     2,PWFM,FREEFB,NODENS,FREEBF,CSAREA,CB,RE2,CHENG
  951 FORMAT (1H0,24HTEST SECTION CONDITIONS.//32X,6HPT2 = ,F5.2,6H TORR
     1.,18X,11HMACH NO. = ,F5.2//25X,13HP INFINITY = ,F6.2,9H MICRONS.,1
     22X,13HT INFINITY = ,F6.2,7H DEG.K.//5X,33HDENSITY RATIO (INFINITY/
     3TOTAL) = ,E11.4,11X,18HVISCOSITY RATIO = ,F5.2//27X,11HVELOCITY =
     4,F7.1,7H M SEC.,11X,15HREYNOLDS NO. = ,E11.4,3H /M//7X,31HPITOT TU
     5BE CORRECTION FACTOR = ,F5.3,//30X,8HV BAR = ,F7.5,8H /M. 1/2,15X,
     610HV BAR * = ,F7.5,8H /M. 1/2//28X,10HCHI BAR = ,F5.2,8H /M. 1/2,1
     75X,12HCHI BAR * = ,F5.2,8H /M. 1/2//19X,19HWALL TEMPERATURE = ,F5.
     81,7H DEG.K.,19X,9HT STAR = ,F5.1,7H DEG.K.//1X,37HCHAPMAN-RUBESIN
     9CONSTANTS,INFINITY = ,F5.3,11X,24HLAMBDA,KINETIC THEORY = ,F5.3,4H
     1 MM./31X,7HSTAR = ,F5.3,16X,19HHARNEY AND BAILEY = ,F5.3,4H MM./7X,
     230HFREE MOLECULAR WALL PRESSURE =,F6.3,9H MICRONS.,20X,5HF B =,F6
     3.3,4H MM./21X,16HNUMBER DENSITY =,E11.4,24X,6HB F = ,F5.3,4H MM./2
     4X,35HVISCOSITY COLLISION CROSS SECTION =,E11.4,5H CM 2,3X,21HBODY
     5MOLECULE SPEED =,E11.4,7H M/SEC./4X,33HREYNOLDS NO.BEHIND NORMAL S
     6HOCK =,E11.4,3H /M,8X,19HCHENGS PARAMETER =,E11.4,3H /M)
 1972 RETURN
      END
```

```
      SUBROUTINE MOOT (MRATIO,P)
      REAL LB,LC,LD,MHOT,MCOLD,MRATIO,MRAT,MACH,MNEW,LMINF1,LMINF2,MACH2
     1,ME,MF,LAMBDA,MOLWT,NODENS
      DIMENSION LB(21),LC(21),LD(21),VIS(6),POLY(11),HOLE(18),X(18),VBM(
     118),VBMST(18),XIM(18),XIMST(18),XFB(18),XBF(18),BECKER(18),SI(18),
     2STEM(18),BW(18),WAVANG(100)
      COMMON LB,LC,LD,SC,TO,PO,P,B,C,D,DB,DC,DD,D2B,D2C,D2D,PATM,Z,RHO,H
     1F,SF,B1,A11,A12,A21,A22,B2,TVIB,P1,FLOW,T1,S1F,H1F,Z1,VEL,NO1,NO2,
     2GAMMA,V1,V2,V3,CAL,CONST,RHO1,VIS,TDASH,ETA0,ETA1,TWALL,TO1,TO2,PI
     3,PITDIA,POLY,TGASCO,VIBCON,TVICON,FACTOR,THROAT,TAU,LAMBDA,ME,HOLE
     4,SIGMU,ALPCON,BOLTZ,MOLWT,ALPHA,DELTA
      PATM=P/PO
      P1=P
      ITEST=1
      ITEST2=1
      MCOUNT=1
      T=TO+TGASCO
  200 P=P1
      PATM=P/PO
      IF (T.LT.3500.0) GO TO 250
      IF (ITEST2.EQ.2) GO TO 280
      ITEST2=2
  250 CALL VIRIAL (T)
      CALL THERMO (T,P)
      CALL CHANGE (T,P)
      IF (ITEST.EQ.2) GO TO 240
      IF (MCOUNT.EQ.2) GO TO 210
      IF (MCOUNT.EQ.3) GO TO 230
      FLCOLD=FLOW
      TCOLD=T1
      MCOUNT=2
      T=(TCOLD*((1.0/MRATIO)**2))
      GO TO 200
  210 MRAT=FLOW/FLCOLD
      DELTAM=(MRATIO-MRAT)
      DT=((T1-TCOLD)/(MRAT-1.0))*DELTAM
      TOLD=T1
      T=T1+DT
      OLDMRA=MRAT
      IF (T.LT.2750.0) GO TO 205
      IF (ABS(DT).LT.5.0) GO TO 220
  205 IF (ABS(DT).LT.1.0) GO TO 220
      MCOUNT=3
      GO TO 200
  230 MRAT=FLOW/FLCOLD
      DELTAM=(MRATIO-MRAT)
      DT=((T1-TOLD)/(MRAT-OLDMRA))*DELTAM
      TOLD=T1
      T=T1+DT
      OLDMRA=MRAT
      IF (T.LT.2750.0) GO TO 215
      IF (ABS(DT).LT.5.0) GO TO 220
  215 IF (ABS(DT).LT.1.0) GO TO 220
      GO TO 200
  220 ITEST=2
  240 MRAT=FLOW/FLCOLD
      MRATIO=MRAT
      GO TO 270
  280 WRITE (6,260) T
  260 FORMAT (1H0,60X,42HTOTAL TEMPERATURE CALCULATION HAS REACHED ,F6.1
     1,7H DEG.K.//65X,57HVIRIAL COEFFICIENT DATA IS UNKNOWN AT THESE TEM
     2PERATURES.//70X,23HCALCULATION TERMINATED.)
  270 RETURN
      END
```

```
    SUBROUTINE VIRIAL (T)
    REAL LB,LC,LD,MHOT,MCOLD,MRATIO,MRAT,MACH,MNEW,LMINF1,LMINF2,MACH2
   1,ME,MF,LAMBDA,MOLWT,NODENS
    DIMENSION LB(21),LC(21),LD(21),VIS(6),POLY(11),HOLE(18),X(18),VBM(
   118),VBMST(18),XIM(18),XIMST(18),XFB(18),XBF(18),BECKER(18),SI(18),
   2SIFM(18),PW(18),WAVANG(100)
    COMMON LB,LC,LD,SO,TO,PO,R,B,C,D,DB,DC,DD,D2B,D2C,D2D,PATM,Z,RHO,H
   1F,SF,B1,A11,A12,A21,A22,B2,TVIB,P1,FLOW,T1,S1F,H1F,Z1,VEL,NO1,NO2,
   2GAMMA,V1,V2,V3,CAL,CONST,RHO1,VIS,TDASH,ETA0,ETA1,TWALL,T01,T02,PI
   3,PITDIA,POLY,TGASCO,VIRCON,TVICON,FACTOR,THROAT,TAU,LAMBDA,ME,HOLE
   4,SIGMU,ALPCON,BOLTZ,MOLWT,ALPHA,DELTA
    T=T/(10.0**3)
    B=LB(1)
    C=LC(1)
    D=LD(1)
    DO 300 I=2,21
    B=B+LB(I)*T**(I-1)
    C=C+LC(I)*T**(I-1)
300 D=D+LD(I)*T**(I-1)
    IF (T.LE.1.000) GO TO 310
    D=0.00
    IF (T.LE.1.750) GO TO 310
    C=0.00
310 DB=LB(2)/(10.0**3)
    DC=LC(2)/(10.0**3)
    DD=LD(2)/(10.0**3)
    DO 320 J=3,21
    DB=DB+FLOAT(J-1)*(LB(J)/(10.0**3))*T**(J-2)
    DC=DC+FLOAT(J-1)*(LC(J)/(10.0**3))*T**(J-2)
320 DD=DD+FLOAT(J-1)*(LD(J)/(10.0**3))*T**(J-2)
    IF (T.LE.1.000) GO TO 330
    DD=0.00
    IF (T.LE.1.750) GO TO 330
    DC=0.00
330 DB=DB*T*(10.0**3)
    DC=DC*T*(10.0**3)
    DD=DD*T*(10.0**3)
    D2B=2.0*LB(3)/(10.0**6)
    D2C=2.0*LC(3)/(10.0**6)
    D2D=2.0*LD(3)/(10.0**6)
    DO 340 K=4,21
    D2B=D2B+FLOAT((K-2)*(K-1))*(LB(K)/(10.0**6))*T**(K-3)
    D2C=D2C+FLOAT((K-2)*(K-1))*(LC(K)/(10.0**6))*T**(K-3)
340 D2D=D2D+FLOAT((K-2)*(K-1))*(LD(K)/(10.0**6))*T**(K-3)
    IF (T.LE.1.000) GO TO 350
    D2D=0.00
    IF (T.LE.1.750) GO TO 350
    D2C=0.00
350 D2B=D2B*(T**2)*(10.0**6)
    D2C=D2C*(T**2)*(10.0**6)
    D2D=D2D*(T**2)*(10.0**6)
    T=T*(10.0**3)
    RETURN
    END
```

```
    SUBROUTINE THERMO (T,P)
    REAL LB,LC,LD,MHOT,MCOLD,MRATIO,MRAT,MACH,MNEW,LMINF1,LMINF2,MACH2
   1,ME,MF,LAMBDA,MOLWT,NODENS
    DIMENSION LB(21),LC(21),LD(21),VIS(6),POLY(11),HOLE(18),X(18),VBM(
   118),VBMST(18),XIM(18),XIMST(18),XFB(18),XBF(18),BECKER(18),SI(18),
   2SIFM(18),PW(18)
    COMMON LB,LC,LD,SO,TO,PO,R,B,C,D,DB,DC,DD,D2B,D2C,D2D,PATM,Z,RHO,H
   1F,SF,B1,A11,A12,A21,A22,B2,TVIB,P1,FLOW,T1,S1F,H1F,Z1,VEL,NO1,NO2,
   2GAMMA,V1,V2,V3,CAL,CONST,RHO1,VIS,TDASH,ETA0,ETA1,TWALL,T01,T02,PI
   3,PITDIA,POLY,TGASCO,VIRCON,TVICON,FACTOR,THROAT,TAU,LAMBDA,ME,HOLE
   4,SIGMU,ALPCON,BOLTZ,MOLWT
    Z=1.00+(B*PATM)+(C*PATM**2)+(D*PATM**3)
    RHO=(P*144.0)/(Z*R*T)
    TRAT=T/TO
    H=(3.50*R*T)+((R*TVIB)/((EXP(TVIB/T))-1.0))
    HF1=H/(R*TO)
    S=(SO*R)+(3.50*R*ALOG(TRAT))-(R*(ALOG(1.0-EXP(-TVIB/T))))+((R*TVIB
   1/T)/((EXP(TVIB/T))-1.0))
    SF1=S/R
    SF=SF1-(ALOG(PATM))-((B+DB)*PATM)-(((C+DC)/2.0)*(PATM**2))-(((D+DD
   1)/3.0)*(PATM**3))
    HF=HF1-(TRAT*DB*PATM)-((TRAT*DC*(PATM**2))/2.0)-((TRAT*DD*(PATM**3
   1))/3.0)
    RETURN
    END
```

```
      SUBROUTINE CHANGE (T,P)
      REAL LB,LC,LD,MHOT,MCOLD,MRATIO,MRAT,MACH,MNEW,LMINF1,LMINF2,MACH2
     1,ME,MF,LAMBDA,MOLWT,NODENS
      DIMENSION LB(21),LC(21),LD(21),VIS(6),POLY(11),HOLE(18),X(18),VBM(
     118),VBMST(18),XIM(18),XIMST(18),XFB(18),XBF(18),BECKER(18),SI(18),
     2SIFM(18),PW(18),WAVANG(100)
      COMMON LB,LC,LD,SC,TO,PO,R,B,C,D,DB,DC,DD,D2B,D2C,D2D,PATM,Z,RHO,H
     1F,SF,B1,A11,A12,A21,A22,B2,TVIB,P1,FLOW,T1,S1F,H1F,Z1,VEL,NO1,NO2,
     2GAMMA,V1,V2,V3,CAL,CONST,RHO1,VIS,TRASH,ETA0,ETA1,TWALL,TO1,TO2,PT
     3,PITDIA,POLY,TGASCO,VIBCON,TVICON,FACTOR,THROAT,TAU,LAMBDA,ME,HOLE
     4,SIGMU,ALPCON,BOLTZ,MOLWT,ALPHA,DELTA
      H=HF*R*TO
      S=SF*R
      H1=H
      S1F=SF
      H1F=HF
      Z1=Z
      RHO1=RHO
      KCOUNT=1
      LCOUNT=1
      T1=T
  530 IF (T.LT.1750.0) 510,505
  510 DELTAH = (H/20.0)
      GO TO 500
  505 DELTAH = (H/50.0)
  500 H=H-DELTAH
  580 CALL NEWTON (T,P,H,S)
      CALL THERMO (T,P)
      VEL=SQRT(2.0*(H1-(HF*R*TO)))
      RHOVEL=RHO*VEL
      IF (KCOUNT.GT.1) GO TO 540
      RHOU=RHOVEL
      KCOUNT=KCOUNT+1
      GO TO 530
  540 SLOPE=(RHOVEL-RHOU)/DELTAH
      IF (LCOUNT.EQ.2) GO TO 570
      IF (LCOUNT.EQ.3) GO TO 535
      IF (LCOUNT.EQ.4) GO TO 535
      IF (SLOPE.LT.0.00) GO TO 570
      RHOU=RHOVEL
      GO TO 530
  570 DELTAH=H/100.0
      IF (LCOUNT.EQ.1) GO TO 555
      IF (RHOU.GT.RHOVEL) GO TO 515
      H=H+DELTAH
      RHOU=RHOVEL
      GO TO 580
  555 LCOUNT=2
      RHOU=RHOVEL
      H=H+DELTAH
      GO TO 580
  515 RHOMAX=RHOU
      HMAX=H
      DELTAH=H/1000.0
      H=H-DELTAH
      LCOUNT=3
      GO TO 580
  535 IF (RHOMAX-RHOVEL) 545,545,565
  545 RHOMAX=RHOVEL
      IF (ABS(RHOMAX-RHOVEL).GT.0.01) GO TO 501
      DELTAH=H/10000.0
      GO TO 502
  501 DELTAH=H/5000.0
  502 H=H-DELTAH
      LCOUNT=4
      GO TO 580
  565 IF (ABS(RHOMAX-RHOVEL).GT.0.01) GO TO 503
      DELTAH=H/10000.0
      GO TO 504
  503 DELTAH=H/1000.0
  504 H=H-DELTAH
      IF (H.LT.(HMAX*0.99)) GO TO 525
      IF (LCOUNT.NE.4) GO TO 580
  525 RHOU=RHOMAX
      THROAT=(0.0412/12.0)
      FLOW=(22.0/7.0)*((THROAT/2.0)**2)*RHOU
      FLOW=FLOW*3600.0
      CALL VIBRAT (T,P)
      IF (FACTOR.GE.1.000) GO TO 520
      FACTOR=1.000
  520 FLOW=FLOW*FACTOR
      RETURN
      END
```

```
      SUBROUTINE NEWTON (T,P,H,S)
      REAL LB,LC,LD,MHOT,MCOLD,MRATIO,MRAT,MACH,MNEW,LMINF1,LMINF2,MACH2
     1,ME,MF,LAMBDA,MOLWT,NODENS
      DIMENSION LB(21),LC(21),LD(21),VIS(6),POLY(11),HOLE(18),X(18),VBM(
     118),VBMST(18),XIM(18),XIMST(18),XFB(18),XBF(18),BECKER(18),SI(18),
     2STEM(18),PW(18),WAVANG(100)
      COMMON LB,LC,LD,SC,TO,PO,R,B,C,D,DB,DC,DD,D2B,D2C,D2D,PATM,Z,RHO,H
     1F,SF,B1,A11,A12,A21,A22,B2,TVIB,P1,FLOW,T1,S1F,H1F,Z1,VEL,NO1,NO2,
     2GAMMA,V1,V2,V3,CAL,CONST,RHO1,VIS,TDASH,ETA0,ETA1,TWALL,TO1,TO2,PI
     3,PITDIA,POLY,TGASCO,VIBCON,TVICON,FACTOR,THROAT,TAU,LAMBDA,ME,HOLE
     4,SIGMU,ALPCON,BOLTZ,MOLWT,ALPHA,DELTA
      JCOUNT=1
  610 PATM=P/PO
      TRAT=T/TO
      CALL VIRIAL (T)
      CALL FNS (T,P,H,S)
      CHECK=(A12*A21-A22*A11)/A12
      IF (ABS(CHECK).LT.1.0E-04) GO TO 680
      DELTAT=((B1*A22/A12)-B2)/(A21-(A22*A11/A12))
      DELTAP=-((B1+(A11*DELTAT))/A12)
  690 T=T+DELTAT
      P=P+DELTAP
      PATM=P/PO
      IF (JCOUNT.GT.1) GO TO 600
      JCOUNT=JCOUNT+1
      GO TO 610
  600 IF(ABS(B1).LT.0.01) GO TO 620
      JCOUNT=JCOUNT+1
      IF (JCOUNT.GT.75) GO TO 640
      IF (JCOUNT.EQ.50) GO TO 660
      GO TO 610
  620 IF (ABS(B2).LT.0.01) GO TO 630
      JCOUNT=JCOUNT+1
      IF (JCOUNT.GT.75) GO TO 640
      IF (JCOUNT.EQ.50) GO TO 660
      GO TO 610
  680 WRITE (6,651)
  651 FORMAT (1H0,60X,45HCALCULATION HAS PASSED THROUGH A SINGULARITY.)
      T=T-ABS(DELTAT)
      P=P-ABS(DELTAP)
  630 RETURN
  660 WRITE (6,670) JCOUNT
  670 FORMAT (1H0,60X,36HWARNING,NEWTONS METHOD ITERATIONS = ,I2)
      GO TO 610
  640 WRITE (6,650) JCOUNT
  650 FORMAT (1H0,60X,26HNEWTONS METHOD HAS FAILED.,I3)
      RETURN
      END


      SUBROUTINE VIBRAT (T,P)
      REAL LB,LC,LD,MHOT,MCOLD,MRATIO,MRAT,MACH,MNEW,LMINF1,LMINF2,MACH2
     1,ME,MF,LAMBDA,MOLWT,NODENS
      DIMENSION LB(21),LC(21),LD(21),VIS(6),POLY(11),HOLE(18),X(18),VBM(
     118),VBMST(18),XIM(18),XIMST(18),XFB(18),XBF(18),BECKER(18),SI(18),
     2STEM(18),PW(18),WAVANG(100)
      COMMON LB,LC,LD,SC,TO,PO,R,B,C,D,DB,DC,DD,D2B,D2C,D2D,PATM,Z,RHO,H
     1F,SF,B1,A11,A12,A21,A22,B2,TVIB,P1,FLOW,T1,S1F,H1F,Z1,VEL,NO1,NO2,
     2GAMMA,V1,V2,V3,CAL,CONST,RHO1,VIS,TDASH,ETA0,ETA1,TWALL,TO1,TO2,PI
     3,PITDIA,POLY,TGASCO,VIBCON,TVICON,FACTOR,THROAT,TAU,LAMBDA,ME,HOLE
     4,SIGMU,ALPCON,BOLTZ,MOLWT,ALPHA,DELTA
C
C     COMPUTE VIBRATIONAL TEMPERATURE AND EQUILIBRIUM FLOW.
C
      E(X)=TV/(EXP(TV/X)-1.0)
      C(X)=((((((((2.0*GAMMA)/(GAMMA-1.0))*(1.0-X))+(2.0*(E(1.0)-E(X))))
     1/X)-1.0)*(((E(X)/X)**2)*EXP(TV/X)))+((2.0/((GAMMA-1.0)*X))*(E(1.0)
     2-E(X))))
      TV=TVIB/T
      TST=0.8
   10 TT=TST
      TST=2.0*GAMMA/(GAMMA*(GAMMA+1.0)-((GAMMA-1.0)**2)*C(TT))
      IF (ABS(TST/TT-1.0).GT.1.0E-05) GO TO 10
      UT=SQRT((((2.0*GAMMA)/(GAMMA-1.0))*(1.0-TST))+(2.0*(E(1.0)-E(TST))
     1))
      ME=UT*(TST**(1.0/(GAMMA-1.0)))*((1.0-EXP(-TV))/(1.0-EXP(-TV/TST)))
     1*EXP((E(TST)-E(1.0))/TV)
C
C     COMPUTE RATE PARAMETER AND FREEZING EFFECT.
C
      P=P/14.7
      TAU=((VIBCON/P)*EXP(TVICON/(T**0.333)))
      LAMBDA=(THROAT/(TAU*SQRT(P*T)))
      DM=(1.0+TANH(ALOG10(LAMBDA/4.2)))/2.0
      MF=SQRT(GAMMA*(2.0/(GAMMA+1.0))**((GAMMA+1.0)/(GAMMA-1.0)))
      FACTOR=(MF-DM*(MF-ME))/ME
      RETURN
      END
```

```
      SUBROUTINE FNS (T,P,H,S)
      REAL LB,LC,LD,MHOT,MCOLD,MRATIO,MPAT,MACH,MNEW,LMINF1,LMINF2,MACH2
     1,ME,MF,LAMBDA,MOLWT,NODENS
      DIMENSION LB(21),LC(21),LD(21),VIS(6),POLY(11),HOLE(18),X(18),VBM(
     118),VBMST(18),XIM(18),XIMST(18),XFB(18),XBF(18),BECKER(18),SI(18),
     2SIFM(18),PW(18)
      COMMON LB,LC,LD,SO,TO,PO,R,B,C,D,DB,DC,DD,D2B,D2C,D2D,PATM,Z,RHO,H
     1F,SF,B1,A11,A12,A21,A22,B2,TVIB,P1,FLOW,T1,S1F,H1F,Z1,VEL,NO1,NO2,
     2GAMMA,V1,V2,V3,CAL,CONST,RHO1,VIS,TDASH,ETA0,ETA1,TWALL,TO1,TO2,PI
     3,PITDIA,POLY,TGASCO,VIBCON,TVICON,FACTOR,THROAT,TAU,LAMBDA,ME,HOLE
     4,SIGMU,ALPCON,BOLTZ,MOLWT
      B1=((3.50*T)-(DB*PATM*T)-((DC*T*(PATM**2))/2.0)-((DD*T*(PATM**3))/
     13.0)-(H/R)+(TVIB/(EXP(TVIB/T)-1.0)))/TO
      A11=(3.50-(PATM*(D2B+(2.0*DB)))-(((PATM**2)/2.0)*(D2C+(2.0*DC)))-(
     1((PATM**3)/3.0)*(D2D+(2.0*DD)))+(((TVIB/T)**2)*((EXP(TVIB/T))/(((E
     2XP(TVIB/T))-1.0)**2))))/TO
      A12=-(1.0/PO)*(DB+(DC*PATM)+(DD*(PATM**2)))
      B2=(3.50*ALOG(T/TO))-(ALOG(PATM))-(PATM*(B+DB))-((PATM**2)*((C+DC)
     1 /2.0))-((PATM**3)*((D+DD)/3.0))+(SO-(S/R))+((TVIB/T)/((EXP(TVIB/T
     2))-1.0))-(ALOG(1.0-(EXP(-TVIB/T))))
      A21=(3.50/T)-((TVIB/(T**2))*EXP(-TVIB/T))/(1.0-(EXP(-TVIB/T)))+(((
     1TVIB/(T**2))*(((EXP(TVIB/T))*((TVIB/T)-1.0))+1.0))/(((EXP(TVIB/T))
     2-1.0)**2))-((PATM/T)*(2.0*DB+D2B))-(((PATM**2)/(2.0*T))*(2.0*DC+D2
     3C))-(((PATM**3)/(3.0*T))*(2.0*DD+D2D))
      A22=-(1.0/PO)*((1.0/PATM)+(B+DB)+((C+DC)*PATM)+((D+DD)*(PATM**2)))
      RETURN
      END
```

```
      SUBROUTINE PITOT (RATIO,MACH)
      REAL LB,LC,LD,MHOT,MCOLD,MRATIO,MPAT,MACH,MNEW,LMINF1,LMINF2,MACH2
     1,ME,MF,LAMBDA,MOLWT,NODENS
      DIMENSION LB(21),LC(21),LD(21),VIS(6),POLY(11),HOLE(18),X(18),VBM(
     118),VBMST(18),XIM(18),XIMST(18),XFB(18),XBF(18),BECKER(18),SI(18),
     2SIFM(18),PW(18)
      COMMON LB,LC,LD,SO,TO,PO,R,B,C,D,DB,DC,DD,D2B,D2C,D2D,PATM,Z,RHO,H
     1F,SF,B1,A11,A12,A21,A22,B2,TVIB,P1,FLOW,T1,S1F,H1F,Z1,VEL,NO1,NO2,
     2GAMMA,V1,V2,V3,CAL,CONST,RHO1,VIS,TDASH,ETA0,ETA1,TWALL,TO1,TO2,PI
     3,PITDIA,POLY,TGASCO,VIBCON,TVICON,FACTOR,THROAT,TAU,LAMBDA,ME,HOLE
     4,SIGMU,ALPCON,BOLTZ,MOLWT
      RATIOX=RATIO*10000.0
      MACH=3.21*RATIOX**2-10.61*RATIOX+27.70
      I=1
      A=(GAMMA+1.0)
      B=(2.0*GAMMA)
      C=(GAMMA-1.0)
  800 FM=(((((A/((B*MACH**2)-(C))))**(1.0/C))*(((A*MACH**2)/((C*MACH**2)
     1+2.0))**(GAMMA/C)))-RATIO)
      DFM=(((A*MACH**2)/((C*MACH**2)+2.0))**(GAMMA/C))*((A/((B*MACH**2)-
     1C))**(1.0/C))*((14.00/(MACH*((C*MACH**2)+2.0)))-((5.0*B*MACH)/((B*
     2MACH**2)-C)))
      MNEW=MACH-FM/DFM
      IF (ABS(MACH-MNEW).LT.1.0E-06) GO TO 810
      IF (I.GT.25) GO TO 820
      I=I+1
      MACH=MNEW
      GO TO 800
  810 MACH=MNEW
      RETURN
  820 WRITE (6,851) I
  851 FORMAT (1H0,60X,25HITERATION HAS FAILED,I = ,I2)
      RETURN
      END
```

THE AERODYNAMICS OF WINGS IN LOW-DENSITY HYPERSONIC FLOW

R.W. JEFFERY. JULY 1975. Ph.D

AMENDMENT SHEET

DEFINITION OF WAVERIDER INCIDENCE

The gun tunnel data is presented in terms of the effective wedge angle, which is the angle between the wedge defining the flow field and the free stream direction. This definition is used throughout for all graphical data presented as a function of incidence; excepting that in global statements such as "5° waverider at 20°" the meaning is that the plane of the leading edges is at 20° to the flow and the effective wedge angle is, in this case, 15°. This is also true for the angle of incidence quoted in the tabulated data.

UNDEFINED SYMBOLS

CHAPTER 2

$G(g_b, Pr, \beta)$ - Strong interaction displacement thickness function

g_b - Dimensionless coefficient in the expansion of the total enthalpy profile for strong interaction evaluated at the body

Pr - Prandtl number

β - Coefficient in expression for the rate of change of displacement thickness

d - Effective molecular diameter

g - Relative molecular velocity

K - Boltzmann's constant

Γ - Gamma function

CHAPTER 3

S - Molecular speed ratio
U - Free stream velocity
R - Gas constant
T_g - Gas temperature at the wall
n_t - Total number density; incident stream plus wall molecules

CHAPTER 5

K_b - Hypersonic similarity parameter based on body angle
M_2 - Mach number downstream of shock (Hayes and Probstein)
M_1 - Mach number downstream of shock (Creager)
T_r - Recovery temperature
T_B - Back face temperature
h - Heat transfer rate
K - Thermal conductivity
α - Thermal diffusivity
c - Specific heat
t - Time

CHAPTER 7

H - Enthalpy
K^2 - Cheng's thin shock layer parameter

APPENDIX

C_s - Chapman-Rubesin constant
ν - Kinematic viscosity
$A(x)$ - Variation of cross-sectional area
$\dot{m}$ - Mass flow rate
Z - Compressibility factor
σ - Vibrational energy
$\bar{\sigma}$ - Local equilibrium value of σ corresponding to translational temperature
θ_v - Characteristic vibrational temperature
D_o - Constant in Widom's expression
$*$ - Subscript; throat conditions